

**ANAEROBIC AND PHOTOCATALYTIC TREATMENT OF  
TEXTILE AND DISTILLERY WASTEWATER IN  
INTEGRATED FLUIDIZED BED REACTORS**

Report to the  
**Water Research Commission**

by

**O Aoyi, MS Onyango, S Apollo, J Akach, N Nyembe, B Otieno & T Brooms**  
Centre for Renewable Energy and Water,  
Vaal University of Technology

**WRC Report No. 2388/1/18**

**ISBN 978-1-4312-0998-9**

**January 2017**

Obtainable from:

**Water Research Commission  
Private Bag X03  
Gezina, 0031**

[orders@wrc.org.za](mailto:orders@wrc.org.za) or download from [www.wrc.org.za](http://www.wrc.org.za)

**DISCLAIMER**

This report has been reviewed by the Water Research Commission (WRC) and approved for publication. Approval does not signify that the contents necessarily reflect the views and policies of the WRC, nor does mention of trade names or commercial products constitute endorsement or recommendation for use.

**Printed in the Republic of South Africa**

**© WATER RESEARCH COMMISSION**

## **EXECUTIVE SUMMARY**

### **Introduction**

Wastewater treatment has experienced many challenges in recent years. On the one hand this has been due to the stringent environmental laws governing discharge limits; on the other hand, due to the emerging contaminants that do not lend themselves to conventional treatment methods. Of prime focus is the poor performance of many anaerobic systems run by municipalities in South Africa. There are numerous challenges related to both the management and technical issues concerning design capacity of the systems and the changing characteristics of the wastes treated.

The response to these challenges has been an effort to develop more robust but low-cost treatment methods. To obtain an optimal balance between cost and robustness, significant amount of scientific and engineering work needs to be done to exploit the competencies at the interface of the relevant disciplines. In this regard, there are several approaches that have been employed recently, including two main ones. The first approach is the integration of conventional methods (biodegradation) with advanced methods (advanced oxidation processes). The second approach is the process intensification often coupled with simulation and modelling techniques. Previous research has shown that integrating biological process with heterogeneous photocatalysis improves the performance of anaerobic digesters. Further, the performance of the integrated systems can be improved through reactor choice and process intensification, in which individual reactors are optimised.

Fluidized bed reactors (FBRs) are of special interest due to their high performance during multiphase operations such as heterogeneous photocatalytic degradation of biorecalcitrant wastewater. The performance of heterogeneous systems depends largely on hydrodynamic and mass transfer processes. To improve the performance of these systems, computational fluid dynamics (CFD) have been used to optimise reactor configuration and hydrodynamic conditions. In the present work, systematic investigations into photodegradation and biodegradation were carried out using biorecalcitrant wastes in several types of FBRs. The initial study focused on preparing and characterising the catalyst, which was later applied in FBRs. Finally, simulation and modelling techniques were employed with the aim of optimising the operating conditions.

### **Nanohybrid photocatalyst preparation, characterisation and application**

Distillery and textile wastewater are some of the most polluting industrial wastewater streams due to the biorecalcitrant nature of some of the chemicals in them. Therefore, many researches have been done to find economical methods of treating such wastewater. The best treatment method has been anaerobic digestion (AD) due to its ability to handle high organic loads and produce biogas energy in the process. However, since anaerobic digesters cannot effectively remove biorecalcitrant chemicals in the distillery and textile wastewater, alternative treatment methods that can be coupled to AD have been studied. Therefore, in this study, a combined AD–photocatalysis treatment method is proposed as a solution to the high-strength biorecalcitrant compounds in the wastewater. Furthermore, of the several reactors that have been employed for AD and photocatalysis, FBRs have shown high reaction rates due to their good

heat and mass transfer at low energy expense. The RBRs will be used in the combined AD–photocatalysis system and the reactors will be optimised using a CFD simulation. The optimisation of systems such as FBRs requires using CFD techniques, which will be employed in this study.

### **Aims and objectives**

The aim of this work was to investigate factors that influence the performance of integrated biodegradation and photodegradation within the context of toxic reduction and bioenergy production. To achieve the aims and objectives, the work was divided into different parts: starting from catalyst preparation to optimisation of the operation parameters using different simulation and modelling techniques.

### **Catalyst composite**

There is an increasing use of composite materials in photocatalysed remediation of wastes such as molasses wastewater (MWW), which is characterised by a high organic load and a characteristic dark-brown colour caused by biorecalcitrant melanoidin compounds. A study was carried out to determine the photocatalytic efficiency of a TiO<sub>2</sub>–ZnO hybrid supported onto activated carbon (AC) to treat MWW. Immobilisation of ZnO onto synthesised TiO<sub>2</sub> formed TiO<sub>2</sub>–ZnO, which was then supported onto AC forming TiO<sub>2</sub>–ZnO–AC. X-ray diffraction, scanning electron, energy-dispersive X-ray, Fourier transform infrared spectroscopies, and transmission electron microscopy revealed the successful hybridisation of TiO<sub>2</sub> and ZnO, and the subsequent support of the hybrid onto AC. Photoluminescence spectroscopy further revealed a restrained electron-hole pair recombination resulting from both the successful formation of a heterojunction in the hybrid, and the introduction of electron-accepting AC support. Photodegradation carried out in batch was monitored in terms of colour and total organic carbon (TOC) reductions, and nitrate formation. The TiO<sub>2</sub>–ZnO hybrid, due to the observed optical properties, had better activity than both TiO<sub>2</sub> and ZnO on their own. On supporting the hybrid onto AC, both adsorption and photocatalytic activities were further enhanced from 68% to 86% with improved overall colour removal. Photodegradation followed pseudo-first-order with the rate constant ( $k_{app}$ ) decreased from 0.0701 min<sup>-1</sup> to 0.0436 min<sup>-1</sup> with increased MWW initial concentration from 3000 ppm to 4000 ppm, while formation of nitrates confirmed the degradation of colour-causing melanoidins. The ultraviolet (UV) photodegradation process was found to be 33-fold less energy intensive for colour reduction than TOC reduction, with energy demands of 35 kWh/m<sup>3</sup> and 1183 kWh/m<sup>3</sup>, respectively. Sorption of MWW onto TiO<sub>2</sub>–ZnO–AC fitted well with the Freundlich isotherm and was found to be endothermic in nature with chemisorption being the rate-determining step. An optimum pH of 5 for the degradation process was determined. The robustness of the composite TiO<sub>2</sub>–ZnO–AC photocatalyst was revealed by its high reusability.

### **Reaction kinetics**

The kinetic analysis of an anaerobic fluidized bed bioreactor treating distillery effluent was carried out. The hydraulic retention time was varied between three days and 20 days while the organic loading rate (OLR) was varied between about 0.33 kg and 9 kg chemical oxygen demand (COD)/m<sup>3</sup>.d corresponding to a TOC loading rate between 0.25 to 8.1 kg TOC/m<sup>3</sup>.d.

The degradation followed first-order kinetics and fitted Michaelis–Menten kinetic model for substrate utilisation. The kinetic analysis showed that 9% of the TOC was non-biodegradable, which corresponds to about 14% COD. The non-biodegradable component was responsible for the dark-brown colour of the distillery effluent; therefore, there was a need to employ a post-treatment technology for their removal. Biomass yield was found to be 0.4658 g/g while the decay coefficient of endogenic microorganisms was 0.0293, which suggested that there was a need to install a sludge-handling unit prior to post-treatment. The maximum microorganism growth rate was found to be 0.136 d<sup>-1</sup> while the specific growth rate of the microorganisms reduced with an increase in hydraulic retention time (HRT) at constant feed concentration. The specific substrate utilisation rate was found to increase linearly with an increase in the ratio of food to microorganisms. The mean cell residence time was found to be at least 2.5 times the HRT due to application of zeolite as microbial support in the reactor.

### **Integrated AD-UV system**

AD can remove substantial amounts of organic load when applied in treating distillery effluent but it is ineffective in colour reduction due to the presence of traces of biorecalcitrant melanoidins. The UV photocatalysis applied as a post-treatment method can be used to remove colour from anaerobically digested effluent. A study on a combined AD and photodegradation treatment of distillery effluent was carried out in fluidized bed batch reactors to evaluate TOC and colour reduction. AD as a stand-alone process removed 78% TOC and 41% colour. The combined process improved colour removal from 41% to 85% compared with that of AD employed as a stand-alone process. Photodegradation post-treatment mineralised the biorecalcitrant melanoidins via a reductive pathway as was indicated by the formation of NH<sub>4</sub><sup>+</sup> in large quantities compared with NO<sub>3</sub><sup>-</sup>. The bioenergy production by the AD step was 14.2 kJ/g TOC biodegraded while UV lamp energy consumption was 900 kJ/g TOC degraded. Electrical energy per order analysis for the photodegradation process showed that the bioenergy produced was 20% of that required by the UV lamp to photodegrade 1 m<sup>3</sup> of undiluted pre-AD treated effluent up to 75% colour reduction. It was concluded that a combined AD-UV system for treatment of distillery effluent is effective in organic load removal and can be operated at a reduced cost.

### **Determination of optimal parameters using response surface methodology (RSM)**

The effects of operating parameters on the performance and energy efficiency of an integrated AD and UV photodegradation were studied. RSM was applied to model the effects of operating parameters on bioenergy production and energy demand of photodegradation with a view to developing a sustainable process in which the biological step could supply energy to the energy intensive photodegradation step. The organic loading rate (OLR<sub>AD</sub>) and hydraulic retention time (HRT<sub>AD</sub>) of the initial biological step were the variables investigated. It was found that the initial biological step removed about 90% of COD and only about 50% of the colour while the photodegradation post-treatment removed 98% of the remaining colour. The energy demand of the UV lamp was lowest at low OLR<sub>AD</sub> irrespective of HRT<sub>AD</sub>, with values ranging between 87 kWh/m<sup>3</sup> and 496 kWh/m<sup>3</sup>. Energy analysis further showed that the electricity requirement of the UV lamp in photodegradation was 80% of the total energy requirement of a fluidized bed photoreactor while mixing consumed 20% of electricity. The AD process

produced 59 kWh/m<sup>3</sup> of electricity that could supplement the electricity demand of the UV lamp by 30% leading to operational cost reduction of about USD 4.8/m<sup>3</sup>. The presumed carbon dioxide emission reduction when electricity from bioenergy was used to power the UV lamp was 28.8 kg CO<sub>2</sub>e/m<sup>3</sup>. Thus, the combined process was effective in removing pollution at a reduced energy cost.

### **CFD modelling and simulation of hydrodynamics**

A comprehensive study was conducted on the hydrodynamics in an FBR used for the photodegradation of petroleum wastewater. The reactor consisted of a cylindrical section and a conical top section (for degassing). The purpose of the study was to apply RSM and CFD to optimise the operating conditions for the photodegradation process in an FBR. This was done by investigating the hydrodynamics, photodegradation efficiency and reaction kinetics that gave a holistic view on the performance of the FBR. The hydrodynamic study focused on modelling the flow behaviour and turbulence properties due to their substantial impact on the design and performance of the FBR. The simulation results were compared with experimental data (obtained from literature) and the desirability function was used to numerically optimise the response variable. A combination of a fine grid size, second-order upwind discretization scheme and a small time step size (0.001) gave the best desirability (0.999). RSM was used to investigate and optimise the photodegradation operating parameters. The maximum degradation efficiency in the current study was found to be 65.9%, which is relatively low when compared with literature. This was attributed to the increase in the catalyst particle size from nanometre to micrometre. Furthermore, the second-order model developed using analysis of variance presented a sufficient correlation to the photodegradation experimental data values. It was noted that the agreement of the simulation data with the experimental results shows that the developed model is effective and may be applied to study other phenomena such as mass transfer.

### **Modelling radiation distribution using the Monte Carlo method**

In this work, the photon distribution in an annular slurry bubble column photocatalytic reactor was simulated using the Monte Carlo method. The effect of catalyst loading and air flow rate on the total transmitted radiation (TTR) and volumetric rate of energy absorption (VREA) was investigated. Very good agreement was obtained between experimental and simulated TTR values at different catalyst loadings and air flow rates. The catalyst showed forward scattering behaviour with a Henyey–Greenstein scattering parameter of 0.81. An increase in the catalyst loading resulted in a decrease in the TTR and an increase in the VREA. Air flow rate had a negligible effect on both the TTR and VREA. This was attributed to the insignificance of bubble scattering as compared with catalyst scattering and the fact that air flow did not significantly affect catalyst agglomeration. For Monte Carlo simulation in the bubble column reactor, the influence of bubbles could be neglected without significant loss in accuracy. For the reactor used and light source, the optimum catalyst loading was found to be 0.4 g/L.

## **Concluding remark**

In our earlier Water Research Commission project, it was shown that the sequence of integrating the AD-advanced oxidation process depends on the type of wastewater. This study, which was a further development of the previous study, has now shown that the AD process can generate energy that can help reduce the cost of running the advanced oxidation process. The performance of the integrated process depends not only on the sequence but also on the hydraulic retention in the AD. The study further showed that different simulation and modelling techniques such as CFD, Monte Carlo and RSM can be used to design and optimise the operating parameters. Future work is needed to improve the performance indicators such as mixing, irradiation penetration or distribution, mass transfer and catalyst efficiency.

## **ACKNOWLEDGEMENT**

We acknowledge the support, advice and stimulating discussions, initiated by Dr Valerie Naidoo, Dr Jo Burgess and the entire team of the Reference Group. Your invaluable contribution and dedication to the project enabled us to achieve our goals. The data used in this report is from the work conducted partly or fully by students listed in Tables I-III in the Technology Transfer section.

## **REFERENCE GROUP**

Dr Jo Burgess	Water Research Commission (Chairperson)
Prof. Maurice S Onyango	Tshwane University of Technology
Ms Mapula Tshangela	Department of Environmental Affairs
Prof. Bobby E Naidoo	Vaal University of Technology
Prof. Freeman Ntuli	University of Johannesburg
Dr J-F Talbot	Talbot & Talbot Ltd
Mr. Jeeten Nathoo	NuWater Ltd
Prof. Sehliselo Ndlovu	University of the Witwatersrand
Prof. Thokozani Majozi	University of the Witwatersrand

## TECHNOLOGY TRANSFER

### BTech degrees, graduated and current (2016)

The BTech students listed in Table I (55 in total) are only those that worked on BTech research projects related to the Water Research Commission (WRC) project, and for which the running costs were carried by the project. However, not all the students listed necessarily received bursaries from the WRC project. Table I shows that the number of students increased from 2014 since some of our master's students graduated in 2013–2015 and then registered for PhD. They have been able to mentor an increasing number of the BTech students and hence supported the main supervisors.

**Table I: BTech students' projects**

2014			2015			2016		
#	Name	Nationality	#	Name	Nationality	#	Name	Nationality
1	Boroko KP		1	Chauke MJ		1	Bhengu, S	
2	Khune MS		2	Khuzwayo Zv		2	Davhana, A	
3	Kubayi VV		3	Mabuza JN		3	Gcukui, PN	
4	Lephallo JT		4	Malahlela GM		4	Ilunga, OM	
5	Mafokoane MA		5	Malete T		5	Lehloo, LP	
6	Maga RM		6	Matjokana NY		6	Lehoko, KP	
7	Maleka M		7	Matshediso BP		8	Lephallo, JT	
8	Matlala NP		8	Mavuso BP		9	Mamugudubi, R	
9	Mogale T		9	Menzi BG		10	Manganye, CC	
10	Mongwe NT		10	Mhlanga RJ		11	Mashile, TTM	
11	Moshoeu A		11	Moitlobo M		12	Masilela, M	
12	Motlounng MM		12	Molokele PM		13	Mbadaliga, ID	
13	Myesi NA		13	Mphahlele K		14	Monika, N	
14	Pretorius J		14	Mphela RKJ		15	Ntsoane, SI	
			15	Msimanga WJ		16	Qhamakoane, LS	
			16	Nkosi TP		17	Runganani, P	
			17	Thulari VR		18	Serage, VM	
			18	Tladi DE		19	Tegua, J	
			19	Tshautshau R		20	Tisane, KR	
						21	Tlhabanelo, KO	
						22	Tsimane, VD	

## Graduated Masters and Doctorate students

It is important to note that a good number of our students who finished their MTech degrees registered for doctoral degrees and continued to work on topics related to this project even though bursaries were not necessarily from this project. The running costs of these postgraduates' projects were taken care of largely by the current WRC projects.

**Table II: MTech degrees graduated**

	<b>Name</b>	<b>Degree</b>	<b>Nationality</b>	<b>Institution</b>	<b>Year completed</b>	<b>Gender</b>
1	Baloyi J	MTech	South African	VUT	2015	M
2	Seadira T	MTech	South African	VUT	2015	M
3	Pete K	MTech	South African	VUT	2014	F
4	Mlungisi AM	MTech	South African	TUT	2016	M
5	Kesi J	MTech	South African	UJ	2016	M
6	Akach J	MTech	Kenyan	VUT	2014	M
7	Apollo S	MTech	Kenyan	VUT	2013	M
8	Mukosha L	DTech	Zambian	TUT	2015	M

**Table III: In progress: master's and doctorate degrees**

	<b>Name</b>	<b>Degree</b>	<b>Nationality</b>	<b>Institution</b>	<b>Gender</b>
1	Nyembe N	MTech	South African	VUT	M
2	Akach J	PhD	Kenyan	VUT	M
3	Apollo S	PhD	Kenyan	VUT	M
4	Brooms T	DTech	South African	TUT	M
5	Kittinya J	DTech	Kenyan	TUT	M
6	Pete K	PhD	South African	VUT	F
7	Achisa M	DTech	Kenyan	TUT	M
8	Mabuza J	MTech	South Africa	VUT	F
9	Otieno B	MTech	Kenya	VUT	M

## Publications in peer-reviewed journals

Apollo, S. & Ochieng, A. (2016). Combined anaerobic digestion and photocatalytic treatment of distillery effluent in fluidised bed reactors focusing on energy conservation, *Environmental Technology (United Kingdom)*, 37(17), 2243–2251.

Apollo, S., Moyo, S., Mabua, G. & Ochieng, A. (2014). Solar photodegradation of methyl orange and phenol using silica supported ZnO catalyst. *International Journal of Innovation, Management and Technology*, 5(3), 203–206.

Apollo, S., Onyango, M.S. & Ochieng, A. (2014). Integrated UV photodegradation and anaerobic digestion of textile dye for efficient biogas production. *Chemical Engineering Journal*, 245, (241–247).

Apollo, S., Onyango, M.S. & Ochieng, A. (2014). UV/H<sub>2</sub>O<sub>2</sub>/TiO<sub>2</sub>/Zeolite hybrid system for treatment of molasses wastewater. *Iranian Journal of Chemistry and Chemical Engineering*, 33(2), 107–117.

Apollo, S., Onyango, M.S. & Ochieng, A. (2016). Modelling energy efficiency of an integrated anaerobic digestion and photodegradation of distillery effluent using response surface methodology, *Environmental Technology (United Kingdom)*, 37(19), 2435–2446.

Baloyi, J., Seadira, T., Raphulu, M. & Ochieng, A. (2015). Preparation, characterization and growth mechanism of dandelionlike TiO<sub>2</sub> nanostructures and their application in photocatalysis towards reduction of Cr(VI). *Materials Today*, 2, 397–3987.

Brooms, T., Mungondori, H., Onyango, M.S. & Ochieng, A. Photodegradation of phenol using TiO<sub>2</sub>, ZnO and TiO<sub>2</sub>/ZnO catalysts in an annular reactor. *Journal of Water Chemistry and Technology* (Accepted).

Kwena, Y.P., Onyango, M.S., Sillanpää, M. & Ochieng, A. Kinetic modeling of the photocatalytic reduction of Cr(VI) in the presence of dye using composite photocatalyst. *Journal of Chemistry and Chemical Engineering* (Accepted). ISSN 1934–7375, USA.

Mecha, A.C., Onyango, M.S., Ochieng, A. & Momba M.N.B. Effect of process parameters on the ozonation of municipal wastewater. *Journal of Water Science and Technology* (Accepted).

Mecha, A.C., Onyango, M.S., Ochieng, A., Fourie, C.J.S. & Momba, M.N.B. (2016). Synergistic effect of UV–vis and solar photocatalytic ozonation on the degradation of phenol in municipal wastewater: A comparative study. *Journal of Catalysis*, 341, 116–125.

Mecha, A.C., Onyango, M.S., Ochieng, A., Jamil, T.S., Fourie, C.J.S. & Momba, M.N.B. (2016). UV and solar light photocatalytic removal of organic contaminants in municipal wastewater. *Separation Science and Technology (Philadelphia)*, 51(10), 1765–1778.

Mthombeni, N.H., Mbakop, S., Ochieng, A. & Onyango, M.S. Vanadium (V) adsorption isotherms and kinetics using polypyrrole coated magnetized natural zeolite. *Journal of the Taiwan Institute of Chemical Engineers* (Accepted). ISSN 1876–1070.

Mungondori, H.H., Tichagwa, L., Katwire, D.M. & Ochieng, A. Preparation of photo-catalytic copolymer grafted asymmetric membranes (NTiO<sub>2</sub>-PMAA-g-PVDF/PAN) and their application on the degradation of bentazon in water. *Iranian Polymer Journal*, ISSN 1026-1265 (Accepted).

Otieno, B., Apollo, S., Naidoo, B. & Ochieng, A. (2016). Photodecolorisation of melanoidins in vinasse with illuminated TiO<sub>2</sub>-ZnO/activated carbon composite. Submitted to the *Journal of Environmental Science and Health Part A* (Accepted).

Otieno, B., Apollo, S., Naidoo, B. & Ochieng, A. (2016). Photodegradation of molasses wastewater using TiO<sub>2</sub>-ZnO nanohybrid photocatalyst supported on activated carbon. *Chemical Engineering Communications*, 6445(11), 1443–1454.

## Conferences

Akach, J., Onyango, M.S. & Ochieng, A. (2015). Solar photocatalysis and adsorption of the antibiotic sulfamethoxazole in wastewater. *5<sup>th</sup> International Conference on Computer, Electrical, Electronics and Biomedical Engineering (ICCEEBE'2015)*, 16–17 August 2015, Bali, Indonesia, pp. 33–36. ISBN 978-93-84468-29-3.

Apollo, S., Akach, J. & Ochieng, A. (2016). Synergistic effects between photodegradation and biodegradation. *The International Conference on Pure and Applied Chemistry*, 18–22 July 2016, Mauritius.

Benton, O., Apollo, S., Naidoo, B. & Ochieng, A. (2016). Response surface methodology modelling of diazinon photodegradation using TiO<sub>2</sub>-ZnO nanohybrid. *100<sup>th</sup> International Conference on Chemical and Biochemical Engineering (ICCBE)*, 29–30 December 2016, Jerusalem, Israel.

Benton, O., Naidoo, B. & Ochieng, A. (2015). Adsorption and photodegradation of molasses wastewater using TiO<sub>2</sub>-ZnO nanocomposite supported on activated carbon. *4<sup>th</sup> Regional South African Young Water Professionals Conference and 1<sup>st</sup> African Young Water Professionals Conference (4<sup>th</sup> YWP-ZA Biennial and 1<sup>st</sup> African YWP Conference)*, 16–18 November 2015 Pretoria.

Benton, O., Naidoo, B. & Ochieng, A. (2015). Photodegradation of molasses wastewater using TiO<sub>2</sub>-ZnO hybrid nanocatalyst for colour removal. *42<sup>nd</sup> National Convention of the South African Chemical Institute Conference*, 29 November–4 December 2015, Durban.

Benton, O., Naidoo, B. & Ochieng, A. (2016). A comparative study of the efficiency of HPLC and UV-vis in monitoring phenol photodegradation using silver doped TiO<sub>2</sub>. *International Conference on Pure and Applied Chemistry: Emerging Trends in Chemical Sciences*, 18–22 July 2016, Mauritius.

Brooms, T.B., Onyango, M.S. & Ochieng, A. (2015). Photocatalytic activity of polyaniline/TiO<sub>2</sub>/ZnO composite for degradation of aromatic compounds in abattoir wastewater. *7<sup>th</sup> International Conference on Climate: Impacts and Responses*, Vancouver, Canada 10–11 April 2015.

Mecha, A.C., Onyango, M.S., Ochieng, A. & Momba, M.N.B. (2014). Enhanced activity of metal doped titanium dioxide in photo catalytic ozonation. *The International Conference on Chemical Engineering and Advanced Computational Technologies (ICCEACT'2014)*, 24–25 November 2014 Pretoria (South Africa) pp. 14–18. ISBN 978-93-84422-00-4, <http://dx.doi.org/10.15242/IIE.E1114010>.

Mecha, A.C., Onyango, M.S., Ochieng, A. & Momba, M.N.B. (2015). Synergistic effect of photocatalytic ozonation in phenol degradation. *2<sup>nd</sup> International Conference on Nanoscience and Nanotechnology*, 2–4 September 2015. The International Institute of Knowledge Management (TIKM) Colombo, Sri Lanka, pp. 19, ISBN: 978-955-4903-32-6.

Mhlanga, R.J., Nyembe, N., Chiririwa, H. & Ochieng, A. (2016). Hydrodynamic conditions and photodegradation of methyl orange in a fluidized bed photoreactor., *Proceedings of 2016 5<sup>th</sup> International Conference on Advances in Engineering and Technology (ICAET'2016)*, 8–9 June 2016, NJ, pp. 23–29, ISBN 978-93-84422-69-1.

Mphela, R.K., Msimanga, W., Kwena, Y.P., Chiririwa, H. & Ochieng, A. (2016). Simultaneous photocatalytic degradation of salicylic acid and reduction of Cr(VI) using TiO<sub>2</sub>, *Proceedings of 2016 5<sup>th</sup> International Conference on Advances in Engineering and Technology (ICAET'2016)*, June 8-9th 2016, New Jersey, pp 30-36, ISBN 978-93-84422-69-1.

Nyembe, N., Ochieng, A. & Letsabisa, L. (2016). CFD simulation of a fluidized bed reactor for petroleum wastewater photodegradation. *10<sup>th</sup> South African Conference on Computational and Applied Mechanics*, Potchefstroom, pp. 1–10.

## TABLE OF CONTENTS

<b>EXECUTIVE SUMMARY .....</b>	<b>iii</b>
<b>ACKNOWLEDGEMENT.....</b>	<b>viii</b>
<b>TECHNOLOGY TRANSFER.....</b>	<b>ix</b>
<b>TABLE OF FIGURES.....</b>	<b>xix</b>
<b>LIST OF TABLES .....</b>	<b>xxii</b>
<b>LIST OF ABBREVIATIONS .....</b>	<b>xxiii</b>
<b>LIST OF SYMBOLS .....</b>	<b>xxiv</b>
<b>1 INTRODUCTION .....</b>	<b>1</b>
1.1 Background .....	1
1.2 Relevance of the Study .....	2
1.3 Significance of the Study .....	2
1.4 Aim and Objectives .....	3
<b>2 LITERATURE REVIEW .....</b>	<b>4</b>
2.1 Wastewater .....	4
2.1.1 Distillery wastewater .....	4
2.1.2 Brewery wastewater .....	4
2.1.3 Textile wastewater.....	5
2.2 Treatment of Distillery and Textile Wastewaters .....	6
2.3 Anaerobic Digestion.....	7
2.3.1 Digester performance .....	7
2.3.2 Operating parameters .....	8
2.3.3 Challenges of AD in the treatment of textile and distillery effluent .....	8
2.4 Photocatalysis.....	9
2.4.1 Mechanism of photocatalysis .....	9
2.4.2 Titanium dioxide photocatalyst .....	11
2.4.3 Supported TiO <sub>2</sub> .....	12
2.4.4 Light sources for photocatalysis.....	14
2.4.5 Effect of inorganic ions on photocatalysis treatment technology .....	15
2.4.6 Challenges of photocatalytic wastewater treatment .....	16
2.5 Integration of AD with Other Treatment Methods.....	16
2.6 Integration With Physico-chemical Methods.....	16
2.7 Reactor Configurations .....	18
2.7.1 Reactor configurations for AD.....	18
2.7.2 Reactor configurations for photocatalysis.....	20
2.7.3 Hydrodynamics modelling of photocatalytic reactors .....	21
2.8 Conclusion.....	25
2.9 References .....	25
<b>3 PHOTODEGRADATION OF MWW USING TiO<sub>2</sub>-ZnO NANOHYBRID PHOTOCATALYST SUPPORTED ON ACTIVATED CARBON.....</b>	<b>32</b>
3.1 Introduction .....	32
3.2 Materials and Methods .....	33

3.2.1	Chemicals and materials.....	33
3.2.2	Preparation of TiO <sub>2</sub> –ZnO nanohybrid and subsequent support onto AC.....	33
3.2.3	Catalyst characterisation .....	34
3.2.4	Adsorption and photocatalytic studies .....	35
3.3	Results and Discussion.....	35
3.3.1	Characterisation studies.....	35
3.3.2	Adsorption and photocatalytic studies .....	40
3.3.3	Photodegradation process.....	46
3.3.4	Comparison of photolysis vs photocatalysis .....	47
3.3.5	Comparison of colour and TOC removal against energy requirement .....	48
3.3.6	Kinetics analysis.....	49
3.3.7	Adsorption isotherms and thermodynamics .....	50
3.4	Conclusion.....	53
3.5	References .....	53
<b>4</b>	<b>PERFORMANCE AND KINETICS OF A FLUIDIZED BED ANAEROBIC REACTOR TREATING DISTILLERY EFFLUENT .....</b>	<b>58</b>
4.1	Introduction .....	58
4.2	Methodology .....	58
4.2.1	Experimental setup.....	58
4.2.2	Start-up and operation of the bioreactor.....	59
4.2.3	Experimental analysis .....	60
4.3	Results and Discussion.....	60
4.3.1	Substrate balance model.....	60
4.3.2	Biorecalcitrant component of distillery effluent .....	62
4.3.3	Substrate utilisation kinetics.....	63
4.3.4	Michaelis–Menten kinetic model .....	64
4.3.5	The mean cell residence time .....	66
4.3.6	Microorganisms’ growth kinetics.....	67
4.3.7	Food-to-microorganism ratio .....	68
4.3.8	MCRT and HRT .....	69
4.3.9	Effect of OLR on AD .....	71
4.3.10	Effect of OLR on biogas production rate .....	71
4.3.11	Effect of OLR on methane production .....	72
4.3.12	Methane production rate and methane yield coefficient .....	72
4.3.13	Effect of OLR on COD and colour reduction .....	73
4.3.14	COD reduction model .....	73
4.3.15	Alkalinity, VFAs and pH .....	75
4.3.16	Effect of OLR on biomass density .....	75
4.4	Conclusion.....	76
4.5	References .....	76

<b>5</b>	<b>COMBINED AD AND PHOTOCATALYTIC TREATMENT OF DISTILLERY EFFLUENT IN BATCH FBR .....</b>	<b>79</b>
5.1	Introduction .....	79
5.2	Methodology .....	79
5.2.1	Materials .....	79
5.2.2	Experimental setup .....	80
5.2.3	Experimental procedure .....	81
5.2.4	Experimental analysis .....	82
5.3	Results and Discussion .....	82
5.3.1	TOC, sulphates and colour reduction .....	82
5.3.2	Biogas production and methane yield .....	83
5.3.3	Alkalinity and pH .....	84
5.3.4	Photodegradation of distillery effluent .....	84
5.3.5	Catalyst loading and catalyst composition .....	84
5.3.6	Colour removal mechanism via $\text{NO}_3^-$ and $\text{NH}_4^+$ evolution during photocatalysis	86
5.3.7	FTIR analysis of the photodegradation process .....	86
5.3.8	Effect of hydrogen peroxide addition .....	87
5.3.9	Photodegradation post-treatment of AD pre-treated effluent .....	89
5.3.10	Combined AD and UV photodegradation .....	89
5.3.11	Energy analysis .....	91
5.3.12	EEO analysis of the combined process for colour reduction .....	91
5.4	Conclusion .....	92
5.5	References .....	93
<b>6</b>	<b>MODELLING THE ENERGY EFFICIENCY OF THE INTEGRATED SYSTEM USING SURFACE RESPONSE METHODOLOGY .....</b>	<b>96</b>
6.1	Introduction .....	96
6.2	Methodology .....	97
6.2.1	Experimental procedure .....	97
6.2.2	Energy analysis .....	97
6.2.3	Experimental design and modelling .....	98
6.2.4	Data analysis .....	99
6.2.5	Experimental analysis .....	99
6.3	Results and Discussion .....	100
6.3.1	Characteristics of distillery effluent .....	100
6.3.2	Determination of the recalcitrant component of distillery effluent .....	100
6.3.3	Performance of the continuously operated fluidized bed anaerobic bioreactor	101
6.3.4	Effects of biodigester parameters on the UV post-treatment .....	102
6.3.5	Kinetics of the integrated process .....	103
6.3.6	Energy efficiency of the integrated AD-UV process .....	104
6.3.7	RSM and ANOVA .....	105

6.3.8	Energy production by the anaerobic process.....	107
6.3.9	UV photodegradation energy consumption.....	109
6.3.10	Energy ratio .....	109
6.3.11	Electrical energy and CER analysis .....	111
6.3.12	Cost analysis of application of renewable energy in photodegradation.....	112
6.4	Conclusion.....	113
6.5	References .....	114
<b>7</b>	<b>CFD MODELLING .....</b>	<b>117</b>
7.1	Introduction .....	117
7.2	Methodology .....	117
7.2.1	Mathematical modelling.....	117
7.2.2	Numerical approach .....	124
7.2.3	Experimental .....	127
7.2.4	Photodegradation experiments .....	129
7.2.5	Reaction kinetics experiments.....	130
7.3	Results and Discussion.....	131
7.3.1	CFD simulation .....	131
7.3.2	Photodegradation.....	142
7.3.3	Reaction kinetics .....	148
7.4	Conclusion.....	150
7.5	References .....	151
<b>8</b>	<b>LIGHT DISTRIBUTION IN A FLUIDIZED BED PHOTOCATALYTIC REACTOR .....</b>	<b>155</b>
8.1	Introduction .....	155
8.2	Methodology .....	156
8.2.1	Reactor setup .....	156
8.2.2	Monte Carlo model.....	156
8.2.3	TTR experiments.....	157
8.3	Results and Discussion.....	158
8.3.1	Experimental TTR measurements .....	158
8.3.2	Effect of scattering parameter .....	158
8.3.3	Effect of bubbles .....	160
8.4	Conclusion.....	163
8.5	References .....	163
<b>9</b>	<b>OVERALL CONCLUSION.....</b>	<b>165</b>
	<b>APPENDIX.....</b>	<b>167</b>
	<b>Appendix A: Monte Carlo algorithm.....</b>	<b>167</b>
	<b>Appendix B: Anaerobic biodegradation of synthetic abattoir wastewater .....</b>	<b>172</b>

## TABLE OF FIGURES

Figure 1: Schematic diagram showing the generation of oxidative species in a photocatalytic study .	10
Figure 2: Steps in heterogeneous catalytic reaction (Fogler, 1999).....	10
Figure 3: Surface silanol OH groups at the silica surface (Li & Bruyn 1966).....	14
Figure 4: Comparison of the transmittance of a 2 mm thick borosilicate glass and the emission of the ASTM reference solar spectrum (Schott, 2012; National Renewable Energy Laboratory).....	21
Figure 5: TEM images of (a) ZnO, (b) TiO <sub>2</sub> and (c) TiO <sub>2</sub> -ZnO.....	35
Figure 6: SEM images of TiO <sub>2</sub> , ZnO, TiO <sub>2</sub> -ZnO and TiO <sub>2</sub> -ZnO/AC.....	36
Figure 7: XRD patterns of TiO <sub>2</sub> , ZnO, TiO <sub>2</sub> -ZnO and TiO <sub>2</sub> -ZnO/AC .....	37
Figure 8: FTIR spectra of (a) TiO <sub>2</sub> , (b) ZnO, (c) TiO <sub>2</sub> -ZnO, (d) TiO <sub>2</sub> -ZnO-AC and (e) AC .....	38
Figure 9: UV-Vis absorption spectra of TiO <sub>2</sub> (—), ZnO (—) and TiO <sub>2</sub> -ZnO (····).....	39
Figure 10: Photoluminescence spectra of TiO <sub>2</sub> , ZnO, TiO <sub>2</sub> -ZnO and TiO <sub>2</sub> -ZnO-AC .....	40
Figure 11: (a) Effect of TiO <sub>2</sub> composition by weight .....	40
Figure 12: Adsorption (■) and photodegradation (○) of 5000 mg/L MWW with different AC loading on TiO <sub>2</sub> -ZnO at 1 g/L composite loading, pH 5 .....	42
Figure 13: Adsorption and photodegradation of 5000 mg/L MWW with TiO <sub>2</sub> (◆), ZnO (●), TiO <sub>2</sub> -ZnO/AC and TiO <sub>2</sub> -ZnO (Δ) at 1 g/L catalyst loading, pH 5 .....	43
Figure 14: Effect of initial pH, pH 12 (■), pH 9 (●), pH 3 (□), pH 5 (○) and pH 7 (Δ) on adsorption and photodegradation of 4000 mg/L MWW at 1 g/L catalyst loading .....	44
Figure 15: Effect of initial concentration on adsorption and photodegradation of 3000 ppm (○), 4000 ppm (□), 5000 ppm (Δ) and 6000 ppm (●)MWW at pH 5 with 1 g/L catalyst loading.....	45
Figure 16: Effect of catalyst loading on adsorption and photodegradation of 4000 ppm MWW at pH 5 .....	46
Figure 17: NO <sub>3</sub> <sup>-</sup> (Δ) formation, and TOC (○) and colour (■) reduction in the photodegradation of 3000 mg/L MWW using TiO <sub>2</sub> -ZnO-AC at 1 g/L catalyst loading .....	47
Figure 18: Comparison of direct photolysis, and TiO <sub>2</sub> (Aeroxide P25), and TiO <sub>2</sub> -ZnO-AC photocatalysed processes .....	47
Figure 19: Comparison of percentage removal against energy requirement for colour and TOC.....	48
Figure 20: Langmuir (i) and Freundlich (ii) adsorption isotherms for 5000 mg/L MWW sorption onto AC (a) and TiO <sub>2</sub> -ZnO-AC (b) at 25°C .....	52
Figure 21: Plot of $\ln K$ vs $1/T$ for 5000 mg/L MWW sorption onto TiO <sub>2</sub> -ZnO-AC.....	53
Figure 22: Setup of the fluidized bed anaerobic digester.....	59
Figure 23: Determination of methane yield coefficient .....	61
Figure 24: (a) Fraction and (b) actual amount of feed TOC converted into biogas, biomass and that which remained in the effluent.....	62
Figure 25: Determination of recalcitrant component of distillery effluent, TOC (●) and COD (▲) ...	63
Figure 26: First-order reaction kinetic of biodegradable and TOC, biodegradable TOC (Δ) and total TOC (○) .....	64
Figure 27: Specific substrate utilisation rate against biodegradable TOC in the reactor .....	65
Figure 28: A plot of $1/r$ against $1/S_b$ to determine $K$ and $K_s$ .....	65

Figure 29: A comparison of the theoretical and experimental specific substrate utilisation rate .....	66
Figure 30: Correlation between sludge age and specific substrate utilisation rate .....	67
Figure 31: Specific microorganisms' growth rate as a function of HRT at constant feed concentration .....	68
Figure 32: A comparison of HRT and MCRT at different F:M values, HRT ( $\Delta$ ), MCRT ( $\circ$ ) and corresponding OLR ( $\bullet$ ).....	70
Figure 33: Effect of F:M on specific substrate utilisation rate.....	70
Figure 34: Effect of OLR ( $\blacksquare$ ) on biogas production rate ( $\Delta$ ) and effluent load ( $\bullet$ ).....	71
Figure 35: The effect of OLR on methane composition .....	72
Figure 36: Effect of OLR (—) on volumetric methane production rate ( $\blacksquare$ ) and methane yield coefficient ( $\circ$ ) .....	72
Figure 37: Effect of OLR on COD ( $\blacktriangle$ ) and colour-reduction efficiency ( $\blacksquare$ ).....	73
Figure 38: The effect of feed concentration on COD removal rate .....	74
Figure 39: Variation of methane production rate with substrate removal.....	74
Figure 40: Alkalinity ( $\square$ ), VFAs ( $\circ$ ) and pH ( $\blacktriangle$ ) profile during AD .....	75
Figure 41: Effect of OLR on microbial density in the reactor and in the effluent .....	76
Figure 42: Experimental setup for the integrated AD and photodegradation .....	80
Figure 43: Colour, TOC and sulphate reduction during AD: TOC ( $\Delta$ ), colour ( $\square$ ), sulphates ( $\circ$ ) .....	82
Figure 44: Biogas and methane production during the anaerobic process: biogas production ( $\blacksquare$ ), methane yield ( $\circ$ ).....	83
Figure 45: Effect of catalyst loading on adsorption (A) and photodegradation (B) using 50% wt/wt $\text{TiO}_2/\text{SiO}_2$ composite catalyst 5 g/L ( $\bullet$ ), 2 g/L ( $\blacksquare$ ), 1 g/L ( $\blacktriangle$ ), 0.5 g/L ( $\circ$ ).....	85
Figure 46: Effect of catalyst composition on adsorption ( $\circ$ ), photodegradation ( $\square$ ) combined adsorption-photodegradation ( $\blacktriangle$ ) using catalyst loading of 2 g/L .....	85
Figure 47: (a) Colour ( $\blacksquare$ ) and TOC ( $\square$ ) reduction; (b) $\text{NO}_3^-$ ( $\circ$ ) and $\text{NH}_4^+$ ( $\square$ ) formation during photodegradation.....	86
Figure 48: FTIR spectra of distillery effluent at different times of photodegradation.....	87
Figure 49: Effect of hydrogen peroxide dose on colour reduction of distillery effluent.....	88
Figure 50: Effect of hydrogen peroxide on TOC reduction ( $\circ$ ) UV/ $\text{H}_2\text{O}_2$ ( $\square$ ) $\text{TiO}_2/\text{silica}$ catalyst/UV ( $\Delta$ ) $\text{TiO}_2/\text{silica}$ catalyst/UV/ $\text{H}_2\text{O}_2$ .....	88
Figure 51: Effect of dilution on colour and TOC reduction during photodegradation: (a) colour (b) TOC; x10 v/v ( $\circ$ ), x3.3 v/v ( $\square$ ), x2 v/v ( $\Delta$ ), x1 v/v ( $\bullet$ ).....	89
Figure 52: Overall performance of the combined AD and UV photodegradation process.....	90
Figure 53: Electrical energy consumption of the UV lamp at various dilutions ( $\blacksquare$ ) and energy content of the biogas produced by the AD process (---).....	92
Figure 54: Determination of the recalcitrant component of distillery effluent .....	101
Figure 55: Effect of OLR on AD .....	101
Figure 56: Effect of HRT on the AD process .....	102
Figure 57: Effect of biodigester operating parameters on photodegradation post-treatment.....	103
Figure 58: Organic removal rate by the AD process ( $\bullet$ ) and reaction rate constant of photodegradation post-treatment ( $\blacktriangle$ ) at various $\text{OLR}_{\text{AD}}$ .....	104

Figure 59: Effect of $OLR_{AD}$ on the energy efficiency of the integrated process.....	104
Figure 60: Effect of $HRT_{AD}$ on energy efficiency of the integrated process .....	105
Figure 61: A plot of the predicted values from the models against the experimental values .....	107
Figure 62: Response surface plot indicating the effects of $OLR_{AD}$ and $HRT_{AD}$ .....	108
Figure 63: Perturbation plot for energy efficiency.....	110
Figure 64: (a) Electricity consumption .....	112
Figure 65: Electricity consumption cost .....	113
Figure 66: Simulation grid for an FBR .....	125
Figure 67: Experimental setup of a solar photocatalytic FBR .....	130
Figure 68: Effect of discretization scheme and number of cells on a response parameter (error) where the time step size was kept constant (0.001).....	132
Figure 69: Comparison between the simulated and experimental axial liquid profiles at different axial positions.....	134
Figure 70: Comparison between (a) XY plot and (b) vector plot of axial liquid velocity profile .....	135
Figure 71: Comparison between the simulated and experimental gas hold-up profiles at different axial positions.....	136
Figure 72: Comparison between: (a) XY plot and (b) contour plot of radial gas hold-up.....	137
Figure 73: Comparison between the simulated and experimental turbulent kinetic energy profiles at different axial positions.....	138
Figure 74: Comparison between the simulated and experimental turbulent dissipation rate profiles at different axial positions.....	139
Figure 75: Effect of superficial gas velocity on the bubble distribution.....	140
Figure 76: Effect of superficial gas velocity on the global gas hold-up: Comparison between CFD simulation and experimental results.....	141
Figure 77: Effect of reaction and initial pH level on the photodegradation of phenol.....	146
Figure 78: Effect of catalyst loading and initial pH level on the photodegradation of phenol .....	147
Figure 79: Effect of superficial gas velocity and catalyst loading on the photodegradation of phenol .....	148
Figure 80: Linear fit for photodegradation reaction.....	149
Figure 81: Reduction of TOC at different time intervals .....	150
Figure 82: Radiation field measurement setup .....	157
Figure 83: Experimental TTR measurements at different catalyst loadings and air flow rates .....	158
Figure 84: Effect of the Henyey–Greenstein phase function scattering parameter and catalyst loading on the TTR.....	159
Figure 85: Comparison of experimental and simulation TTR values at different catalyst loadings and air flow rates .....	160
Figure 86: VREA at different catalyst loadings and air flow rates .....	161
Figure 87: Sum of photon-bubble and photon-catalyst scattering events at different catalyst loadings and air flow rates.....	162
Figure 88: Comparison of experimental TTR with simulation values carried out by neglecting bubble-photon interactions in the Monte Carlo simulation.....	163

## LIST OF TABLES

Table 1: Characteristics of distillery spent wash generated from cane molasses (Satyawili & Balakrishnan, 2008) .....	4
Table 2: Characteristics of raw beer brewery wastewater (Simate et al., 2011) .....	5
Table 3: Characteristics of textile wastewater (Oller et al., 2011) .....	6
Table 4: Advantages and disadvantages of current dye removal methods from industrial effluents....	17
Table 5: Elemental composition (% weight) from the EDX spectra of ZnO, TiO <sub>2</sub> and TiO <sub>2</sub> -ZnO .....	36
Table 6: Wavelength and calculated band gap of the prepared photocatalysts.....	39
Table 7: Kinetics data for photodegradation.....	50
Table 8: Parameters and efficiencies of the FBR at constant feed flow rate .....	60
Table 9: pH and alkalinity values during AD process .....	68
Table 10: Performance of the reactor at different F:M values .....	69
Table 11: Feed and effluent characteristics at various OLRs and fixed HRT.....	71
Table 12: Characteristics of distillery effluent.....	80
Table 13: Operating parameters for the photoreactor and AD reactor.....	81
Table 14: Alkalinity and pH during the AD .....	84
Table 15: Characteristics of wastewater after two-stage treatment.....	90
Table 16: Energy analysis and performance of the combined process .....	91
Table 17: Experimental range and level of variables.....	99
Table 18: Characteristics of distillery wastewater .....	100
Table 19: Anaerobic digestion at different HRT and constant feed concentration.....	100
Table 20: Overall efficiency of the integrated process .....	103
Table 21: Experiments conducted according to design and the corresponding responses.....	106
Table 22: ANOVA for response surface models .....	106
Table 23: Solution initiation .....	126
Table 24: Interfacial forces obtained from literature .....	126
Table 25: Experimental design .....	129
Table 26: Grid independence study .....	132
Table 27: Optimum setting methods for CFD simulations .....	141
Table 28: Full factorial central composite design experimental matrix with experimental and expected responses .....	142
Table 29: ANOVA of the empirical second-order model.....	144
Table 30: RMSE of different scattering parameter values.....	159

## LIST OF ABBREVIATIONS

2FI	Two-Factor Interaction Model
AC	Activated Carbon
AD	Anaerobic Digestion
AFBR	Anaerobic Fluidized Bed Reactor
ANOVA	Analysis of Variance
AOP	Advanced Oxidation Process
BOD	Biochemical Oxygen Demand
CER	Carbon Dioxide Emission Reduction
CFD	Computational Fluid Dynamics
CNT	Carbon Nanotube
COD	Chemical Oxygen Demand
CSTR	Continuously Stirred Tank Reactor
DF	Dilution Factor
EDX	Energy-Dispersive X-Ray
EEO	Electrical Energy per Order
FBB	Fluidized Bed Bioreactor
FBR	Fluidized Bed Reactor
F:M	Food-to-Microorganism Ration
FTIR	Fourier Transform Infrared
HRT	Hydraulic Retention Time
L-H	Langmuir-Hinshelwood
LVREA	Local Volumetric Rate of Energy Absorption
MCRT	Mean Cell Residence Time
MWW	Molasses Wastewater
OLR	Organic Loading Rate
RMSE	Root Mean Square Error
RSM	Response Surface Methodology
RTE	Radiation Transfer Equation
SEM	Scanning Electron Microscopy
SIMPLE	Semi-Implicit Method for Pressure-Linked Equations
TDS	Total Dissolved Solids
TEM	Transmission Electron Microscopy
TKN	Total Kjeldahl Nitrogen
TOC	Total Organic Carbon
TS	TiO <sub>2</sub> and Silica Xerogel Composite
TSS	Total Suspended Solids
TTIP	Titanium Isopropanol
TTR	Total Transmitted Radiation
UASB	Up-flow Anaerobic Sludge Blanket
UHPLC	Ultrahigh Performance Liquid Chromatography
UV	Ultraviolet
UV-Vis	Ultraviolet-Visible
VFA	Volatile Fatty Acid
VLA	Visible Light Active
VREA	Volumetric Rate of Energy Absorption
VSS	Volatile Suspended Solids
XRD	X-Ray Diffraction

## LIST OF SYMBOLS

$1/n$	Freundlich intensity parameter
$C_0$	Initial substrate concentration ( $mg/L$ )
$C_e$	Equilibrium substrate concentration ( $mg/L$ )
$I_A$	Intensity of anatase (101) phase of $TiO_2$
$I_R$	Intensity of the rutile (110) phase of $TiO_2$
$K_F$	Freundlich capacity factor ( $mg/g(1/mg)^{1/n}$ )
$Q_{EA}$	Equilibrium adsorption capacity of the fresh PAC ( $mg/g$ )
$Q_{EAP}$	Equilibrium adsorption capacity of the spent PAC due to photocatalytic regeneration ( $mg/g$ )
$m_{AP}$	Mass of the substrates adsorbed during the second adsorption due to photocatalytic regeneration ( $g$ )
$m_{AT}$	Mass of substrates adsorbed by the spent PAC during the second adsorption ( $g$ )
$m_{AU}$	Mass of the substrates adsorbed by unsaturated sites during the second adsorption ( $g$ )
$q_m$	Maximum Langmuir adsorption capacity ( $mg/g$ )
$A_0$	Initial absorbance
$A_t$	Absorbance at time $t$
$I_A$	Intensity of anatase
$I_R$	Intensity of rutile
$K$	Langmuir equilibrium adsorption constant ( $L/mg$ )
$K$	Reaction rate constant ( $Min^{-1}$ )
$m$	Mass of the adsorbent ( $g$ )
$\emptyset$	% colour removal
$R^2$	Correlation coefficient
$V$	Volume of the substrate solution ( $L$ )
$X_R$	Mass fraction of rutile
$E$	Methane production coefficient ( $CH_4$ L/g COD removed)
$\chi$	Weight fraction of rutile phase of $TiO_2$
$RE$	Regeneration efficiency (%)
$K_{app}$	Apparent reaction rate constant, $min^{-1}$
$b$	Adsorption reaction rate constant
$d_b, d_g$	Bubble diameter, mm
d.f	Degrees of freedom

$d_i$	Desirability function
$d$	Distance closest to the wall
$H_D$	Displaced height during sparging, mm
$\bar{F}_k^D$	Drag force, N
$C_D$	Drag force coefficient
$\bar{U}_{dr}$	Drift velocity
$L$	Effective length of reactor, m
$E$	Energy supplied by the bubbles, J
$D_{lg}$	Fluid-particulate dispersion tensor
$f$	Friction function
$\epsilon_G$	Global gas hold-up
$\bar{g}$	Gravitational acceleration, m/s <sup>2</sup>
$C_o, C$	Initial and final concentration of organic pollutant, mol/L
$I$	Irradiation intensity
$A_i$	Interfacial area, m
$L_{t,l}$	Length scale
$\bar{F}_k^L$	Lift force, N
$C_L$	Lift force coefficient
$L_s$	Mixing length for the subgrid scales
$N$	Number of experiments
$n_c$	Number of replicates at the central point
$Re_p$	Particle Reynolds number
$G$	Production of turbulent kinetic energy
$\nabla P$	Pressure gradient, Pa
$t$	Reaction time, min
$RH$	Relative humidity (%)
$E_i$	Relative error
$\bar{U}_{lg}$	Relative velocity
$e$	Residual error
$T_{ij}$	SGS stress tensor
$V_S$	Slip velocity
$H$	Static liquid height

$SS_{lof}$	Sum of square due to lack of fit
$SS_{pe}$	Sum of square due to pure error
$SS_{reg}$	Sum of square due to regression
$SS_{res}$	Sum of square due to residuals
$SS_{tot}$	Sum of square totals
$\bar{F}_k^T$	Turbulent dispersion force, N
$C_{TD}$	Turbulent dispersion force coefficient
$k$	Turbulent kinetic energy, J/kg
$\bar{n}_w$	Unit normal pointing away from the wall
$\bar{u}_g$	Velocity vector of gas phase, m/s
$\bar{u}_l$	Velocity vector of liquid phase, m/s
$\bar{u}_k$	Velocity vector of phase k, m/s
$Re_\omega$	Vorticity Reynolds number
$\bar{F}_k^{WL}$	Wall lubrication force, N
$C_w$	Wall lubrication force coefficient
$\mu_{BTR,l}$	Bubble-induced viscosity, Pa.s
$\tau_{t,l}$	Characteristic time
$\beta_i$	Coefficients of the linear variables
$\beta_{ii}$	Coefficients of the quadratic variables
$\beta_{ij}$	Coefficients of the interaction variables
$\rho_k$	Density of phase k, kg/m <sup>3</sup>
$\mu_{eff,l}$	Effective viscosity, Pa.s
$\sigma_i$	Interfacial tension
$\epsilon_k$	Volume of fraction of phase k
$\mathcal{E}_j$	Molar extinction coefficient
$\mu_l$	Molecular viscosity, Pa.s
$\tau_g$	Particulate relaxation time
$\sigma_k, \sigma_\epsilon$	Prandtl numbers
$\phi_{ij}$	Pressure strain term
$\Phi_i$	Quantum yield

$\mu_{ref}$	Reference viscosity of water
$\sigma_{lg}$	Schmidt number
$\tau_k$	Shear stress term, Pa
$\kappa_s$	Surface curvature
$\sigma$	Surface tension
$\mathcal{G}_R$	TOC reduction
$\varepsilon$	Turbulent kinetic energy dissipation rate, m <sup>3</sup> /s <sup>3</sup>
$\mu_{T,l}$	Turbulent viscosity, Pa.s
$\kappa$	Von Kármán constant
$C_e$	Concentration at equilibrium
$C_f$	Final concentration
$C_i$	Experimental concentration
$C_o$	Initial concentration
$C_{pri}$	Predicted concentration
$C_t$	Concentration at time t
$E_o$	Electrical energy per order
$E_g$	Band gap
$K_{ad}$	Adsorption constant
$k_{app}$	Pseudo-first-order reaction rate constant
$k_2$	Second-order reaction rate constant
$K_L$	Langmuir adsorption constant
$K_f$	Freundlich isotherm adsorption capacity constant
$k_r$	Reaction rate constant
$\lambda$	Wavelength
n	Freundlich isotherm adsorption intensity constant
P	Relative deviation modulus
$q_e$	Adsorbate uptake at equilibrium
$q_m$	Langmuir maximum sorption capacity
r	Reaction rate
R	Universal gas constant
T	Absolute temperature
t	Time
$\Delta G^\circ$	Change in free energy

$\Delta S^\circ$	Change in entropy
$\Delta H^\circ$	Change in enthalpy
$I_\lambda$	Spectral light intensity
$s$	Light pathlength
$\Omega$	Direction of light travel
$\kappa_\lambda$	Absorption coefficient
$\sigma_\lambda$	Scattering coefficient
$p(\Omega' \rightarrow \Omega)$	Probability of a light scatter from direction $\Omega'$ to $\Omega$ .
$E_{UV}$	UV lamp energy consumption
$E_{bio}$	Bioenergy production
$LHV_{CH_4}$	Low heating value of methane
$El_{bio}$	Electricity from biomethane
$E_{COD}$	COD removal efficiency
$C_{COD}$	Feed concentration
$\alpha_{CH_4}$	Methane production coefficient
$\varepsilon$	Energy ratio

# 1 INTRODUCTION

## 1.1 Background

Biogas technology has not been applied in Africa on the large scale as in Asia. This has been due to a lack of locally generated data appropriate for African conditions. There is a need to apply the right process parameters for African conditions for the process to be feasible. Wastewater treatment can be a very costly operation and the motivation to incur the cost includes meeting environmental legislation standards, implementation of cost reduction techniques and waste beneficiation. The treatment of many industrial wastes requires the application of robust and costly techniques, which is a major deterrent. It is for this reason that biological methods have proved to be very attractive to both industries and local authorities. However, these systems, used as stand-alone techniques, are not efficient in treating some high-strength industrial wastewater.

Generally, biological wastewater treatment has been the technique of choice for many years due to its simplicity and low-cost, especially that of the anaerobic digestion (AD), which has attracted a lot of interest in recent years. Despite the renewed interest in the ADs, major challenges posed by emerging and biorecalcitrant compounds still need to be addressed to improve reactor performance in terms of chemical oxygen demand (COD) reduction and biogas production. The efficiency of ADs can be improved by increasing the biodegradability of feedstock. This can be done by first using a more robust system such as the advanced oxidation process (AOP) by integrating different processes. Integrating conventional biological processes with advanced ones can improve biogas production (Satyawili & Balakrishnan, 2008) from high-strength industrial wastewater.

Molasses-based distilleries and textile industries are among the most polluting industries generating large volumes of high-strength wastewater. The effluent from distillery industries is characterised by extremely high CODs (80 000 mg/L to 100 000 mg/L), biochemical oxygen demands (BODs) (40 000 mg/L to 50 000 mg/L) as well as a strong odour and recalcitrant dark-brown colour (Satyawili & Balakrishnan, 2008). Textile wastewater is characterised by low biodegradability, intense colour as well as high organic load (COD of about 12 000 mg/L) (Oller et al., 2011). Whereas textile wastewater is entirely toxic to microbes (Oller et al., 2011), distillery effluent contains the colour-imparting melanoidin, which is biorecalcitrant, as well as a considerable number of biodegradable compounds.

Despite the AD process being preferred to treat effluent with high organic loads due to the energy recovery potential, the presence of toxic and biorecalcitrant organic contaminants in textile and distillery effluents is a challenge to the AD process. It has been reported that the major challenge facing the AD treatment of distillery wastewater is that AD is incapable of removing the colour associated with distillery wastewater (Satyawili & Balakrishnan, 2008).

Fluidized bed reactors (FBRs) are typically used for either biodegradation only or in integrated systems and the performance has been good. FBRs used in the AOPs consist of three phases (gas, liquid and solid) and quite often the mixing inside the reactor is a challenge. Therefore, analysis of mixing inside the reactor is conducted using computational fluid dynamics (CFD)

as it is a low-cost reactor optimisation technique. Such an approach is aimed at reducing the cost of operation regarding the energy requirements.

## **1.2 Relevance of the Study**

Many AD plants in southern Gauteng (such as Parys and Sebokeng) and in South Africa in general either operate below capacity or have totally collapsed. The quality and quantity of the biogas produced often make the systems unfeasible. The situation is made worse as the engineers and technicians who work in these wastewater treatment plants are either too few to cope with the workload or do not have the required skills. Consequently, AD plants, especially those run by municipalities, discharge effluents that have very high CODs. Furthermore, some municipalities do not have clear environmental policies or where there are, implementation procedures are not followed often. Also, there is a lack of technical skill partly due because some technical staff have either migrated or retired. Quite a number of studies on the application of integrated ultraviolet (UV) photodegradation and biological treatment of various industrial wastewater streams exist in literature of late (Oller et al., 2011; Rizzo et al., 2011). However, these studies focus on integrating UV treatment with aerobic treatment. This integration is costly as a great deal of energy is required to aerate the aerobic process and power the UV light source. To address this problem, Apollo et al. (2013a; 2013b) carried out a study on the integration of UV photodegradation and AD. The work has the potential for practical application as the AD process produces energy in the form of biogas which, if well trapped, could offset the energy demand of the UV process.

## **1.3 Significance of the Study**

In our previous studies (Apollo et al., 2013a; 2013b) it has been shown that up-flow fixed bed reactors can be employed as bioreactors and photoreactors. However, these reactors have the limitation as the mass transfer process is hindered during the reaction because there is no good mixing mechanism during the reaction. Moreover, these kinds of reactor have low working volumes as most parts are packed with biomass support or catalyst support material, for the bioreactor and photoreactor, respectively. This lowers the efficiency of the process in waste removal and energy production. Also, the packed bed photoreactor led to light attenuation resulting in long irradiation time during UV photodegradation. This in turn resulted in high energy consumption and an overall increase in process cost.

The study also could not establish the economic feasibility of the integrated process since there was no energy balance conducted to compare energy produced by the AD process with the energy consumed by the UV process. The integrated AOP-AD process can also be improved by preparing a catalyst that can withstand corrosion and therefore is reusable. Further, the success of this process integration lies on identifying degradation intermediates and determining their toxicity. Lastly, up to now, there has been a lack of information in literature regarding the continuous operation of the integrated AOP-AD process for wastewater treatment; yet, continuous operation depicts real industrial processes better than batch-operated studies.

This proposed project was widely divided into different work packages with a central goal of improving the performance of AOP-AD integrated systems within the context of efficiency in waste removal, energy utilisation and carbon footprint. The major significance of the present work is the analysis of energy efficiency and the carbon footprint of the integrated system and the application of robust techniques including CFD to optimise the operating parameters.

#### **1.4 Aim and Objectives**

The aim of this work was to investigate factors influencing the performance of integrated biodegradation and photodegradation within the context toxic reduction and bioenergy production.

Specific objectives were:

- a) To update the literature review of the previous project in line with new developments.
- b) To evaluate and improve the performance of the developed composite photocatalysts.
- c) To optimise the operating hydrodynamic operating parameters for a fluidized bed photoreactor and bioreactor.
- d) To analyse the reaction kinetics and effects of intermediate compounds for the separate systems (AD and AOP).
- e) To determine the optimum operating conditions for the integrated system.
- f) To conduct energy balance for the integrated system and analyse the reaction adsorption kinetics.
- g) To apply an integrated AD and photodegradation process in a continuous mode.
- h) To apply simulation and modelling techniques to optimise operating conditions.

## 2 LITERATURE REVIEW

### 2.1 Wastewater

Good water quality is one of the basic needs for our existence; however, many water sources in urban and rural communities are contaminated at different concentrations with a wide range of compounds such as dyes, organic matter and heavy metal ions. Most of these contaminants originate from industries, are often toxic, and cause adverse effects to human and animal life if present above certain concentration levels. Distilleries and textile industries are some of the most polluting industries generating large volumes of high-strength wastewater.

#### 2.1.1 Distillery wastewater

The effluent from distillery industries is characterised by an extremely high COD ranging from 80 000 mg/L to 100 000 mg/L and a BOD in the range of 40 000 mg/L to 50 000 mg/L as well as a strong odour and recalcitrant dark-brown colour caused by melanoidin (Satyawili & Balakrishnan, 2008). Distillery wastewater also contains a considerable amount of biodegradable compounds (Kalavathi et al., 2001) as well as several ions such as nitrates, phosphates, sulphates and potassium. Table 1 summarises some characteristics of molasses wastewater (MWW).

**Table 1: Characteristics of distillery spent wash generated from cane molasses (Satyawili & Balakrishnan, 2008)**

Characteristic	Amount
COD (mg/L)	65 000–130 000
BOD (mg/L)	40 000–70 000
Total solids (mg/L)	30 000–100 000
Total dissolved solids (TDS) (mg/L)	80 000–87 000
Total nitrogen (mg/L)	1 000–2 000
Total phosphorus (mg/L)	800–1200
Potassium (mg/L)	8 000–12 000
Sulphates (mg/L)	2 000–6 000
pH	3.0–5.4

#### 2.1.2 Brewery wastewater

The processes involved in beer production (such as cooling, scarification, washing and fermentation) result in a large amount of wastewater. The large amount of brewery wastewater is because 1 L of beer generates 3–10 L wastewater (Simate et al., 2011). Brewery wastewater has been found to have a higher BOD than other wastewaters (Wang et al., 2008). Table 2 summarises some characteristics of brewery wastewater. Brewery wastewater has been found to be harmful to aquatic life due to its high organic content and oxygen demand.

**Table 2: Characteristics of raw beer brewery wastewater (Simate et al., 2011)**

Parameter	Value
pH	3–12
Temperature (°C)	18–40
COD, mg/L	2 000–6 000
BOD, mg/L	1 200–3 600
COD: BOD ratio	1.667
Volatile fatty acids (VFAs) (mg/L)	1 000–2 500
Phosphate as PO <sub>4</sub> , (mg/L)	10–50
Total Kjeldahl Nitrogen (TKN) (mg/L)	25–80
TiO <sub>2</sub> and silica Xerogel composite (TS) (mg/L)	5 100–8 750
Total suspended solids (TSS) (mg/L)	2 901–3 000
XXX (TDS) (mg/L)	2 020–5 940

### 2.1.3 Textile wastewater

Considering both volume discharged and effluent composition, the wastewater generated by the textile industry is rated as the most polluting among all industrial sectors because of the large volumes of water consumed by textile industries and the chemicals used in wet processing of textiles. The chemical reagents used in the textile industry are very diverse in chemical composition, and range from inorganic compounds to polymers and organic products (Juang et al., 1996). Therefore, textile wastewater may contain metal ions originating from metal-containing dyes as is the case for chromium in acid dyes or copper in direct dyes. In addition, the wastewater may contain traces of mercury, which is present in various chemical reagents (Horning, 1978). Heavy metal level contents of less than 100 mg/L have been reported in the case of non-metallized dyestuff (ADMI, 1973). In the case of metallized dyes and metal salt dyes, reported levels of metals have been considerably higher. Horning (1978) found chromium, cadmium, copper, lead, mercury and zinc in samples from 22 fibre/dye systems. This demonstrates the high number of heavy metals that can be present in textile effluents.

Among the heavy metal ions normally found in textile wastewater, Cr(VI) has attracted the most attention since it is a toxic, carcinogenic and mobile contaminant. Chromium is a heavy metal, naturally found in rocks, animals, plants and soil. Its exploitation has increased due to the extensive use of chromate and dichromate in textile, photoengraving processes, leather tanning and the electroplating industry (Park et al., 2005). Naturally, it is available in two common oxidation states; namely, trivalent and hexavalent forms. Hexavalent chromium [Cr(VI)] is mobile and potentially toxic while trivalent chromium [Cr(III)] at a neutral or alkaline pH is readily precipitated on a variety of inorganic and organic substrates (Schrank et al., 2002). The maximum acceptable Cr(VI) level in polluted wastewater is 0.05 mg/L. The preferred treatment is to reduce Cr(VI) to less harmful Cr(III), which can be sorbed in neutral or alkaline solutions such as Cr(OH)<sub>3</sub> (Schrank et al., 2002).

Textile wastewaters tend to contain low TSS levels and moderate to high TDS levels. Electrolytes, acids and alkalis used during dyeing contribute to the total solids. Wastewaters from batch-dyeing cotton with reactive dyes are usually very high in dissolved solids because this dyeing process demands a significantly high concentration of salts (up to 80 g/L NaCl) and

sufficient alkali to raise the pH to between 12 and 12.5 (Venceslau et al., 1994). The most noticeable characteristic of textile wastewater is its strong colour even at small concentrations of dyes. Dye colour is highly visible and may affect the transparency and aesthetics of textile wastewater (Banat et al., 1996). Textile wastewater is also characterised by a high COD of about 12 000 mg/L, low biodegradability and toxicity to microbes (Oller et al., 2011). Some of the characteristics of textile wastewater are listed in Table 3.

**Table 3: Characteristics of textile wastewater (Oller et al., 2011)**

<b>Characteristic</b>	<b>Value</b>
COD (mg/L)	150–2 000
BOD (mg/L)	80–6 000
BOD/COD	0.25
TKN (mg/L)	70–80
TSS	2 900–3 100

Dye wastewater from textile mills is a serious pollution problem due to its undesirable aesthetic impact on receiving waters, toxicity and biorecalcitrant nature. Some dyes are carcinogenic; others yield toxic and carcinogenic compounds such as aromatic amines after transformation or degradation. In addition, dyes accumulate in sediments and leach from soil into groundwater systems (Chakrabarti & Dutta, 2004). Therefore, discharging dyes into water streams even at low concentration can be toxic to aquatic life and affect food webs. The coloured nature of textile wastewater also affects aquatic diversity by blocking the passage of sunlight through receiving water bodies. In humans, dyes in water can cause allergic dermatitis and skin irritations.

## **2.2 Treatment of Distillery and Textile Wastewaters**

The colour and toxic chemicals in distillery and textile wastewaters have a negative impact on aquatic life and humans. Therefore, there is a need to eliminate such pollutants from waste to avoid polluting natural water bodies. Furthermore, in view of large-scale plants for water treatment as well as industries, the water quality of effluents can fluctuate considerably with time. Selecting the best treatment method for remediation of a specific industrial wastewater is a highly complex task. The type of process to be employed depends on the quality of the original wastewater, removal of parent contaminants, the facility's decontamination capacity, process economics, and the life cycle assessment to determine environmental compatibility of the wastewater treatment technology. Based on the concentrations and type of contaminant that exist in wastewater, various treatment methods have been developed to release an environmentally friendly effluent. Decision-making can be based on whether the chemicals are organic or inorganic. They can be branched out based on chemical structure, biodegradability, toxicity, polarity, oxidation potential, adsorbability, electrical charge, and the nature of daughter compounds. Biological treatment, especially anaerobic degradation, has been the most economical method of treating biodegradable high-strength wastewater.

## **2.3 Anaerobic Digestion**

The AD process involves degrading and stabilising organic materials in the absence of oxygen by microbial organisms, which leads to biogas forming (Kelleher et al., 2000). During the anaerobic process, organic matter is degraded by a consortia of microbial strains through multiple degradation steps such as hydrolysis, fermentation, acetogenesis and methanogenesis. These anaerobic microbes – including hydrolytic bacteria, fermentative bacteria, acetogenic bacteria and methanogens – usually form a syntrophic relation (Liu et al., 2002). The interdependence of these bacteria is a key factor in the success of an AD process. Of major influence in the efficiency of the anaerobic degradation is the dynamics and kinetics of the microbe population within the reactor and the narrow limits that thermodynamics places on the process (Aiyuk et al., 2006).

In the first step of AD, complex organic matter (large molecular weight proteins, carbohydrates and lipids) present in wastewater is hydrolysed extracellularly into simpler organic molecules by enzymes excreted by hydrolytic bacteria. The resulting organic molecules are converted into amino acids, alcohols, simple sugars and low carbon fatty acids either through fermentation or acidogenesis. Acetogenic and acidogenic bacteria convert these organic molecules into acetic acid, formic acid, carbon dioxide and hydrogen. The breakdown of simple sugars and amino acids into acetate and hydrogen produces butyrate and propionates as intermediates (Remigi & Buckely, 2006). Finally, the conversion of these products into methane is achieved by a group of bacteria called methanogens. There are two types of methanogens: those that convert hydrogen and carbon dioxide into methane (hydrogenotrophic methanogens) and those that convert acetate into methane (aceticlastic methanogens). About 70% of methane produced is through the acetate route (Winter, 1999; Poulsen & Hansen, 2003; Ramigi & Buckely, 2006).

The AD of high-strength wastewater with a high biodegradable content has several advantages: a high degree of purification with high organic load feed can be attained, a small quantity of sludge is usually produced, and valuable energy in terms of biogas is generated. The biogas produced can be used as a source of energy to operate the anaerobic process and therefore reduce the anaerobic cost. Moreover, this energy can also be used to reduce the cost of production considerably by the industries discharging biodegradable waste as the energy produced can be used to supplement the energy required in production. The efficiency of the anaerobic process in waste management, however, depends on the performance of the digester.

### ***2.3.1 Digester performance***

The performance of an anaerobic digester/reactor strongly depends on the stability within the reactor. Methane yield and reduction in COD of the wastewater are the key parameters used in the evaluation of the digester performance in the AD process. One of the major problems encountered in operating a biogas digester in a continuous mode is reactor instability. This may occur during both the start-up and operation of the anaerobic degradation process, thus affecting the performance of the system due to the low specific growth rate of the methanogenic microorganisms involved (Bjornsson et al., 1997). Under conditions of unstable operation, intermediates such as VFAs and alcohols accumulate at different rates depending on the cause of the instability. The most common causes of imbalance are hydraulic or organic overloading, presence of toxins/inhibitory substances and change in the substrate concentration. Several

parameters are used as indicators of stress, such as variation in gas production rate, gas composition, pH and VFA concentration (Powell & Archer, 1989).

### ***2.3.2 Operating parameters***

The digestion process is temperature dependent since the strains of the microorganisms involved have temperatures at which their activities are optimum. The optimum operating temperatures for the different bacteria types are:

- Cryophilic bacteria below 15°C.
- Mesophilic bacteria from 15°C to 40°C.
- Thermophilic bacteria from 55°C to 65°C.

The growth of microorganisms also depends on the alkalinity of the medium. The optimum pH for most microorganisms ranges from 6.5 to 7.5, and a deviation from the optimum value may be corrected using a low-cost base or acid such as CaO, NaHCO<sub>3</sub>, Ca(OH)<sub>2</sub> or HCl (Farhadian et al., 2007).

Another important factor in the digester affecting the growth of microorganisms is the availability of nutrients. For reactor stability, the nutrients for biodegradation, which are carbon (C), nitrogen (N), and phosphorus (P), must be in a given optimum ratio. Strydom et al. (2001) reported a C:N:P optimum ratio of 100:10:1 while Farhadian et al. (2007) reported an optimal COD:N:P ratio of 350:7:1 in the start-up of bioreactor digesting beet sugar wastewater. Deviation from the optimum ratio can result in substrate limited growth or production of toxic compounds, which inhibits the process (Aiyuk et al., 2003). Also of equal significance is the hydraulic retention time (HRT), which depends on the operating conditions and the wastewater characteristics. Besides, the type of digester employed has great significance in the overall performance of the anaerobic degradation process in waste removal and biogas generation.

### ***2.3.3 Challenges of AD in the treatment of textile and distillery effluent***

Although the AD process is preferred to treat effluent with high organic load due to its energy recovery potential, the presence of toxic and biorecalcitrant organic contaminants in textile and distillery effluents is a challenge to the AD process. Even with the use of robust bioreactors, biorecalcitrant pollutants such as melanoidin, which is a constituent of distillery effluent, cannot be degraded effectively (Satyawili & Balakrishnan, 2008). Gonzalez et al. (1999) reported that the biodegradability of melanoidin is very low. They reported that the AD process can remove only about 6–7% of melanoidin in distillery effluent. It was therefore observed that even after anaerobic treatment, the wastewater still had the dark-brown colour contributed by melanoidin. It has been reported that AD is not efficient when used as a stand-alone process in treating distillery and textile wastewater (Simate et al., 2011; Apollo et al., 2013).

For the AD process to be able to handle the biorecalcitrant components of the distillery and textile industry effluent, these wastewater streams can be pre-treated using appropriate technologies to enhance the biodegradability of their biorecalcitrant constituents before being anaerobically digested. Alternatively, when a given wastewater stream contains large amounts of biodegradable components and traces of recalcitrant compounds, such wastewater can undergo the AD process without any pre-treatment, but appropriate technology should be

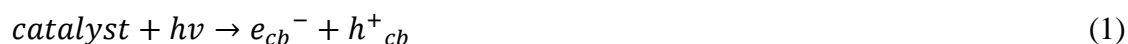
employed as post-treatment method for removing traces of the biorecalcitrant compounds which could not be eliminated by the AD process (Rizzo, 2011).

## 2.4 Photocatalysis

Photodegradation, which is an AOP based on the photogeneration of highly oxidative hydroxyl radicals, has been reported to have a good performance in dye and melanoidin degradation for colour removal (Oller et al., 2011). This process is robust as it can rapidly degrade the melanoidin compounds into their intermediate products or can lead to their total mineralisation, depending on the irradiation period.

### 2.4.1 Mechanism of photocatalysis

Several authors (Gaya & Abdullah, 2008; Fujishima et al., 2000) reported the fundamentals of photophysics and photochemistry underlying the heterogeneous photocatalysis engaging the TiO<sub>2</sub> semiconductor. From a mechanistic point of view, when photon energy ( $h\nu$ ) equal or greater than the bandgap energy  $\Delta E_g$  of the semiconductor is supplied, an excited electron in the valence band is shifted to the empty conduction band. This leads to the generation of a positive hole ( $h_{vb}^+$ ) in the valence band and an electron ( $e_{cb}^-$ ) in the conduction band. As a result, electron-hole pairs are produced according to Eq. 1.



where  $e_{cb}^-$  and  $h_{cb}^+$  are the electrons in the conduction and valence band, respectively. Both the electron and hole move to the photocatalyst surface where they participate in redox reactions with any chemicals present on the surface. The electrons in the valence band react easily with the surface-bound H<sub>2</sub>O to form  $\bullet$ OH radicals, whereas,  $e_{cb}^-$  reacts with O<sub>2</sub> to yield superoxide radical anion of oxygen according to (Eq. 2) to (Eq. 5).



The reaction of oxygen and the electron is crucial as it hinders the undesirable combination of the electron and the hole. The oxidative and reductive reactions do not occur concurrently. Therefore, when an accretion of electrons takes place in the conduction band, the electron is recombined with the positive hole in the absence of the photocatalyst (Eq. 6). Since the photocatalysis reaction is in competition with electron-hole recombination, efficient electron consumption is essential for photocatalysis to occur.



The  $\bullet$ OH and  $\bullet O_2^-$  formed can react with the dye and melanoidin molecules, resulting in the degradation of the organic pollutants. The organic pollutants are degraded to their corresponding intermediates and further mineralised to salts, carbon dioxide and water (Eq. 7).



Figure 1 summarises the mechanism of photocatalysis including bandgap excitation, charge separation and the scavenging of electrons and holes by surface-adsorbed species.

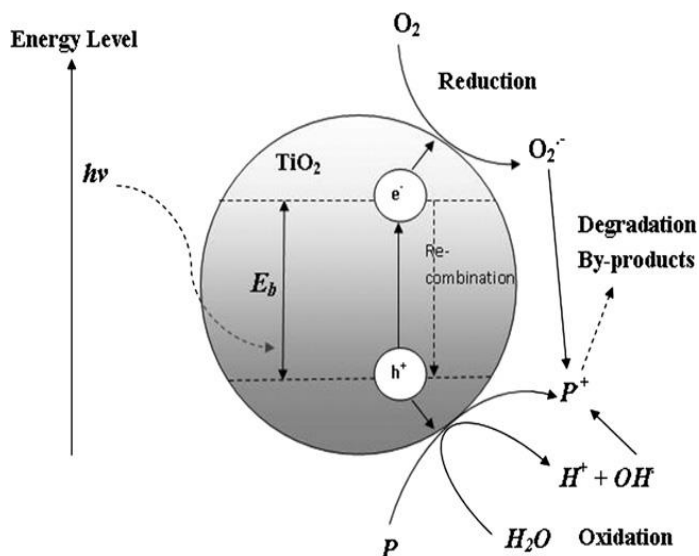


Figure 1: Schematic diagram showing the generation of oxidative species in a photocatalytic study (Chong et al., 2010)

According to Pirkanniemi and Sillanpää (2002), the overall heterogeneous photocatalysis as represented by (Eq. (7)) involves five steps, which are demonstrated in Figure 2:

- Mass transfer of the organic contaminant(s) in the liquid phase to the  $\text{TiO}_2$  surface.
- Adsorption of the organic contaminants onto the photon-activated  $\text{TiO}_2$  surface.
- Photocatalysis reaction for the adsorbed phase on the  $\text{TiO}_2$  surface.
- Desorption of the intermediate products from the  $\text{TiO}_2$  surface.
- Mass transfer of the intermediates from the interface region to the bulk fluid. In terms of rate determination, the overall rate of reaction is equal to the slowest step.

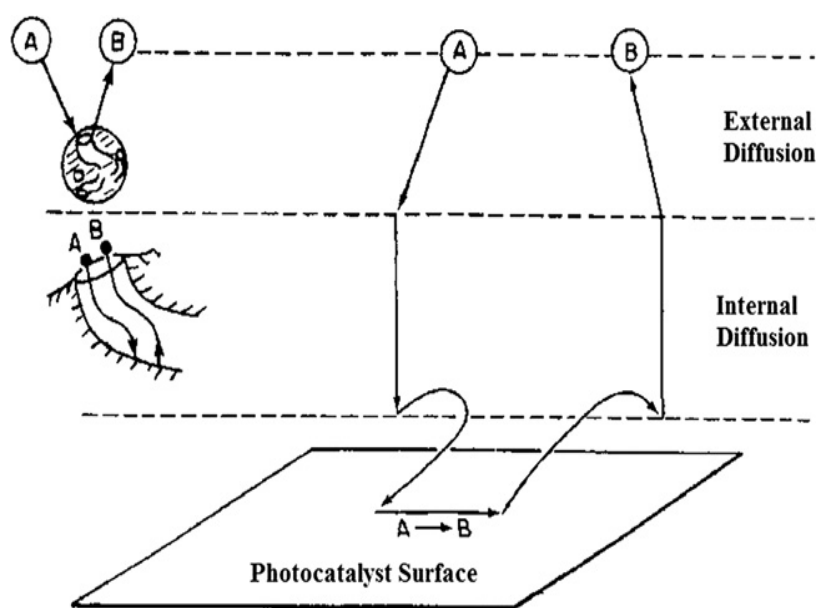


Figure 2: Steps in heterogeneous catalytic reaction (Fogler, 1999)

When the mass transfer stages (a and e) are compared with the reaction stages (b, c and d), the organic concentrations in the immediate vicinity of the active sites are vague from those in the bulk liquid phase. At this stage, the mass transfer steps are not rate-limiting and do not influence the overall rate of photocatalytic reaction. The study completed by Vinodgopal and Kamat (1992) reported the reliance of the photodegradation rate of the organic surrogate on surface coverage of the photocatalysts employed. This outlines the significance of molecules' adsorption or surface contact with the photocatalyst during the photocatalytic degradation process. If the mass transfer steps are rate restrictive, a modification in the aeration or liquid flow conditions past the TiO<sub>2</sub> photocatalyst may change the overall photocatalytic reaction rate.

#### **2.4.2 Titanium dioxide photocatalyst**

TiO<sub>2</sub> has been the most utilised photocatalyst due to its good physical and chemical stability, insolubility in water, resistance to acids, inertness to most chemicals, and long-term photostability. The most common polymorphs of TiO<sub>2</sub> are rutile and anatase with band gaps of 3.0 eV and 3.2 eV, respectively. Both forms of TiO<sub>2</sub> have been reported to be photoactive; however, anatase has been found to be more active than rutile. A mixture of anatase and rutile for photocatalysis has been found to exhibit synergy due to the photo induced interfacial electron transfer from anatase to rutile (Kawahara et al., 2002). Furthermore, Liu et al. (2008) reported that the photogenerated electrons in the rutile conduction band form superoxide radicals and the holes in the anatase valence band play a vital role in oxidation reactions.

The main drawbacks of TiO<sub>2</sub> have been its high electron-hole recombination, large band gap and small size. TiO<sub>2</sub> undergoes fast recombination of electrons and holes during the photo activation step thus reducing photoactivity. The anatase bandgap of 3.2 eV, corresponding to light wavelength 388 nm means that TiO<sub>2</sub> can only be activated by UV light. This limits the use of sunlight, a lower cost and greener energy, for the activation of TiO<sub>2</sub> since UV light forms only about 5% of sunlight. Commercial catalyst grade TiO<sub>2</sub> is about 20 nm in size and therefore requires the use of costly membrane filters to separate it from the reaction solution. The electron-hole recombination and large band gap have been addressed by doping the TiO<sub>2</sub> while the size of the TiO<sub>2</sub> has been increased by attaching the TiO<sub>2</sub> onto inert supports.

##### **2.4.2.1 TiO<sub>2</sub> doping**

Visible light active (VLA) TiO<sub>2</sub> photocatalysts have been developed to utilise more of the solar energy for photocatalysis. The VLA catalysts have been synthesised by doping TiO<sub>2</sub> with metals and non-metals using chemical doping or ion implantation. Ion implantation has resulted in narrowing of band gaps; however, its high cost has limited widespread use. Chemical doping remains a popular and low-cost method of making VLA TiO<sub>2</sub> by narrowing the TiO<sub>2</sub> band gap by introducing impurity energy levels into the TiO<sub>2</sub> crystal lattice (Asahi et al., 2001). Both transition metals and anions have been used in chemical doping. Non-metal dopants (N, C, F, S), with their lower cost have been reported to improve the feasibility of doped TiO<sub>2</sub> catalysts for large-scale application (Fujishima et al., 2000). However, single-ion chemical doping still suffers from poor reactivity of the VLA under UV light due to an increase in electron-hole recombination (Malato et al., 2009). Increasing the number of doping ions by tridoping the TiO<sub>2</sub> has shown an increase in reactivity (Wang & Lim, 2010) and is one of the best chances of producing a low-cost catalyst with a high performance under both UV and visible light.

Since Fermi levels of noble metals such as Ag, Ni, Cu, Pt, Rh, and Pd are lower than that of the TiO<sub>2</sub> photocatalyst, they could be deposited on the TiO<sub>2</sub> surface to improve the charge separation (Ni et al., 2007). Photoexcited electrons can be shifted from the conduction band of TiO<sub>2</sub> to metal particles deposited on the surface TiO<sub>2</sub>, whereas photogenerated holes in the valence band remain on the TiO<sub>2</sub>. This reduces the possibility of electron-hole recombination, resulting in an efficient charge separation and thus enhanced photocatalytic activity. Many studies have found that the efficiency of charge separation using noble metals depends highly on the size of the metal particle, dispersion and composition. For a high photocatalytic activity, the size of the metal particle should be less than 2 nm (Turner et al., 2008) and the concentration of the metal particles should not be too high otherwise the metals become electron-hole recombination centres (Sakthivel et al., 2004). Although noble metals have been effective in improving the charge separation, their high cost has limited their commercial use.

### **2.4.3 Supported TiO<sub>2</sub>**

Traditionally, photocatalysis has been carried out using nanophase TiO<sub>2</sub> due to its high surface area resulting in high photocatalysis rate (Boyjoo et al., 2013). However, the challenging and costly separation of TiO<sub>2</sub> after the reaction has limited the commercialisation of photocatalysis (Shan et al., 2010). Therefore, supported catalysts have been investigated as possible solutions to the costly filtration step after the photocatalysis reaction. However, supported catalysts have been found to show a lower reaction rate due to their low mass transfer area available for reaction. To overcome this difficulty, efficient material supports with adsorption capability that would bring the contaminants into close contact with the catalyst surface have been used (Turchi & Ollis, 1990). Supporting materials such as glass beads, fibre, glass, silica, and zeolite have been investigated as supports for TiO<sub>2</sub>.

#### *2.4.3.1 Membranes as supporting materials*

A membrane itself has been used as an immobiliser to support the photocatalyst and improve the surface contact with pollutants (Kwak & Kim, 2001). Membranes have been attractive as supports since the photocatalytic reaction can be carried out on the membrane surface and the treated wastewater could be constantly discharged without losing photocatalyst particles. Several membranes have been used to support TiO<sub>2</sub> including TiO<sub>2</sub>/Al<sub>2</sub>O<sub>3</sub> composite membranes (Choi et al., 2007) and TiO<sub>2</sub> supported on polymer and metallic membranes. Dotted polymer membranes with TiO<sub>2</sub> particles entrapped within the membrane structure during the membrane fabrication operation (Artale et al., 2001) have also been used. Despite the advantages of membrane supports, the membranes may experience many technical complications such as membrane structure corrosion, low photocatalytic activity and loss of the deposited TiO<sub>2</sub> semiconductor layer over time.

#### *2.4.3.2 Activated carbon as supporting material*

Activated carbon (AC) is a commonly used photocatalyst support material for water and wastewater treatment to remove organic and inorganic contaminants. The application of AC in wastewater treatment is mainly due to its pore structure. Therefore, AC has been broadly used as a support for TiO<sub>2</sub> due to the ability of the AC to accelerate the photodegradation efficiency by concentrating substrate near the TiO<sub>2</sub> (Shan et al., 2010). Although AC has some benefits

as a photocatalyst support in promoting the photocatalytic process, its application requires a reactor that efficiently exposes the photocatalyst surface to the photons of light. Furthermore, it is also a costly supporting material and the surface chemistry of a carbon may obstruct effective coating of TiO<sub>2</sub> on it (Khan et al., 2002).

#### 2.4.3.3 *Fibres as supporting material*

Glass, carbon fibres and woven fibre cloths have been considered as TiO<sub>2</sub> supports in wastewater treatment. Most of these fibres show a longitudinal morphology or protruded rod-shape. When fibrous supports are used, loss of pressure and pore diffusion resistance are lower than with pellet-shaped catalysts (Matatov-Meytal & Sheintuch, 1998). Another good advantage of fibre catalysts is their transparency to UV light in photocatalytic applications.

#### 2.4.3.4 *Zeolite as supporting material*

Zeolites are naturally occurring aluminosilicate minerals, which can also be synthesised artificially. Clinoptilolite is the most abundant, readily available and inexpensive natural zeolite (Ming & Dixon, 1987). Considering their highly crystalline structure, zeolites contain silicon, aluminium and oxygen forming an internal framework with cavities and channels, where cations and/or small molecules may exist. Zeolites have been found to be good photocatalyst supports due to their unique uniform pores and straight channels. Since they provide a large surface area, most degradable molecules find it easier to diffuse to the channels and cages of the order of 4–14 Å resulting in enhanced degradation. Additional studies by Ichiura et al. (2003) confirmed that due to the high adsorption capacity, the role of zeolite particles in the TiO<sub>2</sub>-zeolite composite has been to increase the number of the nitrogen oxide molecules and that of the dye molecules near the active sites of the TiO<sub>2</sub>. The photocatalytic activity of TiO<sub>2</sub>-based zeolite composites is improved due to the zeolite acting as supporting material for the homogeneous dispersion of TiO<sub>2</sub> particles on its surface. Additionally, zeolite also plays a positive role in the processes of charge and electrons transfer during the photocatalytic reaction, which subsequently decreases the recombination of the charge carriers (Dubey et al., 2006).

#### 2.4.3.5 *Silica as supporting material*

Silica materials such as silica gels and mixed oxides of silica titania have also been used as TiO<sub>2</sub> supports (Shan et al., 2010). Since synthetic silica has a higher surface area than naturally occurring forms of silica, synthetic silica provides the best adsorption and catalyst support structure for heterogeneous photocatalysis. Figure 3 shows the different types of surface silanol OH. The surface charge of a mineral surface is the result of the protonation-deprotonation of surface functional groups (mostly OH). The SiOH surface groups are the principal species. The surface concentration of SiOH<sub>2</sub><sup>+</sup> is highest at pH 0, while the concentration of SiO<sup>-</sup> increases with an increasing pH and maximum concentration of SiO<sup>-</sup> is at pH 8 (Londeree, 2002). Moreover, silica, has many advantages over AC as a photocatalyst support. The transparency of silica allows the penetration of photons to the photocatalyst surface. This is extremely beneficial and allows for a fixed bed reactor design that can be highly efficient with respect to input energy. In addition, silica has high mechanical strength, thermal stability, and can be synthetically formed into any shape, such as cylindrical pellets (Yamazaki et al., 2001).

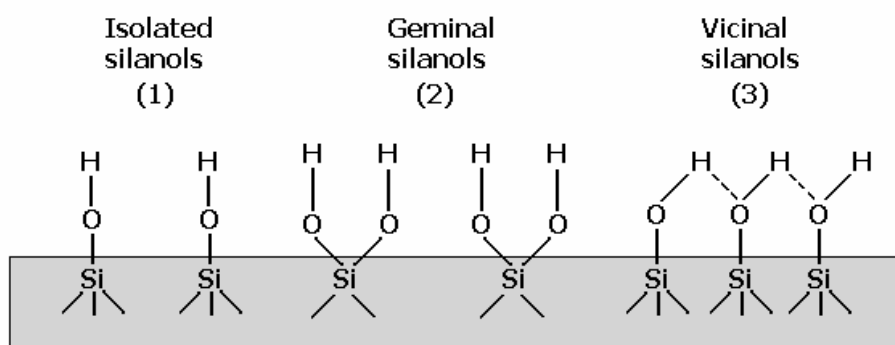


**Figure 3: Surface silanol OH groups at the silica surface (Li & Bruyn 1966)**

Silica-modified  $\text{TiO}_2$  was reported to exhibit a better photocatalytic performance than  $\text{TiO}_2$  itself. The  $\text{TiO}_2\text{-SiO}_2$  photocatalysts permit supporting of the catalyst on both external surfaces and internal surfaces within the porous silica matrix where contaminants are adsorbed. In a study carried out by Anderson and Bard (1997), a strong synergy between titania and silica as a composite oxide was found and it was further reported that the presence of the supporting material was considered to encourage the efficiency by increasing the concentration of the substrate near the  $\text{TiO}_2$  sites relative to the solution concentration. However, for substrates that are not readily adsorbed to the surface of silica, the degradation rates were lower than a slurry of pure  $\text{TiO}_2$ .

#### 2.4.3.6 $\text{TiO}_2$ hollow microspheres

Recently, hollow  $\text{TiO}_2$  microspheres have been suggested as better alternatives to nanophase  $\text{TiO}_2$ . The  $\text{TiO}_2$  hollow microspheres are advantageous due to their large size, low density, high surface area, good surface permeability, and high light harvesting capability (Li et al., 2010). Several methods such as hydrothermal (Ye et al., 2010), spray-drying (Ai et al., 2012), soft template (Wang et al., 2008), hard template (Xiong et al., 2012) and spray hydrolysis (Nagamine et al., 2008) have been used to synthesise  $\text{TiO}_2$  hollow microspheres. Most of these methods are complicated multistep procedures that require costly precursors to synthesise hollow microspheres (Zhang et al., 2011). However, spray hydrolysis is a simple method involving the spraying of water droplets onto the normal sol-gel  $\text{TiO}_2$  precursors (Nagamine et al., 2008).

#### 2.4.4 Light sources for photocatalysis

The  $\text{TiO}_2$  photocatalyst has a band gap energy of 3.2 eV and therefore can only be activated with UV light of wavelength below 400 nm (Malato et al., 2009). The most common UV lamps for photocatalysis have been mercury lamps. To reduce energy cost, sunlight has been used as an alternative source of UV light. However, the intensity of solar UV is only 5% of the solar spectrum and it fluctuates with time of day, weather conditions and season of the year (Natarajan et al., 2011). These drawbacks of solar energy can be addressed by using a suitable catalyst and compensating for any fluctuations in solar intensity.

### 2.4.5 *Effect of inorganic ions on photocatalysis treatment technology*

Most wastewaters have inorganic ions; therefore, a basic understanding of the ions on the effectiveness of photocatalysis is essential. Crittenden et al. (1996) reported that when a photocatalyst is used in either a slurry or fixed-bed configuration to treat real waters with different inorganic ions, photocatalyst deactivation was usually observed. This results from a strong inhibition of the inorganic ions on the surface of the TiO<sub>2</sub> semiconductor used. Thus, the presence of these inorganic ions together with their permissible levels on the photocatalysis in water treatment must be determined to ensure minimal disturbances on the efficient operation of the TiO<sub>2</sub> catalytic performance. Several studies have been conducted on the effects of different inorganic anions or cations, on both TiO<sub>2</sub> photo-mineralisation and photo-disinfection reactions (Guillard et al., 2003; Rincón & Pulgarin, 2004; Habibi et al., 2005). It must be emphasized, however, that most of these studies have concentrated on how different inorganic ions affect the rates of photocatalytic reactions with a model surrogate organic compound. The surrogate model organic compound can be biased towards its photocatalytic performance owing to its underlying chemical properties and the main constituent groups that form the compound. For instance, the model compounds with either electron withdrawing or donating groups will contribute a different degree of interaction to degradation pathways (Herrmann, 1999).

Currently, the effects of both inorganic cations, (such as Na<sup>+</sup>, K<sup>+</sup>, Ca<sup>2+</sup>, Cu<sup>2+</sup> and Al<sup>3+</sup>) and inorganic anions (such as Cl<sup>-</sup>, NO<sub>3</sub><sup>-</sup>, HCO<sub>3</sub><sup>-</sup>, SO<sub>4</sub><sup>2-</sup> and HPO<sub>4</sub><sup>2-</sup>) on the photocatalytic water treatment have been investigated (Guillard et al., 2003; Rincón & Pulgarin, 2004; Habibi et al., 2005). Results from these studies report that Cu<sup>2+</sup>, Fe<sup>2+</sup>, Al<sup>3+</sup>, Cl<sup>-</sup> and PO<sub>4</sub><sup>-</sup> at certain levels may decrease photo-mineralisation reaction rates while Ca<sup>2+</sup>, Mg<sup>2+</sup> and Zn<sup>2+</sup> may have negligible effects. This is because Ca<sup>2+</sup>, Mg<sup>2+</sup> and Zn<sup>2+</sup> are at their maximum oxidation states, resulting in their inability to inhibit the photocatalysis reaction. The presence of Fe<sup>2+</sup> can catalyse both the Fenton and photo-Fenton reactions. However, Choi et al. (1994) observed that Fe<sup>2+</sup> fouled the photocatalysts surface by introducing a rusty orange colour change via the formation of Fe(OH)<sub>3</sub>, while the PO<sub>4</sub><sup>3-</sup> in the nominal pH range remains strongly adsorbed onto the TiO<sub>2</sub> surface and further inhibits its photoactivity. Habibi et al. (2005) observed that NO<sub>3</sub><sup>-</sup>, SO<sub>4</sub><sup>2-</sup> and ClO<sub>4</sub><sup>-</sup> inhibit the surface activity of the photocatalysts.

The presence of salts is also known to diminish the colloidal stability as screening effects become more profound. This was followed by the double-layer compression and surface charge neutralisation, which increase the mass transfer limitations and reduce surface contacts between the pollutants and catalysts. Other inorganic ions also affect photodegradation rates, where the presence of SO<sub>4</sub><sup>2-</sup> in a TiO<sub>2</sub>-coated glass spiral reactor could double the disappearance rate of the pesticide Monocrotophos (Zhu et al., 1995). The Mn<sup>2+</sup> improved the photoactivity by simultaneously increasing the electron-hole pairs and preventing their recombination (Mu et al., 2004).

To treat heavy metals present in wastewater, the TiO<sub>2</sub> photocatalytic process has been reported to simultaneously convert these metals into non-toxic ionic states and further reduce them into their corresponding elemental form on the TiO<sub>2</sub> surface for metal recovery. Prairie et al. (1994) reported that metals of Cr(IV), Hg(II) and Pt(II) were easily treated with TiO<sub>2</sub> of 0.1 wt%

whereas Cd(II), Cu(II) and Ni(II) could not be reduced. The extent of such metals' conversion and recovery process is highly dependent on the standard reduction potential of the metals for the reduction reactions. It was reported that for an efficient removal of the metals, a positive potential greater than 0.4 V or the flat band potential of TiO<sub>2</sub> was required (Herrmann, 1999). Since the rates of both oxidation (organics) and reduction (metals) on the TiO<sub>2</sub> surface are intrinsically interrelated, the presence of sufficient organics in the water matrices were found to facilitate the metal recovery.

To better simulate real wastewater, the synthetic wastewaters used for investigating photocatalysis should have a complex mixture of inorganic ions. In investigating multicomponent systems, some problems such as daughter compounds' formation during oxidation, interaction between existing compounds besides difficulty of modelling and simulation of such systems make experimentation very complicated. Therefore, an effective treatment method for wastewater contaminated with both organic and inorganic compounds is highly needed.

#### ***2.4.6 Challenges of photocatalytic wastewater treatment***

Even though photodegradation performs well in the mineralisation of toxic and recalcitrant organic compounds that cannot be biodegraded easily, there are some challenges. Firstly, the major challenge of this process is a high energy requirement in cases where artificial irradiation such as UV light is used (Oller et al., 2011). In this case, the associated cost can often be prohibitive for wastewater treatment. Secondly, another problem is encountered in the treatment of wastewater with high colour intensity. In this case, the high colour intensity hinders the penetration of light rays thus lowering the performance of the process. It therefore means that to improve photocatalytic degradation in the treatment of such wastewater, high dilutions are required. This again is not economical as a larger reactor volume is required.

#### **2.5 Integration of AD with Other Treatment Methods**

Due to the recalcitrant nature of the distillery and textile effluents, it is inefficient to apply AD as a stand-alone process (Oller et al., 2011). Therefore, many attempts have been made to integrate at least two treatment techniques for their efficient treatment. It has been proposed that other treatment techniques (physico-chemical and biological methods) can be integrated with the AD process for efficient treatment of distillery effluent (Simate et al., 2011). These techniques have been applied either as pre-treatment or post-treatment methods to the AD process to achieve total colour and COD removal. Of these techniques, an integrated anaerobic-aerobic process has been established to achieve a significant colour removal (Satyawili & Balakrishnan, 2008). The only alternative methods that can be integrated with AD are the physico-chemical methods such as adsorption, coagulation/flocculation, oxidation processes and membrane separation.

#### **2.6 Integration With Physico-chemical Methods**

Integration of AD with physico-chemical methods such as adsorption, coagulation/flocculation, oxidation processes and membrane separation have also been investigated for colour removal. Even though these methods are effective in colour removal, sludge generation and disposal are major constraints in their applicability. Some adsorption processes suffer from slow kinetics, irreversible adsorption of target compounds and loss of mechanical stability

(Jal et al., 2004). Also, the need to regenerate the adsorbent has led to an increase in the cost of adsorption. Adsorption also does not destroy pollutants but just transfers the contaminant from water to solid matrix (Hoffman & Martin, 1995). Moreover, the cost of chemicals, adsorbents and membranes pose a challenge in the adoption of these methods (Rajor et al., 2002). Membrane filtration treatment for spent wash is also characterised by significant membrane fouling, which limits its applicability (Jain & Balakrishnan, 2004). Coagulation may be good for dispersive dyes; however, it may not eradicate highly soluble dyes and it produces a large quantity of sludge. In light of these challenges, AOPs are increasingly attracting the attention of researchers.

### 2.6.1.1 AOPs

AOPs such as photo-Fenton, ozonation, electrochemical oxidation, sonocatalysis and photocatalysis involve the generation of oxidising chemical species to attack and break down organics. Table 4 summarises the advantages and disadvantages of several AOPs. Although the photo-Fenton process is an appropriate chemical means of treating polluted wastewaters, the method generates a significant amount of sludge due to the flocculation of the reagent and the dye molecules (Slokar & Le Marechal, 1997). Oxidation by ozone has been widely used to degrade phenols, pesticides, chlorinated hydrocarbons and aromatic hydrocarbons (Xu & Lebrun, 1999). Ozonation has the benefit of being used in its gaseous state thus not increasing the quantity of sludge. However, ozonation alone has been found to be ineffective for degrading disperse dyes (Solozhenko et al., 1995) due to its short half-life (about 20 minutes), which requires the use of costly continuous ozonation. One of the best AOPs has been semiconductor photocatalysis due to its low cost, stability and high activity.

**Table 4: Advantages and disadvantages of current dye removal methods from industrial effluents (Robinson et al., 2001)**

<b>Physical/chemical methods</b>	<b>Advantages</b>	<b>Disadvantages</b>
Fenton's reagent	Effective for decolourisation of both soluble and insoluble dyes	It generates sludge
Ozonation	Applied in gaseous state: no alteration of volume	Short half-life (20 minutes)
Photochemical	No sludge	Formation of by-products
Electrochemical destruction	Breakdown compounds are non-hazardous	High cost of electricity
Electrokinetic coagulation	Economically feasible	High sludge production

### 2.6.1.2 *Photocatalysis*

Integration of the UV photodegradation process and biological treatment has been reported (Oller et al., 2011). However, most of these integrations have focused on aerobic treatment and UV photodegradation. This integration is costly as a significant amount of energy is required to aerate the aerobic process and power the UV light source. Moreover, the aerobic process produces a great deal of sludge. To mitigate these problems, a study on integration of UV photodegradation and AD has been reported (Apollo et al., 2013). In the study, fixed bed reactors were applied. This form of integration has the advantage in that by applying the AD process instead of the aerobic process, aeration and sludge production are avoided, moreover, the AD process produces renewable energy which can be used to power the UV system. However, the fixed bed reactors employed in the integrated AD-UV studies have limitations as there is no adequate mass transfer because there is no good mixing during reaction. Also, the fixed bed reactors have low working volume as most part is packed with biomass support or catalyst support material for the bioreactor and photoreactor respectively. This lowers the efficiency of the process in waste removal and energy production. Besides, the packed bed photoreactor leads to light attenuation resulting in long irradiation time during UV photodegradation. This in turn results in high energy consumption and consequently an overall increase in process cost. This set of problems associated with fixed bed reactors can be addressed by employing FBRs. This is because FBRs can achieve good mixing, which enhances mass transfer resulting in faster reaction rates. FBRs also have improved working volumes that lead to a reduced light attenuation during UV photodegradation.

In this work, it is proposed that the solution to the challenges facing both the anaerobic degradation and photocatalytic degradation of organic pollutants reside in the integration of the two processes. This is based on the possibility that photocatalytic pre-treatment of toxic pollutants can increase their biodegradability before conducting the anaerobic process. This means that the photodegradation process will be carried out for a shorter period since complete mineralisation is not required. Moreover, the cost of energy required by the photodegradation process can be offset by the energy generated by the anaerobic process. Alternatively, photodegradation can be employed for final polishing of the anaerobically treated effluent. Used in this manner, the resulting effluent may not only be safe for discharge but can be clean enough for reuse.

## **2.7 Reactor Configurations**

### **2.7.1 *Reactor configurations for AD***

There are various reactor configurations that have been used for AD. The most used reactors are the continuously stirred tank reactor (CSTR), up-flow anaerobic sludge blanket (UASB) reactor, fixed bed reactor and fluidized bed bioreactor (FBB).

#### **CSTR**

In the CSTR, stirring ensures good contact between the biomass and substrate. However, the setback of stirring is that the agitator generates high shear, which causes attrition resulting in retarded cell growth. Moreover, since there is no mechanism of preventing microbial washout, CSTR has longer HRTs than other reactors. In order to reduce washout, a high volume of the

reactor is required with respect to the volume of waste to be processed (Montalvo et al., 2012). Another method that can be used to minimise the washout is sludge recycling, though it is not efficient.

### **Fixed bed bioreactor**

This kind of reactor is packed with some inert material to prevent microbial washout and it can be operated in up-flow or down-flow modes. The microbes attach to the support material and therefore are not washed out with the reactor effluent. This enables the reactor to provide good COD removal at a relatively shorter HRT and a better tolerance to toxic and organic shock loading. Also, this system has the advantage of being easy to construct, operate and maintain. Moreover, its effluent contains less suspended solids due to filtration across the bed. However, the shortcomings of this system include that a significant amount of energy is needed to pump the influent across the bed, there is often channelling and clogging across the bed, finally, the working reactor volume is low due to the space occupied by the packing material.

### **UASB reactor**

The UASB reactor operates on the principle of formation of granules from biomass during the anaerobic degradation. In this system, a blanket of granular sludge is formed and suspended in the reactor during the process. In the up-flow anaerobic sludge bed, the microorganisms are freely suspended in the tank and the feed introduced from the bottom suspends the granules formed by the biomass. The granules act as biomass support and prevent biomass washout. This system is therefore very efficient as it attains both proper mixing and biomass retention. The UASB reactor is the most popular of the current high rate reactors that have been applied to treat various industrial wastewater streams. A COD reduction of up to about 75% has been reported when UASB is applied in the treatment of sugar cane molasses spent wash (Satyawili & Balakrishnana, 2008). Wolmarans and De Villiers (2002) also reported a COD removal efficiency of 90% over a period of three seasons in a UASB plant treating distillery wastewater.

### **FBB**

The fluidized bed reactor combines the attributes of the fixed bed reactor and the UASB in that it employs a biomass support material as in fixed bed and also achieves good mixing as in the UASB. In this reactor type, the inert support material is fluidized by the influent and/or gas, resulting in efficient mixing and mass transfer. The FBB has been demonstrated in various studies to have good performance in the treatment of both low- and high-strength industrial wastewater streams (Fernández et al., 2001; García-Encina & Hidalgo, 2005; Shida et al., 2009). García-Bernet et al. (1998) treated distillery wastewater using a fluidized bed reactor and reported a reduction in carbon content of between 75% and 95%. The use of small size packing materials enables the media to retain high biomass due to the availability of a larger surface area resulting in a lower HRT. Fluidization also overcomes operating problems such as bed clogging and high pressure drops encountered in the fixed bed reactor. Generally, the use of biomass support material has become very essential in improving digester performance. Even of more significance is the selection of an appropriate support material that has some specific desired properties that can contribute more to the digester efficiency.

### 2.7.2 *Reactor configurations for photocatalysis*

A good photocatalytic reactor should efficiently convey pollutants and photons to the surface of the photocatalyst for the photocatalysis reaction. Braham and Harris (2009) carried out an extensive review of the effectiveness of different designs of solar photocatalytic reactors such as a parabolic trough, compound parabolic, inclined plate, double skin sheet, rotating disk, water bell, fibre optic, fixed bed and fluidized bed photocatalytic reactors. They identified the FBR as a system that requires further research due to its potential for use in solar photocatalysis as a result of its exceptionally high photon efficiencies, and mass and heat transfer rates.

FBRs come in different configurations based on the number of phases and the identity of the dispersed and continuous phases. Based on the number of phases, there are two- or three-phase FBRs. Three-phase reactors find application in the Fischer–Tropsh process (Schulz, 1999), airlift bioreactors (Vunjak-Novakovic et al., 2005) and photocatalysis (Kimura et al., 2004). Most fluidized bed photocatalytic reactors have the liquid as the main fluidizing medium (Vega et al., 2011). Very few studies report the use of fluidized bed photocatalytic reactors with air as the main fluidizing medium (Kimura et al., 2004). Using air instead of liquid for fluidization is advantageous since for the same level of fluidization, lower power consumption is required in contrast to liquid fluidized systems. Additionally, there is a lower level of hydrodynamic shear in air fluidized systems than in liquid fluidized systems (Vunjak-Novakovic et al., 2005). This low hydrodynamic shear is especially attractive when fluidizing supports catalysts as this minimises the separation of TiO<sub>2</sub> from its support.

Another advantage of air fluidized systems is that a high level of dissolved oxygen can be maintained in the solution at a low cost due the continuous sparging of air (Kimura et al., 2004). Dissolved oxygen is necessary to trap conduction band electrons thus preventing electron-hole recombination, which greatly reduces the quantum efficiencies of photocatalysts. In water fluidized reactor types, oxygen is usually added into the substrate solution by bubbling air in a mixing tank upstream of the reactor (Vega et al., 2011). This is costly due to the use of a water pump and compressor for fluidization and introduction of dissolved oxygen into the solution, respectively. The air fluidized system utilises a single compressor for both fluidization and introduction of oxygen into the reactor.

Several materials have been used for the construction of solar photocatalytic reactors. Malato et al. (2009) proposed that of all the materials used to construct solar photocatalytic reactors, fluoropolymers and borosilicate glass were the best. Although fluoropolymers are less costly than borosilicate glass in normal operation, their thickness would have to be increased to withstand the weight of the liquid, which would increase their cost. On the other hand, borosilicate glass has a high tensile strength and therefore could endure high pressures with thin walls and reduce the overall cost of the reactor material. Therefore, borosilicate glass was chosen as the material for the construction of the reactors.

A graph comparing the transmittance spectrum of Scott–Duran borosilicate glass and the emission spectrum of sunlight (Figure 4) shows that a very high percentage of sunlight could pass through the borosilicate glass walls. The only part of the solar spectrum outside the borosilicate glass transmittance line was a small section between 445 nm and 600 nm. The whole UV region of the solar spectrum (below 400 nm) was well within the borosilicate transmittance

line. This shows that borosilicate glass could transmit all the sunlight within the solar UV region. Blanco et al. (1999) reported that normal borosilicate glass could transmit only 81% of UV. However, they carried out their experiments using UV lamps and not sunlight. UV lamps emit more UV radiation than sunlight, which could explain the low transmission of UV light from the lamps through borosilicate glass.

Most photocatalysis studies use batch or semi-batch reactors to investigate substrate or catalyst characteristics with little focus on the reactor itself. Consequently, the development of low-cost, continuous-flow and scalable photocatalytic reactors that can be commercialised has lagged. For commercial application, hydrodynamics and light distribution inside the reactor at different operating conditions need to be understood to enable optimisation and scale-up of the reactor design. The reactor hydrodynamics and light distribution can be effectively modelled using CFD and Monte Carlo simulation, respectively. The CFD model can be solved using a finite volume method employing a commercial code such as ANSYS Fluent (Troshko & Zdravistch, 2009).

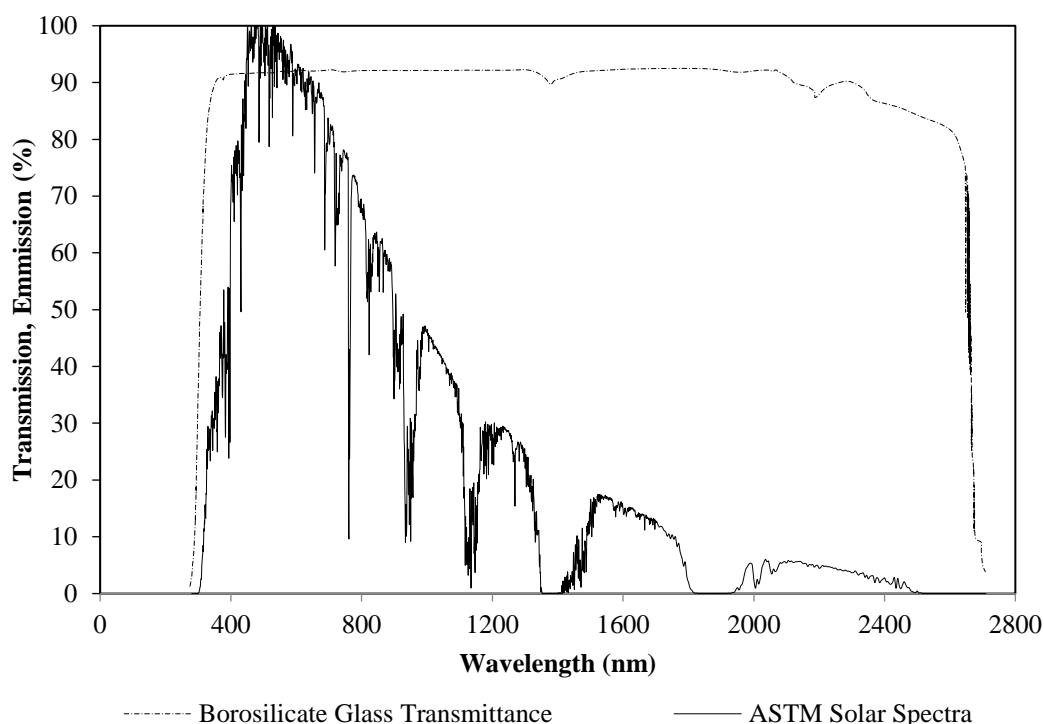


**Figure 4: Comparison of the transmittance of a 2 mm thick borosilicate glass and the emission of the ASTM reference solar spectrum (Schott, 2012; National Renewable Energy Laboratory)**

### **2.7.3 Hydrodynamics modelling of photocatalytic reactors**

FBRs for photocatalysis consist of three phases (solid, liquid and gas). FBRs are complex systems; therefore, hydrodynamics is the most important issue depending on the geometrical properties and operating conditions of the system. Consequently, the modelling, design and scale-up of these reactors necessitate accurate prediction of the hydrodynamics. A conventional method for predicting the hydrodynamics of FBRs is through mathematical modelling and correlations (Kumar & Bansal, 2013). Many of these correlations have been developed in the past although the drawback of these correlations is that they are only applicable to specific

reactor configurations and hydrodynamic conditions. Therefore, FBRs require a different method of predicting hydrodynamics.

### **Pre-processing**

Pre-processing is a first in building and analysing a flow model. Pre-processing consists of input of a flow problem by means of an operator interface and subsequent transformation of this input to form a suitable flow model that can be solved by the solver. Pre-processing involves a two- or three-dimensional model of the system of interest, followed by meshing the geometry. Mesh generation is the process of dividing the geometric model into a number of discrete parts or finite elements. The shape of these elements can be tetrahedral, prism or hexahedral depending on the type of geometry and analysis. The finer the mesh, the more accurate the results are but the longer the analysis time. Therefore, a compromise between accuracy and solution speed is usually made. Wang et al. (2012) used 1 million hexahedral volume cells to discretize three-dimensional domain and concluded that they obtained mesh-independent results. Periyathamby & Ray (1999) stated that to obtain accurate results, they had to divide the three-dimensional domain into control volumes ranging from 500 000 to 1 000 000 cells distributed unevenly within the computational domain. Solving any fluid dynamics problem using CFD involves three steps: pre-processing, solver and post-processing. Most commercial software for CFD has specific functions to carry out these steps in a sequential and logical manner.

### **Solver**

The data from the mesh is fed to the solver and tells it the exact problem to solve. The solver involves specifying and performing the following tasks:

- Specify the type of model (multiphase, Eulerian, and volume of fluid).
- Specify fluid properties such as viscosity, density, heat capacity and thermal conductivity.
- Determine which flow-related variables need to be calculated.
- Specify the boundary conditions to each set of faces.
- Define the initial conditions for the simulation.

ANSYS Fluent uses two types of numerical method to solve governing equations, namely, density-based solver and pressure-based solver. The density-based solver was developed for high-speed compressible flows; the pressure-based solver was developed for low-speed incompressible flows. Photocatalytic reactors are usually operated under low-speed flows; therefore, the pressure-based solver is appropriate. Discretization is a technique for converting partial differential (governing) equations into algebraic equations that can be solved numerically by iteration. The types of discretization technique found in ANSYS are spatial, temporal, gradient limiters and evaluation of gradients and derivatives. Selection varies based on the type of analysis. For multiphase flows, the solver can use two approaches for numerical calculation, namely, The Euler–Lagrange approach and the Euler–Euler approach.

### *Euler–Lagrange approach*

The fluid phase is treated as a continuum by solving the time-averaged Navier–Stokes equations. The dispersed phase is solved by tracking a large number of particles, bubbles, or droplets through the calculated flow field. The dispersed phase can exchange momentum, mass and energy with the fluid phase. This model is appropriate for modelling of spray dryers, particle laden flows and coal and liquid fuel combustion (Fluent, 2013).

### *Euler–Euler approach*

In the Euler–Euler approach, the different phases are treated mathematically as interpenetrating continua. Since the volume of a phase cannot be occupied by the other phase, the concept of the volume fraction is introduced. These volume fractions are assumed to be continuous functions of space and time and their sum is equal to one. Conservation equations for each phase are derived to obtain a set of equations, which have similar structure for all phases. This model is appropriate for fluidized bed, bubble columns and slug flows (Fluent, 2013).

The solver finds a solution to several equations that describe the physics of the flow. These equations are known as the governing equations and include mass conservation, momentum conservation and the standard k-ε model.

### **Volume of fraction**

The description of multiphase flow as interpenetrating continua involves the concept of phase volume fraction (Fluent, 2013). The volume fraction equation (Eq. 8) is used to keep a check on the volume fraction of the dispersed and continuous phases so that estimates of the density, viscosity and mass averaged velocity can be made using (Eq. 9) to (Eq. 11).

$$\frac{\partial}{\partial t}(\varphi_k \rho_k) + \frac{\partial}{\partial x_i}(\varphi_k \rho_k u_{m,i}) = -\frac{\partial}{\partial x_i}(\varphi_k \rho_k u_{D_k,i}) \quad (8)$$

The mixture density,  $\rho_m$ , is expressed by

$$\rho_m = \sum \varphi_k \rho_k \quad (9)$$

The mixture viscosity,  $\mu_m$ , is

$$\mu_m = \sum_{k=1}^n \varphi_k \mu_k \quad (10)$$

and the mass averaged velocity vector,  $u_m$ , is represented by the relationship

$$u_m = \frac{\sum_{k=1}^n \varphi_k \mu_k}{\rho_m} \quad (11)$$

## Mass conservation

The continuity equation for the mixture phase is

$$\frac{\partial \rho_m}{\partial t} + \frac{\partial}{\partial x_i} (\rho_m u_{m,i}) = 0 \quad (12)$$

where  $u_{m,i}$  is the mixture velocity in the  $i$ -th direction, and  $\partial \rho_m / \partial t$  is the partial differential operator for the  $i$ -th direction.

## Momentum conservation

Momentum equation for the mixture is given by

$$\begin{aligned} \frac{\partial}{\partial t} (\rho_m u_{m,j}) + \frac{\partial}{\partial x_i} (\rho_m u_{m,i} u_{m,j}) = & -\frac{\partial p}{\partial x_j} + \frac{\partial}{\partial x_i} \mu_m \left( \frac{\partial}{\partial x_j} (u_{m,i}) + \frac{\partial}{\partial x_i} (u_{m,j}) \right) + \\ & \rho_m g_j + F_j + \frac{\partial}{\partial x_i} \sum_{k=1}^n \varphi_k \rho_k u_{D_k,i} u_{D_k,j} \end{aligned} \quad (13)$$

where on the right-hand side, the forces acting on the mixture phase are collected together and include the effects of pressure  $\partial p / \partial x_j$ , viscous stress  $\partial \mu_m / \partial x_j$ , gravitational acceleration in the  $j$ -th direction  $g_j$ , momentum sources in the  $j$ -th direction  $F_j$ , and interphase momentum interactions.

## Standard $k$ - $\varepsilon$ model

The  $k$ - $\varepsilon$  turbulence model (Eq. 14 and Eq. 15) is a two-equation model in which fluctuating velocities and Reynolds stresses have been related to the properties of the turbulent flow itself such as  $k$  and  $\varepsilon$ .

$$\frac{\partial \rho k}{\partial t} + \nabla \cdot \mathbf{v} k = \nabla \cdot \left[ \left( \mu + \frac{\mu_t}{\sigma_k} \right) \nabla k \right] + G - \rho \varepsilon \quad (14)$$

$$\frac{\partial \rho \varepsilon}{\partial t} + \nabla \cdot \mathbf{v} \varepsilon = \nabla \cdot \left[ \left( \mu + \frac{\mu_t}{\sigma_\varepsilon} \right) \nabla \varepsilon \right] + \frac{\varepsilon}{k} G C_{1\varepsilon} - \rho \frac{\varepsilon^2}{k} C_{2\varepsilon} \quad (15)$$

where  $k$  is the turbulent kinetic energy,  $\varepsilon$  is the turbulent kinetic energy dissipation rate,  $C_{1\varepsilon}$  and  $C_{2\varepsilon}$  are model parameters found experimentally,  $G$  is the turbulence production term,  $\mu_t$  is the turbulent or eddy viscosity,  $\mu$  is the dynamic molecular viscosity and  $\sigma_k$ , &  $\sigma_\varepsilon$  are Prandtl numbers that connect the diffusivity of  $k$  and  $\varepsilon$ .

## Post-processing

After running the calculation, the post-processing option allows the user to view, set up and examine the results. This is done by generating contours plots, velocity vectors, path lines and iso-surfaces. For a more detailed analysis of results, the user can create XY plots of the different variables of interest.

## 2.8 Conclusion

Distillery and textile wastewater are environmental pollutants that are detrimental to both aquatic and human lives. Therefore, robust and low-cost methods need to be developed to eliminate the colour and chemicals present in such wastewater. AD is an appropriate technology for treating industrial wastewater with high organic load. The prominent advantage of this technology is its ability to convert organic pollutants into biomethane, which is a renewable energy source. However, wastewater containing biorecalcitrant and toxic organic pollutants are usually not treated efficiently by this method. It is proposed that photodegradation can be combined with AD to treat wastewater with biorecalcitrant/toxic components. The photodegradation can be applied as a pre-treatment step to increase the biodegradability of biorecalcitrant components or it can be employed as a post-treatment technique to the anaerobic system to eliminate recalcitrant organics that might have passed through the AD system without being degraded. Employing FBRs in the integrated system can enhance wastewater treatment efficiency since FBRs achieve adequate mixing and efficient mass transfer. To use FBRs, their configuration and operating conditions need to be optimised. This can be achieved by modelling the reactors using computational fluid dynamics simulation.

## 2.9 References

- Ai, Z., Gao, Z., Su, K., Ho, W. & Zhang, L. (2012). Aerosol flow synthesis of N, Si-codoped TiO<sub>2</sub> hollow microspheres with enhanced visible-light driven photocatalytic performance. *Catalysis Communications*, 29:0, 189–193.
- Anderson, C. & Bard, A. (1997). Improved photocatalytic activity and characterization of mixed TiO<sub>2</sub>/SiO<sub>2</sub> and TiO<sub>2</sub>/Al<sub>2</sub>O<sub>3</sub> materials. *Journal of Physical Chemistry, B*, 101:2611–2616.
- Artale, M.A. et al. (2001). Preparation and characterization of membranes with entrapped TiO<sub>2</sub> and preliminary photocatalytic tests. *Annali de Chimie*, 91:127–136
- Asahi, R., Morikawa, T., Ohwaki, T., Aoki, K. & Taga, Y. (2001). Visible-light photocatalysis in nitrogen-doped titanium dioxides. *Science*, 293:269–271.
- Banat, I.M., Nigam, P., Singh, D. & Marchant, R. (1996). Microbiology decolourization of textile-dye containing effluents: A review. *Bioresources Technology*, 58:217–27.
- Bjornsson, L., Mattiasson, B. & Henrysson, T. (1997). Effects of support material on the pattern of volatile fatty acid accumulation at overload in anaerobic digestion of semi-solid wastes. *Applied Microbiology and Biotechnology*, 47, 640–644.
- Blanco, J. et al. (1999). Compound parabolic concentrator technology development to commercial solar detoxification applications. *Solar Energy*, 67(4), 317–330.
- Boyjoo, Y., Ang, M. & Pareek, V. (2014). CFD simulation of a pilot scale slurry photocatalytic reactor and design of multiple-lamp reactors. *Chemical Engineering Science*, 111:266–7.
- Braham, R.J. & Harris, A.T. (2009). Review of major design and scale-up considerations for solar photocatalytic reactors. *Industrial & Engineering Chemistry Research*, 48(19), 8890–8905.

- Chakrabarti, S. & Dutta, B. K. (2004). Photocatalytic degradation of model textile dyes in wastewater using ZnO as semiconductor catalyst. *Journal of Hazardous Materials*, 112(3):269–78.
- Choi, H., Stathatos, E. & Dionysiou, D.D. (2007). Photocatalytic TiO<sub>2</sub> films and membranes for the development of efficient wastewater treatment and reuse systems. *Desalination*, 202:199–206.
- Choi, W., Termin, A. & Hoffman, M.R. (1994). The role of metal ion dopants in quantum-sized TiO<sub>2</sub>: Correlation between photoreactivity and charge carrier recombination dynamics. *Journal of Physical Chemistry*, 98, 13669–13679.
- Chong, M.N, Jin, B., Chow, C.W.K. & Saint, C. (2010). Recent developments in photocatalytic water treatment technology: A review. *Water Research*, 44(10):2997–3027.
- Crittenden, J.C., Zhang, Y., Hand, D.W., Perram, D.L. & Marchand, E.G. (1996). Solar detoxification of fuel-contaminated groundwater using fixed-bed photocatalysts. *Water Environmental and Research*, 68, 270–278.
- Dubey, N., Rayalu, S.S., Labhsetwar, N.K., Naidu, R.R., Chatti, R.V. & Devotta, S. (2006). Photocatalytic properties of zeolite-based materials for the photoreduction of methyl orange. *Applied Catalysis*, 303, 152–157.
- Fernández, N., Fernández-Polanco, F., Montalvo, S. & Toledano, D. (2001). Use of activated carbon and natural zeolite as support materials, in an anaerobic fluidised bed reactor, for vinasse treatment. *Water Science and Technology*, 44, 1–6.
- Fluent. (2013). *ANSYS Fluent Theory Guide*, Version 15.0, Fluent Inc.
- Fogler, H.S. (1999). *Elements of Chemical Reaction Engineering*: Chapter 10: Catalysis and Catalytic Reactors. Prentice-Hall PTR Inc, 581–685.
- Fujishima, A., Rao, T.N. & Tryk, D.A. (2000). Titanium dioxide photocatalysis. *Journal of Photochemical, Photobiology C: Photochem: Review*, 1–21.
- García-Bernet, D., Buffiére, P., Elmaleh, S., Moletta, R. (1998). Application of the down-flow fluidized bed to the anaerobic treatment of wine distillery wastewater. *Water Science and Technology*, 38 (8–9), 393–399.
- García-Encina, P.A. & Hidalgo, M.D. (2005). Influence of substrate feed patterns on biofilm development in anaerobic fluidized bed reactors (AFBR). *Process Biochemistry*, 40, 2509–2516.
- Gaya, U.I. & Abdullah, A.H. (2008). Heterogeneous photocatalytic degradation of organic contaminants over titanium dioxide: A review of fundamentals, progress and problems. *Journal of Photochemical. Photobiology, C: Photochemical: Review*, 9:1–12.
- Gonzalez, G., Pena, M.M., García, M.T. & Uruena, M.A. (1999). Decolorization of molasses effluents by coagulation–flocculation process. *Zuckerindustrie*, 124 (5), 406–410.
- Guillard, C., Lachheb, H., Houas, A., Ksibi, M., Elaloui, E. & Hermann, J.M. (2003). Influence of chemical structure of dyes, of pH and of inorganic salts on their photocatalytic degradation by TiO<sub>2</sub> comparison of the efficiency of powder and supported TiO<sub>2</sub>. *Journal of Photochemistry and Photobiology A: Chemistry*, 158, 27–36.

- Habibi, M.H., Hassanzadeh, A. & Mahdavi, S. (2005). The effect of operational parameters on the photocatalytic degradation of three textile azo dyes in aqueous TiO<sub>2</sub> suspensions. *Journal of Photochemistry and Photobiology A: Chemistry*, 172, 89–96.
- Herrmann, J.M. (1999). Heterogeneous photocatalysis: Fundamentals and applications to the removal of various types of aqueous pollutants. *Catalysis Today*, 53:115–129.
- Hoffmann, M.R. & Martin ST. (1995). Environmental applications of semiconductor photocatalysis. *Chemical Review*, 95:69–95.
- Horning R.H. (1978). Textile Dyeing Wastewaters: Characterization and Treatment. US Department of Commerce, National Technical Information Service, PB–285 115.
- Ichiura, H., Kitaoka, T. & Tanaka, H. 2003. Preparation of composite TiO<sub>2</sub>-zeolite sheets using a papermaking technique and their application to environmental improvement. *Journal of Material Science*, 38:1611–1615.
- Jal, P.K., Patel, S. & Mishra, B.K. (2004). Chemical modification of silica surface by immobilization of functional groups for extractive concentration of metal ions. *Talanta*, 62:1005–1028.
- Juang, R.S., Tseng, R.L., Wu, F.C. & Lin, S.J. (1996). Use of chitin and chitosan in lobster shell wastes for colour removal from aqueous solutions. *Journal of Environmental Science and Health*, 31, 325–338.
- Kawahara, T., Konishi, Y., Tada, H., Tohge, N., Nishii, J. & Ito, S. (2002). A patterned TiO<sub>2</sub> (anatase)/TiO<sub>2</sub> (rutile) bilayer-type photocatalysis: Effect of the anatase/rutile junction on the photocatalytic activity. *Angewandte Chemie International Edition*, 41, 2811–2813.
- Kelleher, B.P., Leahy, J.J., Henihan, A.M., O’Dweyer, T.F., Sutton, D. & Leahy, M.J. (2000). Advances in poultry litter disposal technology: A review. *Bioresource Technology*, 83, 27–36.
- Khan, A., Mazyck, D. & Wu, C. (2002). TiO<sub>2</sub> coated activated carbon: A regenerative technology for water recovery, 021CES-73, International Conference on Environmental Systems, San Antonio.
- Khataee, A. (2009). Photocatalytic removal of CI Basic Red 46 on immobilized TiO<sub>2</sub> nanoparticles: Artificial neural network modelling. *Environmental Technology*, 30(11), 1155–1168.
- Kimura, T., Yoshikawa, N., Matsumura, N. & Kawase, Y. (2004). Photocatalytic degradation of nonionic surfactants with immobilized TiO<sub>2</sub> in an airlift reactor. *Journal of Environmental Science and Health, Part A*, 39(11–12), 2867–2881.
- Kumar, J. & Bansal, A. (2013). Photocatalytic degradation in annular reactor: Modelization and optimization using computational fluid dynamics (CFD) and response surface methodology (RSM), *Journal of Environmental Chemical Engineering*, 1:398–405.
- Kwak, S.Y. & Kim, S.H. (2001). Hybrid organic/inorganic reverse osmosis (RO) membrane for bactericidal anti-fouling: Preparation and characterization of TiO<sub>2</sub> nanoparticle self-assembled aromatic polyamide thin-film-composite (TFC) membrane. *Environmental Science and Technology*, 35:2388–2394.

- Li, G., Liu, F. & Zhang, Z. (2010). Enhanced photocatalytic activity of silica-embedded TiO<sub>2</sub> hollow microspheres prepared by one-pot approach. *Journal of Alloys and Compounds*, 493(1–2), L1–L7.
- Li, Y., Sun, S., Ma, M., Ouyang, Y. & Yan, W. (2008). Kinetic study and model of the photocatalytic degradation of rhodamine B (RhB) by a TiO<sub>2</sub>-coated activated carbon catalyst: Effects of initial RhB content, light intensity and TiO<sub>2</sub> content in the catalyst. *Chemical Engineering Journal*, 142(2), 147–155.
- Liu, W.T., Chan, O.C. & Fang, H.H.P. (2002). Characterization of microbial community in granular sludge treating brewery wastewater. *Water Research*, 36, 1767–1775.
- Londeree, D.J. (2002). Silica-titania composites for water treatment. MSc. Dissertation. University of Florida.
- Malato, S., Fernandez-Ibanez, P., Maldonado, M.I., Blanco, J. & Gernjak, W. (2009). Decontamination and disinfection of water by solar photocatalysis: Recent overview and trends. *Catalysis Today*, 147:1–59.
- Matatov-Meytal, Y.I. & Sheintuch, M. (1998). Catalytic abatement of water pollutants. *Industrial and Engineering Chemistry Research*, 37(2):309–326.
- Ming, D.W. & Dixon, J.B. (1987). Quantitative determination of clinoptilolite in soils by a cation exchange capacity method. *Clays Clay Mineral*, 35:463–468.
- Montalvo, S. et al. (2012). Application of natural zeolites in anaerobic digestion processes: A review. *Applied Clay Science*, 58, 125–133.
- Mu, Y., Yu, H.Q., Zheng, J.C. & Zhang, S.J. (2004). TiO<sub>2</sub>-mediated photocatalytic degradation of Orange II with the presence of Mn<sup>2+</sup> in solution. *Journal of Photochemistry and Photobiology A: Chemistry*, 163, 311–316.
- Nagamine, S., Sugioka, A., Iwamoto, H. & Konishi, Y. (2008). Formation of TiO<sub>2</sub> hollow microparticles by spraying water droplets into an organic solution of titanium tetraisopropoxide (TTIP): Effects of TTIP concentration and TTIP-protecting additives. *Powder Technology*, 186(2), 168–175.
- Natarajan, T.S., Thomas, M., Natarajan, K., Bajaj, H.C. & Tayade, R.J. (2011). Study on UV-LED/TiO<sub>2</sub> process for degradation of Rhodamine B dye. *Chemical Engineering Journal*, 169(1–3), 126–134.
- Ni, M., Leung, M.K.H., Leung, D.Y.C. & Sumathy, K. (2007). A review and recent developments in photocatalytic water-splitting using TiO<sub>2</sub> for hydrogen production. *Renewable and Sustainable Energy Reviews*, 11:401–425.
- Oller, I., Malato, S. & Sanchez-Perez, J.A. (2011). Combination of advanced oxidation processes and biological treatments for wastewater decontamination: A review. *Science of the Total Environment*, 409, 4141–4166.
- Park, D., Yun, Y.S. & Park, J.M. (2005). Use of dead fungal biomass for the detoxification of hexavalent chromium: Screening and kinetics. *Process Biochemistry*, 40:2559–2565.
- Periyathamby, U. & Ray, A.K. (1999). Computer simulation of a novel photocatalytic reactor using distributive computing environment. *Chemical Engineering Technology*, 22, 881–8.

- Pirkanniemi, K. & Sillanpää, M. (2002). Heterogeneous water phase catalysis as an environmental application: a review. *Chemosphere*, 48:1047–1060.
- Portela, R. et al. (2012). Photocatalysis for continuous air purification in wastewater treatment plants: From lab to reality. *Environmental Science & Technology*, 46(9), 5040–5048.
- Poulsen, T.G. & Hansen, J.A. (2003). Strategic environmental assessment of alternative sewage sludge management scenarios. *Waste Management Resource*, 21(1), 19–28.
- Powell, G.E. & Archer, D.B. (1989). On-line titration method for monitoring buffer capacity and total volatile fatty acid levels in anaerobic digestion. *Biotechnology Bioengineering* 33, 570–577.
- Prairie, M.R., Evans, L.R. & Martinez, S.L. (1994). Destruction of organics and removal of heavy metals in water via TiO<sub>2</sub> photocatalysis. In: Eckenfelder, W.W., Roth, J.A., Bowers, A.R. (Eds.), *Chemical Oxidation: Technologies for the Nineties*, vol. 2. Technomic Publishing Company Inc, Pennsylvania US, 428–441.
- Remigi, E.U. & Buckley, C.A. (2006). Co-digestion of high strength/toxic organic effluents in anaerobic digesters at wastewater treatment works. *Water Research Commission* report no. 1074/1/06.
- Rincón, A.G. & Pulgarin, C. (2004). Effect of pH, inorganic ions, organic matter and H<sub>2</sub>O<sub>2</sub> on *E. coli* K12 photocatalytic inactivation by TiO<sub>2</sub>-implications in solar water disinfection. *Applied Catalysis B: Environmental*, 51, 283–302.
- Rizzo, L. (2011). Bioassays as a tool for evaluating advanced oxidation processes in water and wastewater treatment. *Water Research* 45, 4311–4340.
- Sakthivel, S, Shankar, M.V., Palanichamy, M., Banumathi A., Bahnemanna, D.W. & Murugesanb, V. (2004). Enhancement of photocatalytic activity by metal deposition: Characterization and photonic efficiency of Pt, Au and Pd deposited on TiO<sub>2</sub> catalyst. *Water Research*, 38, 3001–3008.
- Satyawali, Y. & Balakrishanan, M. (2008). Wastewater treatment in molasses based alcohol distilleries for COD and color removal: A review. *Journal of Environmental Management*, 86, 481–497.
- Schrank, S.G., José, H.J. & Moreira, R.F.P.M. (2002). Simultaneous photocatalytic Cr(VI) reduction and dye oxidation in a TiO<sub>2</sub> slurry reactor. *Journal of Photochemistry and Photobiology. A: Chemistry*, 147:71–76.
- Schulz, H. (1999). Short history and present trends of Fischer–Tropsch synthesis. *Applied Catalysis A: General*, 186(1), 3–12.
- Shan, A.Y., Ghazi, T.I.M. & Rashid, S.A. (2010). Immobilisation of titanium dioxide onto supporting materials in heterogeneous photocatalysis: A review. *Applied Catalysis A: General*, 389(1), 1–8.
- Shida, G.M. et al. (2009). Long-term stability of hydrogen and organic acids production in an anaerobic fluidized-bed reactor using heat treated anaerobic sludge inoculum. *International Journal of Hydrogen Energy*, 34, 3679–3688.
- Simate, S.G. et al. (2011). The treatment of brewery wastewater for reuse: state of the art. *Desalination*, 273, 235–247.

- Slokar, Y.M. & Le Marechal, A.M. (1997). Methods of decoloration of textile wastewaters. *Dyes Pigments*, 37:335–356.
- Solozhenko, E.G., Soboleva, N.M. & Goncharuk, V.V. (1995). Decolorization of azo dye solutions by Fenton's oxidation. *Water Research*, 29 (9):2206–2210.
- Troshko, A.A. & Zdravistch, F. (2009). CFD modeling of slurry bubble column reactors for Fisher–Tropsch synthesis. *Chemical Engineering Science*, 64(5), 892–903.
- Turchi, C. & Ollis, D. (1990). Photocatalytic degradation of organic water contaminant: Mechanisms involving hydroxyl radical attack. *Journal of Catalysis*, 122, 178–192.
- Turner, M. et al. (2008). Selective oxidation with dioxygen by gold nanoparticle catalysts derived from 55-atom clusters. *Nature*, 454, 981–983.
- Vega, A.A., Keshmiri, M. & Mohseni, M. (2011). Composite template-free TiO<sub>2</sub> photocatalyst: Synthesis, characteristics and photocatalytic activity. *Applied Catalysis B: Environmental*, 104(1–2), 127–135.
- Venceslau M.C., Stephenson, T. & Simon J.J. (1994). Characterization of textile wastewaters: A review. *Environmental Technology*, 15:10, 917–929.
- Vinodgopal, K. & Kamat, P.V. (1992). Photochemistry on surfaces: Photodegradation of 1,3-diphenylisobenzofuran over metal oxide particles. *Journal of Physical Chemistry*, 96:5053–5059.
- Vunjak-Novakovic, G., Kim, Y., Wu, X., Berzin, I. & Merchuk, J.C. (2005). Air-lift bioreactors for algal growth on flue gas: Mathematical modeling and pilot-plant studies. *Industrial & Engineering Chemistry Research*, 44(16), 6154–6163.
- Wang, X., Feng, Y. J. & Lee, H. (2008). Electricity production from beer brewery wastewater using single chamber microbial fuel cell. *Water Science and Technology*, 57(7), 1117–1122.
- Wang, X. & Lim, T. (2010). Solvothermal synthesis of C–N codoped TiO<sub>2</sub> and photocatalytic evaluation for bisphenol A degradation using a visible-light irradiated LED photoreactor. *Applied Catalysis B: Environmental*, 100(1–2), 355–364.
- Wang, Y., Zhou, A. & Yang, Z. (2008). Preparation of hollow TiO<sub>2</sub> microspheres by the reverse microemulsions. *Materials Letters*, 62(12–13), 1930–1932.
- Wang, Z., Liu, J., Dai, Y., Dong, W., Zhang, S. & Chen, J. (2012). CFD modelling of a UV-LED photocatalytic odor abatement process in a continuous reactor. *Journal of Hazardous Materials*, Vol. 215, 25–7.
- Winter, C.G.J. (1999). Bacterial metabolism in wastewater treatment systems. *Biotechnology*, 11, 17–53.
- Xiong, X., Lin, M., Duan, J., Wang, Y. & Yu, Z. (2012). Preparation of hollow TiO<sub>2</sub> microspheres using a novel polymer microsphere template. *Reactive and Functional Polymers*, 72(6), 365–371.
- Xu, Y. & Lebrun, R.E. (1999). Treatment of textile dye plant effluent by nano filtration membrane. *Separation Science and Technology*, 34, 2501–2519.
- Yamazaki, S., Matsunaga, S. & Hori, K. 2001. Photocatalytic degradation of trichloroethylene in water using TiO<sub>2</sub> pellets. *Water Resources*, 35:1022–1028.

- Ye, M., Chen, Z., Wang, W., Shen, J. & Ma, J. (2010). Hydrothermal synthesis of TiO<sub>2</sub> hollow microspheres for the photocatalytic degradation of 4-chloronitrobenzene. *Journal of Hazardous Materials*, 184(1–3), 612–619.
- Zhang, F., Zhang, Y., Song, S. & Zhang, H. (2011). Superior electrode performance of mesoporous hollow TiO<sub>2</sub> microspheres through efficient hierarchical nanostructures. *Journal of Power Sources*, 196(20), 8618–8624.
- Zhu, H., Zhang, M., Xia, Z. & Low, G.K.C. (1995). Titanium dioxide mediated photocatalytic degradation of monocrotophos. *Water Research*, 29, 2681–2688.

### 3 PHOTODEGRADATION OF MWW USING TiO<sub>2</sub>-ZnO NANOHYBRID PHOTOCATALYST SUPPORTED ON ACTIVATED CARBON

#### 3.1 Introduction

Molasses-based distilleries are some of the most polluting industries generating large volumes of high-strength wastewater (Apollo et al., 2013). The final effluent after the distillation process is MWW, a viscous hydrophilic dark-coloured liquid with a strong objectionable odour. MWW pollutes the aquatic ecosystem because of its intense brown colour, which hinders light penetration, prevents photosynthesis and thus causes anaerobic conditions. The dark-brown colour is mainly due to the presence of brown polymeric melanoidin pigments that are recalcitrant to conventional treatment methods (Apollo et al., 2016). Effective treatment of MWW has been achieved by chemical, flocculation and physiochemical treatment methods such as adsorption and ozonation (Apollo et al., 2016). However, these methods are not economically feasible due to the high cost involved and in some cases are non-destructive as they only transfer the pollutants from one phase to another leading to secondary pollution (Duan et al., 2015). Other methods such as biological treatment through aerobic and anaerobic degradation barely remove the pigments with approximately only 6–7% degradation reported (Ojijo et al., 2010).

Photocatalysis offers the advantage of destroying pollutants in contrast to other methods that transfer the contaminants from one form to another. In this way, organic and inorganic substances are transformed or degraded into less harmful products. The use of TiO<sub>2</sub> and ZnO as photocatalysts for degradation of organic compounds has received a great deal of interest. TiO<sub>2</sub> has been used extensively in environmental applications because of its high activity, chemical stability, robustness against photocorrosion, low toxicity and availability at low cost (Song et al., 2014). Depending on the crystalline structure (rutile or anatase), the wideband gap ranges of 3.0 eV to 3.2 eV for TiO<sub>2</sub> result in the reduction of its overall photocatalytic activity since it only absorbs a small fraction (4%) of incident solar (Navgire et al., 2012). Another semiconductor of interest is ZnO due to its wideband gap (3.37 eV), large excitation binding energy (60 meV), which permits laser emission at room temperature, piezoelectric properties (Avcı et al., 2013), and exhibits better efficiency than TiO<sub>2</sub> under UV light (Ahmad et al., 2014). However, ZnO suffers drawbacks such as photocorrosion during light irradiation and instability (Jonidi-Jafari et al., 2015). In low band gap semiconductors, photocatalysis is hampered by recombination of photogenerated holes and electrons thus lowering the overall quantum yield (Abdullah et al., 2013).

Hybrid materials have been investigated for environmental remediation as they exhibit the properties of different components in the same structure. Photodegradation of molasses by MoO<sub>3</sub>-TiO<sub>2</sub> composite material (Navgire et al., 2012), degradation of Rhodamine B using a ZnO-carbon nanotube (CNT) composite (Ahmad et al., 2014), UV/H<sub>2</sub>O<sub>2</sub>/TiO<sub>2</sub>/Zeolite for the treatment of MWW (Apollo et al., 2014), and removal of phenol by monocrystalline TiO<sub>2</sub>/AC (Ngamsopasiriskun et al., 2010) have all been reported. Compared with separate systems of ZnO and TiO<sub>2</sub>, the TiO<sub>2</sub>-ZnO hybrid system displays a largely improved photocatalytic activity as reported for the degradation of diazinon (Jonidi-Jafari et al., 2015), methyl orange and 4-

nitrophenol (Zhang et al., 2012), and for the photodegradation of phenol (Prabha & Lathasree, 2014). To further enhance the activity of TiO<sub>2</sub>-ZnO nanohybrid and also reduce the cost associated with post-treatment catalyst separation, immobilisation onto a support material should be considered (Ngamsopasiriskun et al., 2010). Coating the catalyst onto the adsorbent surface integrates its photocatalytic activity with the adsorption properties of the adsorbent thus inducing a synergistic effect resulting in enhanced photocatalytic efficiency (Apollo et al., 2014). AC is widely used as a support material due to its good adsorption properties, mechanical resistance, high surface area, optimum porosity, low cost and seems to be an attractive support for TiO<sub>2</sub> (Pan et al., 2013). The AC support can be introduced to the composite through various preparation methods such as mixing, sol-gel precipitation, dip-hydrothermal method or pyrolysis of hydrolysed TiCl<sub>4</sub> (Li et al., 2012). Nanoparticles of ZnO and TiO<sub>2</sub> have been used separately over the time in several photocatalytic research activities with limited studies focusing on the advantages of TiO<sub>2</sub>-ZnO hybrid system (Avcı et al., 2013).

While some few studies have considered the application of TiO<sub>2</sub>-ZnO hybrid systems in the remediation of wastewater containing recalcitrant compounds, to the best of the authors' knowledge, so far there has been no reported application of the same or of supported TiO<sub>2</sub>-ZnO in MWW treatment. Hence, in this study, application of TiO<sub>2</sub>-ZnO hybrid nanocatalyst supported on AC as an efficient catalyst in the treatment of MWW was evaluated to determine the synergistic effects of coupling TiO<sub>2</sub> and ZnO into TiO<sub>2</sub>-ZnO hybrid, and also the photo-degradation enhancing effect of employing AC as a support material. Moreover, a novel method for determining degradation of melanoidin by monitoring nitrate formation is presented. The effect of pH on the process was investigated in addition to the study of adsorption thermodynamics and reaction kinetics.

## **3.2 Materials and Methods**

### **3.2.1 Chemicals and materials**

Zinc chloride (97%), titanium (IV) isopropoxide (97%), commercial TiO<sub>2</sub> (Aeroxide P25), Ludox colloidal silica and methanol (99.5%), were all obtained from Sigma Aldrich and used as received. Granular AC (150-200 mesh) was purchased from Industrial Analytical. A batch photoreactor with 12 W UV-C low-pressure lamp and 250 ml capacity was obtained from Puritech, South Africa. The lamp had a shortwave range (100–280 nm) concentrated at 254 nm, important for the production of the much needed hydroxyl radicals, with a total UV output of 300 watts/m<sup>2</sup> on the surface. Molasses was purchased from local stores in Vanderbijlpark, South Africa.

### **3.2.2 Preparation of TiO<sub>2</sub>-ZnO nanohybrid and subsequent support onto AC**

To prepare TiO<sub>2</sub>-ZnO nanohybrid catalyst, TiO<sub>2</sub> was first synthesised before immobilising ZnO on its surface. Reflux method was employed in synthesising TiO<sub>2</sub>, adopting a method reported by Behnajady et al. (2011). Per the method, a precursor solution containing 3.55 ml titanium Isopropanol (TTIP) and 0.48 ml methanol was sonicated in an ultrasonic bath and thereafter hydrolysed by adding 14.04 ml of water drop by drop under reflux and magnetic

stirring at 80°C. After adding water, reflux was continued for three hours. Here, TTIP:H<sub>2</sub>O:methanol molar ratios were 1:65:1. The obtained sol was redispersed in methanol and then centrifuged to remove the solvent before drying at 80°C for 12 hours obtaining 1 g of TiO<sub>2</sub> powder, which was finally calcined at 500°C for three hours.

Stock solutions of 0.1 M zinc chloride (ZnCl<sub>2</sub>) and 0.2 M sodium hydroxide (NaOH) with pH of 6 and 13, respectively, were prepared for ZnO synthesis. TiO<sub>2</sub> was first oven-dried at 103°C for three hours before immobilising ZnO on its surface (Jonidi-Jafari et al., 2015). The dry TiO<sub>2</sub> was added to the ZnCl<sub>2</sub> solution at different proportions to obtain catalysts with different ratios of TiO<sub>2</sub>:ZnO. A sodium hydroxide solution was then added to the TiO<sub>2</sub>-ZnCl<sub>2</sub> precursor obtaining an alkaline medium (pH 12), which resulted in the production of white and gelatinous TiO<sub>2</sub>-ZnO. This reaction was performed for seven hours under continuous stirring. The products in aqueous solution were centrifuged, washed with deionised water, dried at 100°C for 12 hours before calcining at 500°C for three hours. ZnO was obtained through the same procedure, but without the addition of TiO<sub>2</sub>.

The AC was washed with deionised water before applying it as a support. The support was introduced modifying a method reported by Zainudin et al. (2010). In the modified method, predetermined masses of nano-sized TiO<sub>2</sub>-ZnO and AC (150–200 mesh) were mixed together and then uniformly dispersed in colloidal silica binder (30% binder loading). The binder is inert, transparent to UV radiation and has a good adherence between support and catalyst, in addition to exhibiting long-term stability (Haque et al., 2005). Uniform mixing of the catalyst and support was obtained through ultra-sonication at 25°C for five minutes. The mixture was then dried at 100°C obtaining granules. The obtained granules were gently crushed then screened with 325 mesh sieve. The resultant AC supported catalyst referred to as TiO<sub>2</sub>-ZnO-AC was obtained with different AC compositions by weight ranging from 0% to 60%.

### ***3.2.3 Catalyst characterisation***

Transmission electron microscopy (TEM; FEI Tecnai G2 20 S-Twin HR TEM with embedded Oxford INCA X-Sight EDX System), scanning electron microscopy (SEM; FEI Quanta 250 FEG ESEM with integrated Oxford X-Max 20 EDX system) and energy-dispersive X-ray (EDX) spectroscopy analyses were carried out to determine the particle sizes, particle shapes, surface morphologies and composition of the synthesised nanoparticles. UV visible (UV-Vis; T80+ UV/VIS Spectrometer, PG Instruments Ltd.) and photoluminescence (Jasco spectrofluorometer FP-8600) spectroscopies were used in determining the optical properties of the catalysts. Fourier transform infrared (FTIR; PerkinElmer FT-IR/NIR Spectrometer) was used to determine the functional groups present on the surface of the synthesised catalysts. To obtain the crystal structure of the catalysts, X-ray diffraction (XRD; Rigaku – Ultima IV XRD, Scan speed 4.00 deg/min, and scan range of 3–90 deg) was used.

### 3.2.4 Adsorption and photocatalytic studies

Samples of MWW were prepared by dissolving molasses in distilled water to obtain synthetic wastewater of required initial concentrations. Adsorption equilibrium experiments were carried out by adding catalyst to MWW at a predetermined catalyst loading. The solution was then kept in the dark while stirring for one hour. Sampling was carried out at predetermined time intervals. The samples were analysed for colour removal to monitor the adsorption process.

Photocatalytic experiments were carried out in a 250 ml batch photoreactor with a 12 W UV-C lamp. The solution, after adsorption in the dark, was transferred to the reactor through a peristaltic pump. Air was continuously pumped through to ensure uniform mixing of the catalyst and solution in the reactor. Sampling was carried out at predetermined time intervals to monitor the degradation rate. To monitor the photodegradation process, colour and total organic carbon (TOC) reduction, and formation of nitrate were determined. To analyse colour, the absorbance of samples taken at predetermined time intervals was measured using a spectrophotometer (T80+ UV/VIS Spectrometer, PG Instruments Ltd) at a maximum absorption wavelength ( $\lambda_{\text{max}}$ ) of 475 nm. The extent of decolourisation of MWW was monitored by measuring the decrease in colour intensity of the MWW and is expressed in terms of the degree of absorbance against time at  $\lambda_{\text{max}}$  (Navgire et al., 2012). The TOC and nitrate formation were analysed using a TOC analyser (Teledyne Tekmar) and ion chromatography (882 compact IC plus fitted with an 863 compact auto-sampler), respectively. The effects of parameters such as pH, AC loading and TiO<sub>2</sub>: ZnO ratio on the adsorption and degradation of MWW were also investigated.

## 3.3 Results and Discussion

### 3.3.1 Characterisation studies

#### 3.3.1.1 TEM, SEM-EDX, XRD and FTIR catalyst characterisations

From the TEM images shown in Figure 5, the average particle size of TiO<sub>2</sub>-ZnO determined from size distribution histogram was about 35–45 nm, confirming the successful synthesis of a nanohybrid. The TEM analysis showed that the TiO<sub>2</sub> nanoparticles had irregular shapes consisting of both spherical and tetrahedral, while ZnO nanoparticles had regular hexagonal shapes with large agglomeration. Similar observations were made by Zainudin et al. (2010) and Prabha and Lathasree (2014).

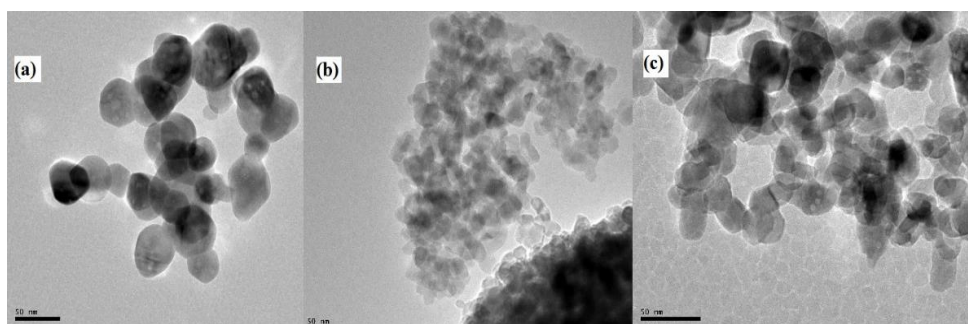


Figure 5: TEM images of (a) ZnO, (b) TiO<sub>2</sub> and (c) TiO<sub>2</sub>-ZnO

The SEM image of TiO<sub>2</sub>-ZnO in Figure 5 shows a possible hybridisation between TiO<sub>2</sub> and ZnO nanoparticles as shown by the well-dispersed ZnO on the surface of TiO<sub>2</sub>, similarly observed by Jonidi-Jafari et al. (2015).

The elemental composition of nano-sized ZnO, TiO<sub>2</sub> and TiO<sub>2</sub>-ZnO composite was analysed by EDX. As depicted in Table 5, the only elements present in TiO<sub>2</sub>-ZnO were Ti, O and Zn, indicating a distinct hybridisation between TiO<sub>2</sub> and ZnO. It is also evident from the EDX analysis that nano-ZnO was composed only of Zn and O, and nano TiO<sub>2</sub> consisted only of Ti and O elements. The SEM image of TiO<sub>2</sub>-ZnO/AC, Figure 6, shows the nanohybrid TiO<sub>2</sub>-ZnO well attached onto the surface of AC.

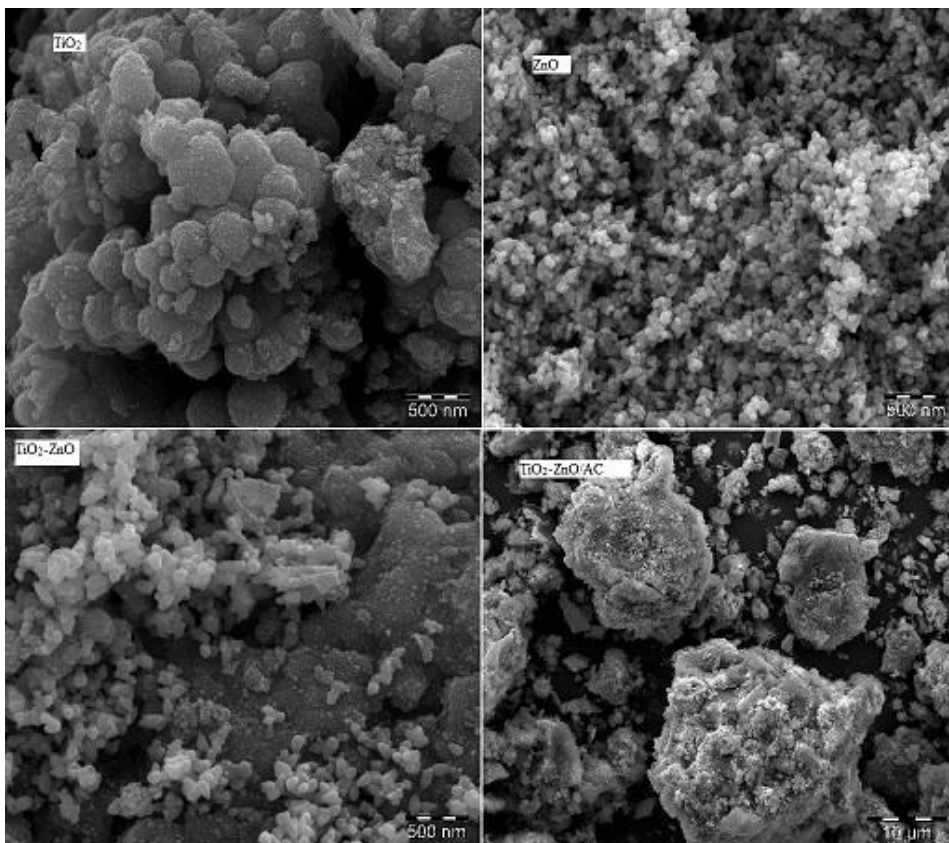
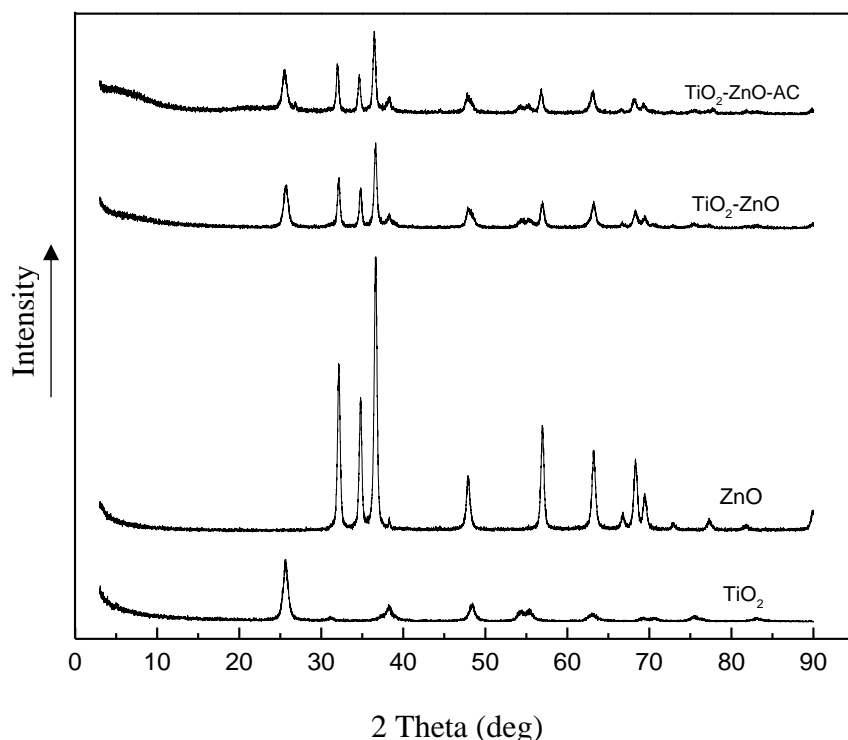


Figure 6: SEM images of TiO<sub>2</sub>, ZnO, TiO<sub>2</sub>-ZnO and TiO<sub>2</sub>-ZnO/AC

Table 5: Elemental composition (% weight) from the EDX spectra of ZnO, TiO<sub>2</sub> and TiO<sub>2</sub>-ZnO

Spectrum	Ti	Zn	O
ZnO		80.34	19.66
TiO <sub>2</sub>	59.95		40.05
TiO <sub>2</sub> -ZnO	28.05	42.75	29.2

A possible hybridisation of TiO<sub>2</sub> and ZnO in the hybrid catalyst is also shown by XRD, Figure 7. The XRD patterns show crystalline structure of TiO<sub>2</sub> and ZnO both before and after immobilisation of ZnO on TiO<sub>2</sub>. Peaks observed at 2 $\theta$  values of 31.92°, 34.6°, 36.48°, 47.54°, 56.60°, 62.86°, 66.38°, 67.96° and 69.10° for ZnO corresponds to (100), (002), (101), (102), (110), (103), (200), (112) and (201) planes of hexagonal wurtzite ZnO, respectively (Ba-Abbad et al., 2014; Zhang et al., 2012). The TiO<sub>2</sub> pattern has a dominant anatase phase corresponding to 2 $\theta$  = 25.3° (Liao et al., 2008). In the TiO<sub>2</sub>-ZnO nanocomposite, both the characteristic peaks of wurtzite ZnO and anatase TiO<sub>2</sub> were gradually decreased. The XRD results indicate a successful preparation of TiO<sub>2</sub>-ZnO nanohybrid and its subsequent support onto AC.



**Figure 7: XRD patterns of TiO<sub>2</sub>, ZnO, TiO<sub>2</sub>-ZnO and TiO<sub>2</sub>-ZnO/AC**

Successful hybridisation was also confirmed from the FTIR analysis. The IR spectrum of TiO<sub>2</sub>-ZnO hybrid was found to contain peaks observed in ZnO and TiO<sub>2</sub> spectra, Figure 8, confirming the formation of a new substance. The peaks observed at 3400 cm<sup>-1</sup> and 1650 cm<sup>-1</sup> were attributed to water bending and OH stretching, respectively. Similar observations have been made by Wang et al. (2013). The band observed at around 1400 cm<sup>-1</sup> was attributed to the vibration mode of Ti-O bond, also observed by Bahadur et al. (2010). The weak band observed at around 1590 cm<sup>-1</sup> for ZnO could be attributed to H-O-H bending vibration mode (Naimi-Joubani et al., 2015), which might have resulted from adsorption of moisture by the catalyst during sample preparation. The introduction of AC support led to a slight modification of the TiO<sub>2</sub>-ZnO-AC spectrum with a new weak and broad peak observed at around 1070 cm<sup>-1</sup>, which is attributable to C-N stretching vibration. The peak observed at around 1070 cm<sup>-1</sup> for TiO<sub>2</sub>-ZnO-AC is a broadened version of the corresponding peak observed for AC (Laginhas et al., 2016). The broadening could have resulted from the exposure of C-N,

which might have been inaccessible before the introduction of the hybrid and lengthy drying of the resultant composite.

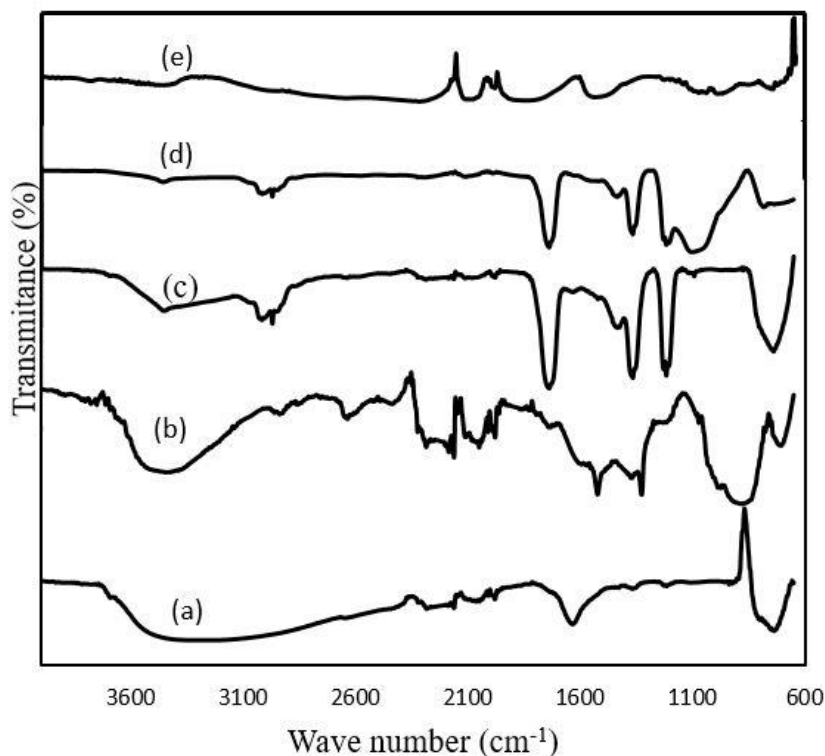


**Figure 8:** FTIR spectra of (a) TiO<sub>2</sub>, (b) ZnO, (c) TiO<sub>2</sub>-ZnO, (d) TiO<sub>2</sub>-ZnO-AC and (e) AC

### 3.3.1.2 Characterisation of optical properties

Optical properties of the catalyst were determined from UV-Vis and photoluminescence spectroscopies. The interactions between photocatalysts and photon energies can be sighted by UV-Vis spectroscopy. It was therefore of absolute importance to investigate the UV-Vis absorbance properties of the synthesised catalyst in order to determine their response to light irradiation. The UV-Vis absorbance spectra of TiO<sub>2</sub>, ZnO and TiO<sub>2</sub>-ZnO, Figure 9, were obtained in the wavelength region of 200 nm to 900 nm using methanol as solvent. Change in energy band gap due to coupling of semiconductors is primarily represented by UV-Vis absorption spectrum. A significant red shift is observed with TiO<sub>2</sub>-ZnO as compared with TiO<sub>2</sub> and ZnO. This shift is attributable to the energy needs of the three different catalysts. The hybrid TiO<sub>2</sub>-ZnO needs lower energy to be excited than both TiO<sub>2</sub> and ZnO. The direct band gaps ( $E_g$ ) of ZnO, TiO<sub>2</sub> and TiO<sub>2</sub>-ZnO were determined as:

$$E_g = 1240/\lambda \quad (16)$$

where  $\lambda$  is the wavelength of the exciting light (Hamal & Klabunde, 2007; Saheed Olalekan Sanni, 2014). At 380 nm and above, TiO<sub>2</sub> had a higher energy requirement than ZnO as shown with the crisscrossing curves. The higher energy requirement is attributable to the low photoactivity of TiO<sub>2</sub> in the visible region. ZnO with a larger optical band of 425 nm than TiO<sub>2</sub> with an optical band of 385 nm can absorb over a wider range of the UV spectrum (Wang et al., 2013).

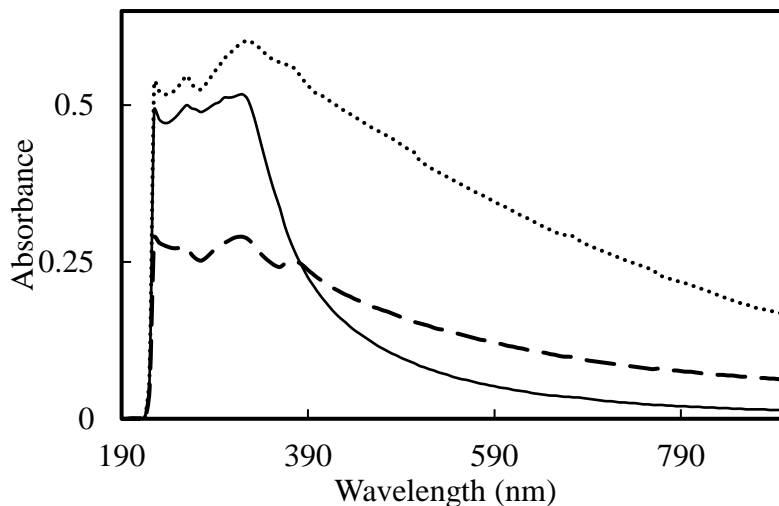


**Figure 9:** UV-Vis absorption spectra of TiO<sub>2</sub> (—), ZnO (---) and TiO<sub>2</sub>-ZnO (....)

**Table 6:** Wavelength and calculated band gap of the prepared photocatalysts

Catalyst	Wavelength (nm)	Band gap (eV)
TiO <sub>2</sub>	325	3.81
ZnO	380	3.3
TiO <sub>2</sub> -ZnO	410	3.0

Photoluminescence, an optical property of a photocatalyst, plays an important role in determining the fate of photogenerated species. Photoluminescence is caused by the emission of photons resulting from electron-hole pair recombination after a photocatalyst is irradiated, thus there is a correspondence between relative recombination rate of electron-hole pairs and the photoluminescence intensity (Zou et al., 2014). The higher the recombination, the higher the photoluminescence intensity. Also, the lower the recombination rate, the lower the photoluminescence intensity. On combining TiO<sub>2</sub> and ZnO into a nanohybrid, the photoluminescence intensity was greatly decreased as observed in Figure 10. The lower photoluminescence intensity shown by TiO<sub>2</sub>-ZnO could be attributed to the reduced recombination rate of photogenerated pairs resulting from the possible formation of a heterojunction.

In such a heterojunction, electron transfer can occur from the conduction band of TiO<sub>2</sub> to that of ZnO; the hole transfer can also take place from valence band of ZnO to that of TiO<sub>2</sub> (Wang et al., 2013), causing efficient charge separation and increased lifetime of charged carriers, which ultimately results in the reduced recombination rate. The further reduction in photoluminescence intensity observed after supporting TiO<sub>2</sub>-ZnO onto AC implies effective suppressing of recombination of the photogenerated species, and is attributable to the introduction of AC. Since AC is reported to be a relatively good electron acceptor (Ahmad et al., 2014), and TiO<sub>2</sub>-ZnO is a good electron donor, a synergistic effect between the two components would effectively reduce electron-hole pair recombination, with AC further acting as an electron sequester.

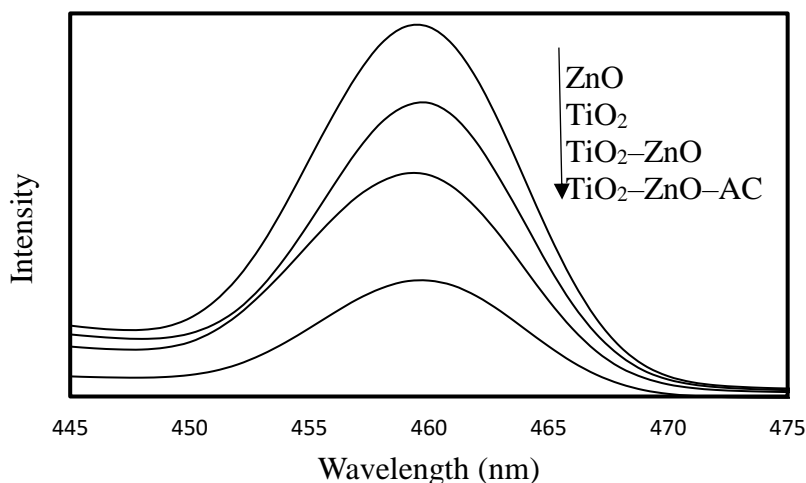


Figure 10: Photoluminescence spectra of  $\text{TiO}_2$ ,  $\text{ZnO}$ ,  $\text{TiO}_2\text{-ZnO}$  and  $\text{TiO}_2\text{-ZnO-AC}$

### 3.3.2 Adsorption and photocatalytic studies

#### 3.3.2.1 Effect of percentage fraction $\text{TiO}_2$ on the activity of $\text{TiO}_2\text{-ZnO}$

The effect of  $\text{TiO}_2\text{:ZnO}$  ratios was studied by varying the amount of  $\text{ZnO}$  immobilised on the surface of  $\text{TiO}_2$ . Different fractions of  $\text{TiO}_2$  in the range from 0% to 100% were investigated. The ratio with the highest activity was determined in the photodegradation of 4000 mg/L MWW, and it was observed that ratio 3:1 of  $\text{TiO}_2\text{:ZnO}$  (corresponding to 75%  $\text{TiO}_2$  composition by weight) had the highest activity of the ratios (Figure 11a), with the highest colour removal of 92.45%. A synergistic effect, Figure 11b, was therefore achieved as  $\text{TiO}_2\text{-ZnO}$  nanohybrid with 75%  $\text{TiO}_2$  composition showed the highest colour removal of 92.45%, higher than  $\text{TiO}_2$  and  $\text{ZnO}$ , which had 82.14% and 53.57%, respectively when used on their own.

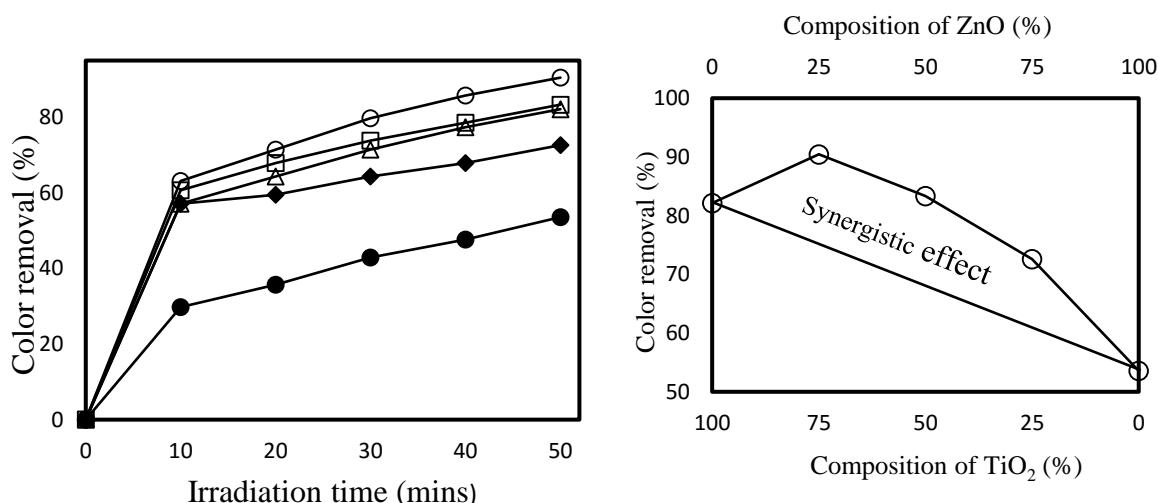


Figure 11: (a) Effect of  $\text{TiO}_2$  composition by weight, 0% (●), 25% (◆), 50% (□), 75% (○) and 100% (Δ), on the activity of  $\text{TiO}_2\text{-ZnO}$  nanocomposite in adsorption and photodegradation of 4000 mg/L MWW, 1 g/L catalyst loading at pH 5, and (b) synergistic representation of relative activity

Synergy is realised when the overall activity of two semiconductor photocatalysts used in a composite exceeds the sum of activities of each semiconductor (Ohtani, 2010). Synergy was obtained with an increased ZnO composition from 0% to 50% and was maximum at 25%. Increase in ZnO composition above 50% in the hybrid only improved the activity of ZnO but lowered that of TiO<sub>2</sub>. The improved activity of the hybrid can be attributed to the reduced electron-hole pair recombination observed in the reduced photoluminescence intensity (see Figure 10), that resulted in efficient charge separation, increased lifetime of charged carriers and the enhanced efficiency of interfacial to the adsorbed substrates (Habib et al., 2013). Moreover, the highest photocatalytic activity observed with 75% TiO<sub>2</sub> composition can be related to the amount of ZnO (25%) that has to be sufficient to trap photogenerated holes (Habib et al., 2013). Low decolonisation efficiency observed for 25% and 0% TiO<sub>2</sub> composition could be attributed to the limited amount of TiO<sub>2</sub> that resulted in low photogenerated holes. Subsequently in this study, TiO<sub>2</sub>-ZnO with TiO<sub>2</sub>:ZnO ratio of 3:1 has been used throughout.

The percentage composition of TiO<sub>2</sub> in TiO<sub>2</sub>-ZnO composite that results in highest synergistic effect varies from study to study. A 25% TiO<sub>2</sub> composition in ZnO-TiO<sub>2</sub> nanocomposite composition showed highest decolourisation in the photodegradation of brilliant golden yellow dye (Habib et al., 2013). A 50% TiO<sub>2</sub> composition in TiO<sub>2</sub>-ZnO resulted in highest photocatalytic reduction of hexavalent chromium (Naimi-Joubani et al., 2015), and photodegradation of diazinon (Jonidi-Jafari et al., 2015). The variation could be due to the properties of the substrate undergoing degradation as both TiO<sub>2</sub> and ZnO have different surface behaviour towards different substrates, or due to different sizes of the individual semiconductor photocatalysts in the composites, as is the case in the current study.

### 3.3.2.2 Effect of AC loading on TiO<sub>2</sub>-ZnO

Selection of an optimum support loading is important for obtaining the best conditions in which both adsorption and degradation are achieved simultaneously, resulting in enhanced activity of the supported catalyst. To compare the activities of the supported catalyst with different AC loadings, colour removal due to adsorption and photocatalytic degradation was studied separately.

Colour removal due to adsorption was carried out by monitoring adsorption in the dark for 60 minutes until equilibrium was achieved. Thereafter, the solution was irradiated for 120 minutes to monitor colour removal due to photodegradation. Figure 12 shows that the supported catalyst exhibited increased colour removal efficiency with increased AC loading up to 30% during photodegradation, which confirm the effect of AC support as a photocatalytic activity enhancer (Gao et al., 2011). The low colour removal due to adsorption alone at AC loading of 30% is catered for by the highest colour removal observed upon light irradiation as shown by the big difference between colour removal in the dark and in the light. Above 30% AC loading, the photocatalytic efficiency was decreased with increased support loading. The decreased efficiency was as a result of the decreased amount of photocatalyst present as more of the composite catalyst consisted of AC than TiO<sub>2</sub>-ZnO.

Conversely, colour removal due to adsorption alone in the dark was continuously increased with increased support loading. This is as a result of more adsorption sites present as a result of an increased amount of AC. The increased colour removal in the dark due to high adsorbent

loading, however, is not feasible as the organic pollutants are not fully degraded, but only transformed from one phase to another on the surface of the adsorbent. Support material loading of 30% was therefore adopted for use in the subsequent experiments and it is herein referred to as TiO<sub>2</sub>-ZnO-AC. Gao et al. (2011) reported a 20% AC loading in TiO<sub>2</sub>/AC composite for the photocatalytic degradation of acid red.

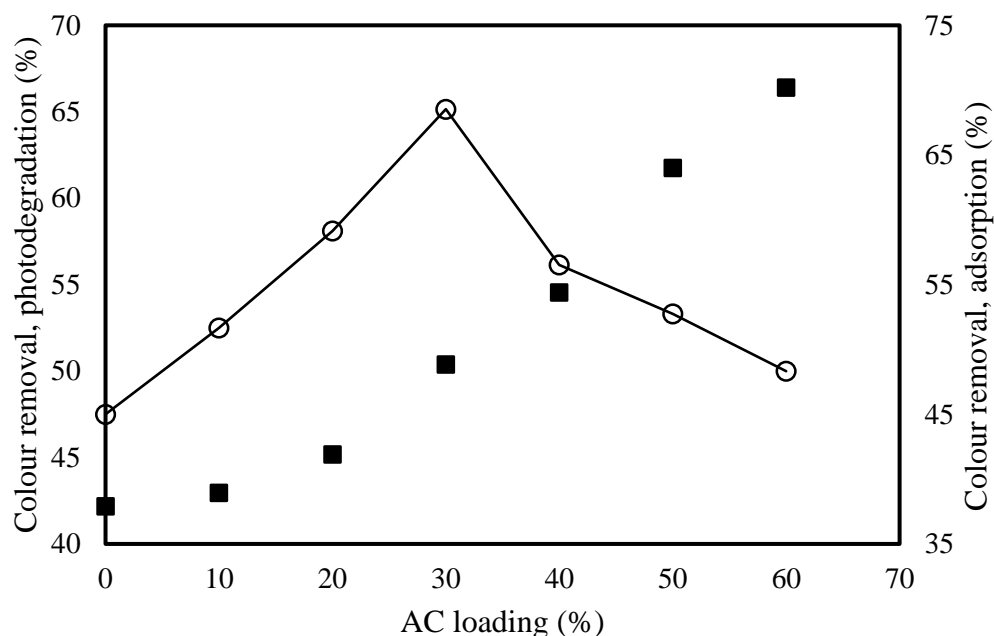


**Figure 12: Adsorption (■) and photodegradation (○) of 5000 mg/L MWW with different AC loading on TiO<sub>2</sub>-ZnO at 1 g/L composite loading, pH 5**

### 3.3.2.3 Activity of TiO<sub>2</sub>-ZnO/AC against TiO<sub>2</sub>-ZnO, TiO<sub>2</sub> and ZnO

The adsorption and photocatalytic activity of the supported catalyst was compared against that of the unsupported TiO<sub>2</sub>-ZnO, TiO<sub>2</sub> and ZnO (Figure 13). The AC support increased both adsorptive capacity and photocatalytic activity of the hybrid catalyst. Support increases the illuminated specific catalyst area, adsorption capacity and surface area of the photocatalyst. A common contact interface is created between AC and TiO<sub>2</sub>-ZnO, in which AC acts as an efficient adsorption trap for the organic pollutants, which are then transferred to the TiO<sub>2</sub>-ZnO surface, where they are immediately degraded (Slimen et al., 2011). During the first 10 minutes of irradiation, a high rate of colour removal is observed for all the catalysts. This is due to enhanced rate of degradation for the already pre-adsorbed organic compounds. Supporting ZnO-TiO<sub>2</sub> onto bamboo charcoal resulted in an improved removal of humic acid through adsorption and photodegradation (Wang et al., 2013). An improved decolourisation was also realized by supporting TiO<sub>2</sub> on zeolite for the adsorption and photodegradation of MWW (Apollo et al., 2014).

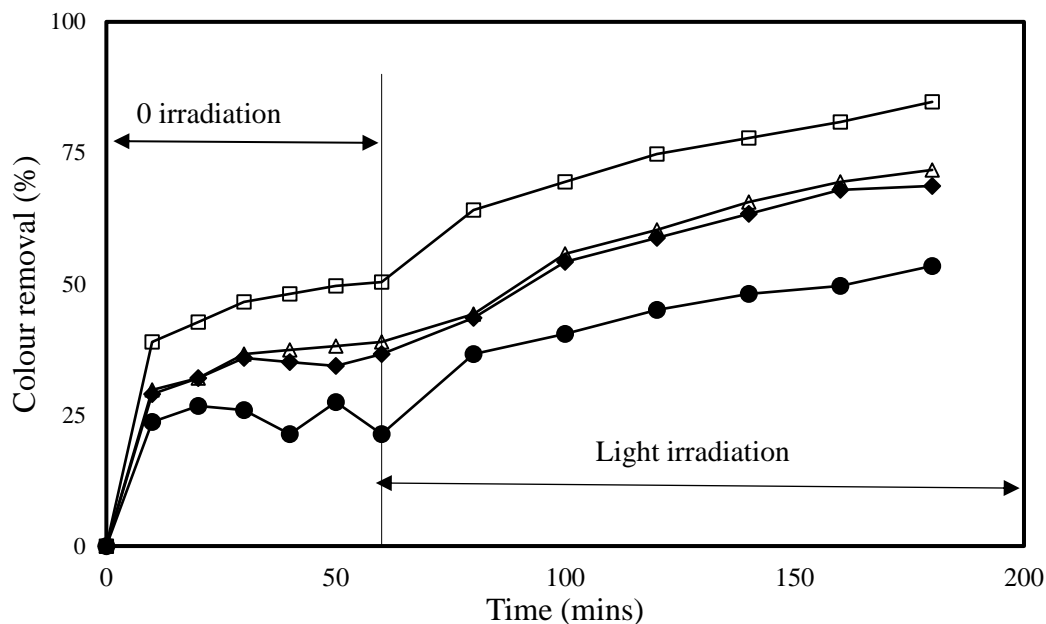


**Figure 13: Adsorption and photodegradation of 5000 mg/L MWW with TiO<sub>2</sub> (♦), ZnO (●), TiO<sub>2</sub>-ZnO/AC and TiO<sub>2</sub>-ZnO (Δ) at 1 g/L catalyst loading, pH 5**

#### 3.3.2.4 Effect of initial pH on the adsorption and photodegradation of MWW

The pH of a solution is one of the most important parameters involved in adsorption and degradation of aqueous solutions. The effect of initial pH on adsorption and photodegradation of MWW using TiO<sub>2</sub>-ZnO/AC was investigated by varying pH from 3 to 11. The initial concentration was read after each adjustment to take the resulting changes in MWW absorbance properties into consideration. The maximum adsorption was first carried out in the dark for one hour before light irradiation. The highest adsorption-photodegradation efficiency was achieved at pH 5 (Figure 14), resulting in the highest overall colour removal of 95%. It can also be seen that the acidic media pH 3 and pH 5, had higher overall colour removal of 89% and 95% respectively, than the basic media, which had the lowest colour removal of 86% and 73% for pH 9 and pH 11, respectively. The higher colour removal in acidic media than basic media could be as a result of the amphoteric nature of TiO<sub>2</sub> in aqueous solutions.

The point zero charge of TiO<sub>2</sub> and ZnO are 6.8 and 5.8–9, respectively. Below the pH value of 6, the surface of TiO<sub>2</sub>-ZnO is positively charged, resulting in high adsorption of the negatively charged melanoidin compounds (Prabha & Lathasree, 2014; Apollo et al., 2014). Hence both the adsorption rate and photodegradation rate increase with decreasing pH. A pH<sub>pzc</sub> of 7.2 was reported for TiO<sub>2</sub>-ZnO supported on bamboo charcoal (Wang et al., 2013). Adsorption alone in the dark was more enhanced in the acidic than the basic media. At pH above 7, the TiO<sub>2</sub>-ZnO surface is highly negatively charged due to the high TiO<sub>2</sub> (75%) composition, resulting in lower adsorption of the anionic substrate due to electrostatic repulsion (Sarkar et al., 2015).

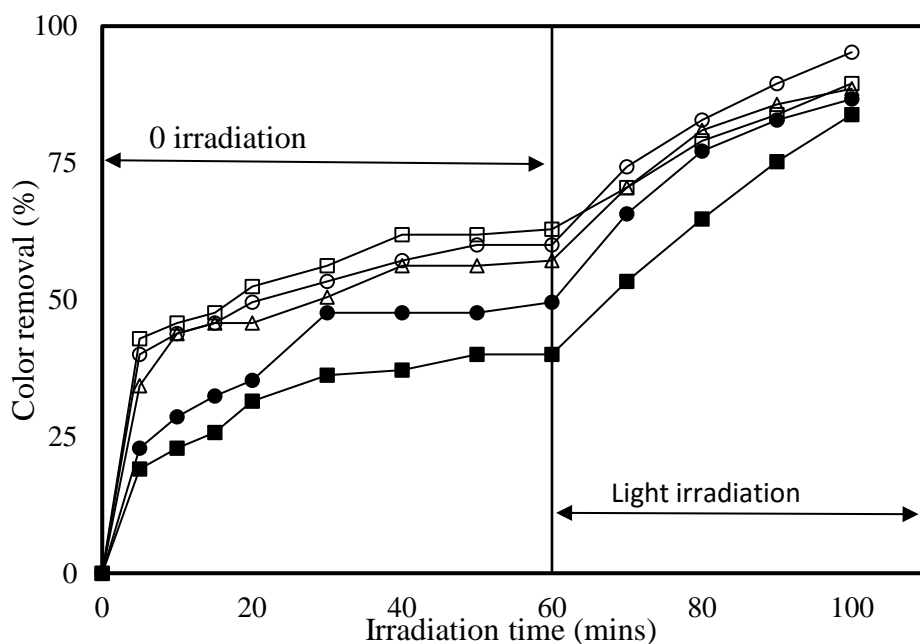


**Figure 14: Effect of initial pH, pH 12 (■), pH 9 (●), pH 3 (□), pH 5 (○) and pH 7 (△) on adsorption and photodegradation of 4000 mg/L MWW at 1 g/L catalyst loading**

The overall reaction is enhanced or hindered depending on whether attractive or repulsive forces prevail. However, if the pH is very low, the amphoteric metal oxide ZnO cannot exist; thus the photocatalytic activity of the composite will be greatly affected (Zhang et al., 2007). The reduced photocatalytic activity at high and low pH can also be attributed to the photocorrosion of ZnO (Jonidi-Jafari et al., 2015). Apollo et al. (2014) reported an optimum pH of 4 for the photodegradation of MWW using TiO<sub>2</sub> supported on zeolite, while pH 3 was reported to be the optimum for the degradation of anionic methyl orange using TiO<sub>2</sub> modified ZnO nanorods (Xiao et al., 2014). It should be noted that adsorption equilibrium was achieved after approximately 20 minutes. The solution should therefore be irradiated after 20 minutes of adsorption to save time. An experiment carried out where adsorption was varied for 20 and 60 minutes before light irradiation for 40 minutes at pH 7 resulted in almost similar overall colour removal of 84 and 86%, respectively.

### 3.3.2.5 Effect of initial concentration

The change in initial concentration corresponds to the change in the number of organic molecules present per unit volume. Colour reduction of MWW was investigated by varying the initial concentration. Colour removal was decreased from 100% to 82% after 40 minutes of irradiation (Figure 15) by increasing the initial concentration from 3000 ppm to 6000 ppm. The trend observed in colour reduction with increased initial concentration leading to a minimal drop of 18% reduction is an indication of the effectiveness of UV irradiation for colour removal under a photocatalysed process, even at high concentrations. As the initial concentration increases, the number of organic compounds, including the colour-causing melanoidins, increases. This leads to enhanced intramolecular competition by the organic compounds to reach the surface of TiO<sub>2</sub>-ZnO-AC, which results in increased molecular movement to the active site in each unit time for a fixed catalyst concentration. Increased concentration results in saturation of active sites by the target organic molecules thereby causing an inhibitive effect

on further photodegradation (Li et al., 2015). A similar observation was made by Jonidi-Jafari et al. (2015) and Prabha and Lathasree (2014). The reduced colour removal is also attributable to the reduction in light penetration to the surface of TiO<sub>2</sub>-ZnO-AC (Habib et al., 2013). The colour of MWW intensifies as the initial concentration increases.

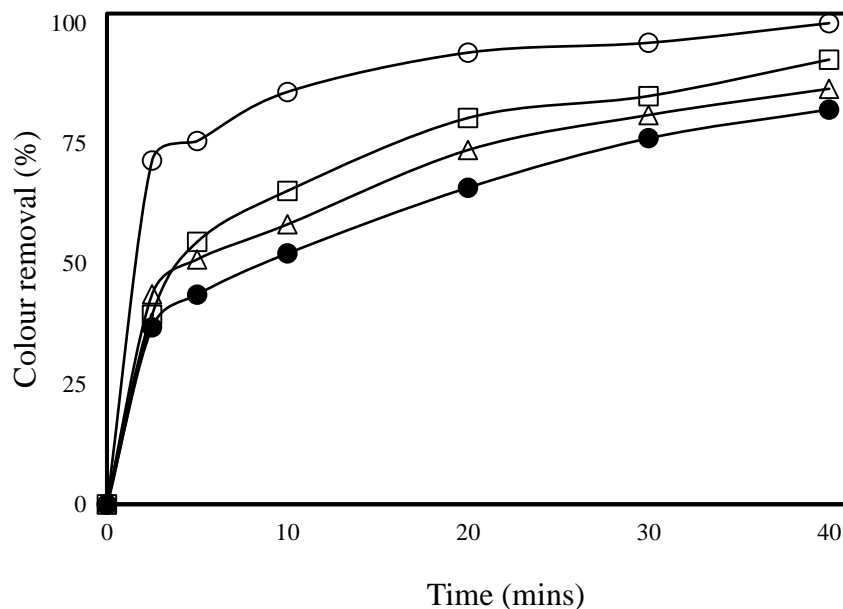


**Figure 15: Effect of initial concentration on adsorption and photodegradation of 3000 ppm (○), 4000 ppm (□), 5000 ppm (△) and 6000 ppm (●)MWW at pH 5 with 1 g/L catalyst loading**

### 3.3.2.6 Effect of catalyst loading

Optimum catalyst loading of 1 g/L, Figure 16, was determined from a series of experiments carried out at varied catalyst loading from 0.25 g/L to 3 g/L. Colour removal was increased from 74% to 95% with increased catalyst loading from 0.25 g/L to 1 g/L. Colour removal was slightly decreased above 1 g/L catalyst loading. The amount of photocatalyst present strongly influenced the rate of degradation (Prabha & Lathasree, 2014). At lower catalyst loadings of 0.25 g/L and 0.5 g/L, the rate of MWW photodegradation is photonic adsorption controlled due to the limited surface area of catalyst available for reaction. A significant increase in rate of reaction represented by highest colour removal of 95% was observed with increased catalyst loading to 1 g/L. The catalytic performance was enhanced with increased catalyst loading due to the increase in number of sites available for adsorption and catalytic processes. Moreover, at or below 1 g/L catalyst loading there was minimal hindrance of UV light penetration allowing for maximum irradiation of the surface of catalyst (Apollo et al., 2014).

Increased loading above the optimum value signifying a higher amount of catalyst in the MWW solution resulted in a possible catalyst aggregation as well as reduction in irradiation field due to the scattering of light, hence the decreasing colour removal with loading above 1 g/L (Sakthivel et al., 2003). The reaction rate may also decrease due to loss in surface area availability at high solid catalyst concentration. At high solid concentration, there is catalyst agglomeration resulting from particle-to-particle interactions making the solution very turbid, lowering the transmittance of the MWW solution thus, hindering light penetration. Treatment processes relying on light irradiation for dissociating O<sub>3</sub> or H<sub>2</sub>O display decreased efficiency

as turbidity increases. Agglomeration also limits catalyst surface available for photon absorption.

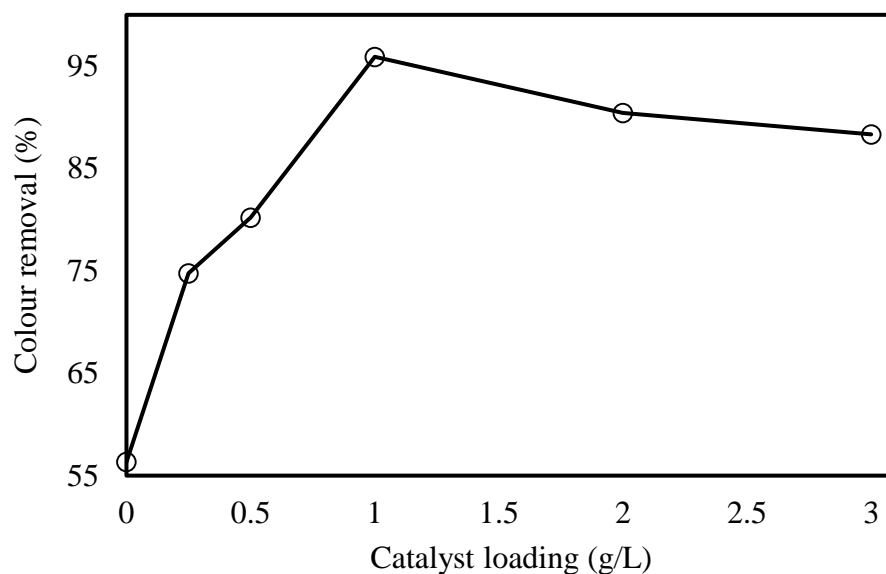


**Figure 16: Effect of catalyst loading on adsorption and photodegradation of 4000 ppm MWW at pH 5**

### 3.3.3 Photodegradation process

The photodegradation process was evaluated by monitoring formation of nitrates ( $\text{NO}_3^-$ ) and reduction of colour and TOC concurrently during the degradation of 3000 mg/L MWW with a catalyst loading of 1 g/L at pH 5. After 120 minutes of light irradiation, Figure 17, colour removal of 100% was achieved as compared with a partly 14% TOC removal. Formation of  $\text{NO}_3^-$  was also observed with increased irradiation time. The superior colour removal is an indicator of the effectiveness of photocatalysis in colour remediation for MWW. However, the low TOC removal confirms that photocatalysis alone cannot remove the high organic loading of MWW effectively. Apollo et al. (2013) found that photocatalysis should be employed as a post-treatment method for anaerobically treated MWW. In such a system, both TOC and colour are effectively removed by anaerobic treatment and photodegradation, respectively.

Non-biodegradable melanoidin compounds (responsible for colour) constitute approximately 2% of MWW with a total nitrogen content of 1 g/L to 2 g/L (Tsiptsias et al., 2015). Coloured organic pollutants are constituted by chromophores such as  $-\text{C}=\text{C}-$ ,  $-\text{C}=\text{N}-$ ,  $-\text{C}=\text{O}-$ ,  $-\text{N}=\text{N}-$  and  $-\text{NO}_2$  having delocalised electron systems with conjugated double bonds that alter the overall energy of the electron system thus intensifying the colour (Panthi et al., 2015). During photodegradation of chromophoric substances, the sites near the bonds containing C bonded to N is generally the attacked area. The formation of  $\text{NO}_3^-$  is thus attributable to the breaking down of the nitrogen-containing melanoidin compounds (Chandra et al., 2008). Moreover, since melanoidins are highly negatively charged even in neutral conditions (Wang et al., 2011), photodegradation by the positively charged photocatalyst is thus expected to prefer the degradation of melanoidins to other organic compounds present.

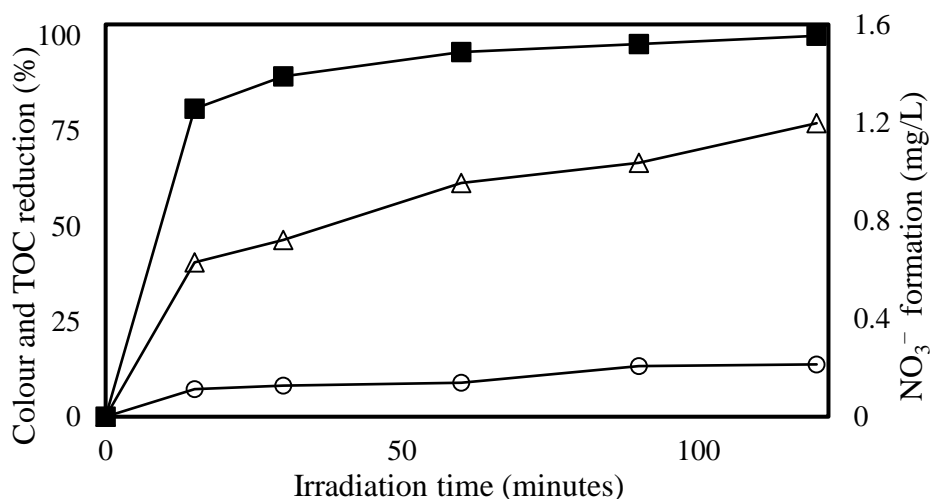


**Figure 17:** NO<sub>3</sub><sup>-</sup> (Δ) formation, and TOC (○) and colour (■) reduction in the photodegradation of 3000 mg/L MWW using TiO<sub>2</sub>-ZnO-AC at 1 g/L catalyst loading

### 3.3.4 Comparison of photolysis vs photocatalysis

Direct UV photolysis and photocatalytic processes involving both commercial TiO<sub>2</sub> (Aeroxide P25) and the synthesised TiO<sub>2</sub>-ZnO-AC, with identical degradation time, are shown in Figure 18. It was observed that photocatalysis, with 97% colour removal, is a more powerful way to degrade melanoidin than direct photolysis, which achieved a moderate removal of 57%. The moderate removal by direct photolysis is an indication of partial instability of melanoidin to UV-C illumination. This instability further explains the effectiveness of a photocatalysed UV process for colour removal as compared with the removal of the more UV-C stable organic compounds responsible for TOC. In the photocatalytic process, the synthesised TiO<sub>2</sub>-ZnO-AC showed a better colour removal (97%) than the widely used commercial TiO<sub>2</sub>, with 87% removal. The high activity of the composite catalyst in addition to its high settling ability makes it a better choice than commercial TiO<sub>2</sub>.

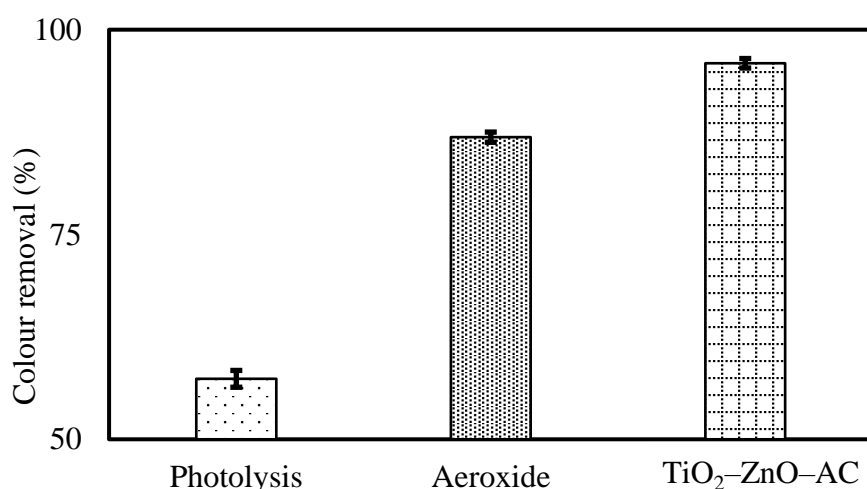


**Figure 18:** Comparison of direct photolysis, and TiO<sub>2</sub> (Aeroxide P25), and TiO<sub>2</sub>-ZnO-AC photocatalysed processes in the adsorption and photodegradation of 3000 mg/L MWW after 60 minutes of irradiation at pH 5 with 1 g/L catalyst loading

### 3.3.5 Comparison of colour and TOC removal against energy requirement

The photo-decolourisation process was evaluated by monitoring reduction in colour and TOC concurrently. After 60 minutes of light irradiation, Figure 19, colour removal of 96% was achieved as compared with a paltry 9% of TOC removal. The superior colour removal is an indication of the effectiveness of photocatalysis in colour remediation. However, the low TOC removal indicates that photocatalysis alone cannot remove the high organic loading of industrial wastewater such as vinasse effectively. In the photocatalytic degradation of chromophoric substances such as melanoidins, the sites near the azo bonds, i.e. bonds containing C bonded to N, are generally the attacked areas (Konstantinou & Albanis, 2004). Since melanoidin compounds are mostly responsible for the vinasse colour due to their colour-causing azo bonds, their degradation can be best explained by the high colour removal of 96%. The high rate of colour removal further demonstrates relative instability of melanoidin to UV irradiation as compared with the more UV stable organic compounds responsible for TOC. The slow mineralisation, as depicted by low reduction in TOC, could be due to the formation of intermediate products such as carboxyl acids, which are more difficult to oxidise than their parent compounds. Moreover, the intermediate compounds have a much slower rate of reaction leading to complete oxidation (Trabelsi et al., 2013). For successful removal of TOC using photocatalysis alone, more aggressive conditions are required than those employed in breaking down melanoidin chromophores.

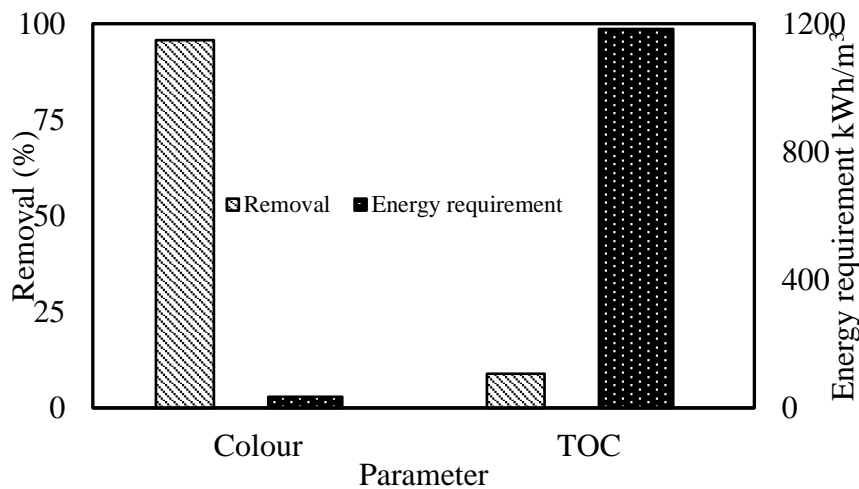


**Figure 19: Comparison of percentage removal against energy requirement for colour and TOC after 60 minutes of photo-decolourisation of 3000 ppm MWW using TiO<sub>2</sub>-ZnO-AC at pH 7 with 1 g/L catalyst loading**

Moreover, from an economic point of view, the electrical energy efficiency of the UV photocatalysed process was determined from electrical energy per order ( $E_0$ ) given by:

$$E_0 = \frac{P \times t \times 1000}{V \times 60 \times \log(C_i/C_f)} \quad (17)$$

where  $P$  is the lamp power (kW),  $t$  is the duration of irradiation (minutes),  $V$  is the amount of wastewater degraded (L), and  $C_f$  and  $C_i$  are the final and initial concentrations, respectively (Jonidi-Jafari et al., 2015).

It was observed that colour removal of 96% only required 35 kWh/m<sup>3</sup> of energy as compared with the 1183 kWh/m<sup>3</sup> of energy required for the paltry 9% TOC removal, Figure 12, further demonstrating the high energy requirement for UV photo-reduction of TOC.

For effective treatment of vinasse, photocatalysis should therefore be employed alongside other treatment methods such as biological degradation. In a strategy for the selection of a treatment option for industrial wastewater, Oller et al. (2011) suggested that highly biodegradable wastewater such as vinasse should first undergo biodegradation before being subjected to AOPs to remove recalcitrant compounds to achieve standard COD discharge guidelines. Similarly, in an earlier research work carried out in our research laboratory involving combined anaerobic and photocatalytic treatment of vinasse, Apollo et al. (2013) found that photocatalysis should be employed as a post-treatment method for anaerobically treated vinasse. In such a system, both TOC and colour are effectively removed by anaerobic treatment and photo-decolourisation processes, respectively.

### 3.3.6 Kinetics analysis

The kinetics of heterogeneous photocatalysts reaction in aqueous solutions is widely described using the Langmuir–Hinshelwood model given by:

$$r = \frac{-dc}{dt} = k_r \theta = \frac{k_r K_{ad} C}{1 + K_{ad} C} \quad (18)$$

where  $r$  is the reaction rate and is proportional to surface covered by reactant  $\theta$ ,  $k_r$  is the rate constant (mM/h) and  $K_{ad}$  is the adsorption constant (mM<sup>-1</sup>). When the pollutant concentration is low,  $K_{ad} C$  becomes negligible and the degradation process follows first-order reaction:

$$r = \frac{-dC}{dt} = k_r K_{ad} C = k_{app} C \quad (19)$$

where  $k_{app}$  is the first-order rate constant (h<sup>-1</sup>). Eq. 19 can be integrated to:

$$\ln \frac{C_o}{C} = k_{app} t \quad (20)$$

The introduction of AC support and the adsorption process thereof can be best monitored by the second-order reaction model given by (Jonidi-Jafari et al., 2015):

$$\frac{1}{C} - \frac{1}{C_o} = k_2 t \quad (21)$$

To obtain the reaction kinetic data from the initial rate of reaction summarised in Table 7, from the effect of support loading on the first and second-order reaction models,  $\ln \frac{C_o}{C}$  vs  $t$  and  $\frac{1}{C_t} - \frac{1}{C_o}$  vs  $t$  were plotted, respectively, where  $k_{app}$  is the first-order reaction rate constant (min<sup>-1</sup>),  $k_2$  is second-order reaction rate constant (min<sup>-1</sup>),  $C_o$  is the initial concentration,  $t$  is time and  $C$  is the concentration at time  $t$ .

For statistical modelling, relative deviation modulus (P) given by (Eq. 22) was used as a measure of model adequacy, with P values less than 10% indicating a good fit for practical purposes (Özdemir & Devres, 1999; Park et al., 2002).

$$P = \frac{100}{n} \sum \frac{C_i - C_{pri}}{C_i} \quad (22)$$

where  $C_i$  is the experimental concentration at any time,  $C_{pri}$  is the corresponding predicted concentration per the model and  $n$  is the number of observations. Photodegradation of MWW with TiO<sub>2</sub>-ZnO (0% AC) fitted well with the first-order model, Table 7, with the P values obtained being less than 5%. Support loading of 30% had highest  $k_{app}$  of 0.0229 min<sup>-1</sup> indicating highest reaction rate, which agrees with the observed highest colour removal during photodegradation at a similar loading (see Figure 12).

**Table 7: Kinetics data for photodegradation of 5000 mg/L MWW using different AC (% composition) supported TiO<sub>2</sub>-ZnO at 1 g/L composite loading and pH 5**

AC Composition (%)	First Order			Second Order		
	$k_{app}$ (min <sup>-1</sup> )	R <sup>2</sup>	P (%)	$k_2$ (min <sup>-1</sup> )	R <sup>2</sup>	P (%)
0	0.0139	0.9765	3.2	0.0898	0.9549	10
10	0.0126	0.9413	7	0.0921	0.9859	3
20	0.0150	0.9372	8	0.0121	0.9727	4
30	0.0229	0.9227	5.8	0.1811	0.9771	5.2
40	0.0153	0.8175	2.8	0.1686	0.9892	3.5
50	0.0150	0.4623	4.8	0.2371	0.9973	1.2
60	0.0160	0.4975	5.8	0.2544	0.9937	0.6

Upon the introduction of the support, an increase in AC composition resulted in a decreasing R<sup>2</sup> value, indicating that reaction for the supported catalyst does not fit the first-order model. On the contrary, supported catalyst fitted well with the second-order model as observed with the increasing R<sup>2</sup> values. At high AC loading, adsorption predominates over photodegradation, and since it has been shown that AC adsorption fits the second-order model (Shirzad-Siboni et al., 2013), the trend shown for R<sup>2</sup> is therefore expected. At higher AC loading, the amount of TiO<sub>2</sub>-ZnO present was greatly reduced hence adsorption was favoured as compared with photodegradation.

### 3.3.7 Adsorption isotherms and thermodynamics

Adsorption studies for TiO<sub>2</sub>-ZnO-AC and AC were carried out with different adsorbent loading ranging from 0.5 g/L to 3.0 g/L, in the adsorption of 5000 mg/L MWW at a constant pH of 5. Adsorption was done in the dark until an equilibrium was achieved. Sampling was carried out at predetermined time intervals and the samples analysed to monitor decolourisation. The data obtained were fitted to Langmuir and Freundlich isotherms, the two most commonly used for adsorption with AC, in order to find the isotherm that best fits the process (Shirzad-Siboni et al., 2013).

Langmuir isotherm:

$$q_e = \frac{q_m K_L C_e}{1 + K_L C_e} \quad (23)$$

where  $q_e$  is the adsorbate uptake at equilibrium,  $q_m$  is the Langmuir maximum sorption capacity,  $K_L$  is the Langmuir adsorption constant and  $C_e$  is the concentration at equilibrium. Eq. 23 can be expressed in a linear form as:

$$\frac{C_e}{q_e} = \frac{1}{K_A q_m} + \frac{1}{q_m} C_e \quad (24)$$

A plot of  $C_e/q_e$  vs.  $C_e$  should produce a straight line with slope  $1/q_m$  and intercept  $1/K_A q_m$ . Also, Eq. 24 can be rearranged as:

$$\frac{1}{q_e} = \frac{1}{q_m} + \frac{1}{K_A q_m C_e} \quad (25)$$

From which a plot of  $1/q_e$  vs.  $1/C_e$  gives  $1/K_A q_m$  as the slope and  $1/q_m$  as the intercept.

Freundlich isotherm:

$$q_e = K_f C_e^{\frac{1}{n}} \quad (26)$$

where  $K_f$  and  $n$  are the Freundlich isotherm constants representing adsorption capacity and intensity, respectively. Eq. 27 shows the linear form of equation Eq. 26.

$$\ln q_e = \ln K_f + \frac{1}{n} \ln C_e \quad (27)$$

Plotting  $\ln q_e$  against  $\ln C_e$  gives a straight line with  $1/n$  as the slope and  $\ln K_f$  as the intercept. From the graphs obtained in Figure 20, adsorption by AC and TiO<sub>2</sub>-ZnO-AC fits well with the Freundlich isotherm, which is used for non-ideal adsorption involving heterogeneous surface systems (Ojijo et al., 2010), and assumes that adsorption occurs at sites of different energy in contrast to the Langmuir isotherm that describes adsorption on homogeneous surfaces based on the assumptions of uniform monolayer adsorption with no interactions between adsorbates (Sarkar et al., 2015).

On comparing AC and TiO<sub>2</sub>-ZnO-AC Freundlich isotherm models, a better fit was observed with the latter than the former. This can be attributed to the heterogeneous surface of TiO<sub>2</sub>-ZnO-AC consisting of spherical and tetrahedral TiO<sub>2</sub>, hexagonal ZnO and AC with possibly different energies.

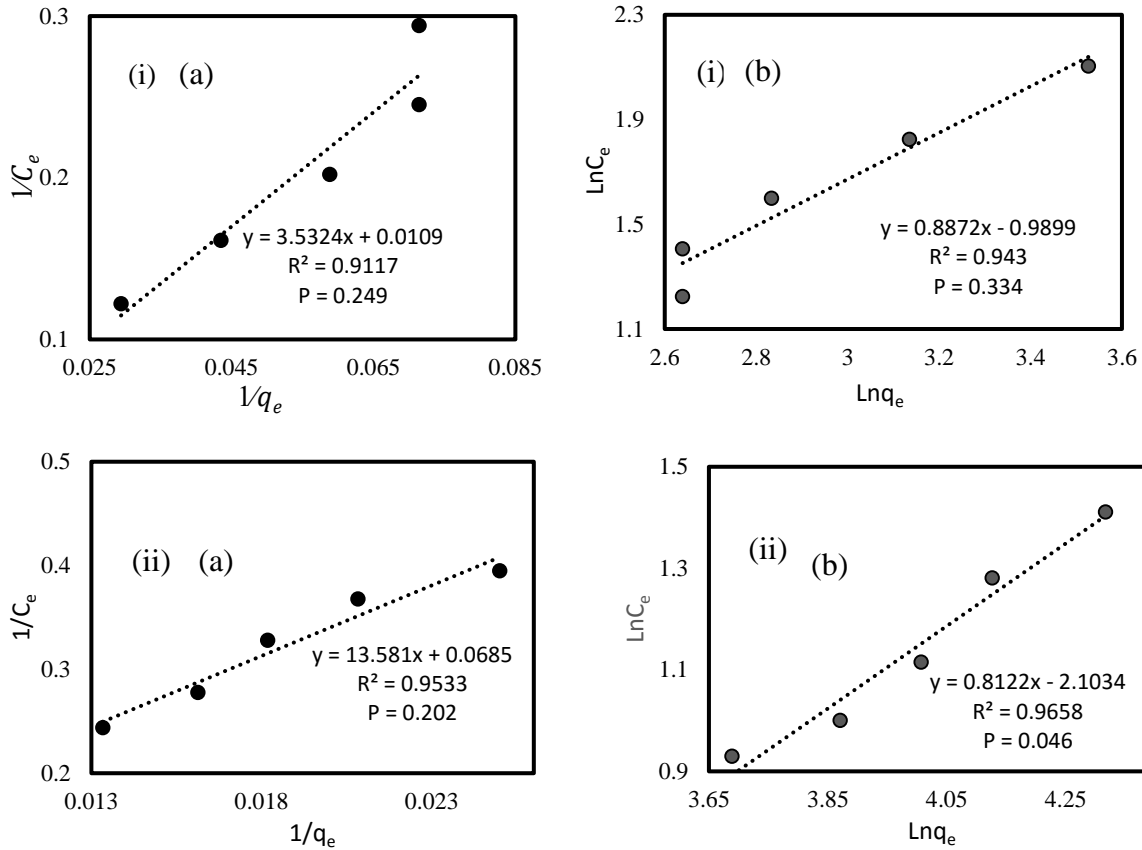


**Figure 20: Langmuir (i) and Freundlich (ii) adsorption isotherms for 5000 mg/L MWW sorption onto AC (a) and TiO<sub>2</sub>-ZnO-AC (b) at 25°C**

The thermodynamics parameters for the adsorption of MWW by TiO<sub>2</sub>-ZnO-AC were determined using the equilibrium constant,  $K$  ( $q_e/C_e$ ) that is temperature dependent. Adsorption experiments were carried out at a range of reaction temperatures (298K, 308K, 318K, 328K, 338K and 348K) with 1 g/L catalyst loading and initial concentration of 5000 mg/L. Change in free energy ( $\Delta G^\circ$ ), entropy ( $\Delta S^\circ$ ) and enthalpy ( $\Delta H^\circ$ ) can be calculated by (Tu et al., 2012):

$$\Delta G^\circ = -RT \ln K \quad (28)$$

where  $R$  is the universal gas constant ( $8.314 \text{ Jmol}^{-1}\cdot\text{K}^{-1}$ ) and  $T$  is the absolute temperature (K). The average standard enthalpy change ( $\Delta H^\circ$ ) and entropy change ( $\Delta S^\circ$ ) can be determined by:

$$\ln K = \frac{\Delta S^\circ}{R} - \frac{\Delta H^\circ}{RT} \quad (29)$$

A plot of  $\ln K$  vs  $1/T$  gives a straight line, Figure 21, with the slope of  $\Delta H^\circ/R$  and intercept of  $\Delta S^\circ/R$ . The  $\Delta H^\circ$  and  $\Delta S^\circ$  parameters had values of 7.56 kJ/mol and 27.97 kJ/mol, respectively. The positive value of  $\Delta H^\circ$  confirmed the endothermic nature of the process of adsorption by TiO<sub>2</sub>-ZnO-AC, whereas the positive  $\Delta S^\circ$ , which also confirms the endothermic nature of the process, can be associated with increased randomness at the solid-solute interface (Tu et al., 2012). Similar attribution of positive value of  $\Delta S^\circ$  to increased randomness at the solid-solute interface was obtained in the adsorption of melanoidin containing wastewater using coal fly ash (Ojijo et al., 2010). Since the adsorption process by TiO<sub>2</sub>-ZnO-AC was found to be

endothermic and it also increased with an increase in temperature; therefore, chemisorption was the significant and rate controlling process (Ofomaja et al., 2009).

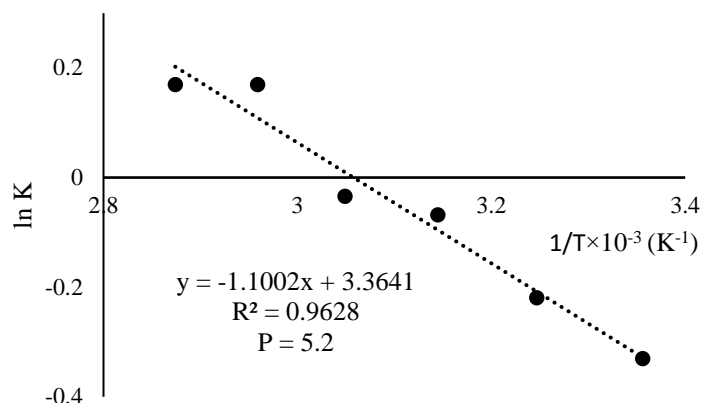


Figure 21: Plot of  $\ln K$  vs  $1/T$  for 5000 mg/L MWW sorption onto  $\text{TiO}_2\text{-ZnO-AC}$

### 3.4 Conclusion

A composite photocatalyst was employed for treating MWW. The adsorption and photodegradation activities of nano-sized  $\text{TiO}_2$ ,  $\text{TiO}_2\text{-ZnO}$  and  $\text{ZnO}$  were compared against that of  $\text{TiO}_2\text{-ZnO}$  supported onto AC ( $\text{TiO}_2\text{-ZnO/AC}$ ) for the degradation of MWW. It was observed that  $\text{TiO}_2\text{-ZnO/AC}$  exhibited the highest photocatalytic activity, followed by  $\text{TiO}_2\text{-ZnO}$ , then  $\text{TiO}_2$  and lastly  $\text{ZnO}$  as indicated by overall colour removal of 85%, 71%, 67% and 53%, respectively. The adsorption capacity of  $\text{TiO}_2\text{-ZnO-AC}$  was also enhanced by the AC support material as it resulted in an increased colour removal from 38% to 50% due to adsorption alone in the dark. The experimental results demonstrated the effectiveness of using hybrid catalysts for remediation of MWW. Support material is important as it enhances both the adsorption capacity and degradation activity of the hybrid catalyst. Support materials also reduce the cost associated with post-treatment activities as the supported nanocatalyst can easily settle leading to ease of catalyst separation from the treated solution. The remediation of MWW using UV photodegradation was very effective in colour removal but was ineffective in TOC removal. The energy required by the photodegradation process for 95% colour removal was  $35 \text{ kWh/m}^3$  while it required  $1183 \text{ kWh/m}^3$  for a paltry 9% TOC removal. From the energy requirement point of view, it was noted that photodegradation is very costly for TOC removal but more economically viable for colour removal. Therefore, UV photodegradation of MWW should be employed alongside other treatment methods such as biological degradation.

### 3.5 References

- Abdullah, A.H., Mun, L.K., Zainal, Z. & Hussein, M.Z. (2013). Photodegradation of chlorophenoxyacetic acids by  $\text{ZnO/r-Fe}_2\text{O}_3$  nanocatalysts: A comparative study. *International Journal of Chemistry*, 5, 56–65.
- Ahmad, M., Ahmed, E. & Hong, Z. (2014). Photocatalytic, sonocatalytic and sonophotocatalytic degradation of Rhodamine B using  $\text{ZnO/CNTs}$  composites photocatalysts. *Ultrasonics*, 21, 761–773.

- Apollo, S., Onyango, M.S. & Ochieng, A. (2013). An integrated anaerobic digestion and UV photocatalytic treatment of distillery wastewater. *Journal of Hazardous Materials*, 261, 435–42.
- Apollo, S., Onyango, M.S. & Ochieng, A. (2014). UV/H<sub>2</sub>O<sub>2</sub>/TiO<sub>2</sub>/zeolite hybrid system for treatment of molasses wastewater. *Iranian Journal of Chemistry and Chemical Engineering*, 33, 107–117.
- Apollo, S., Onyango, M.S. & Ochieng, A. (2016). Modelling energy efficiency of an integrated anaerobic digestion and photodegradation of distillery effluent using response surface methodology. *Environmental Technology*, 33(30), 1–12.
- Avcı, A., Eskizeybek, V., Gülce, H., Haspulat, B. & Şahin, Ö.S. (2014). ZnO–TiO<sub>2</sub> nanocomposites formed under submerged DC arc discharge: Preparation, characterization and photocatalytic properties. *Applied Physics A*, 116, 1119–1125.
- Bahadur, N.M., Furusawa, T., Sato, M., Kurayama, F. & Suzuki, N. (2010). Rapid synthesis, characterization and optical properties of TiO<sub>2</sub> coated ZnO nanocomposite particles by a novel microwave irradiation method. *Materials Research Bulletin*, 45, 1383–1388.
- Behnajady, M.A., Eskandarloo, H., Modirshahla, N. & Shokri, M. (2011). Investigation of the effect of sol–gel synthesis variables on structural and photocatalytic properties of TiO<sub>2</sub> nanoparticles. *Desalination*, 278, 10–17.
- Chandra, R., Bharagava, R.N. & Rai, V. (2008). Melanoidins as major colourant in sugarcane molasses based distillery effluent and its degradation. *Bioresource Technology*, 99, 4648–4660.
- Daneshvar, N., Aber, S., Seyeddoraji, M., Khataee, A. & Rasoulifard, M. (2007). Photocatalytic degradation of the insecticide diazinon in the presence of prepared nanocrystalline ZnO powders under irradiation of UV-C light. *Separation and Purification Technology*, 58, 91–98.
- Duan, L., Wang, H., Sun, Y. & Xie, X. (2015). Biodegradation of phenol from wastewater by microorganism immobilized in bentonite and carboxymethyl cellulose gel. *Chemical Engineering Communication*, 6445, 150804053542007.
- Gao, B., Yap, P.S., Lim, T.M. & Lim, T.-T. (2011). Adsorption-photocatalytic degradation of Acid Red 88 by supported TiO<sub>2</sub>: Effect of activated carbon support and aqueous anions. *Chemical Engineering Journal*, 171, 1098–1107.
- Habib, A., Shahadat, T., Bahadur, N.M., Ismail, I.M.I. & Mahmood, A.J. (2013). Synthesis and characterization of ZnO-TiO<sub>2</sub> nanocomposites and their application as photocatalysts. *International Nano Letters*, 3, 1–8.
- Hamal, D.B. & Klabunde, K.J. (2007). Synthesis, characterization, and visible light activity of new nanoparticle photocatalysts based on silver, carbon, and sulfur-doped TiO<sub>2</sub>. *Journal of Colloid and Interface Science*, 311, 514–522.
- Haque, F., Vaisman, E., Langford, C.H. & Kantzas, A. (2005). Preparation and performance of integrated photocatalyst adsorbent (IPCA) employed to degrade model organic compounds in synthetic wastewater. *Journal of Photochemistry and Photobiology A: Chemistry*, 169, 21–27.

- Isah U., Abdulraheem, G., Bala, S., Muhammad, S. & Abdullahi, M. (2015). Kinetics, equilibrium and thermodynamics studies of C.I. Reactive Blue 19 dye adsorption on coconut shell based activated carbon. *International Biodeterioration and Biodegradation*, 102, 265–273.
- Jonidi-Jafari, A., Shirzad-Siboni, M., Yang, J.-K., Naimi-Joubani, M. & Farrokhi, M. (2015). Photocatalytic degradation of diazinon with illuminated ZnO–TiO<sub>2</sub> composite. *Journal of the Taiwan Institute of Chemical Engineers*, 50, 100–107.
- Konstantinou, I.K. & Albanis, T. A (2004). TiO<sub>2</sub>-assisted photocatalytic degradation of azo dyes in aqueous solution: Kinetic and mechanistic investigations. *Applied Catalysis B: Environmental*, 49, 1–14.
- Laginhas, C., Nabais, J.M.V. & Titirici, M.M. (2016). Activated carbons with high nitrogen content by a combination of hydrothermal carbonization with activation. *Microporous Mesoporous Materials*, 226, 125–132.
- Li, Y. et al. (2012). Photodecolorization of Rhodamine B on tungsten-doped TiO<sub>2</sub>/activated carbon under visible-light irradiation. *Journal of Hazardous Materials*, 227-228, 25–33.
- Liao, D.L., Badour, C.A. & Liao, B.Q. (2008). Preparation of nanosized TiO<sub>2</sub>/ZnO composite catalyst and its photocatalytic activity for degradation of methyl orange. *Journal of Photochemistry and Photobiology A: Chemistry*, 194, 11–19.
- Naimi-Joubani, M., Shirzad-Siboni, M., Yang, J.-K., Gholami, M. & Farzadkia, M. (2015). Photocatalytic reduction of hexavalent chromium with illuminated ZnO/TiO<sub>2</sub> composite. *Journal of Industrial and Engineering Chemistry*, 22, 317–323.
- Navgire, M., Yelwande, A., Tayde, D., Arbad, B. & Lande, M. (2012). Photodegradation of molasses by a MoO<sub>3</sub>-TiO<sub>2</sub> nanocrystalline composite material. *Chinese Journal of Catalysis*, 33, 261–266.
- Ngamsopasiriskun, C., Charnsethikul, S., Thachepan, S. & Songsasen, A. (2010). Removal of phenol in aqueous solution by nanocrystalline TiO<sub>2</sub>/activated carbon composite catalyst. *Journal of Natural Sciences*, 1182, 1176–1182.
- Ofomaja, A.E., Naidoo, E.B. & Modise, S.J. (2009). Removal of copper(II) from aqueous solution by pine and base modified pine cone powder as biosorbent. *Journal of Hazardous Materials*, 168, 909–917.
- Ohtani, B. (2010). Photocatalysis A to Z: What we know and what we do not know in a scientific sense. *Journal of Photochemistry and Photobiology C: Photochemistry Reviews*, 11, 157–178.
- Ojijo, V.O., Onyango, M.S. & Ochieng, A. (2010). Decolourization of melanoidin containing wastewater using South African coal fly ash. *International Journal of Chemical and Molecular Engineering*, 4, 1–7.
- Oller, I., Malato, S. & Sánchez-Pérez, J.A. (2011). Combination of advanced oxidation processes and biological treatments for wastewater decontamination: A review. *Science of the Total Environment*, 409, 4141–4166.
- Özdemir, M. & Devres, Y.O. (1999). The thin layer drying characteristics of hazelnuts during roasting. *Journal of Food Engineering*, 42, 225–233.

- Pan, H., Wang, X.D., Xiao, S.S., Yu, L.G. & Zhang, Z.J. (2013). Preparation and characterization of TiO<sub>2</sub> nanoparticles surface-modified by octadecyltrimethoxysilane. *Indian Journal of Engineering and Materials Sciences*, 20, 561–567.
- Panthi, G., Park, M., Kim, H.-Y., Lee, S.-Y. & Park, S.-J. (2015). Electrospun ZnO hybrid nanofibers for photodegradation of wastewater containing organic dyes: A review. *Journal of Industrial and Engineering Chemistry*, 21, 26–35.
- Park, K.J., Vohnikova, Z. & Brod, F.P.R. (2002). Evaluation of drying parameters and desorption isotherms of garden mint leaves (*Mentha crispa* L.). *Journal of Food Engineering*, 51, 193–199.
- Prabha, I. & Lathasree, S. (2014). Photodegradation of phenol by zinc oxide, titania and zinc oxide–titania composites: Nanoparticle synthesis, characterization and comparative photocatalytic efficiencies. *Materials Science in Semiconductor Processing*, 26, 603–613.
- Sarkar, S., Bhattacharjee, C. & Curcio, S. (2015). Studies on adsorption, reaction mechanisms and kinetics for photocatalytic degradation of CHD, a pharmaceutical waste. *Ecotoxicology and Environmental Safety*, 121, 154–163.
- Shirzad-Siboni, M., Jafari, S.J., Giahhi, O., Kim, I., Lee, S.M. & Yang, J.K. (2013). Removal of acid blue 113 and reactive black 5 dye from aqueous solutions by activated red mud. *Journal of Industrial and Engineering Chemistry*, 20, 1432–1437.
- Slimen, H., Houas, A. & Nogier, J.P. (2011). Elaboration of stable anatase TiO<sub>2</sub> through activated carbon addition with high photocatalytic activity under visible light. *Journal of Photochemistry and Photobiology A: Chemistry*, 221, 13–21.
- Song, Z., Sun, X. & Qiu, J. (2014). Preparation, characterization and photocatalytic activity of B, La co-doped mesoporous TiO<sub>2</sub> for methylene blue degradation. *Indian Journal of Chemistry*, 53, 1332–1337.
- Trabelsi, H., Khadhraoui, M., Hentati, O. & Ksibi, M. (2013). Titanium dioxide mediated photo-degradation of methyl orange by ultraviolet light. *Toxicological & Environmental Chemistry*, 95, 543–558.
- Tsiptsias, C., Petridis, D., Athanasakis, N., Lemonidis, I., Deligiannis, A. & Samaras, P. (2015). Post-treatment of molasses wastewater by electrocoagulation and process optimization through response surface analysis. *Journal of Environmental Management*, 164, 104–113.
- Tu, Y.-J., You, C.-F. & Chang, C.-K. (2012). Kinetics and thermodynamics of adsorption for Cd on green manufactured nano-particles. *Journal of Hazardous Materials*, 235-236, 116–22.
- Wang, H.-Y., Qian, H. & Yao, W.-R. (2011). Melanoidins produced by the Maillard reaction: Structure and biological activity. *Food Chemistry*, 128, 573–584.
- Wang, J., Mi, W., Tian, J., Dai, J., Wang, X. & Liu, X. (2013a). Effect of calcinations of TiO<sub>2</sub>/ZnO composite powder at high temperature on photodegradation of methyl orange. *Composites Part B: Engineering*, 45, 758–767.

- Wang, X. et al. (2013b). Adsorption–photodegradation of humic acid in water by using ZnO coupled TiO<sub>2</sub>/bamboo charcoal under visible light irradiation. *Journal of Hazardous Materials*, 262, 16–24.
- Xiao, S., Zhao, L., Leng, X., Lang, X. & Lian, J. (2014). Synthesis of amorphous TiO<sub>2</sub> modified ZnO nanorod film with enhanced photocatalytic properties. *Applied Surface Science*, 299, 97–104.
- Zainudin, N.F., Abdullah, A.Z. & Mohamed, A.R. (2010). Characteristics of supported nano-TiO<sub>2</sub>/ZSM-5/silica gel (SNTZS): Photocatalytic degradation of phenol. *Journal of Hazardous Materials*, 174, 299–306.
- Zhang, P. et al. (2012). In situ assembly of well-dispersed Au nanoparticles on TiO<sub>2</sub>/ZnO nanofibers: a three-way synergistic heterostructure with enhanced photocatalytic activity. *Journal of Hazardous Materials*, 237-238, 331–8.
- Zhang, Z., Yuan, Y., Fang, Y., Liang, L., Ding, H. & Jin, L. (2007). Preparation of photocatalytic nano-ZnO/TiO<sub>2</sub> film and application for determination of chemical oxygen demand. *Talanta*, 73, 523–528.
- Zou, X., Dong, X., Wang, L., Ma, H., Zhang, X. & Zhang, X. (2014). Preparation of Ni doped ZnO-TiO<sub>2</sub> composites and their enhanced photocatalytic activity. *International Journal of Photoenergy*, 2014.

## **4 PERFORMANCE AND KINETICS OF A FLUIDIZED BED ANAEROBIC REACTOR TREATING DISTILLERY EFFLUENT**

### **4.1 Introduction**

The AD process is widely applied in organic load removal and bioenergy recovery from distillery wastewater (Satyawali & Balakrishnan, 2008). Robust anaerobic digesters such as FBRs achieve high organic removal efficiency and good energy recovery in terms of biomethane due to efficient mixing in the reactor (Andalib et al., 2012). Bioconversion of organic matter into biomethane is a complex process involving consortia of microorganisms. Due to the complex nature of the process, a poorly operated digester is often prone to inhibition due to accumulation of VFAs, which may lead to total digester failure (Aiyuk et al., 2006). During AD, the operating parameters such as organic loading rate (OLR), HRT, pH and food-to-microorganism ratio needs to be well regulated to avoid a possible digester failure because these parameters directly affect the microorganisms' activity in the digester.

Significant research work has been done to improve the performance of FBRs in the treatment of distillery effluent. One of the improvements is the application of appropriate biomass support material with large surface area such as zeolite or AC (Fernández et al., 2008). These support materials have the advantage that they have high capacity to carry microorganisms, thereby increasing the contact between the pollutants and the microbes leading to an increased reaction rate (Montalvo et al., 2012). Also, the effect of superficial liquid velocity has been studied as this affects both mixing and microbial growth (Jaafari et al., 2014). For instance, operating an FBR at an excessively high superficial liquid velocity results in dislodging of the microbes attached onto the carrier resulting in reduced efficiency while operating at very low velocities hinders adequate mixing (Rabah & Dahab, 2004; Jaafari et al., 2014).

It is therefore important to obtain important information regarding the state of the reactor during AD to avoid impending reactor failure due to poor operation. Kinetic modelling is an acceptable approach to determine the condition in the bioreactor based on substrate utilisation and microbial growth (Senturk et al., 2013). The result of kinetic modelling can be used to determine suitable system parameters, which leads to stability and therefore high efficiency of the reactor. Moreover, the results obtained from the kinetic modelling can be used to design an industrial-scale reactor operating under similar conditions. In this study, AD was carried out in an FBR and its operation defined using various kinetic models to determine the most suitable reactor operating conditions.

### **4.2 Methodology**

#### **4.2.1 Experimental setup**

The fluidized bed used had an internal diameter of 118 mm and height of 760 mm with a total and working volume of 8.3 L and 6 L respectively. The reactor was packed with 50 g of zeolite (particle size 150–300  $\mu\text{m}$ ) and fluidization was attained by the recycling stream using a centrifugal pump (Figure 22). The superficial velocity was maintained at about 0.6 cm/s and monitored by a flow meter. The reactor was fed using a peristaltic pump and the biogas produced was collected using the water displacement method.

#### 4.2.2 Start-up and operation of the bioreactor

The start-up of the reactor was first carried out in batch mode followed by continuous mode. In batch start-up, the reactor was first inoculated with cow dung slurry filtered through 0.3 mm sieve to remove large particulate solids (Hampannavar & Shivayogimath, 2010). Diluted distillery effluent (COD = 650 mg/L) and glucose (COD = 400 mg/L) in a ratio of 1:1 was added to the cow dung slurry in the reactor and digestion was allowed to proceed for 15 days while monitoring pH, COD, biogas and methane.

Once biogas production had stopped, fresh feed was added to the reactor with the concentration of distillery effluent gradually increased stepwise as the concentration of glucose was reduced such that the ratio of glucose to distillery wastewater was reduced progressively in the order 1:1, 1:1.5, 1:2, 1:4 and 0:1 for another 15 days. The ratio was changed every time stability had been achieved. By the 30<sup>th</sup> day, the reactor could achieve 80% TOC reduction with methane production of about 65% and the pH and alkalinity were stable. The operation of the reactor was then changed from batch to continuous at mesophilic conditions with low organic loading of 0.33 kg COD/m<sup>3</sup>.d at HRT of six days for three retentions. At this point, the reactor was very stable as was indicated by constant daily methane production, nearly constant effluent COD and nearly constant pH (Fernández et al., 2008). Once stable conditions were attained, the reactor was operated at OLRs ranging between 0.33 kg COD/m<sup>3</sup>.d and 9 kg COD/m<sup>3</sup>.d corresponding to 0.25 kg TOC/m<sup>3</sup>.d to 8.1 kg TOC/m<sup>3</sup>.d at constant HRT of 6 at a feed flow rate of 1 L/d.

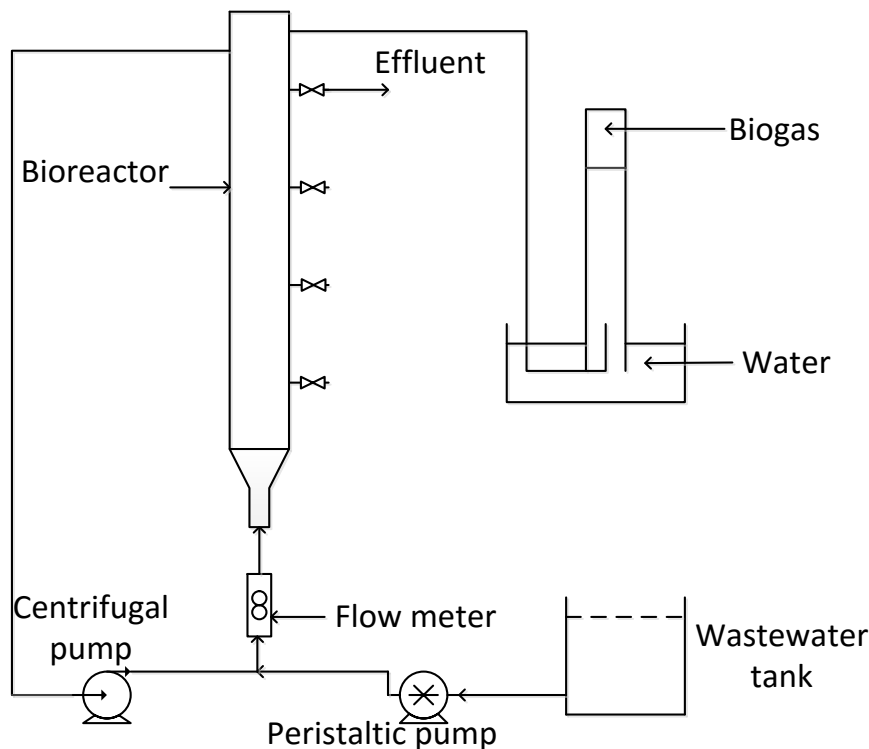


Figure 22: Setup of the fluidized bed anaerobic digester

### 4.2.3 Experimental analysis

Samples were centrifuged before analysis. TOC was analysed using a TOC analyser (Teledyne Tekmar), gas was analysed using a gas chromatograph (Trace 1310 gas chromatograph) fitted with thermal conductivity detector, while colour was analysed using UV-Vis spectrophotometer (T80 + UV/VIS Spectrophotometer, PG instruments Ltd). Alkalinity was analysed per standard method for wastewater analysis involving titrating samples against a 0.02 N H<sub>2</sub>SO<sub>4</sub> solution. Biomass concentration was determined as volatile suspended solids (VSS). The VSS were determined by evaporating the residue obtained from centrifuged samples at 105°C for 24 hours (until constant mass was obtained) and then calcined at 450°C for an hour.

### 4.3 Results and Discussion

The TOC and colour reduction efficiencies were found to slightly increase with an increase in HRT (Table 8). This was because at high HRT, the substrate had higher residence time in the reactor than at low HRT. Longer time in the reactor means increased contact with microorganisms leading to higher removal efficiency. The colour reduction efficiency was found to be much lower than that of the TOC due to the presence of biorecalcitrant components of distillery effluent, which causes colour. The biorecalcitrant component is mostly melanoidin (Wang et al., 2011).

**Table 8: Parameters and efficiencies of the FBR at constant feed flow rate**

HRT (d)	OLR kg TOC/ m <sup>3</sup> .d	Influent flow, Q (L/d)	Influent		Effluent		Efficiency	
			tTOC (g/L)	sTOC (g/L)	tTOC (g/L)	sTOC (g/L)	TOC removal%	Colour removal%
3	1.77	2	5.82	5.315	1.56	1.151	78	34
6	0.88	1	5.82	5.315	1.3	0.803	85	40
10	0.53	0.6	5.82	5.315	1.18	0.635	88	50
15	0.35	0.4	5.82	5.315	1.04	0.552	90	52
20	0.26	0.3	5.82	5.315	0.89	0.472	91	54

#### 4.3.1 Substrate balance model

The substrate balance around the reactor was formulated based on the assumption (Borja et al., 2002; Rincón et al., 2006) that the anaerobic reactor operated at steady-state conditions as depicted by nearly constant effluent substrate concentration and biogas production rate. A further assumption is that even though the feed carried suspended solids, it was too little as it was only 2.3% of the feed total TOC. These suspended solids were assumed to be biodegradable, thus it was considered that the VSS in the reactor and effluent corresponded to generated biomass.

Therefore, TOC balance for the reactor could be expressed as:

$$(tTOC)_o = (sTOC)_e + (tTOC)_{biogas} + (tTOC)_{vss}_e + (tTOC)_m \quad (30)$$

where  $(tTOC)_o$  is the influent total TOC,  $(sTOC)_e$  is soluble TOC in the effluent,  $(tTOC)_{biogas}$  is the fraction of  $(tTOC)_o$  converted into biogas,  $(tTOC)_{vss}$  is the fraction of  $(tTOC)_o$  converted into biomass and  $(tTOC)_m$  is the fraction of  $(tTOC)_o$  used for cell maintenance and growth.

Considering feed flow rate and methane flow rate, Eq. 30 can be expressed as:

$$QS_{to} = QS_e + qCH_4Y_{s/g} + q(S_{te}-S_{se}) + K_mXV \quad (31)$$

where  $Q$  is the feed flow rate ( $Ld^{-1}$ ),  $S_{to}$  is the feed concentration ( $g\ tTOCL^{-1}$ ),  $S_{te}$  is the total effluent concentration ( $g\ tTOCL^{-1}$ ),  $S_{se}$  is the soluble effluent concentration ( $g\ sTOCL^{-1}$ ),  $qCH_4$  is methane production rate ( $LCH_4d^{-1}$ ),  $Y_{substrate/gas}$  is the coefficient of substrate conversion into methane ( $g\ tTOCL^{-1}CH_4$ ),  $K_m$  is cell maintenance coefficient, and  $X$  and  $V$  are the biomass concentration and reactor volume (L), respectively.

On rearrangement, Eq. 31 can be written as:

$$q(S_{to}-S_{te}) = qCH_4Y_{s/g} + k_mXV \quad (32)$$

Since  $HRT=V/q$ , by dividing both sides by  $V$ , Eq. 32 becomes:

$$(S_{to}-S_{te})/HRT = qCH_4Y_{s/g}/V + XK_m \quad (33)$$

From Eq. 33, a plot of  $(S_{to}-S_{te})/HRT$  versus  $qCH_4/V$  gives a straight line with a slope equal to  $Y_{s/g}$  and y-axis intercept equals to  $XK_m$ . In Figure 23, the plot supports the validity of this model in describing the anaerobic process in this particular study with a regression coefficient of 0.996. The y-axis intercept was very small indicating that a very small portion of the feed TOC was used for cell maintenance. The  $Y_{s/g}$  value was found to be 3.58 g tTOC/LCH<sub>4</sub>. The inverse of the  $Y_{s/g}$  (which is  $Y_{g/s}$ ) is the methane yield coefficient which was found to be 0.28 LCH<sub>4</sub>/g tTOC corresponding to 0.257 L CH<sub>4</sub>/g COD. This is close to a theoretical methane yield of 0.35 LCH<sub>4</sub>/g tTOC when glucose is used as substrate (Fernández et al., 2008).

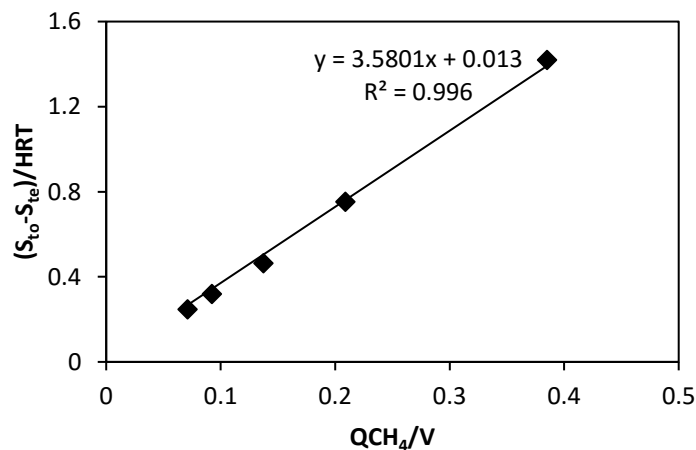


**Figure 23: Determination of methane yield coefficient**

The fraction of influent tTOC converted into biogas, biomass and that which is in the effluent can be calculated from Eq. 1 by expressing each term in the right-hand side as a fraction of  $(tTOC)_o$ . Figure 24a shows the percentages of TOC converted into biogas, biomass and unremoved TOC. It was found that, generally, most of the feed TOC was converted into biogas. The percentage converted to biogas increased slightly with an increase in HRT. This suggests that at high HRT, the feed had higher residence time in the reactor, thus achieving maximum conversion than at lower HRTs where the residence time is shorter. The proportion of feed converted into biomass was nearly constant at various HRTs while there was a slight decrease in the proportion of feed in the effluent with an increase in HRT. However, the proportion of feed TOC converted into biogas, biomass and that which remained in the effluent do not give a very clear indication of the possible characteristics of the effluent in terms of residual pollution load as it only presents percentages. Figure 24b shows the actual amount of TOC converted and the residual TOC in effluent. The information on the amount of residual TOC in the effluent is necessary as it determines whether a post-treatment technique is required or not. Moreover, determination of the amount of biomass in effluent is necessary; more so if photodegradation is to be applied as a post-treatment. This is because for photodegradation as a post-treatment technique, quantification of the biomass generated in AD step is necessary as suspended biomass may lead to light attenuation during UV photodegradation. Besides, determination of biomass yield is necessary in designing a system for sludge handling.

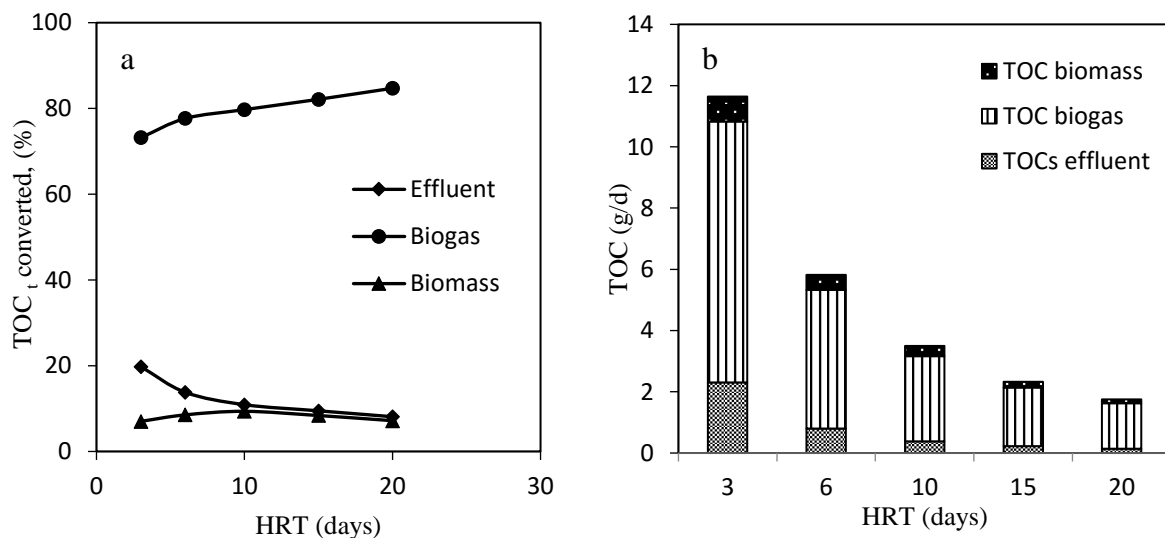


**Figure 24:** (a) Fraction and (b) actual amount of feed TOC converted into biogas, biomass and that which remained in the effluent

#### 4.3.2 Biorecalcitrant component of distillery effluent

Distillery effluent is considered as fairly biodegradable with traces of biorecalcitrant compounds such as melanoidins (Acharya et al., 2008). The biodegradability of the distillery effluent was measured by determining the  $BOD_5/COD$  ratio, which was found to be 0.41. This indicates that the distillery effluent is biodegradable. Good biodegradability is achieved when  $BOD_5/COD$  is greater than 0.25 (Sankaran et al., 2014). However, the recalcitrant parts of distillery effluent, which are majorly melanoidins, often pass through anaerobic treatment

without being degraded and they impart a dark colour to biomethanated effluent (Satyawali & Balakrishnan, 2008; Kalavathi et al., 2001). The amount of non-biodegradable component can be determined by the relationship between the organics remaining after digestion and HRT. It is proposed that a plot of  $\ln(COD_{effluent}$  or  $TOC_{effluent})$  against  $1/HRT$  gives a straight line, and the recalcitrant component can be calculated at infinite HRT. A similar model has been applied to determine the biodegradable component of some food waste wastewater (Rincón et al., 2006; Borja et al., 2002). In Figure 25, the amount of non-biodegradable component is calculated as TOC or COD equivalent at y-axis intercept when HRT is infinite.

It was found that the non-biodegradable TOC and COD were 477 mg/L and 756 mg/L, respectively, under prevailing digestion conditions. The amount of non-biodegradable COD was higher than TOC because TOC only caters for carbons while COD caters for all oxidisable compounds in wastewater. Apart from organics, distillery effluent has high concentrations of cations and halogen ions (Satyawali & Balakrishnan, 2008). Considering that the influent TOC was 5318 mg/L, the non-biodegradable TOC only formed ~9% of the feed TOC indicating that distillery effluent is biodegradable. However, the non-biodegradable portion is mostly melanoidins that impart a dark-brown colour to distillery effluent (Kalavathi et al., 2001; Satyawali & Balakrishnan, 2008). Thus, anaerobic treatment of distillery effluent is not effective for colour removal as shown in Table 8.

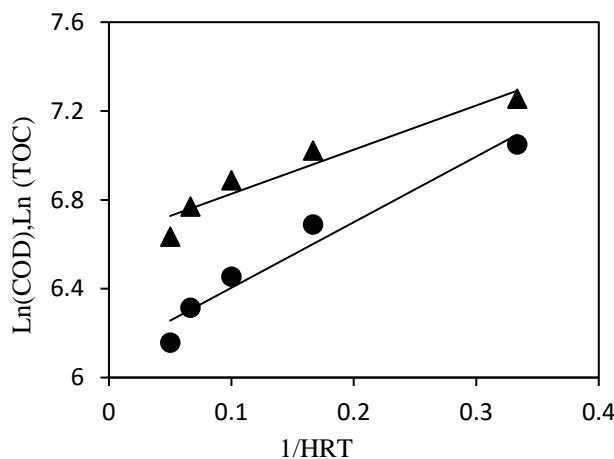


Figure 25: Determination of recalcitrant component of distillery effluent, TOC (●) and COD (▲)

#### 4.3.3 Substrate utilisation kinetics

The kinetics of degradation of total and biodegradable constituents of the effluent was compared applying first-order rate model:

$$\ln\left(\frac{S_e}{S_o}\right) = kt \quad (34)$$

where  $S_o$  and  $S_e$  are feed and effluent TOC respectively,  $k$  is rate constant ( $d^{-1}$ ) and  $t$  is HRT (days). For the biodegradable component,  $S_o$  and  $S_e$  were modified to  $S_{ob}$  and  $S_{eb}$  for biodegradable feed and effluent, respectively. Figure 26 shows that the rate of uptake of biodegradable constituent was four times faster than that of the total organic compounds in the wastewater sample. The uptake of the biodegradation component fitted first-order kinetics better than that of total organic substrate with  $R^2$  values of 0.9754 and 0.9096, respectively.

The difference can be attributed to a larger proportion of undigested TOC when considering total feed TOC than in the case of biodegradable TOC due to the slow degradation of the recalcitrant components.

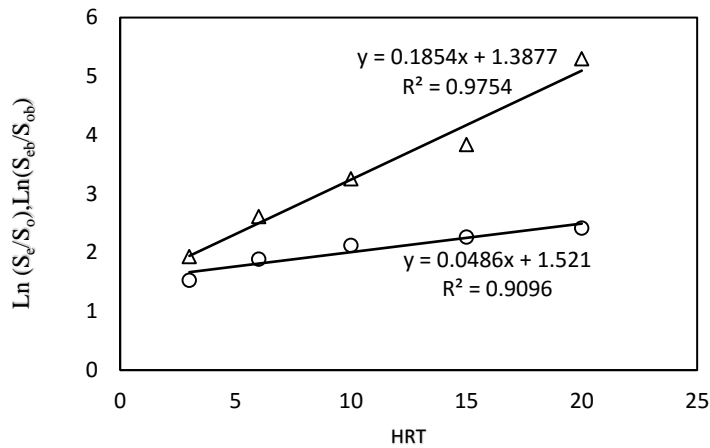


Figure 26: First-order reaction kinetic of biodegradable and TOC, biodegradable TOC (Δ) and total TOC (○)

#### 4.3.4 Michaelis–Menten kinetic model

According to the Michaelis–Menten kinetic model, the specific substrate utilisation rate and biodegradable substrate concentration can be related by the following equation:

$$r = \frac{kS_b}{(K_s + S_b)} \quad (35)$$

where  $r$  is the specific substrate utilisation rate,  $k$  is the maximum substrate utilisation rate ( $\text{g sTOCg}^{-1}\text{VSSd}^{-1}$ ),  $S_b$  is the concentration of the biodegradable substrate in the reactor and  $K_s$  is the Michaelis constant. The non-biodegradable TOC obtained in Figure 25 was subtracted from the experimental total TOC to obtain the biodegradable TOC in this experiment (Rincón et al., 2006). The specific substrate utilisation rate can be expressed as (Rincón et al., 2006):

$$r = \frac{(S_o - S_b)}{HRT \cdot X} \quad (36)$$

where  $S_o$  is the biodegradable feed concentration and  $X$  is the biomass concentration in the reactor ( $\text{g VSSL}^{-1}$ ). By combining Eq. 35 and Eq. 36, we obtain Eq. 37. The specific substrate utilisation rate ( $r$ ) is plotted against  $S_b$  (Figure 27).

$$r = \frac{(S_o - S_b)}{HRT \cdot X} = \frac{kS_b}{(K_s + S_b)} \quad (37)$$

The plot was found to represent a hyperbolic function, which is an indication that the substrate utilisation followed the Michaelis–Menten model (Borja et al., 2002).

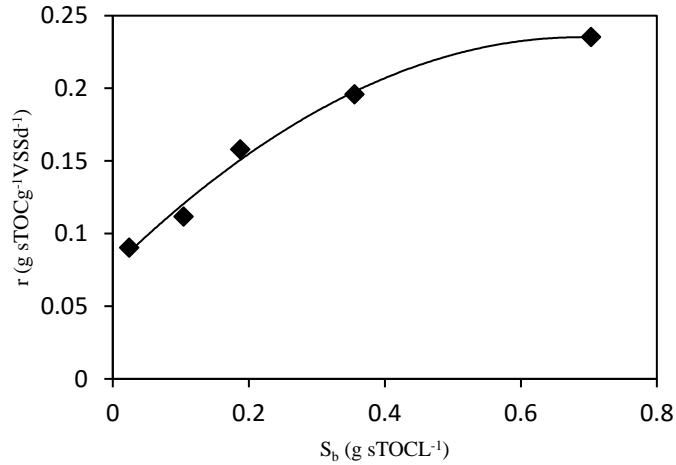


**Figure 27: Specific substrate utilisation rate against biodegradable TOC in the reactor**

To determine  $k$  and  $K_s$ , Eq. 37 was linearized as Eq. 38 and  $1/r$  was plotted against  $1/S_b$  where  $K_s$  was determined from the slope and  $k$  from the y intercept. Accordingly, from Figure 28, the values of  $k$  and  $K_s$  were found to be  $0.2916 \text{ sTOC g}^{-1} \text{ VSSd}^{-1}$  and  $0.166 \text{ g sTOC L}^{-1}$ . Senturk et al. (2013) reported a maximum substrate utilisation rate ( $k$ ) of  $0.106 \text{ g sCOD g}^{-1} \text{ VSSd}^{-1}$  and a  $K_s$  value of  $0.535 \text{ g sCOD L}^{-1}$ .

$$\frac{1}{r} = \frac{K_s}{k} \left( \frac{1}{S_b} \right) + \frac{1}{k} \quad (38)$$

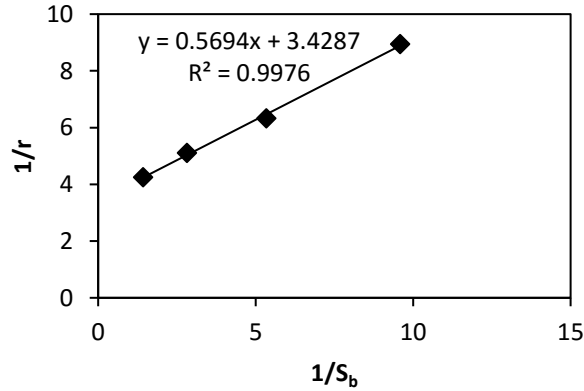


**Figure 28: A plot of  $1/r$  against  $1/S_b$  to determine  $K$  and  $K_s$**

If the values of  $K$  and  $K_s$  are substituted in Eq. 6, the theoretical rate of substrate uptake can be determined (Rincón et al., 2006). Figure 29 shows that the model predicts the kinetic activity of the microorganisms involved in the degradation well. The model strongly depicts the behaviour of the reactor at experimental  $r$  values greater than  $0.09 \text{ g sTOC g}^{-1} \text{ VSSd}^{-1}$ .

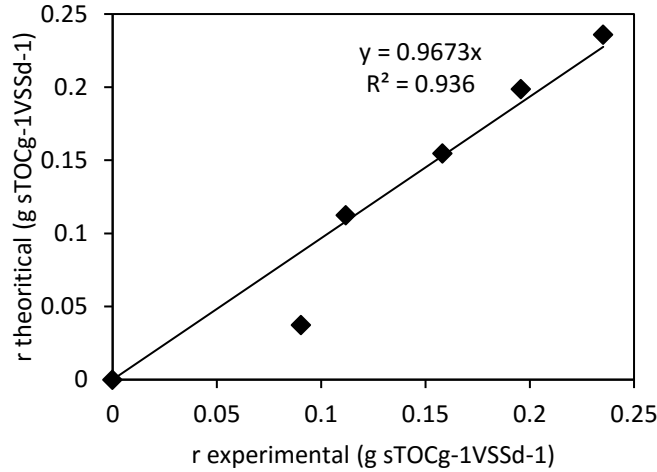


Figure 29: A comparison of the theoretical and experimental specific substrate utilisation rate

#### 4.3.5 The mean cell residence time

The mean cell residence time (MCRT) or sludge retention time, also known as the sludge age, is the average amount of time the anaerobic microorganisms are retained in the reactor. The MCRT directly affects the kinetics of substrate utilisation, biogas production and sludge production. It also affects microorganisms' growth kinetics since the time spent in the reactor determines feed-microbes contact time that affects growth. It is a function of biosolids in the system and rate of biosolids loss from the system. MCRT is calculated as (Ng et al., 2006):

$$\theta = \frac{B_r V}{Q \cdot B_{eff}} \quad (39)$$

where  $\theta$  is MCRT (days),  $B_r$  is the concentration of biomass in the reactor (g VSS/L),  $V$  is the reactor volume (L),  $Q$  is the effluent flow rate (L/d) and  $B_{eff}$  is the biomass concentration in the effluent (g VSS/L). The MCRT can be related to the specific substrate utilisation rate as (Nweke et al., 2014):

$$\frac{1}{\theta} = Yr - K_d \quad (40)$$

where  $r$  is the specific rate of substrate utilisation,  $Y$  is the microbial growth yield (biomass yield) and  $K_d$  is the endogenous decay coefficient ( $d^{-1}$ ). This correlation helps to calculate  $Y$  and  $K_d$ . These two parameters are significant as biomass yield can be applied to estimate the amount of sludge produced during anaerobic treatment, while  $K_d$  is used to calculate the nett amount of sludge to be handled. This information can be useful in choosing and designing a post-treatment system. In case UV photodegradation is to be applied as an appropriate post-treatment method, then sludge production should be minimised or an appropriate method should be applied to remove the sludge produced. If not regulated or removed, suspended sludge will lead to light attenuation thereby reducing the efficiency of the UV post-treatment process.

A plot of  $1/\theta$  against  $r$  gives a straight line with  $Y$  as gradient and y-axis intercept as the  $K_d$ . In Figure 30, the  $Y$  value was found to be 0.4658 g/g while  $K_d$  was 0.0293  $d^{-1}$ . This compares well with the values in literature of 0.357 g/g and 0.083  $d^{-1}$  for  $Y$  and  $K_d$ , respectively (Enitan &

Adeyemo, 2014). The specific rate of substrate utilisation has an inverse relationship with the MCRT because low MCRT is achieved at high feed flow rate, which translates into a higher OLR. Therefore, there is significantly more substrate available as feed at low MCRT than at high MCRT. However, this also depends and interlinks with microorganisms' growth kinetics and food-to-microorganism ratio at any time in the reactor.

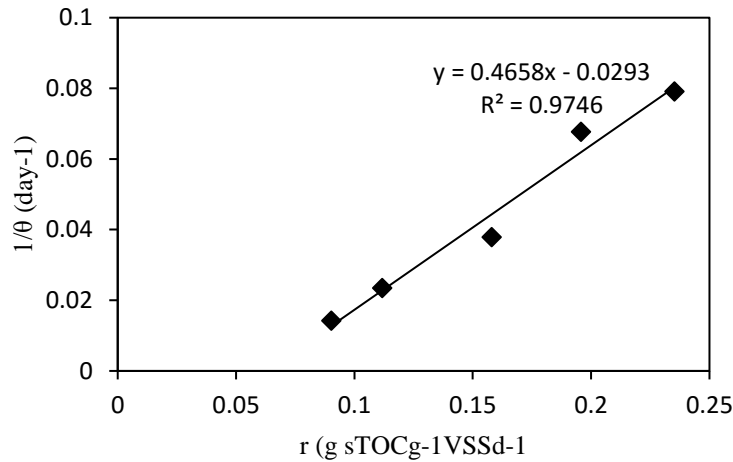


Figure 30: Correlation between sludge age and specific substrate utilisation rate

#### 4.3.6 Microorganisms' growth kinetics

Substrate utilisation rate and methane production rate are functions of the microorganism population in the reactor. Microorganisms present in sufficient numbers effectively convert substrate into methane whereas the process can be inhibited if the number of microorganisms is below a given limit compared with the available feed. It is therefore important to monitor the growth rate of microorganisms in the reactor, which is a function of biomass yield. Maximum specific microorganisms' growth rate ( $\mu_{max}$ ) ( $d^{-1}$ ) can be determined using  $Y$  ( $g/g$ ) and  $K$  ( $g\ sTOCg^{-1}VSSd^{-1}$ ).

$$K = \frac{\mu_{max}}{Y} \quad (41)$$

The maximum microorganisms' growth rate was found to be  $0.1358\ d^{-1}$ . Consider Monod equation that relates the specific microorganisms' growth rate with substrate concentration as follows (Yu et al., 2013);

$$\mu = \mu_{max} \frac{S}{K_s + S} - K_d \quad (42)$$

where  $\mu$  is the specific growth rate of the microorganisms,  $\mu_{max}$  is the maximum specific growth rate of the microorganisms,  $S$  is the concentration of the limiting substrate for growth,  $K_d$  is the endogenous decay coefficient, and  $K_s$  is the substrate utilisation constant, which is numerically equal to the substrate concentration when  $\mu = \frac{1}{2} \mu_{max}$ .

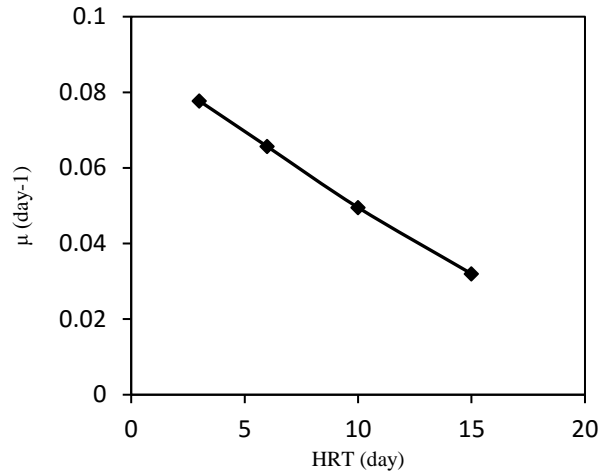


**Figure 31: Specific microorganisms' growth rate as a function of HRT at constant feed concentration**

In Figure 31, the nett specific growth rate of microorganisms reduced with an increase in HRT. This may be because at low HRTs, more feed was available in the reactor due to the high flow rates applied than at high HRTs when less food is available. At low HRT, the high OLR, which did not show any substantial organic loading shock (as indicated by pH and alkalinity in Table 9) led to increased activity of the microorganisms resulting in a higher specific growth rate. The slight increase in pH can be due to the consumption of VFAs, which results in a corresponding slight increase in alkalinity.

**Table 9: pH and alkalinity values during AD process**

HRT (d)	3	6	10	15	20
pH	7.21	7.34	7.5	7.4	7.4
Alkalinity (mg/L)	2320	2840	3020	3040	3018

#### 4.3.7 Food-to-microorganism ratio

The food-to-microorganism ratio (F:M) is the amount of biodegradable substrate exposed to microorganisms per day. The F:M can be used as a parameter to evaluate the performance of a digester as it can directly affect the TOC conversion efficiency (substrate utilisation rate), methane production rate and sludge production (Perez et al., 2001). The F:M can be calculated as:

$$\frac{F}{M} = \frac{Q \cdot S_0}{B_r \cdot V} \quad (43)$$

where  $Q$  is the feed flow (L/d),  $S_0$  is the feed concentration (g TOC/L),  $B_r$  is the biomass concentration in the reactor (g VSS/L) and  $V$  is the volume of the reactor. Table 10 shows the effect of the F:M on biogas production rate and methane yield. Biogas production increased with an increase in F:M while methane composition of the biogas reduced slightly after F:M values were 0.16 g TOC/g VSS.d and above. The increase in gas production with an increase in F:M can be due to more feed being available for digestion at higher F:M ratios. The reduction in methane composition at higher F:M values cannot be attributed to organic overloading as the VFA-to-alkalinity ratio (Table 10) showed that it was at a value under which the reactor

was stable. The reactor is stable when this ratio is below 0.3 to 0.4 (Hampannavar & Shivayogimath, 2010). According to Cardinali-Rezende et al. (2013), variation in the F:M has an impact on the diversity of microorganisms in the reactor, which directly affects methanogenic activity. The study reported that shifts in the composition of the methanogenic community at different F:M values can lead to variation in the pathway of methane formation. The study showed that at high F:M, acetotrophic methanogens are in abundance and methane is produced mostly via the acetate route. At low F:M there is a mixture of hydrogenotrophic, methylotrophic and acetotrophic methanogens; therefore, methane production is through multiple pathways. This can explain the superior methane quality at lower F:M compared with higher F:M values.

**Table 10: Performance of the reactor at different F:M values**

F/M	VFA/alk	Biogas (L/d)	CH <sub>4</sub> %	TOC <sub>effluent</sub> /TOC <sub>feed</sub>
0.27	0.34	3.3	70	0.22
0.21	0.26	1.75	71.6	0.15
0.16	0.24	1.1	75	0.12
0.11	0.23	0.74	75	0.10
0.09	0.22	0.58	74.5	0.09

There was a slight decrease in TOC reduction with an increase in F:M. This observation may be due to high organic load at high F:M, which means there was excess feed for microbes to degrade, while at low F:M the microorganism population was sufficient to consume most of the feed. A similar observation has been reported by Perez et al. (2001). Alternatively, the reduction in efficiency at high F:M could be attributed to the low MCRT attained (Figure 32) due to high flow rate. Moreover, even though there is an increase in feeding rate at high F:M, there is also a corresponding increase in biomass as compared with that at a low F:M due to the increase in the available food, which results in rapid cell growth. Therefore, the relative increase in biomass at a fixed reactor volume can increase the viscosity of the wastewater in the reactor due to the increase in VSS leading to mass transfer hindrance. Cardinali-Rezende et al. (2013) reported a decrease in bacterial cell density at lower F:M than at higher F:M; however, a higher bacterial diversity was recorded at a low F:M than at a higher F:M. Therefore, the high bacterial diversity at low F:M could degrade more diversified substrates leading to high substrate conversion. Generally, at high F:M the amount of biomass available was not sufficient to remove a substantial amount of TOC; similar observations have been reported (Hafez et al., 2012; Perez et al., 2001).

#### **4.3.8 MCRT and HRT**

The total duration that the biomass resides in the reactor as compared with liquid retention time is an important factor in anaerobic wastewater treatment. In Figure 32, the MCRT was compared with HRT at various F:Ms. Generally, the MCRT was always at least 2.5 times higher than the HRT. The higher MCRT than HRT can be attributed to the biomass being attached onto zeolite thus being retained in the reactor instead of being washed out by the effluent. The advantage of attached biomass is that the biomass is able to reside in the reactor

for a longer time fostering adaptation to the environment than if old cells are frequently replaced by new ones in a case where the biomass is not attached in the reactor. Attachment also ensures that a sufficient amount of biomass is usually in the reactor, thereby ensuring high efficiency.

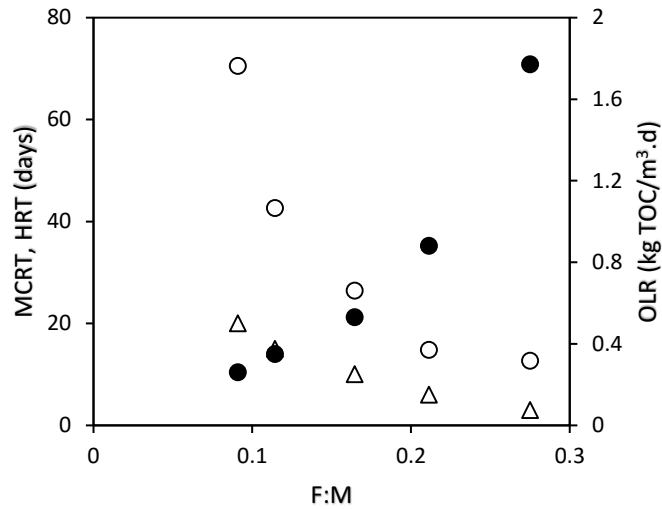


**Figure 32: A comparison of HRT and MCRT at different F:M values, HRT (Δ), MCRT (○) and corresponding OLR (●)**

The specific rate of substrate utilisation,  $r$  (g TOC/gVSS.d), at various F:M values was evaluated. In Figure 33 it was found that  $r$  increased linearly with an increase in F:M. This is an indication that at low F:M the microorganisms were near starvation as the feed was little. As the feed increased, thus an increase in F:M, the TOC uptake per unit biomass increased as there was sufficient feed.

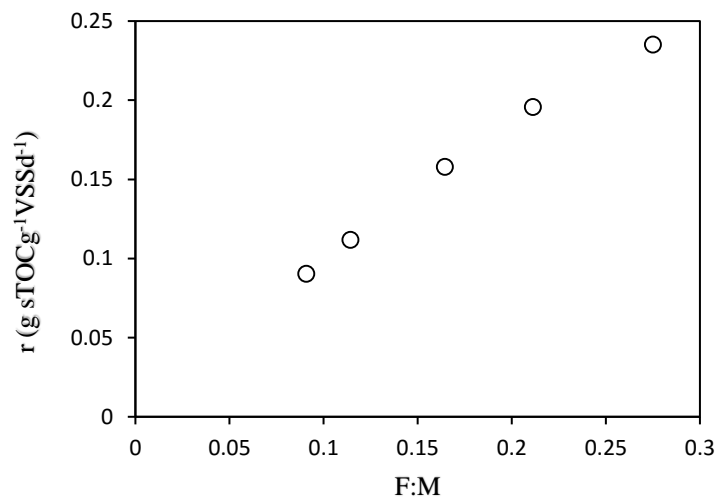


**Figure 33: Effect of F:M on specific substrate utilisation rate**

### 4.3.9 Effect of OLR on AD

The effect of OLR at fixed HRT was studied and the kinetics of biogas production and organic removal was analysed. The influent COD was varied as: 2 g/L, 5.8 g/L, 19.7 g/L, 37.1 g/L and 54.2 g/L at constant feed flow rate of 1 L/d corresponding to an HRT of six days. This corresponded to OLRs of 0.33 COD/m<sup>3</sup>.d, 0.97 COD/m<sup>3</sup>.d, 3.3 COD/m<sup>3</sup>.d, 6.1 COD/m<sup>3</sup>.d and 9 kg COD/m<sup>3</sup>.d respectively, as shown in Table 11.

**Table 11: Feed and effluent characteristics at various OLRs and fixed HRT**

OLR (kg COD/m <sup>3</sup> .d)	Feed		Effluent	
	COD (mg/L)	TOC (mg/L)	COD (mg/L)	TOC (mg/L)
0.33	2 108	1 384	306	252
0.97	5 807	4 230	740	520
3.3	19 700	12 680	4 620	2 300
6.2	37 100	30 900	10 400	6 030
9	54 200	41 700	19 800	13 500

### 4.3.10 Effect of OLR on biogas production rate

During the study, steady state in each OLR was indicated by constant biogas production, constant methane production, constant pH and constant effluent COD concentration for at least three consecutive days after running the experiments for two to three HRTs for each OLR (Fernández et al., 2008). Figure 34 shows that the biogas production rate increased with an increase in OLR. This was due to the increase in the available organic substrate that could be consumed by microorganisms. This may be an indication that the activity of the consortia of biogas-producing bacteria was not hampered within the OLR range studied (Fernández et al., 2008). Figure 34 further shows that for low OLRs (0.33–3.28 kg COD/m<sup>3</sup>.d), the stability of the reactor was achieved faster than for higher OLRs (6.2–9 kg COD/m<sup>3</sup>.d) as indicated by the effluent load. This implies that at higher concentrations, microorganisms need a longer time to adapt. An increase in effluent COD with the increase in OLR was observed, which has been reported in continuous AD of distillery effluent and various other effluents (Acharya et al., 2008; Borja, 2001; Wang & Wu, 2004).

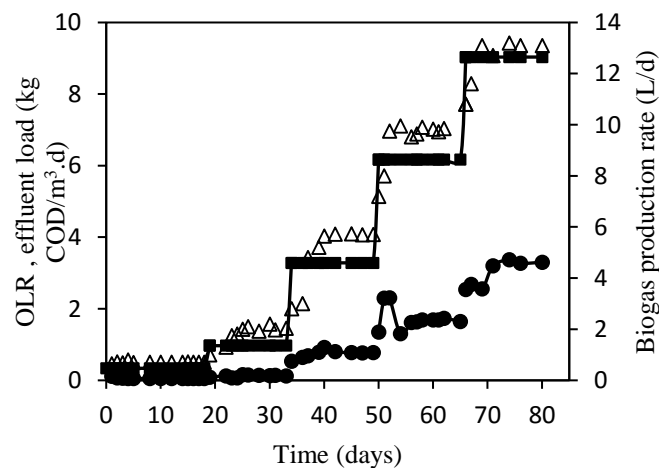


**Figure 34: Effect of OLR (■) on biogas production rate (Δ) and effluent load (●)**

#### 4.3.11 Effect of OLR on methane production

Analysis of the methane proportion of the biogas produced at different OLRs showed that biogas with a methane content of above 63% was produced up to an OLR of 6 kg COD/m<sup>3</sup> while at 9 kg COD/m<sup>3</sup> it dropped to 33% (Figure 35). This indicated that high OLR inhibited methanogenesis due to organic overloading. Organic overloading may lead to production of high amounts of VFAs, which cause acidity as shown in Figure 40. Consequently, high acidity in the reactor compromises the ability of the digester to buffer itself as methanogenesis is hindered while acidogenesis is favoured.

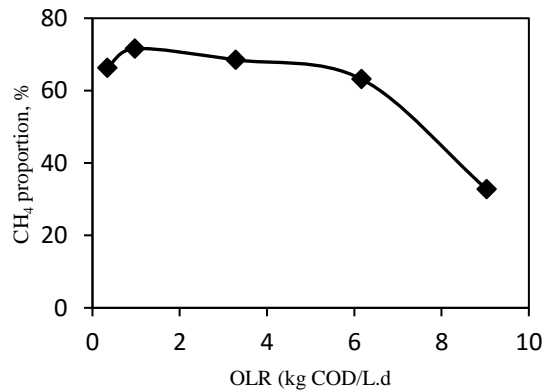


Figure 35: The effect of OLR on methane composition

#### 4.3.12 Methane production rate and methane yield coefficient

In Figure 36, methane production rate was found to increase with an increase in OLR up to 9 kg COD/m<sup>3</sup>. Below this OLR, the reactor was stable and the organic load feed could be converted efficiently into biogas, indicating that methanogenesis was not inhibited.

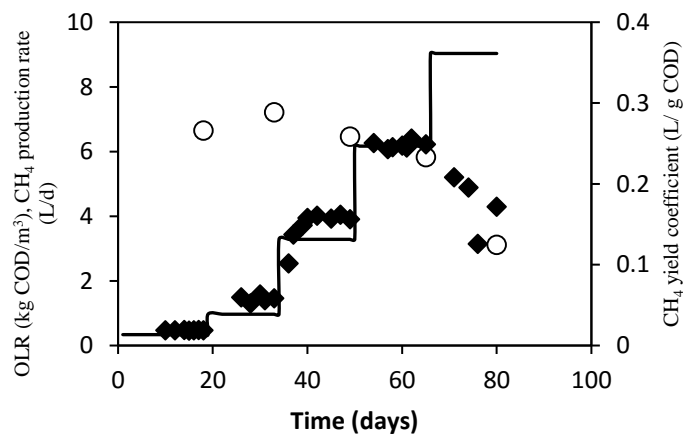


Figure 36: Effect of OLR (—) on volumetric methane production rate (■) and methane yield coefficient (○)

A methane yield of between 0.29 L/g COD and 0.23 L/g COD was recorded during steady operation; however, at 6 kg COD/m<sup>3</sup> the methane coefficient dropped to 0.124 L/g COD. Generally, the theoretical methane coefficient is 0.35 L/g COD, assuming that all of the COD fed into the reactor is transformed into methane and that there are no biorecalcitrant components of the feed, also assuming further that there is no COD used for cell growth and

cell maintenance (Borja et al., 2004). Moreover, the presence of other substances, such as sulphates that consume COD without producing methane via the sulphate-reducing bacteria pathway, are not accounted for as ideal in the case (Fernández et al., 2008). Values close to the theoretical yield can be obtained if a biodegradable substrate like glucose is used (Borja, 2001).

#### 4.3.13 Effect of OLR on COD and colour reduction

The performance of wastewater treatment system is evaluated based on the pollution-reduction efficiency. The efficiency of the system in COD and colour reduction was evaluated at different OLRs (Figure 37). A COD reduction of 85% was achieved at lower OLRs while the efficiency reduced to 64% at high OLRs. At an OLR of 6 kg COD/m<sup>3</sup>.d, COD reduction of 73% could still be achieved. However, colour reduction was always low ranging between 56% and 21%, from low to high OLRs. The low colour reduction is attributed to the presence of biorecalcitrant melanoidins in distillery effluent.

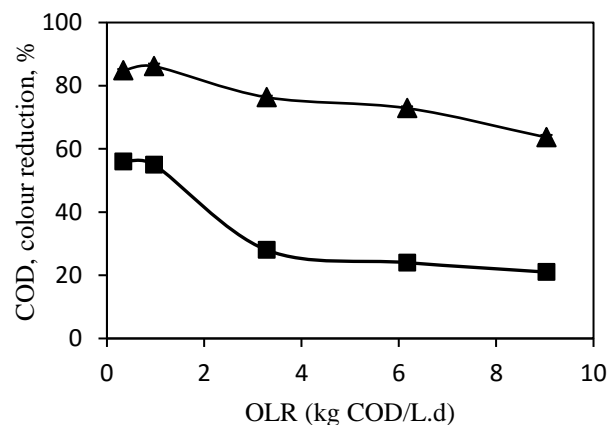


Figure 37: Effect of OLR on COD (▲) and colour-reduction efficiency (■)

#### 4.3.14 COD reduction model

The investigation into the variation in COD removal rates with OLR showed that the removal rate increased linearly with OLR (Figure 37). The effect of feed concentration on the COD removal rate can be described by Eq. 44 (Fernández et al., 2008; Borja et al., 2004):

$$R_s = K(S)^n \quad (44)$$

where  $R_s$  is the COD removal rate (kg COD/m<sup>3</sup>.d),  $K$  is the reaction constant (d<sup>-1</sup>),  $S$  is the feed substrate concentration (kg COD/m<sup>3</sup>) and  $n$  is the reaction order. Considering first-order reaction kinetics,  $n$  is equal to unity. Therefore, a plot of  $R_s$  against  $S$  gives a straight line with slope equal to  $K$  and the  $y$  intercept equal to zero. This describes the influence of feed concentration on COD reduction rate. In Figure 38, the experimental data fitted the theoretical model with a reaction constant equal to 0.67 d<sup>-1</sup> and  $R^2$  equal to 0.9806. A similar model has been used to describe AD in FBRs (Borja et al., 2004; Fernández et al., 2008). The observed increase in COD removal rate with an increase in OLR can be attributed to a corresponding increase in the concentration gradient between the fluid and biofilm (Fernández et al., 2008). The increase in COD removal rate with an increase in feed concentration can also be attributed

to the stability of the anaerobic FBR attributed to the immobilisation of microorganisms to small fluidized zeolite particles (Borja et al., 2004).

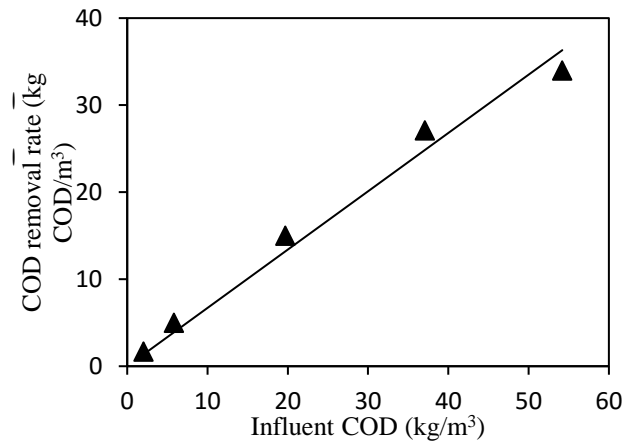


**Figure 38: The effect of feed concentration on COD removal rate**

A model has been proposed to determine methane yield coefficient using experimental data of volumetric methane production rate and COD removed. Based on the assumption that the volume of methane produced per day is proportional to the amount of COD consumed, the following equation can be used to relate the parameters (Fernández et al., 2008);

$$\eta = Y_p Q(S_o - S_e) \quad (45)$$

where  $\eta$  is methane production rate (L/d),  $Y_p$  is the methane yield coefficient,  $Q$  is feed flow rate (L/d), and  $S_o$  and  $S_e$  are feed and effluent concentrations (g COD/L), respectively.

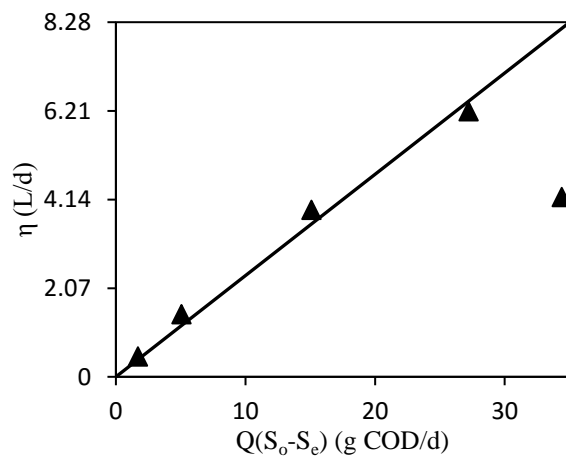


**Figure 39: Variation of methane production rate with substrate removal**

A plot of  $V_{CH_4}$  against  $Q(S_o - S_e)$  in Figure 39 gives a straight line with a slope of 0.236 g COD/L corresponding to  $Y_p$  for the first four OLRs studied. However, the point corresponding to OLR of 9 kg COD/m<sup>3</sup> was out of the model limit. This is due to reactor instability caused by organic overloading, which results in accumulation of VFAs (Figure 19). A  $Y_p$  value of 0.29 g COD/L was reported for the anaerobic treatment of distillery effluent in an FBR (Fernández et al., 2008).

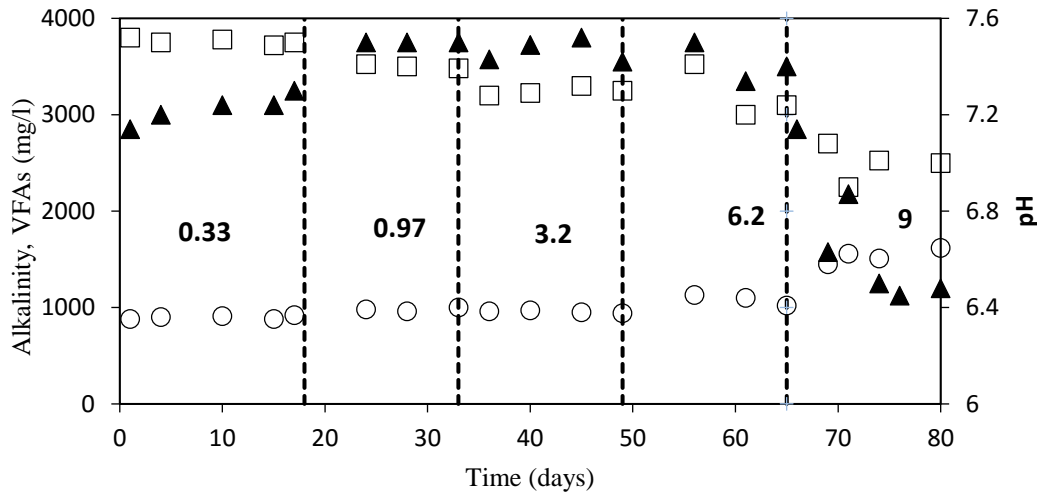


**Figure 40: Alkalinity (□), VFAs (○) and pH (▲) profile during AD**

#### 4.3.15 Alkalinity, VFAs and pH

The balance between VFAs, alkalinity and pH can be used as a measure for bioreactor stability. A stable reactor will operate at a pH range of between 6.7 and 8 with total alkalinity higher than VFA concentration. Figure 39 shows that the anaerobic process was stable until day 65, which marked the onset of operation at OLR of 9 kg COD/m<sup>3</sup>. The reduction in methane composition (Figure 35) and the reduction in total alkalinity and pH with a corresponding increase in VFAs at high OLR (Figure 40) are indications that the process was unstable at 9 kg COD/m<sup>3</sup>. In Figure 39, the pH dropped from stable value of about 7.3 to 6.4 at high OLR while alkalinity reduced from 3100 mg/L to 2500 mg/L as a result of VFAs increasing from 1020 mg/L to 1620 mg/L. The decrease in pH was as a result of the high VFA production rate. The increase in VFA production led to an increase in the consumption of alkalinity, causing a significant drop in alkalinity. Normally, the VFA:alkalinity ratio is used to evaluate reactor stability, with a ratio below 0.3 to 0.4 indicating a stable operating reactor (Hampannavar & Shivayogimath, 2010; Borja et al. 2004). The VFA:alkalinity ratio was always below 0.3 but it increased to above 0.5 at OLR of 9 kg COD/m<sup>3</sup>, indicating instability.

#### 4.3.16 Effect of OLR on biomass density

Determining the amount of biomass in the reactor and in the effluent is important for two major reasons. Firstly, the microbial mass in the reactor is responsible for substrate conversion and maintaining their density is very important. Secondly, the amount of biomass in the effluent can be used as an indication of microbial washout capacity. Moreover, information about biomass in effluent can be used when designing a post-treatment facility.

Figure 41 shows the amount of biomass in the reactor and in the effluent where it was observed that the amount of biomass (g VSS/L) in the reactor and in the effluent increased with an increase in OLR. However, the amount of biomass expressed as g VSS/g feed COD.d decreased with an increase in OLR in the reactor while it was always almost negligible for the effluent. The wide difference in the amount of biomass in the reactor from that in the effluent indicates biomass retention in the reactor, which can be attributed to zeolite, which is a good biomass

support. A further comparative study was conducted using abattoir wastewater to analyse biodegradability of aromatic compounds in such wastes (Appendix B). It was shown that COD reduction was influenced by the degree of mixing.

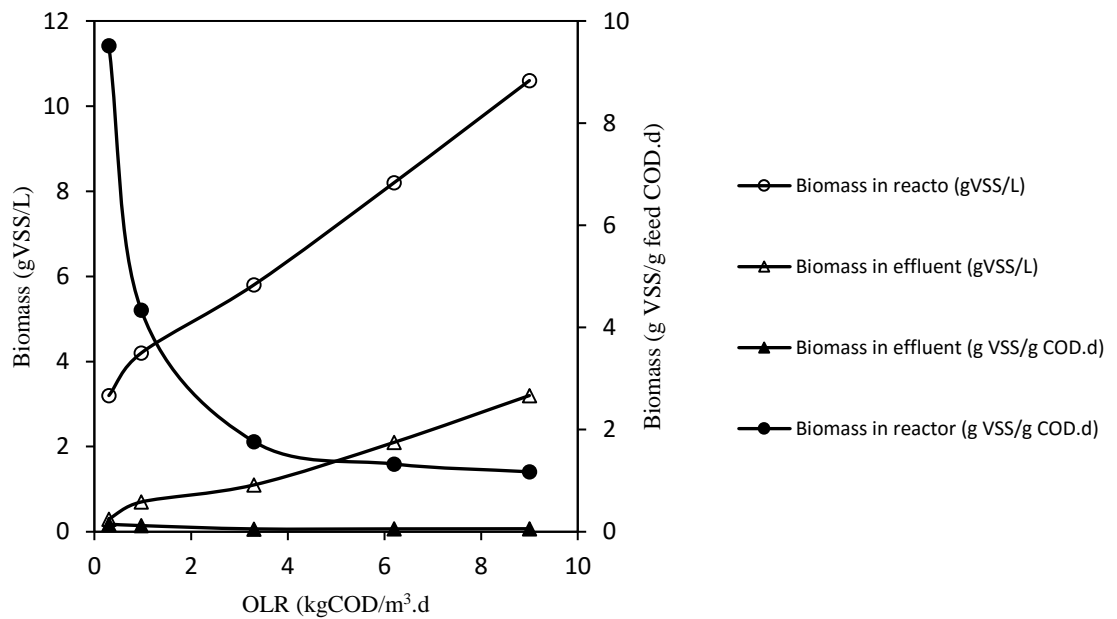


**Figure 41: Effect of OLR on microbial density in the reactor and in the effluent**

#### 4.4 Conclusion

The kinetics of a fluidized bed anaerobic digester treating distillery effluent was evaluated. Degradation in the reactor followed first-order rate kinetics and the recalcitrant component of the effluent was determined to be ~10% TOC of the feed. The amount of biorecalcitrant organic compounds suggested that a post-treatment method is required. The biorecalcitrant compounds were found to be the major colour-causing compounds in distillery effluent. This was because AD was ineffective in colour reduction despite a superior TOC reduction. The bioreactor was found to be stable when operating at an OLR of below 6 kg COD/m<sup>3</sup>d; above this, VFAs accumulated in the reactor. The zeolite applied in the reactor was very effective in biomass retention as the sludge retention time was 2.5 higher than the HRT. The maximum growth rate of the microorganisms was 0.136 d<sup>-1</sup> and the biomass yield was 0.4658 g/g. The microorganisms' decay coefficient of 0.03 was an indication that the bioreactor effluent needed a settling tank to remove suspended biomass if photocatalysis is to be applied as a preferred post-treatment method.

#### 4.5 References

- Acharya, B.K., Mohana, S. & Madamwar, D. (2008). Anaerobic treatment of distillery spent wash: A study on upflow anaerobic fixed film bioreactor. *Bioresource Technology*, 99, 4621–6.
- Aiyuk, S., Forrez, I., Lieven, D.K., Van Haandel, A. & Verstraete, W. (2006). Anaerobic and complementary treatment of domestic sewage in regions with hot climates: A review. *Bioresource Technology*, 97, 2225–41.

- Andalib, M., Hafez, H., Elbeshbishy, E., Nakhla, G. & Zhu, J. (2012). Treatment of thin stillage in a high-rate anaerobic fluidized bed bioreactor (AFBR). *Bioresource Technology*, 121, 411–8.
- Borja, R. (2001). Performance evaluation of a mesophilic anaerobic fluidized-bed reactor treating wastewater derived from the production of proteins from extracted sunflower flour. *Bioresource Technology*, 76, 45–52.
- Borja, R., Gonzalez, E., Raposo, F., Millan, F. & Martin, A. (2002). Kinetic analysis of the psychrophilic anaerobic digestion of wastewater derived from the production of proteins from extracted sunflower flour. *Journal of Agricultural and Food Chemistry*, 50, 4628–4633.
- Borja, R., Rincón, B., Raposo, F., Domínguez, J.R., Millán, F. & Martín, A. (2004). Mesophilic anaerobic digestion in a fluidised-bed reactor of wastewater from the production of protein isolates from chickpea flour. *Process Biochemistry*, 39, 1913–1921.
- Cardinali-Rezende, J. et al. (2013). Organic loading rate and food-to-microorganism ratio shape prokaryotic diversity in a demo-scale up-flow anaerobic sludge blanket reactor treating domestic wastewater. *Antonie van Leeuwenhoek, International Journal of General and Molecular Microbiology*, 104, 993–1003.
- Enitan, A.M. & Adeyemo, J. (2014). Estimation of bio-kinetic coefficients for treatment of brewery wastewater, *International Journal of Environmental, Chemical, Ecological, Geological and Geophysical Engineering*, 8, 400–404.
- Fernández, N. et al. (2008). Performance evaluation of an anaerobic fluidized bed reactor with natural zeolite as support material when treating high-strength distillery wastewater. *Renewable Energy*, 33, 2458–2466.
- Hafez, A.I., Khedr, M.A. & Osman, R.M. (2012). Flax retting wastewater: Part 1: Anaerobic treatment by using UASB reactor, *Natural Resources*, 2012, 3, 191–200.
- Hampannavar, U. & Shivayogimath, C. (2010). Anaerobic treatment of sugar industry wastewater by upflow anaerobic. *International Journal of Environmental Science and Technology*, 1, 631–639.
- Jaafari, J., Mesdaghinia, A., Nabizadeh, R. & Hoseini, M. (2014). Environmental health influence of upflow velocity on performance and biofilm characteristics of anaerobic fluidized bed reactor (AFBR) in treating high-strength wastewater, *Journal of Environmental Health Science and Engineering*, 1–10.
- Kalavathi, D., Uma, L. & Subramanian, G. (2001). Degradation and metabolization of the pigment-melanoidin in distillery effluent by the marine cyanobacterium *Oscillatoria boryana* BDU 92181. *Enzyme and Microbial Technology*, 29, 246–251.
- Montalvo, S. et al. (2012). Application of natural zeolites in anaerobic digestion processes: A review. *Applied Clay Science*, 58, 125–133.
- Ng, H.Y., Tan, T.W. & Ong, S.L. (2006). Membrane fouling of submerged membrane bioreactors: Impact of mean cell residence time and the contributing factors. *Environmental Science & Technology*, 40, 2706–2713.

- Nweke, C., Igbokwe, P. & Nwabanne, J. (2014). Kinetics of batch anaerobic digestion of vegetable oil wastewater. *Open Journal of Water Pollution and Treatment*, 2014, 1–10.
- Perez, M., Romero, L.I. & Sales, D. (2001). Organic matter degradation kinetics in an anaerobic thermophilic fluidised bed bioreactor. *Anaerobe*, 7, 25–35.
- Rabah, F.K.J. & Dahab, M.F. (2004). Biofilm and biomass characteristics in high-performance fluidized-bed biofilm reactors. *Water Research*, 38, 4262–4270.
- Rincón, B. et al. (2006). Kinetic models of an anaerobic bioreactor for restoring wastewater generated by industrial chickpea protein production. *International Biodeterioration and Biodegradation*, 57, 114–120.
- Sankaran, K., Premalatha, M., Vijayasekaran, M. & Somasundaram, V.T. (2014). Distillery wastewater treatment through anaerobic digestion and phycoremediation: A green industrial approach. *Renewable and Sustainable Energy Reviews*, 37, 634–643.
- Satyawali, Y. & Balakrishnan, M. (2008). Wastewater treatment in molasses-based alcohol distilleries for COD and color removal: A review. *Journal of Environmental Management*, 86, 481–97.
- Senturk, E., Ýnce, M. & Onkal Engin, G. (2013). Assessment of kinetic parameters for thermophilic anaerobic contact reactor treating food-processing wastewater. *International Journal of Environmental Research*, 7, 293–302.
- Wang, H.-Y., Qian, H. & Yao, W.-R. (2011). Melanoidins produced by the Maillard reaction: Structure and biological activity. *Food Chemistry*, 128, 573–584.
- Wang, J.-L. & Wu, L.-B. (2004). Wastewater treatment in a hybrid biological reactor (HBR): Nitrification characteristics. *Biomedical and Environmental Sciences*, 17, 373–379.
- Yu, L., Wensel, P., Ma, J. & Chen, S. (2013). Mathematical modeling in anaerobic digestion (AD). *Journal of Bioremediation and Biodegradation*, S4, 12.

## **5 COMBINED AD AND PHOTOCATALYTIC TREATMENT OF DISTILLERY EFFLUENT IN BATCH FBR**

### **5.1 Introduction**

The AD process is effective in converting huge amounts of organic load of distillery effluent into biomethane. However, it is ineffective in colour reduction (Satyawali & Balakrishnan, 2008) due to the presence of colour-causing biorecalcitrant melanoidins (Wang et al., 2011). Therefore, different post-treatment methods for biomethanated distillery effluent have been proposed for colour removal. Physico-chemical methods such as coagulation (Arimi et al., 2015; Chaudhari et al., 2007), adsorption (Onyango et al., 2011), catalytic thermolysis and wet oxidation (Chaudhari et al., 2005) have been applied with varying degrees of success.

Recently, studies have been carried out on AOPs such as the application of photodegradation in the treatment of distillery effluent and good colour removal has been reported (Apollo et al., 2014b; Vineetha et al., 2013). Photodegradation has an advantage in that it can rapidly degrade organic contaminants to mineralisation without producing sludge. Even though photodegradation can be used as pre-treatment before the AD process to enhance the biodegradability of recalcitrant compounds (Apollo et al., 2014a), this step is not recommended for wastewater with a high proportion of biodegradable components with traces of biorecalcitrant components such as distillery effluent. This is because biodegradable components will compete with recalcitrant compounds during photodegradation, leading to unnecessary consumption of chemicals and longer irradiation times (Oller et al., 2011). In such a case, an initial step involving biological treatment to remove biodegradable components followed by an AOP post-treatment as a polishing step is more economical due to reduced energy and chemical consumption (Hörsch et al., 2003; Vidal et al., 2004). Moreover, photodegradation was found not to significantly improve biodegradability of distillery effluent towards anaerobes (Apollo et al., 2013). It is therefore more effective to apply photodegradation as a post-treatment to AD pre-treated distillery effluent.

The application of FBRs in a combined AD and photodegradation process can result in better pollution removal due to the good mixing attained by FBRs, which promotes mass transfer and thereby increases the reaction rate. Due to the achievable fast reaction rates, chemical dose and the energy requirement of the UV, photodegradation could be reduced while the bioenergy from the AD process could be enhanced. This may result in improvement on the overall efficiency of the integrated process. In this study, the efficiency of FBRs in a combined AD and photodegradation process was investigated for TOC and colour reduction when treating distillery effluent.

### **5.2 Methodology**

#### **5.2.1 Materials**

Distillery effluent with the characteristics listed in Table 12 was outsourced from a local treatment plant and stored in a fridge at 4°C before use. Titanium dioxide catalyst, Degussa P25, was purchased from Acros Organics.

**Table 12: Characteristics of distillery effluent**

Parameter	Value
COD (mg/L)	2600 ± 250
TOC (mg/L)	1807 ± 120
TSS (mg/L)	43 ± 5
Total sulphates (mg/L)	249 ± 21
Total phosphates (mg/L)	35 ± 4
pH	5.5

### 5.2.2 Experimental setup

An anaerobic fluidized bed reactor (AFBR) and fluidized bed annular photoreactor assembled as shown in Figure 42 were used. The dimensions of the anaerobic digester were 760 mm height and 118 mm in diameter, resulting in a total volume of 8.3 L and a working volume of 6 L. The volume of the photoreactor was 0.45 L. The detailed photoreactor description can be found in our previous work (Apollo et al., 2013).

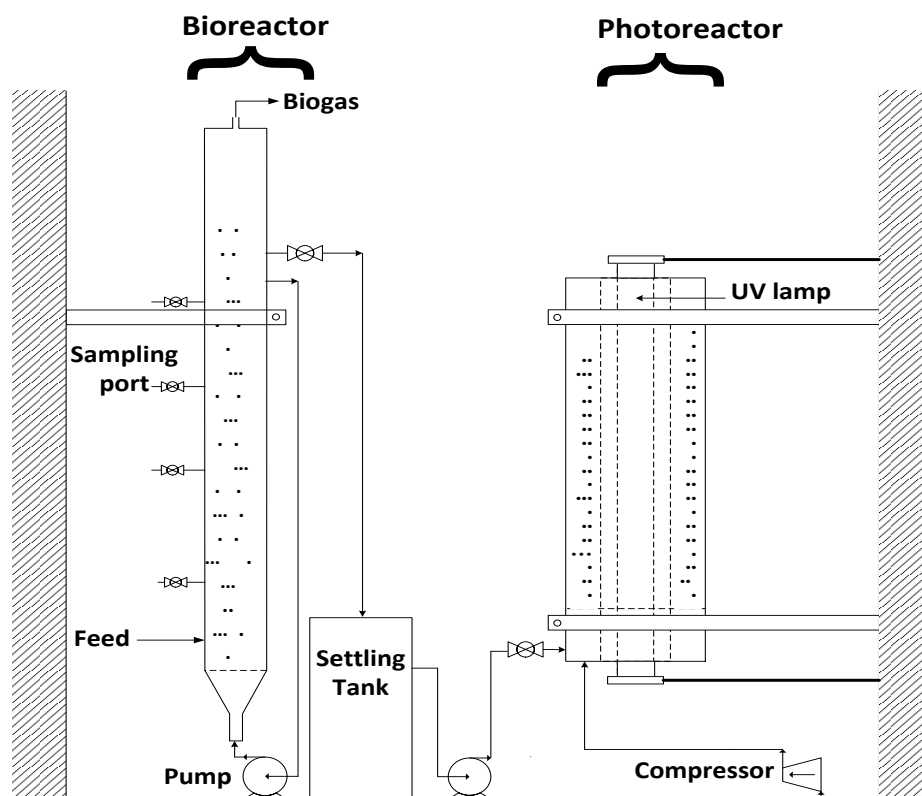


**Figure 42: Experimental setup for the integrated AD and photodegradation**

Fluidization in the AD reactor was achieved by a centrifugal pump (Foras Veronilla, Italy) that was used to circulate the effluent in the reactor while fluidization in the photoreactor was achieved by air from a compressor (Jun-Air OF302). The effluent from AFBR was fed into a settling tank to remove suspended solids, which resulted from flocs formed by biomass in the bioreactor. Prior to photodegradation, the sample was further centrifuged and the pH was lowered to 4 using 0.1 M H<sub>2</sub>SO<sub>4</sub> solution, which was the best pH for photodegradation of distillery effluent (Apollo et al., 2014b). For the photoreactor, the catalyst and wastewater were thoroughly mixed using a magnetic stirrer to ensure uniform catalyst distribution. The mixture was then fed into the reactor using a peristaltic pump. Air from the compressor was passed upward through a column of distillery wastewater containing suspended TiO<sub>2</sub> catalyst via a flow distributor compartment at the bottom of the reactor.

### 5.2.3 Experimental procedure

The optimum superficial gas velocity or liquid velocity for the photoreactor and bioreactor, respectively, were determined from hydrodynamic studies. However, preliminary experiments were carried out to find the best operating conditions such as the amount of TiO<sub>2</sub> in the composite catalyst, catalyst loading and hydrogen peroxide dose as indicated in Table 13.

**Table 13: Operating parameters for the photoreactor and AD reactor**

Photoreactor		Biodigester	
Parameter	Value	Parameter	Value
Average catalyst size	57 μm	Zeolite particle size	150–300 μm
TiO <sub>2</sub> /silica ratio of catalyst	10–95%	Zeolite amount	50 g
Catalyst amount	0.5–5 g/L	Superficial liquid velocity (U <sub>L</sub> )	0.6 cm/s
Superficial air velocity (U <sub>g</sub> )	0.92 cm/s	Bed height at U <sub>L</sub>	500 mm
H <sub>2</sub> O <sub>2</sub> dosage	1.2–19.6 mM		

After establishing these conditions, firstly, the anaerobic process was conducted in batch mode at 37°C and biogas was collected by the water displacement method. The biogas was analysed for methane content using a gas chromatograph. The anaerobically treated effluent was centrifuged and then fed into the photoreactor for further colour and TOC reduction. The electrical energy efficiency of the photodegradation process was analysed using electrical energy per order (EEO). The EEO (kWhm<sup>-3</sup>order<sup>-1</sup>) is defined as the electrical energy (kWh) required to degrade a contaminant by one order of magnitude in 1.0 m<sup>3</sup> water, which is expressed as (Shu et al., 2013):

$$EEO = \frac{P t}{V \log\left(\frac{C_i}{C_f}\right)} \quad (46)$$

where  $P$  is the lamp power (kW),  $t$  is the irradiation time (hours),  $V$  is the volume (m<sup>3</sup>) of water treated, and  $C_i$  and  $C_f$  are the initial and final concentrations of the target contaminant. The energy consumption of the photodegradation process was compared with the energy produced by the AD process.

### 5.2.4 Experimental analysis

The performance of each treatment process was monitored by analysing aliquot samples after a specific period of treatment. For AD, samples were centrifuged before analysis while for photodegradation process, samples were filtered using a 0.45  $\mu\text{m}$  filter syringe. The TOC was analysed using a TOC analyser (Teledyne Tekmar), and sulphates, nitrates and ammonium were analysed using ion chromatography (882 Compact IC Plus fitted with an 863 Compact auto-sampler), gas was analysed using a gas chromatograph (Trace 1310 gas chromatograph) fitted with a thermal conductivity detector, while colour was analysed using a UV-Vis spectrophotometer (T80 + UV/VIS Spectrophotometer, PG instruments Ltd). Alkalinity, VFAs, COD and BOD<sub>5</sub> were analysed per standard methods. According to the standard method for wastewater analysis, VFAs and alkalinity were analysed by titration (Lahav & Morgan, 2004) while COD was analysed by nano-colour calorimeter after digestion using potassium permanganate.

## 5.3 Results and Discussion

### 5.3.1 TOC, sulphates and colour reduction

After the reactor had acclimatised/stabilised, its efficiency in TOC, colour and sulphates reduction was evaluated. A high TOC reduction of 78% was achieved after seven days with a corresponding colour reduction of 41% (Figure 43). The AD process in FBRs has been reported as an efficient treatment technology for TOC reduction when treating distillery effluent because the major component of distillery effluent is biodegradable (Satyawali & Balakrishnan, 2008). Despite containing large amounts of biodegradable organic substances, distillery effluent also contains melanoidins, which are biorecalcitrant. Melanoidins form about 2% of distillery effluent and are responsible for the intense dark-brown colour (Kalavathi et al., 2001). Due to the biorecalcitrant nature of melanoidin, AD treatment of distillery effluent has been reported to result in low colour reduction (Satyawali & Balakrishnan, 2008).

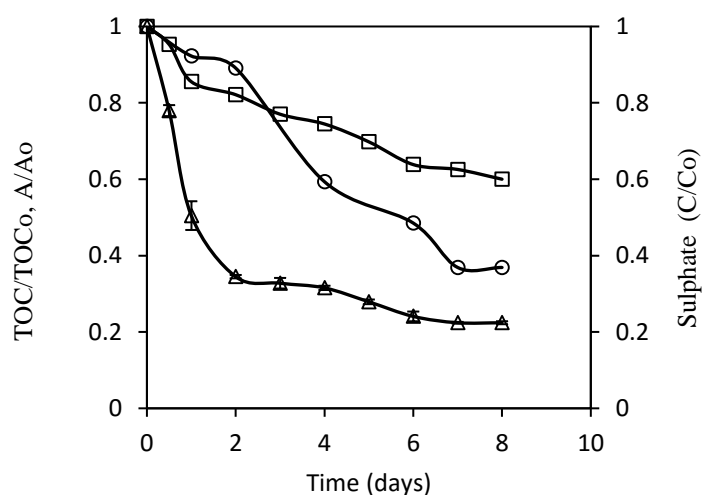
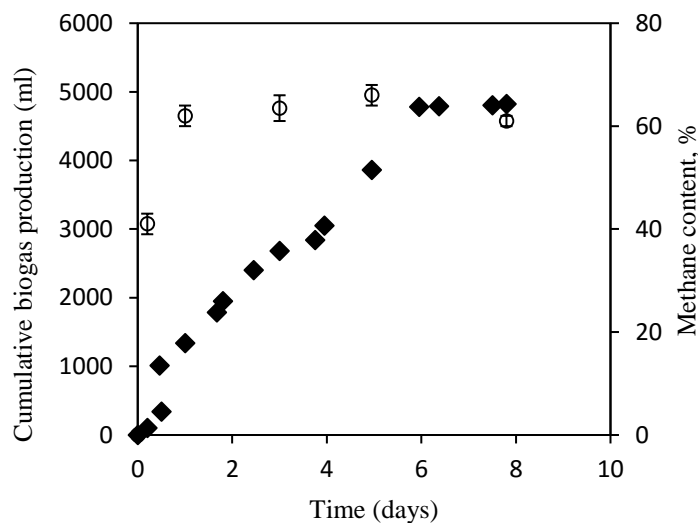


Figure 43: Colour, TOC and sulphate reduction during AD: TOC ( $\Delta$ ), colour ( $\square$ ), sulphates ( $\circ$ )

Sulphate reduction was also observed during the AD process. In anaerobic conditions, sulphate-reducing bacteria use sulphate as a terminal electron acceptor to degrade organic compounds and hydrogen. Therefore, in the presence of sulphates, methanogens compete with sulphate-reducing bacteria for available organic substrates. This competition may result in low methane production in cases where sulphate-rich wastewater is treated as hydrogen sulphide will be produced (Acharya et al., 2008). In this study, the methane content of biogas produced (Figure 44) was within the expected range, suggesting that substrate utilisation by methanogens predominated that of sulphate-reducing bacteria. Under stable conditions and when the sulphate concentration is much lower than TOC, sulphate reduction can mostly be due to the use as nutrients by microorganisms (Vijayaraghavan & Ramanujam, 2000).

### 5.3.2 Biogas production and methane yield

Figure 44 shows that the AD produced about 4.82 L of biogas after seven days. This corresponded to a biogas production rate of 0.57 L of biogas/g TOC. The methane content of the biogas produced within the first day was 41%; its production increased with time reaching a maximum of 66% on day 5. The mean methane production was therefore calculated as ~0.35 L CH<sub>4</sub>/g TOC while the value in literature varies between 0.29 CH<sub>4</sub>/g and 0.4 CH<sub>4</sub>/g (Fernández et al., 2008; Zupancic et al., 2007).



**Figure 44: Biogas and methane production during the anaerobic process: biogas production (■), methane yield (○)**

The low methane content of the biogas during the onset of the anaerobic process could have been due to the acclimatisation of microorganisms to the fresh organic load. Also, it could have been because acidogenesis proceeded faster than methanogenesis at this stage leading to the production of carbon dioxide. However, by day 2, stability was achieved between acidogenesis and methanogenesis; thus acidogenesis products were consumed in the methanogenesis process producing CH<sub>4</sub>. From day 6, biogas production reduced remarkably and nearly came to a stop. The reduction in biogas production during this period could have been because most organic carbon had been removed, therefore little substrate was available for the microorganisms.

### 5.3.3 Alkalinity and pH

Alkalinity and pH analysis showed that there was adequate buffering in the reactor (Table 14). The AD process is pH sensitive with an optimum operational pH of about 7 (Acharya et al., 2008). Stable operating bioreactors often have the ability for self-buffering since the acid produced by acidogenesis is neutralised by methanogenesis, which is an alkalisng step as it consumes hydrogen and  $H_3O^+$  ions (Patel & Madamwar, 2000).

**Table 14: Alkalinity and pH during the AD**

Time (days)	0	1	2	4	6	7	8
pH	7.11	7.18	7.29	7.44	7.58	7.62	7.62
Alkalinity (mg/L)	4760	4114	4100	4160	4060	4100	4100

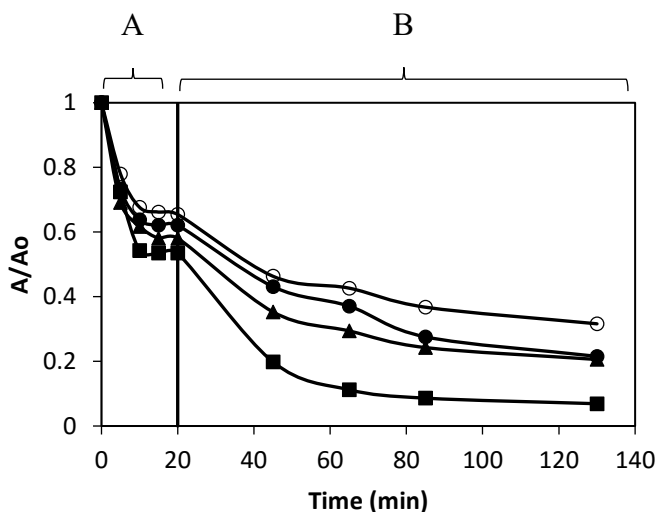
### 5.3.4 Photodegradation of distillery effluent

The efficiency of photodegradation on the decolourisation of the distillery effluent was studied. This was necessary because AD was not effective in colour removal. Firstly, various factors that affect photodegradation were investigated to establish the best operating conditions. Secondly, the possible mechanism of melanoidin photodegradation was investigated.

### 5.3.5 Catalyst loading and catalyst composition

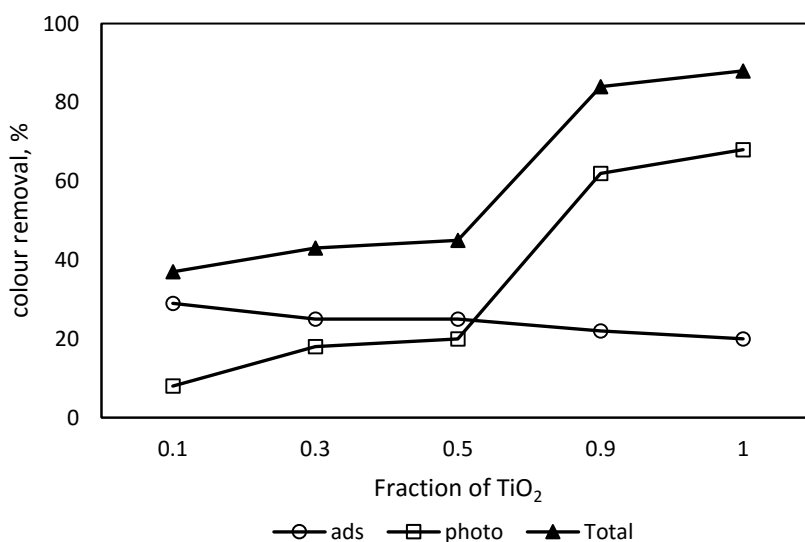
The experiments were conducted with catalyst loading ranging from 0.5 g/L to 5 g/L while keeping other parameters constant (air velocity of 0.9 cm/s and initial effluent concentration of 120 mg/L TOC). Initially, adsorption studies were conducted in the dark before photodegradation. Generally, adsorption concentrates the pollutants on the catalyst surface, thus facilitating the photodegradation process. In Figure 45, the adsorption equilibrium was achieved after 20 minutes for all catalyst loadings. However, catalyst loading above optimum value led to a reduction in adsorption due to hindered mass transfer. Similarly, the photodegradation efficiency increased when catalyst loading was increased from 0.5 g/L to 2 g/L, after which there was a decrease in the photodegradation efficiency when the catalyst loading was increased to 5 g/L. This may be attributed to the light scattering effect caused by the catalyst at high loading, leading to a reduction in reaction rate. Moreover, at very high catalyst loading, mass transfer is reduced due to the increased viscosity of the solution (Zhu et al., 2011; Nawi et al., 2012).

Silica materials such as silica gels have commonly been applied as photocatalyst supports to facilitate the separation of the photocatalyst after the photocatalytic reaction in aqueous systems due to the high sedimentation ability of silica gel (Shan et al., 2010). Moreover, silica gel has become famous for supporting  $TiO_2$  as it is an adsorbent; therefore, it concentrates the pollutants on the catalyst surface and it also allows penetration of photons to the catalyst due to its transparent nature (Lim & Kim, 2005).



**Figure 45: Effect of catalyst loading on adsorption (A) and photodegradation (B) using 50% wt/wt  $\text{TiO}_2/\text{SiO}_2$  composite catalyst 5 g/L (●), 2 g/L (■), 1 g/L (▲), 0.5 g/L (○)**

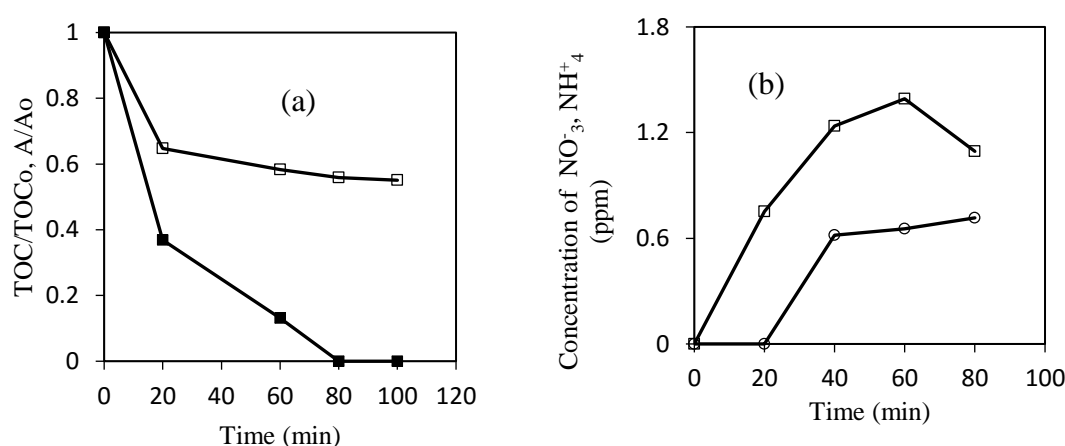
In Figure 46, colour removal by the photodegradation process increased with an increase in the amount of  $\text{TiO}_2$  in the  $\text{TiO}_2/\text{silica}$  composite catalyst. However, removal by adsorption decreased with an increase in  $\text{TiO}_2$  composition, suggesting that the  $\text{SiO}_2$  had a higher adsorption ability than the  $\text{TiO}_2$ . It has been reported that an increase in the amount of  $\text{TiO}_2$  in the composite leads to a reduction in the surface area and pore size of the silica gel, therefore, resulting in a reduction in adsorption (Lim & Kim, 2005; Shan et al., 2010). Generally, silica gel is mainly used to bind  $\text{TiO}_2$  to facilitate post-treatment separation, which can be expensive if  $\text{TiO}_2$  is used as slurry since it has poor settling ability.



**Figure 46: Effect of catalyst composition on adsorption (○), photodegradation (□) combined adsorption-photodegradation (▲) using catalyst loading of 2 g/L**

### 5.3.6 Colour removal mechanism via $\text{NO}_3^-$ and $\text{NH}_4^+$ evolution during photocatalysis

More insight into the degradation of organic compounds such as melanoidins, which have heteroatoms, can be obtained by monitoring the formation of inorganic ions formed in solution due to the degradation of the associated heteroatoms (Alberici et al., 2001). Melanoidins in distillery effluent are formed because of a reaction between amino acids and glucose; therefore, melanoidins contain a nitrogen atom as heteroatom (Wang et al., 2011). In Figure 47a, the colour removal efficiency by the photodegradation was higher than that of TOC reduction. This suggests that photocatalysis degraded the colour-causing bonds (chromophores) of the melanoidin faster than organic carbon mineralisation. Since the colour in melanoidin is caused by C–N and C=C bonds (Chandra et al., 2008), it is therefore inferred that the photogenerated radicals attacked the chromophores faster than the C–C bond due to the highly reactive centres in the chromophore compared with those in C–C bonds.



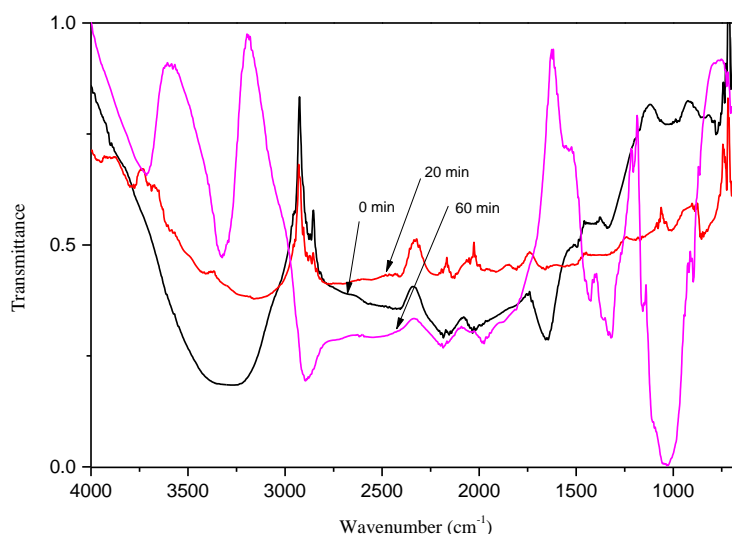
**Figure 47: (a) Colour (■) and TOC (□) reduction; (b)  $\text{NO}_3^-$  (○) and  $\text{NH}_4^+$  (□) formation during photodegradation**

Figure 47 shows the production of nitrate and ammonium during photodegradation indicating the mineralisation of nitrogen in the melanoidin structure, which led to colour reduction. Photocatalytic degradation of nitrogen-containing organic compounds like melanoidins depends largely on the position and oxidation state of the nitrogen atom within the organic structure (Jing et al., 2011). In the degradation of such compounds,  $\text{NH}_4^+$  and  $\text{NO}_3^-$  are produced in different proportions depending on the degradation pathway. If a nitrogen atom exists in a high oxidation state, the nitrogen constituent degrades through a reductive pathway and  $\text{NH}_4^+$  is formed from unstable intermediates. However, if the initial oxidation state of nitrogen in organic compound is low, the nitrogen constituent is degraded through the initial oxidation step to produce  $\text{NO}_3^-$  (Jing et al., 2011). In this study, more  $\text{NH}_4^+$  evolved than  $\text{NO}_3^-$ , indicating that more nitrogen atoms in melanoidin structure had a high oxidation state, and therefore they were degraded through the reductive pathway.

### 5.3.7 FTIR analysis of the photodegradation process

To further analyse the effect of photodegradation in breaking down the organic molecules in the distillery effluent, the photodegraded samples were analysed using FTIR after a 20-minute interval of UV irradiation. The appearance and disappearance of some peaks and the shift in

peaks are indications of degradation. In Figure 48, the FTIR spectrum of melanoidin shows peaks mostly at  $3400\text{ cm}^{-1}$  due to the stretching vibration of OH and  $\text{NH}_2$  bonds, at  $2850\text{ cm}^{-1}$  due to CH stretching vibration, and at  $1620\text{ cm}^{-1}$  due to amide (Dolphen & Thiravetyan, 2011; Kim et al., 1985; Olennikov & Tankhaeva, 2012).



**Figure 48: FTIR spectra of distillery effluent at different times of photodegradation**

Generally, the peak at  $3400\text{ cm}^{-1}$  reduced after 60 minutes of irradiation while the peak at  $2850\text{ cm}^{-1}$  increased suggesting a likely reduction in OH and/or  $\text{NH}_2$  groups and an increase in CH groups, respectively. The absorption due to amide at  $1620\text{ cm}^{-1}$  (Kim et al., 1985) also decreased during photodegradation. The increase in the C–H peak with a decrease in  $\text{NH}_2$  or amide peaks may explain the high colour reduction with a corresponding low TOC reduction recorded during photodegradation since colour in melanoidin is caused by C–N and C=C bonds (Chandra et al., 2008). The emerging of absorbance peaks at  $1250\text{ cm}^{-1}$  and  $1050\text{ cm}^{-1}$  may indicate C–H deformation and C–O stretching, respectively (Dolphen & Thiravetyan, 2011; Olennikov & Tankhaeva, 2012). It was observed that photodegradation was effective in colour reduction but was inefficient in TOC reduction. However, AD was effective in TOC reduction but performed poorly in colour reduction. Therefore, integration of the two processes is necessary for both colour and TOC reduction. From these observations, AD treatment can be applied in the initial step to remove the TOC with bioenergy recovery while photodegradation can be employed as the final step to remove the colour resulting from low concentration of biorecalcitrant compounds (melanoidins).

### 5.3.8 Effect of hydrogen peroxide addition

Hydrogen peroxide improves the photodegradation process as it acts as an additional source of the hydroxyl radical that degrades organic contaminants. However, it is important to determine the most suitable amount of hydrogen peroxide required to achieve optimum degradation as a very low hydrogen peroxide concentration does not improve photodegradation as it generates insignificantly low amounts of peroxide radicals. In contrast, at very high hydrogen peroxide concentrations, the reaction is retarded due to the scavenging effects of the excess peroxide radicals produced (Huang et al., 2008). In this study, colour removal efficiency was used to

determine the optimal hydrogen peroxide dosage for the reactor used under the prevailing conditions of 2 g/L, 95% TiO<sub>2</sub>/silica composite catalyst and 120 mg/L TOC of the wastewater.

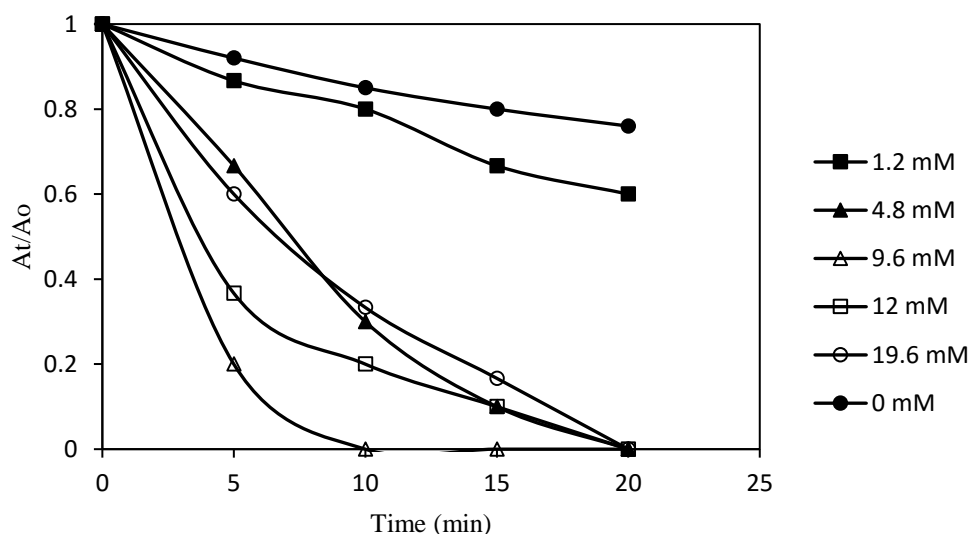


**Figure 49: Effect of hydrogen peroxide dose on colour reduction of distillery effluent**

In Figure 49, it was found that the optimal hydrogen peroxide dose was 9.6 mM, which could remove total colour within 10 minutes of irradiation. The optimal hydrogen peroxide dose was used to study TOC reduction under similar reactor conditions. In Figure 50 it was observed that a TOC reduction of 81% was achieved using hydrogen peroxide while without adding hydrogen peroxide only 31% of TOC was removed. Hydrogen peroxide and UV irradiation alone achieved TOC reduction of about 20%. The increase in TOC reduction efficiency by the TiO<sub>2</sub>/silica catalyst/UV/H<sub>2</sub>O<sub>2</sub> system compared with that of the TiO<sub>2</sub>/silica catalyst/UV and UV/H<sub>2</sub>O<sub>2</sub> is an indication that hydrogen peroxide increased the number of peroxide radicals produced by the TiO<sub>2</sub>/silica catalyst/system resulting in improved degradation efficiency. However, TOC reduction was much slower than colour reduction, indicating that photodegradation is most suitable for colour reduction.

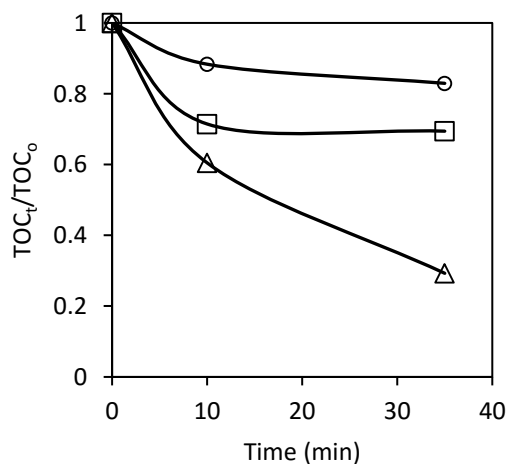


**Figure 50: Effect of hydrogen peroxide on TOC reduction (○) UV/H<sub>2</sub>O<sub>2</sub> (□) TiO<sub>2</sub>/silica catalyst/UV (Δ) TiO<sub>2</sub>/silica catalyst/UV/H<sub>2</sub>O<sub>2</sub>**

### 5.3.9 Photodegradation post-treatment of AD pre-treated effluent

The AD treated effluent, though it had low TOC, was still very dark as the AD process achieved only 41% colour reduction. Therefore, even though the AD process is efficient in TOC reduction, it cannot be applied as a stand-alone process for distillery effluent treatment; a post-treatment method is necessary (Travieso et al., 2008). The anaerobically treated effluent from the AD reactor was centrifuged and then treated by UV photodegradation since photodegradation is very effective in colour reduction. Due to the intense dark colour of the anaerobically digested effluent, dilution may be required for effective colour reduction during UV post-treatment depending on the photoreactor design. To study the effect of dilution of the AD effluent on the ensued photodegradation process, the dilution factor was calculated as;

$$DF = \frac{V_e + V_w}{V_e} \quad (47)$$

where  $DF$  is the dilution factor,  $V_e$  is the effluent volume (L), and  $V_w$  is the volume of dilution water (L). From the equation, a  $DF$  value of 1 indicates no dilution since  $V_w = 0$ . Colour and TOC reduction rates increased with an increase in dilution (Figure 51a and Figure 51b) because dilution reduced the colour intensity leading to a reduction in light attenuation effect caused by the dark colour. Dilution is generally not an encouraged approach; however; in this case, part of the treated effluent can be used for dilution to reduce the water requirement of the process.

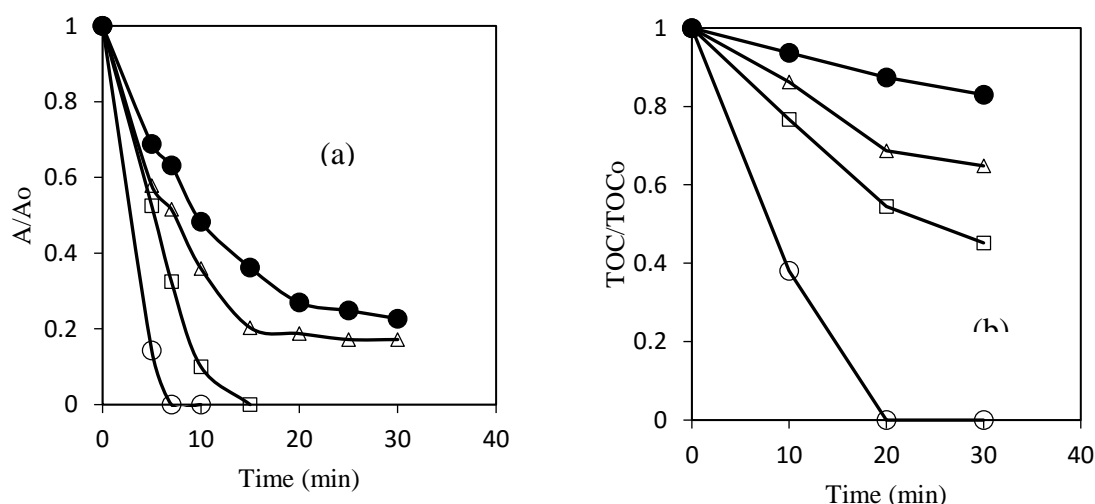


**Figure 51: Effect of dilution on colour and TOC reduction during photodegradation: (a) colour (b) TOC; x10 v/v (○), x3.3 v/v (□), x2 v/v (Δ), x1v/v (●)**

Irrespective of the dilution, colour removal was always higher than TOC reduction. This could be an indication that the UV radiation process is more rapid in cleaving the chromophore bonds of melanoidin but that it is slower in mineralisation of the melanoidins. Photodegradation has been reported to result in better colour reduction but low TOC reduction when treating distillery effluent (Vineetha et al., 2013). It was also observed that photodegradation could remove 77% and 11% colour and TOC, respectively, when treating undiluted (x1 v/v) effluent.

### 5.3.10 Combined AD and UV photodegradation

As mentioned earlier, AD was found to perform better in TOC reduction while it had a low performance on colour reduction due to the biorecalcitrant melanoidins in distillery effluent.

However, photodegradation was found to be effective in colour reduction but performed low in TOC reduction. A combined treatment in which photodegradation was used as post-treatment for the AD treated effluent was found to be very effective in both colour and TOC reduction as shown in Figure 52. It was found that AD as a first treatment step removed 78% of TOC and 41% of colour; photodegradation post-treatment resulted in additional 5% TOC reduction and additional 46% colour reduction of the original effluent. Therefore, the combined process resulted in an overall efficiency of 83% and 87% TOC and colour reduction, respectively.

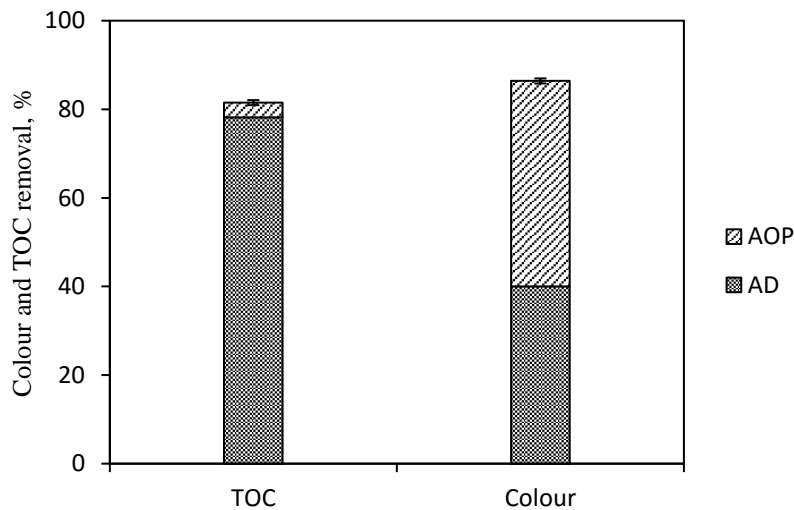


**Figure 52: Overall performance of the combined AD and UV photodegradation process after seven days of AD and 30 minutes of photodegradation**

Table 15 summarises the pollution load removal by each step and the final effluent concentration. The AD process produces energy by breaking down organic molecules while UV photodegradation consumes energy to degrade organic molecules. Thus, it is necessary to do an energy analysis of the integrated process to determine the specific energy demand.

**Table 15: Characteristics of wastewater after two-stage treatment**

Parameter	Before treatment	After initial AD treatment	After UV post-treatment
COD (mg/L)	2600	728	650
TOC (mg/L)	1807	405	325
BOD <sub>5</sub> (mg/L)	1079	162	122
Total suspended solids (mg/L)	43	–	–
Total sulphates (mg/L)	249	92	92
Total phosphates (mg/L)	35	7.5	7.5
pH	5.5	7.62	4.4
Colour (abs at 475 nm)	0.235	0.141	0.032

### 5.3.11 Energy analysis

The specific energy (kJ/g TOC) production rate of AD and the specific energy consumption rate of UV photodegradation were determined. In the UV case, the energy required by the lamp to degrade unit mass of pollutant was considered. In this study, the average methane production of the AD process was 0.35 L/g TOC removed, which had an energy content of 14.2 kJ/g TOC removed, taking the reported energy value of methane as 38 mJ/m<sup>3</sup> (Duerr et al., 2007).

Methane production from brewery slurry or molasses effluent has been reported to be in the range of 0.23 L CH<sub>4</sub>/g COD to 0.42 L CH<sub>4</sub>/g COD (Jiménez et al., 2004; Zupancic et al., 2007) resulting in energy of 8.74 kJ/g COD to 15.96 kJ/g COD. The specific energy consumption for photodegradation was found to be about 900 kJ/g TOC, leading to colour reduction of between 52% and 100% depending on dilution (Table 16).

**Table 16: Energy analysis and performance of the combined process**

<b>Dilution factor</b>	<b>×10</b>	<b>×3.3</b>	<b>×2</b>	<b>×1</b>
Colour reduction (%)	100	90	64	52
TOC reduction (%)	62	24	14	6
Energy UV lamp (kJ/g TOC)	970	900	900	1000
AD (kJ/g TOC)	14.2	14.2	14.2	14.2

Table 16 further observed that, unlike colour reduction, the energy requirement of the UV lamp to degrade a unit mass of pollutant was constant and did not depend on dilutions. Dilution only led to a faster reaction rate due to lower concentrations but did not lead to reduction in energy consumption per unit mass of pollutants removed. Considering the faster colour removal rate than TOC reduction rate (Figure 47), colour reduction can consume less energy than TOC reduction. Considering the fact that UV photodegradation post-treatment is mostly for colour reduction since most of the TOC had been removed by the initial AD step, energy analysis for colour reduction is necessary.

### 5.3.12 EEO analysis of the combined process for colour reduction

The EEO is a key scale-up parameter for photodegradation systems at it combines the key design variables (UV radiation time, effluent volume, concentration and the targeted number of orders of magnitude of contaminant concentration to be removed) into a single function. Application of EEO in this work can give an insight into the performance of the integrated AD-UV system in a scaled-up process for colour reduction. The EEO was calculated as shown in Eq. 46. Since the initial anaerobic treatment step had removed 78% and 41% of TOC and colour, respectively, the UV post-treatment was evaluated based on removing a further 75% of colour. In this case, the EEO was calculated for 75% colour reduction. The study was conducted for raw effluent from the bioreactor and for diluted effluent. The electrical energy required to power the UV lamp to treat 1 m<sup>3</sup> effluent to 75% colour reduction was compared with the energy content of the biogas produced in the AD unit (Figure 53). It was found that the energy required to treat 1 m<sup>3</sup> of the effluent almost increased linearly with a reduction in dilution factor.

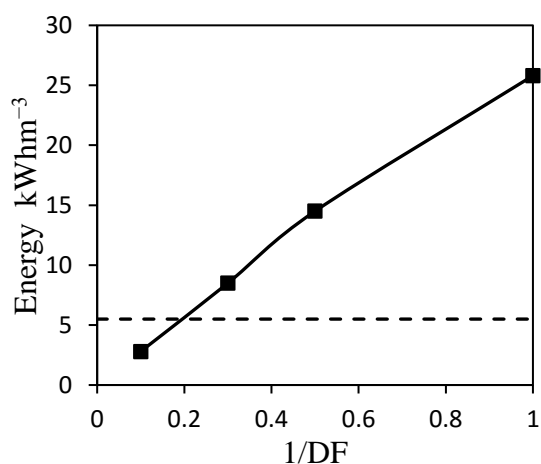


**Figure 53: Electrical energy consumption of the UV lamp at various dilutions (■) and energy content of the biogas produced by the AD process (---)**

Based on biogas production of 4.82 L with an average methane production of 65% recorded, the energy content of the biogas produced was calculated as 5.5 kWhm<sup>-3</sup> of wastewater treated. It was found that at dilutions of 20% v/v and less, the energy produced by the AD system was equivalent or lower than the energy required by the UV lamp to treat the diluted wastewater to a further 75% colour reduction. However, as the dilution factor reduced, more energy was required since more concentrated effluent has a darker colour, which leads to light attenuation in the reactor. Energy analysis further showed that the bioenergy produced could subsidise up to 20% of the energy required by the UV lamp to photodegrade undiluted pre-AD-treated effluent up to 75% colour reduction. Therefore, integrating the two processes has a potential of lowering the operational cost of photodegradation while ensuring effective pollution reduction.

#### 5.4 Conclusion

A study on combined AD and photodegradation treatment of distillery effluent in batch FBRs was carried out. It was found that AD as a single unit was efficient in TOC reduction but not in colour reduction while photodegradation was efficient in colour reduction but not in TOC reduction. However, a combined process resulted in about 85% colour and TOC reduction. During photodegradation, nitrate (NO<sub>3</sub><sup>-</sup>) and ammonium (NH<sub>4</sub><sup>+</sup>) were formed, which indicated the degradation of the biorecalcitrant melanoidins.

Energy analysis showed that AD produced 14.2 kJ/g TOC of energy while the UV lamp consumed 900 kJ/g TOC to further treat biodigested effluent. The EEO analysis showed that the bioenergy produced by AD was equivalent to that required to photodegrade 1 m<sup>3</sup> of pre-digested distillery effluent diluted by 20% to achieve 75% colour reduction. The energy analysis further showed that the bioenergy produced could subsidise up to 20% of energy required by the UV lamp to further photodegrade 1 m<sup>3</sup> undiluted biodigested effluent up to 75% colour reduction. Therefore, AD can subsidise the cost of UV photodegradation when applied combined in the treatment of distillery effluent. However, process optimisation needs to be done to determine the best combination of factors, such as organic load and retention time on overall performance of the integrated process. Furthermore, the performance of a continuously operated integrated process needs to be investigated to better assess the potential of its applicability in large-scale wastewater treatment units.

## 5.5 References

- Acharya, B.K., Mohana, S. & Madamwar, D. (2008). Anaerobic treatment of distillery spent wash: A study on upflow anaerobic fixed film bioreactor. *Bioresource Technology*, 99, 4621–6.
- Alberici, R.M., Canela, M.C., Eberlin, M.N. & Jardim, W.F. (2001). Catalyst deactivation in the gas phase destruction of nitrogen-containing organic compounds using TiO<sub>2</sub>/UV–VIS. *Applied Catalysis B: Environmental*, 30, 389–397.
- Apollo, S., Onyango, M.S. & Ochieng, A. (2013). An integrated anaerobic digestion and UV photocatalytic treatment of distillery wastewater. *Journal of Hazardous Materials*, 261, 435–42.
- Apollo, S., Onyango, M.S. & Ochieng, A. (2014a). Integrated UV photodegradation and anaerobic digestion of textile dye for efficient biogas production using zeolite. *Chemical Engineering Journal*, 245, 241–247.
- Apollo, S., Onyango, M.S. & Ochieng, A. (2014b). UV/H<sub>2</sub>O<sub>2</sub>/TiO<sub>2</sub>/zeolite hybrid system for treatment of molasses wastewater. *Iranian Journal of Chemistry and Chemical Engineering*, 33, 107–117.
- Arimi, M.M., Zhang, Y., Götz, G. & Geißen, S.-U. (2015). Treatment of melanoidin wastewater by anaerobic digestion and coagulation. *Environmental Technology*, 36, 2410–2418.
- Chandra, R., Bharagava, R.N. & Rai, V. (2008). Melanoidins as major colourant in sugarcane molasses based distillery effluent and its degradation. *Bioresource Technology*, 99, 4648–4660.
- Chaudhari, P.K., Mishra, I.M. & Chand, S. (2005). Catalytic thermal treatment (catalytic thermolysis) of a biodigester effluent of an alcohol distillery plant. *Industrial & Engineering Chemistry Research*, 44, 5518–5525.
- Chaudhari, P.K., Mishra, I.M. & Chand, S. (2007). Decolourization and removal of chemical oxygen demand (COD) with energy recovery: Treatment of biodigester effluent of a molasses-based alcohol distillery using inorganic coagulants. *Colloids and Surfaces A: Physicochemical and Engineering Aspects*, 296, 238–247.
- Dolphen, R. & Thiravetyan, P. (2011). Adsorption of melanoidins by chitin nanofibers. *Chemical Engineering Journal*, 166, 890–895.
- Duerr, M., Gair, S., Cruden, A. & McDonald, J. (2007). Hydrogen and electrical energy from organic waste treatment. *International Journal of Hydrogen Energy*, 32, 705–709.
- Fernández, N. et al. (2008). Performance evaluation of an anaerobic fluidized bed reactor with natural zeolite as support material when treating high-strength distillery wastewater. *Renewable Energy*, 33, 2458–2466.
- Hörsch, P., Speck, A. & Frimmel, F.H. (2003). Combined advanced oxidation and biodegradation of industrial effluents from the production of stilbene-based fluorescent whitening agents. *Water Research*, 37, 2748–56.

- Jiménez, A.M., Borja, R. & Martín, A. (2004). A comparative kinetic evaluation of the anaerobic digestion of untreated molasses and molasses previously fermented with *Penicillium decumbens* in batch reactors. *BioChemical Engineering Journal*, 18, 121–132.
- Jing, J., Liu, M., Colvin, V.L., Li, W. & Yu, W.W. (2011). Photocatalytic degradation of nitrogen-containing organic compounds over TiO<sub>2</sub>. *Journal of Molecular Catalysis A: Chemical*, 351, 17–28.
- Kalavathi, D., Uma, L. & Subramanian, G. (2001). Degradation and metabolization of the pigment–melanoidin in distillery effluent by the marine cyanobacterium *Oscillatoria boryana* BDU 92181. *Enzyme and Microbial Technology*, 29, 246–251.
- Kim, S.B., Hayase, F. & Kato, H. (1985). Decolorization and degradation products of melanoidins on ozonolysis. *Agricultural and Biological Chemistry*, 49, 785–792.
- Lahav, O. & Morgan, B.E. (2004). Titration methodologies for monitoring of anaerobic digestion in developing countries: A review. *Journal of Chemical Technology and Biotechnology*, 79, 1331–1341.
- Lim, T.H. & Kim, S.D. (2005). Photocatalytic degradation of trichloroethylene (TCE) over TiO<sub>2</sub>/silica gel in a circulating fluidized bed (CFB) photoreactor. *Chemical Engineering and Processing: Process Intensification*, 44, 327–334.
- Olennikov, D.N. & Tankhaeva, L.M. (2012). Physicochemical characteristics and antioxidant activity of melanoidin pigment from the fermented leaves of *Orthosiphon stamineus*. *Brazilian Journal of Pharmacognosy*, 22, 284–290.
- Oller, I., Malato, S. & Sánchez-Pérez, J.A. (2011). Combination of advanced oxidation processes and biological treatments for wastewater decontamination: A review. *Science of the Total Environment*, 409, 4141–66.
- Onyango, M., Kittinya, J., Hadebe, N., Ojijo, V. & Ochieng, A. (2011). Sorption of melanoidin onto surfactant modified zeolite. *The Chemical Industry & Chemical Engineering Quarterly*, 17, 385–395.
- Patel, H. & Madamwar, D. (2000). Biomethanation of low pH petrochemical wastewater using up-flow fixed-film anaerobic bioreactors. *World Journal of Microbiology & Biotechnology*, 16, 69–75.
- Satyawali, Y. & Balakrishnan, M. (2008). Wastewater treatment in molasses-based alcohol distilleries for COD and color removal: A review. *Journal of Environmental Management*, 86, 481–97.
- Shan, A.Y., Ghazi, T.I.M. & Rashid, S.A. (2010). Immobilisation of titanium dioxide onto supporting materials in heterogeneous photocatalysis: A review. *Applied Catalysis A: General*, 389, 1–8.
- Shu, Z., Bolton, J.R., Belosevic, M. & El Din, M.G. (2013). Photodegradation of emerging micropollutants using the medium-pressure UV/H<sub>2</sub>O<sub>2</sub> advanced oxidation process. *Water Research*, 47, 2881–9.

- Travieso, L. et al. (2008). Assessment of a microalgae pond for post-treatment of the effluent from an anaerobic fixed bed reactor treating distillery wastewater. *Environmental Technology*, 29, 985–992.
- Vidal, G., Nieto, J., Mansilla, H.D. & Bornhardt, C. (2004). Combined oxidative and biological treatment of separated streams of tannery wastewater. *Water Science and Technology*, 49, 287–292.
- Vijayaraghavan, K. & Ramanujam, T.K. (2000). Performance of anaerobic contact filter in series for treating distillery spentwash. *Bioprocess Engineering*, 22, 109–114.
- Vineetha, M.N., Matheswaran, M. & Sheeba, K.N. (2013). Photocatalytic colour and COD removal in the distillery effluent by solar radiation. *Solar Energy*, 91, 368–373.
- Wang, H.-Y., Qian, H. & Yao, W.-R. (2011). Melanoidins produced by the Maillard reaction: Structure and biological activity. *Food Chemistry*, 128, 573–584.
- Zupancic, G.D., Straziscar, M. & Ros, M. (2007). Treatment of brewery slurry in thermophilic anaerobic sequencing batch reactor. *Bioresource Technology*, 98, 2714–22.

## 6 MODELLING THE ENERGY EFFICIENCY OF THE INTEGRATED SYSTEM USING SURFACE RESPONSE METHODOLOGY

### 6.1 Introduction

The AD process has been the preferred process for treating distillery effluent due to its good performance in organic load reduction and bioenergy recovery potential in the form of biomethane (Satyawali & Balakrishnan, 2008). The AD treatment of distillery effluent has electricity generation potential of up to 74 kWh/m<sup>3</sup> and 50 kg/m<sup>3</sup> of steam in a cogeneration process (Yasar et al., 2015). However, AD is not effective to remove colour from distillery effluent since melanoidins, which impart dark-brown colour to distillery effluent, are biorecalcitrant. The UV photocatalysis process has been proposed for the post-treatment of anaerobically treated distillery effluent for colour removal.

Photocatalysis has the advantage that it can rapidly degrade the pollutant without generating sludge; unlike the case of other treatment methods such as adsorption, coagulation and flocculation. However, photocatalysis is costly as the UV lamp used for irradiation is energy intensive. Oller et al. (2011) reported that electricity forms about 60% of the cost of operating a UV photoreactor with the UV lamp being one of the most energy demanding components. This was evidenced in a comparative study by Yasar et al. (2006) on energy requirements of various AOPs in wastewater treatment where it was reported that UV photolysis and UV/H<sub>2</sub>O<sub>2</sub> required 160 kWh/m<sup>3</sup> and 86 kWh/m<sup>3</sup>, respectively, to treat mixed industrial wastewater with COD of 108 mg/L and colour absorbance of 0.085. The UV energy requirement compares well with the electricity production potential of AD treatment of distillery wastewater, which is about 74 kWh/m<sup>3</sup> (Yasar et al., 2015). This suggests that the AD process has the potential to produce energy to offset the energy requirement cost of UV photocatalysis in an integrated AD-photodegradation treatment system.

The challenge facing studies on the integrated wastewater process is that most studies have been conducted without considering the impact of the operating parameters of the initial step on the performance of the ensuing post-treatment step (Chaudhari et al., 2007; Yasar et al., 2007). This trend has led to the modelling of the individual processes forming the integrated system instead of modelling the whole integrated system as a single unit as asserted by Oller et al. (2011). Therefore, Oller et al. (2011) recommended that modelling the effects of operating parameters of an integrated biological and chemical process as a unit for wastewater treatment, besides considering the individual processes, is necessary for process optimisation and scale-up. In the case of an integrated AD-UV system, the OLR and HRT employed in the initial AD step are significant in evaluating the overall process performance. This is because these factors not only determine the AD stability and biogas production rate but also affect the characteristics of the AD treated effluent, which in turn affects the efficiency of the post-treatment process.

To obtain the best operating conditions for the integrated process, response surface methodology (RSM) using factorial experimental design is an appropriate technique. The RSM methodology enables determination of the optimum operating conditions in an effective manner and evaluates the effect of interaction of multivariable systems using statistical methods compared with a one-variable-at-a-time experimental design, which is time-consuming and does not cater for the interactive effects of variables (Chen et al., 2011). In this

work, the performance of an integrated AD-UV system was evaluated in COD and colour reduction. Further, the bioenergy production of the initial AD step and the energy utilisation of a UV lamp in the photodegradation process were modelled using RSM. The interactive effects of HRT and OLR applied in the initial AD step on the overall process efficiency and best operating conditions were established.

## 6.2 Methodology

### 6.2.1 Experimental procedure

The experimental setup for the combined AD and photodegradation shown in Figure 42 of Chapter 5 was applied in this study. The FBB was operated in continuous mode where the OLR was varied between 0.33 kg COD/m<sup>3</sup>d and 9 kg COD/m<sup>3</sup>d. The HRT was varied between three days and 20 days. The effects of OLR and HRT in the anaerobic digester (OLR<sub>AD</sub> and HRT<sub>AD</sub> respectively) on the subsequent batch photodegradation process were studied. Subsequently, energy analysis of the integrated process per unit wastewater treated was carried out based on the effect of the OLR<sub>AD</sub> and HRT<sub>AD</sub> on the energy production by the initial AD step and energy use by the final UV step. Finally, the energy efficiency of the integrated process was modelled using RSM.

### 6.2.2 Energy analysis

The energy production of the anaerobic unit was compared with the energy demand of the photodegradation process with a view of developing a system in which the AD step could provide energy for UV photodegradation. The energy production by the AD process was calculated as (Moraes et al., 2014):

$$E_{bio} = LHV_{CH_4} \times E_{COD} \times C_{COD} \times \alpha_{CH_4} \quad (48)$$

where  $E_{bio}$  is the AD energy production kWh/m<sup>3</sup>,  $LHV_{CH_4}$  is the low heating value of methane, which is 38 MJ/m<sup>3</sup> (10.55 kWh/m<sup>3</sup>) (Duerr et al., 2007),  $E_{COD}$  is the COD removal efficiency,  $C_{COD}$  is the feed concentration (kg COD/m<sup>3</sup>) and  $\alpha_{CH_4}$  is the methane production coefficient (m<sup>3</sup>/kg COD removed). EEO was used to calculate the energy consumption of the UV photodegradation process ( $E_{UV}$ ). The EEO (kWhm<sup>-3</sup>order<sup>-1</sup>) is defined as the electrical energy (kWh) required to degrade a contaminant by one order of magnitude in 1.0 m<sup>3</sup> water and it was adopted from Shu et al. (2013):

$$E_{UV} = \frac{Pt}{V \log\left(\frac{C_i}{C_f}\right)} \quad (49)$$

where  $P$  is the UV lamp or compressor power consumption (kW),  $t$  is the irradiation time (hours),  $V$  is the volume (m<sup>3</sup>) of water treated, and  $C_i$  and  $C_f$  are the initial and final concentrations of the target contaminant. The calculation was based on additional colour reduction after the initial AD step by UV treatment after 30 minutes irradiation. Wastewater samples were diluted as appropriate and the dilution factors were incorporated in Eq. 48. Energy ratio ( $\beta$ ), which is the efficiency indicator of the integrated system, was calculated as:

$$\beta = \left[ \frac{E_{bio}}{E_{UV}} \right] \times 100 \quad (50)$$

where  $E_{UV}$  is the UV lamp energy consumption (kWh/m<sup>3</sup>) and  $E_{bio}$  is the bioenergy production (kWh/m<sup>3</sup>).

To evaluate the energy efficiency and the environmental impact of the integrated process, the electricity from the national grid that was saved as a result of the application of electricity from bioenergy was determined. The conversion of biomethane to electricity was estimated assuming a generator with an overall output efficiency of 78% of which 33% was electricity and 45% was heat in a cogeneration process (Moraes et al., 2015). Therefore, electricity generated from biomethane was given as:

$$El_{bio} = 0.33[E_{bio}] \quad (51)$$

where  $El_{bio}$  is the electricity generated from biomethane per unit effluent volume (kWh/m<sup>3</sup>) and  $E_{bio}$  is the total bioenergy from the AD (kWh/m<sup>3</sup><sub>feed</sub>). The energy consumption of the centrifugal pump in the AD system was approximated as (Bagheri & Mohseni, 2015):

$$E_p = \frac{Q_c \rho h g}{\omega} \quad (52)$$

where  $E_p$  is pump power (W),  $Q_c$  is the flow rate of the recycle stream (m<sup>3</sup>/s),  $\rho$  is fluid density (kg/m<sup>3</sup>),  $g$  is the gravitational acceleration (m/s<sup>2</sup>),  $h$  is the head (m) and  $\omega$  is the pump efficiency, which was assumed to be 0.6 (Bagheri & Mohseni, 2015). The carbon dioxide emission (when electricity from the national grid was applied to power the UV lamp of the photoreactor) was calculated as a product of the electricity requirement of the UV lamp (kWh/m<sup>3</sup>) and the base line grid emission factor of 0.957 kg CO<sub>2</sub>e/kWh of electricity used (Spalding-Fecher, 2011). The carbon dioxide emission reduction (CER) when electricity from biomethane was presumably used to power the UV lamp as an alternative energy source, replacing that from national grid was calculated as:

$$CER = GEF \times El_{bio} \quad (53)$$

where  $CER$  is the carbon dioxide emission reduction (kg CO<sub>2</sub>e/m<sup>3</sup><sub>feed</sub>),  $GEF$  is the grid emission factor (0.957 kg CO<sub>2</sub>e/kWh) and  $El_{bio}$  is the electricity generated from biomethane (kWh/m<sup>3</sup><sub>feed</sub>) and presumably applied to power the UV lamp.

### 6.2.3 Experimental design and modelling

To analyse the interaction between HRT<sub>AD</sub> and OLR<sub>AD</sub> regarding energy production of AD process and energy utilisation by the UV lamp in the photodegradation post-treatment process, Design expert software (version 6.0.6) was used. In the software, RSM using three-level factorial experimental design with four centre points was applied. Different OLR<sub>AD</sub> values were obtained by varying feed concentrations by diluting the raw distillery effluent as appropriate at fixed feed flow rates over the ranges of OLR<sub>AD</sub> and HRT<sub>AD</sub> studied, ensuring that OLR<sub>AD</sub> and HRT<sub>AD</sub> were independent variables (Zinatizadeh et al., 2010). For instance, at HRT of 6 days, the feed concentrations were varied as 2 g/L, 10 g/L and 19 g/L to obtain OLR of about 0.3 COD/m<sup>3</sup>d, 1.7 COD/m<sup>3</sup>d and 3 kg COD/m<sup>3</sup>d, respectively, at a fixed feed flow rate of 1 L/d. This procedure was repeated for other HRTs studied according to Eq. 54 and the ranges of the variables studied are shown in Table 17.

$$OLR = \frac{S \cdot Q}{V} \quad (54)$$

where  $S$  is the feed concentration  $\text{kg/m}^3$ ,  $Q$  is the feed flow rate  $\text{m}^3/\text{d}$  and  $V$  is the reactor volume ( $\text{m}^3$ ).

**Table 17: Experimental range and level of variables**

Parameters	Code	Range and variables		
		-1	0	1
OLR ( $\text{kg COD/m}^3\text{d}$ )	A	0.3	1.7	3
HRT (days)	B	6	13	20

In the RSM study, the responses were bioenergy production by the AD process, UV lamp energy consumption of the photodegradation process, and energy ratio of the two processes. In each case, the data obtained was used to develop a mathematical model that best correlates  $\text{HRT}_{\text{AD}}$  and  $\text{OLR}_{\text{AD}}$  to the various responses in the form of a quadratic polynomial equation:

$$Y = b_o + \sum_{i=1}^k b_i x_i + \sum_{i=1}^k b_{ii} x_i^2 + \sum_{i=1}^k \sum_{j>1}^k b_{ij} x_i x_j \quad (55)$$

where  $Y$  is the response,  $b_o$  is the offset term,  $b_i$  is the linear effect,  $b_{ii}$  is the quadratic effect and  $b_{ij}$  is the interaction effect.

#### 6.2.4 Data analysis

The response data was analysed using the Design expert software and the fitting of the models was determined based on analysis of variance (ANOVA). Parameters such as F value, probability > F and adequate precision, which is a measure of error or the signal-to-noise ratio, were used as indicators of how the quadratic models fit the experimental values. A probability > F value < 0.05 indicates that the model term is significant while an adequate precision value of  $\geq 4$  is desired.

#### 6.2.5 Experimental analysis

AD samples were centrifuged before analysis. For the photodegradation process, samples were filtered using a  $0.45 \mu\text{m}$  filter syringe. The TOC was analysed using a TOC analyser (Teledyne Tekmar) while biogas was analysed using a gas chromatograph (Trace 1310 gas chromatograph) fitted with a thermal conductivity detector using helium as carrier gas. Colour was analysed using a UV-Vis spectrophotometer (T80 + UV/VIS Spectrophotometer, PG instruments Ltd) at 475 nm. The BOD and COD were analysed per standard procedure (APHA 1998), in which the COD was analysed using the closed reflux method where a potassium dichromate solution was used as oxidant and a Nanocolor colorimeter was used for colour analysis. Alkalinity was analysed according to the standard method for wastewater analysis involving titrating samples against  $0.02 \text{ N H}_2\text{SO}_4$  solution using methyl orange indicator (Wilson, 2013).

## 6.3 Results and Discussion

### 6.3.1 Characteristics of distillery effluent

Distillery effluent is considered as fairly biodegradable with traces of recalcitrant compounds such as melanoidins (Acharya et al., 2008). The biodegradability of the distillery effluent was measured by determining the BOD<sub>5</sub>/COD ratio (Table 18); it was found to be 0.41, indicating that the distillery effluent is biodegradable. Good biodegradability is achieved when the BOD<sub>5</sub>/COD is greater than 0.25–0.4 (Sankaran et al., 2014; Al-Momani et al., 2002). However, the biorecalcitrant part of distillery effluent, which is mostly composed of melanoidins (which form a small proportion of the total effluent), often pass through anaerobic treatment without being degraded and they impart a dark colour to biomethanated effluent (Satyawali & Balakrishnan, 2008; Kalavathi et al., 2001).

**Table 18: Characteristics of distillery wastewater**

Parameter	Mean value
COD (mg/L)	68 062 ± 320
TOC (mg/L)	45 175 ± 147
BOD (mg/L)	28 066 ± 237
BOD <sub>5</sub> /COD	0.412 ± 0.002
Total sulphates (mg/L)	7 525 ± 78
Total phosphates (mg/L)	1 009 ± 59
pH	5.45 ± 0.35

### 6.3.2 Determination of the recalcitrant component of distillery effluent

The amount of non-biodegradable component can be determined by the relationship between the organics remaining after digestion and HRT. The AD process was carried out at various HRTs in the AFBR at constant feed concentration and the recalcitrant component was determined from data in Table 19.

**Table 19: Anaerobic digestion at different HRT and constant feed concentration**

HRT	COD <sub>feed</sub>	COD <sub>effluent</sub>	Ln (COD <sub>effluent</sub> )
3	5810	1415	7.25
6	5810	1120	7.02
10	5810	980	6.88
15	5810	871	6.76
20	5810	760	6.63

It is proposed that a plot of  $Ln(COD_{effluent})$  against  $1/HRT$  gives a straight line, and the recalcitrant component is calculated at infinite HRT. A similar model has been to determine the biodegradable component of some food waste wastewater (Rincón et al., 2006; Borja et al., 2002). In Figure 54, the amount of non-biodegradable component was calculated as COD equivalent at y-axis intercept when HRT is infinite. It was found that the non-biodegradable COD was about 756 mg/L constituting ~13% of the feed and corresponding to a TOC of

477 mg/L under the prevailing digestion conditions. The low value suggests that distillery effluent was fairly biodegradable.

Kalavathi et al. (2001) reported that melanoidins constitute about 2% of distillery effluent with the rest being mainly biodegradable organic compounds. Removal of melanoidins from distillery effluent can be achieved by applying photodegradation.

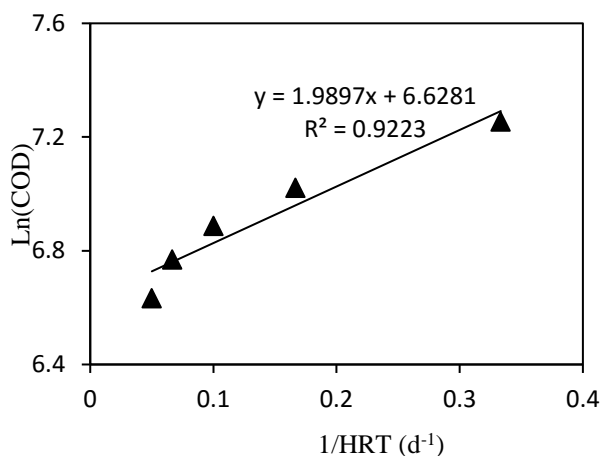


**Figure 54: Determination of the recalcitrant component of distillery effluent**

### 6.3.3 Performance of the continuously operated fluidized bed anaerobic bioreactor

The stability of the bioreactor at various OLRs was studied at a fixed HRT of six days. In Figure 55, the reactor was stable up to an OLR of 6 kg COD/m<sup>3</sup>d as shown by the VFA: alkalinity ratio of below 0.3 (Hampannavar & Shivayogimath, 2010). Under stable conditions, the COD and colour reductions were 86–73% and 56–40%, respectively. This indicates that the anaerobic process has good efficiency in COD reduction but is not efficient in colour reduction due to the presence of melanoidins. However, at a high OLR, acidogenesis takes place faster than methanogenesis, which leads to the accumulation of VFAs that reduces performance as indicated by low COD and colour reduction as well as low methane production.

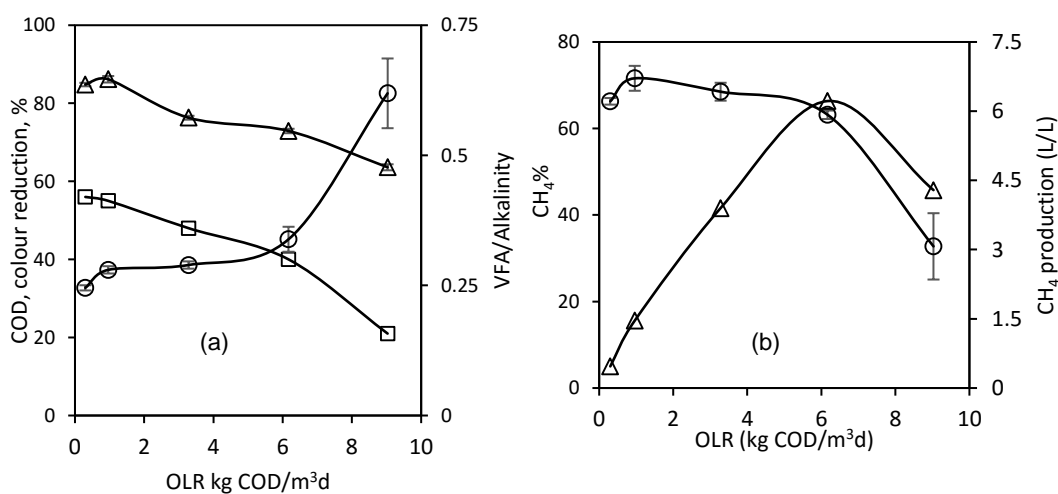


**Figure 55: Effect of OLR on AD: (a) colour (□), COD (Δ), VFA/alkalinity (○); (b) methane production (Δ), methane proportion of the biogas (○)**

The effect of HRT on the performance of the reactor at a fixed OLR of 3 kg COD/m<sup>3</sup>d showed that an increase in HRT led to a corresponding increase in COD and colour reduction as well as an increase in methane production (Figure 56). This is due to sufficient contact time between the microbes and the substrate at a high HRT compared with that at a low HRT.

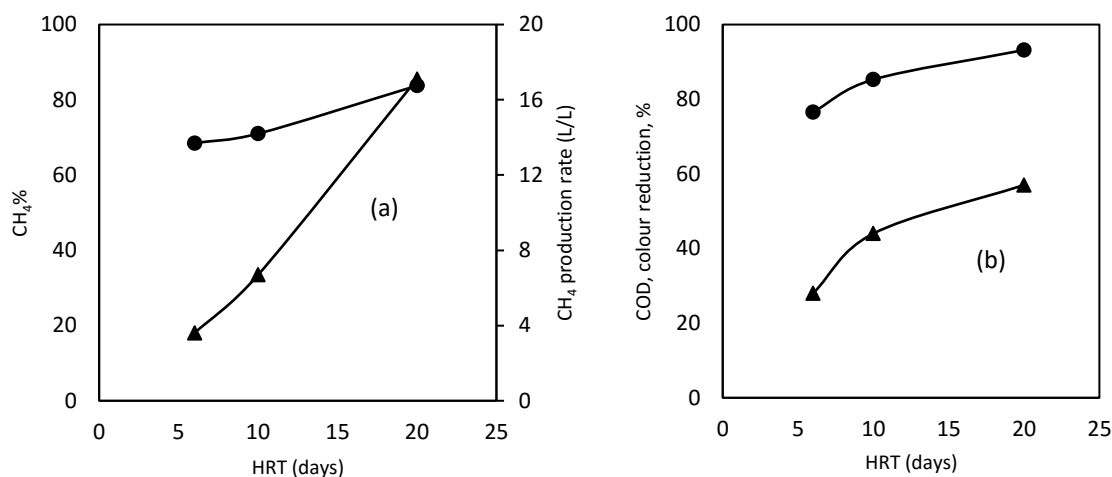


**Figure 56: Effect of HRT on the AD process: (a) CH<sub>4</sub> proportion of the biogas (●), CH<sub>4</sub> production (▲); (b) COD reduction (●) and colour reduction (▲)**

The substantial increase in colour reduction with an increase in HRT could be an indication that melanoidins need a long degradation time. The increase in methane production per unit feed volume with an increase in HRT at fixed OLR is due to an increase in feed concentration at low flow rates.

#### 6.3.4 Effects of biodigester parameters on the UV post-treatment

The AD effluent characteristic is important when considering the design of a post-treatment process. It affects the performance of the post-treatment facility because it determines the reaction kinetics, energy requirement and the overall size of the post-treatment facility required to handle the discharge. Figure 57a shows the effects of applied AD OLR (OLR<sub>AD</sub>) on the subsequent UV photodegradation process at a constant HRT<sub>AD</sub> of six days. Generally, the photodegradation process was more efficient in colour reduction than TOC reduction for all OLR<sub>AD</sub> studied. This is contrary to the AD treatment, which had a higher organic load reduction but a low colour reduction; therefore, integration of these two processes is necessary as they complement each other.

It was further established that the efficiency of the photodegradation process reduced with an increase in OLR<sub>AD</sub> applied in the preceding AD process (Figure 57a). This was because at a high OLR<sub>AD</sub> the AD effluent had a higher concentration and more intense colour than at a low OLR. This led to light attenuation in the preceding photodegradation process.

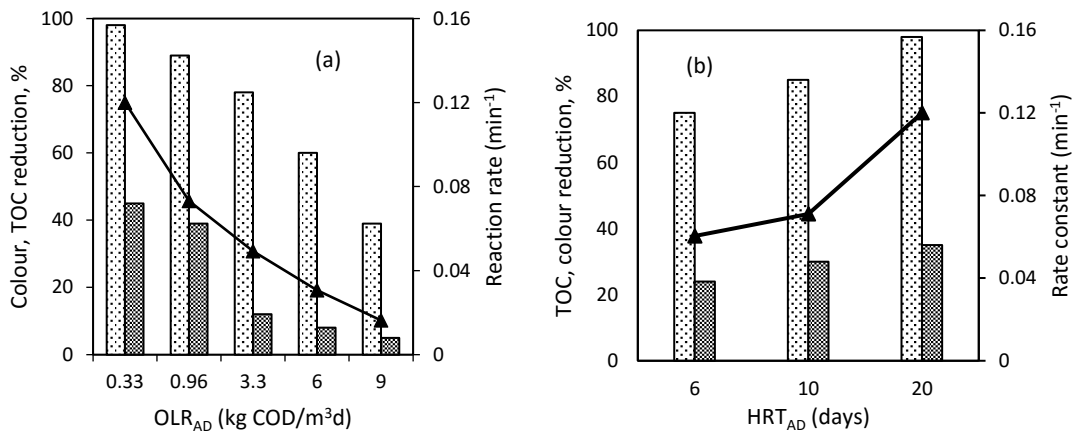


**Figure 57: Effect of bioreactor operating parameters on photodegradation post-treatment: (a) OLR<sub>AD</sub> and (b) HRT<sub>AD</sub>, Colour (●), TOC (■), reaction constant (▲)**

When the OLR<sub>AD</sub> was fixed at 3 kg COD/m<sup>3</sup>d while the HRT<sub>AD</sub> was varied from six to 20 days (Figure 57b), it was found that the photodegradation efficiency increased with an increase in applied HRT<sub>AD</sub> from 75% to 98% colour removal. The longer time the wastewater spent in the AD reactor, the more the biodegradable organic pollutants were removed due to sufficient contact time between pollutants and microorganisms. Moreover, the AD effluent had a more intense colour at a low HRT<sub>AD</sub> than at a high HRT<sub>AD</sub>. The overall performance of the integrated process is shown in Table 20 where photodegradation post-treatment complemented AD process in colour removal.

**Table 20: Overall efficiency of the integrated process at various HRT<sub>AD</sub> at fixed OLR<sub>AD</sub> of 3 kg COD/m<sup>3</sup>d**

HRT (d)	Initial removal by AD, %		Additional removal by UV, %		Combined process, %	
	Colour	TOC	Colour	TOC	Colour	TOC
6	28	81	54	4.5	74	84.5
10	44	90.4	48	3	92	93.4
20	57	95.7	42	1.4	99	99

### 6.3.5 Kinetics of the integrated process

Both AD and photodegradation were found to follow the first-order rate model. Therefore, the first-order rate model was used to study the effect of the AD rate on the rate of ensued photodegradation process at various OLR<sub>AD</sub>. In Table 21, the rate of substrate utilisation in the AD process increased with an increase in OLR. However, the rate of the succeeding photodegradation process decreased with an increase in OLR<sub>AD</sub>.

The observed increase in organic removal rate (AD rate) with increasing OLR<sub>AD</sub> in AD could be attributed to a corresponding increase in the concentration gradient between the fluid and biofilm due to an increase in available feed (Fernández et al., 2008). It could also be attributed to the stability of the AFBR owed to immobilisation of microorganisms to small fluidized zeolite particles (Borja et al., 2004). In contrast, the reduction in photodegradation rate with an

increase in  $OLR_{AD}$  could be attributed to light attenuation caused by high colour intensity when the system was operated at high  $OLR_{AD}$ . The performance of the photodegradation post-treatment process increased with an increase in the colour and COD removal efficiency in the initial AD step but reduced with an increase in substrate utilisation rate (Figure 55 and Figure 58). At high  $OLR_{AD}$  the substrate utilisation is high due to the available feed and the effluent has a higher colour intensity than at low  $HRT_{AD}$ .

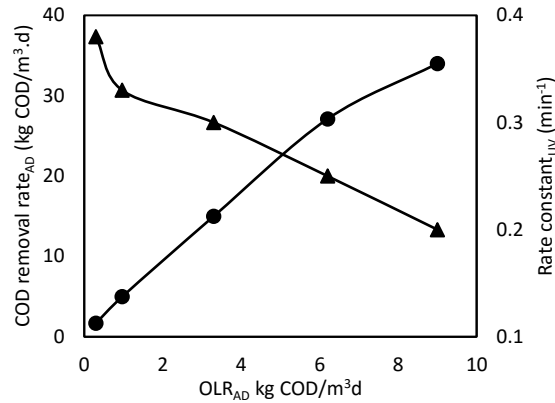


**Figure 58: Organic removal rate by the AD process (●) and reaction rate constant of photodegradation post-treatment (▲) at various  $OLR_{AD}$**

### 6.3.6 Energy efficiency of the integrated AD-UV process

The photodegradation process is energy intensive mainly due to the energy demand of the UV lamp while the AD process produces energy in the form of methane. The effect of  $OLR_{AD}$  at a fixed  $HRT_{AD}$  of six days showed that the energy demand of the UV lamp always increased with an increase in  $OLR_{AD}$  due to increasing AD effluent concentration. In the case of AD, the energy production was at maximum at  $OLR_{AD}$  of 6 kg COD/m<sup>3</sup>d, after which it dropped due to inhibition caused by accumulation of VFAs as a result of organic overloading (Figure 59a). The energy ratio of the integrated process ( $\beta$ ) was highest between an  $OLR$  of 3 kg COD/m<sup>3</sup>d and 6 kg COD/m<sup>3</sup>d (Figure 6.6b). The low efficiency at  $OLR_{AD}$  of 9 kg COD/m<sup>3</sup>d was due to both low bioenergy production due to organic overloading and high effluent load with intense colour, which hindered photodegradation.

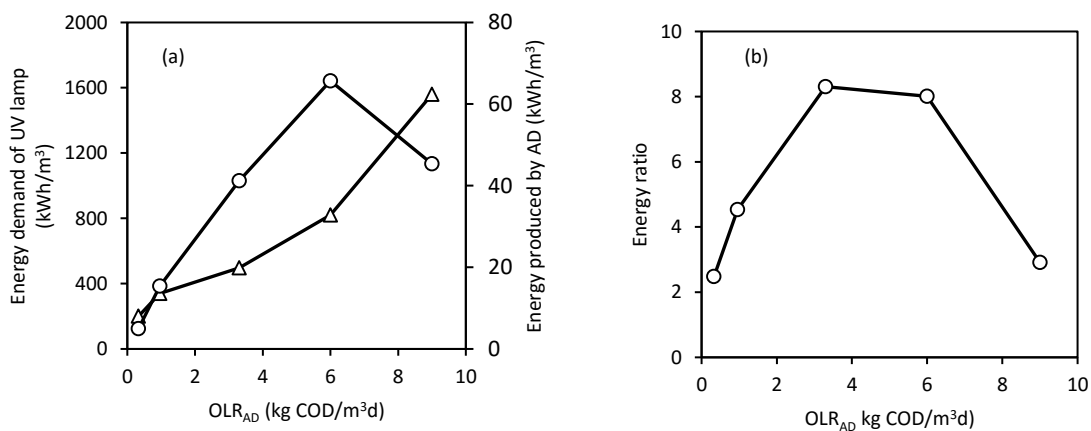


**Figure 59: Effect of  $OLR_{AD}$  on the energy efficiency of the integrated process: (a) (○) Bioenergy production, (Δ) UV lamp energy consumption and (b) Energy ratio**

To increase the efficiency of the integrated process, the  $HRT_{AD}$  was increased stepwise from six to 20 days at a constant  $OLR_{AD}$  of 3 kg COD/m<sup>3</sup>d. The  $OLR_{AD}$  of 3 kg COD/m<sup>3</sup>d was chosen due because it had good organic removal efficiency for both the processes and the best energy ratio was attained at this  $OLR$ . In Figure 60 it was found that increasing the  $HRT_{AD}$  from six to 20 days at a constant  $OLR_{AD}$  of 3 kg COD/m<sup>3</sup>d increased the energy efficiency from ~9% to 93%. There were two combined factors that led to the high increase in efficiency with an increase in  $HRT_{AD}$ . Firstly, the high  $HRT$  in the AD unit led to a high degradation of biodegradable constituents as well as better colour reduction, resulting in a relatively easy to photodegrade effluent due to low concentration or colour intensity thus leading to lower  $E_{UV}$  than at low  $HRT_{AD}$ . Secondly, to achieve high  $HRT_{AD}$  at constant  $OLR_{AD}$ , a feed with a high concentration was fed into the digester at a very low flow rate. This led to a higher methane production per unit feed volume than at the low  $HRT_{AD}$  where relatively low concentrated feed was applied at high flow rate. However, increasing the  $HRT_{AD}$  may lead to an increase in the cost of operating the AD unit, which may compromise the overall efficiency of the integrated process (this is discussed in Section 6.3.11 and 6.3.12, which deals with cost analysis).

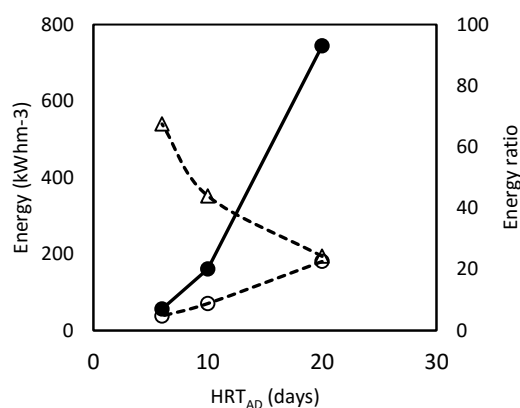


**Figure 60: Effect of  $HRT_{AD}$  on energy efficiency of the integrated process: (○) Bioenergy production, (△) UV lamp energy consumption and (●) Energy ratio**

Generally, operating a bioreactor at an appropriately high  $OLR_{AD}$  (which the bioreactor can handle without shock) and high  $HRT_{AD}$  means a higher biogas production per unit feed volume and lower effluent volume with less concentration than operating it at the same  $OLR_{AD}$  but at a low  $HRT_{AD}$  (Zinatizadeh et al., 2010). This can easily or effectively be handled by the UV post-treatment. However, this study could not investigate an  $HRT_{AD}$  of beyond 20 days at an  $OLR_{AD}$  of 3 kg COD/m<sup>3</sup>d due to limitations in available feed concentration and reactor size.

### 6.3.7 RSM and ANOVA

Per the experimental design, 13 experimental runs were conducted including four centre points (Run 10–13) as indicated in Table 21. The responses of the centre points showed little variation indicating the consistency of the experimental runs. In all experimental conditions studied, biogas production ranged from 0.714 L/L<sub>feed</sub> to 20.6 L/L<sub>feed</sub> corresponding to bioenergy production in the range of 4.96 kWh/m<sup>3</sup> to 180.5 kWh/m<sup>3</sup> while the energy consumption of the UV lamp ranged from 93 kWh/m<sup>3</sup> to 496 kWh/m<sup>3</sup> corresponding to overall efficiencies of between 2.5% and 93% as shown in Table 21.

**Table 21: Experiments conducted according to design and the corresponding responses**

Experiment	OLR (xi)	HRT (xii)	Biogas (L/L <sub>feed</sub> )	CH <sub>4</sub> %	E <sub>bio</sub>	E <sub>UV</sub>	ε
1	0.3	6	0.714	66	4.96	200	2.5
2	1.65	6	3.1	74	24.3	135	18
3	3	6	5.7	68.5	38	496	7.6
4	0.3	13	1.85	75	14.5	105	13.8
5	1.65	13	5.08	74	40.1	115	34.8
6	3	13	9.4	71	70.6	352	20
7	0.3	20	1.93	73.5	14.7	87	16.9
8	1.65	20	10.1	71	76	100	76
9	3	20	20.6	83.7	180.5	194	93
10	1.65	13	5.08	74	40.1	119	33.7
11	1.65	13	5.1	73.8	40	115	34.8
12	1.65	13	5.12	73.5	40	115	34.8
13	1.65	13	5.08	74	40.1	110	36.4

**Table 22: ANOVA for response surface models**

Response	Polynomial model	Source	Sum of squares	DF	Mean square	F value	Prob > F	Adeq. precision
Bioenergy	2 FI	Model	23 510.75	3	7 836.92	177.4	< 0.0001	44.25
		A	13 088.46	1	13 088.46	296.28	< 0.0001	
		B	7 715.97	1	7 715.97	174.67	< 0.0001	
		AB	4 962.38	1	4 962.38	112.33	< 0.0001	
		Residual	397.58	9	44.18			
UV lamp energy	Quadratic	Model	1.65E+05	5	32 962.17	22.67	0.0003	16.23
		A	60 122.16	1	60 122.16	41.36	0.0004	
		B	33 750	1	33 750	23.22	0.0019	
		A <sup>2</sup>	40 681.72	1	40 681.72	27.98	0.0011	
		B <sup>2</sup>	4 601.6	1	4 601.6	3.17	0.1184	
		AB	9 612.48	1	9 612.48	6.61	0.0369	
		Residual	10 176.25	7	1 453.75			
E <sub>bio</sub> /E <sub>UV</sub> (ε, %)	Quadratic	Model	7 948.3	5	1 589.66	69.41	< 0.0001	27.89
		A	1 746.88	1	1 746.88	76.28	< 0.0001	
		B	4 144.88	1	4 144.88	180.99	< 0.0001	
		A <sup>2</sup>	895.37	1	895.37	39.1	0.0004	
		B <sup>2</sup>	1.76	1	1.76	0.077	0.7898	
		AB	1 543.44	1	1 543.44	67.4	< 0.0001	
		Residual	160.31	7	22.9			

Based on the probability > F values, the summary of ANOVA for various polynomial models relating the variables to the responses (Table 22) indicates that a two-factor interaction model (2FI) described the interaction of OLR<sub>AD</sub> (A) and HRT<sub>AD</sub> (B) in bioenergy production while the quadratic model described UV lamp energy requirement and the energy efficiency. All variables and their linear interactions were significant in the proposed models except the quadratic term of the HRT<sub>AD</sub> (B) as indicated by probability > F value being greater than 0.05. A significant interaction between OLR<sub>AD</sub> and HRT<sub>AD</sub> means that the effect of each of the variables depends on the value of the other variable. Adequate precision for all the models was greater than 4, which suggests a high signal; hence, the models can be used to navigate the design space.

### 6.3.8 Energy production by the anaerobic process

By applying multiple regression analysis, the bioenergy production was correlated to the operating parameters as described by Eq. 56. The predictive 2FI model that correlates bioenergy production to the applied OLR<sub>AD</sub> and HRT<sub>AD</sub> in the reactor in terms of coded values is presented as:

$$E_{bio} = 55.90 + 47.37 A + 34.21B + 34.19AB \quad (56)$$

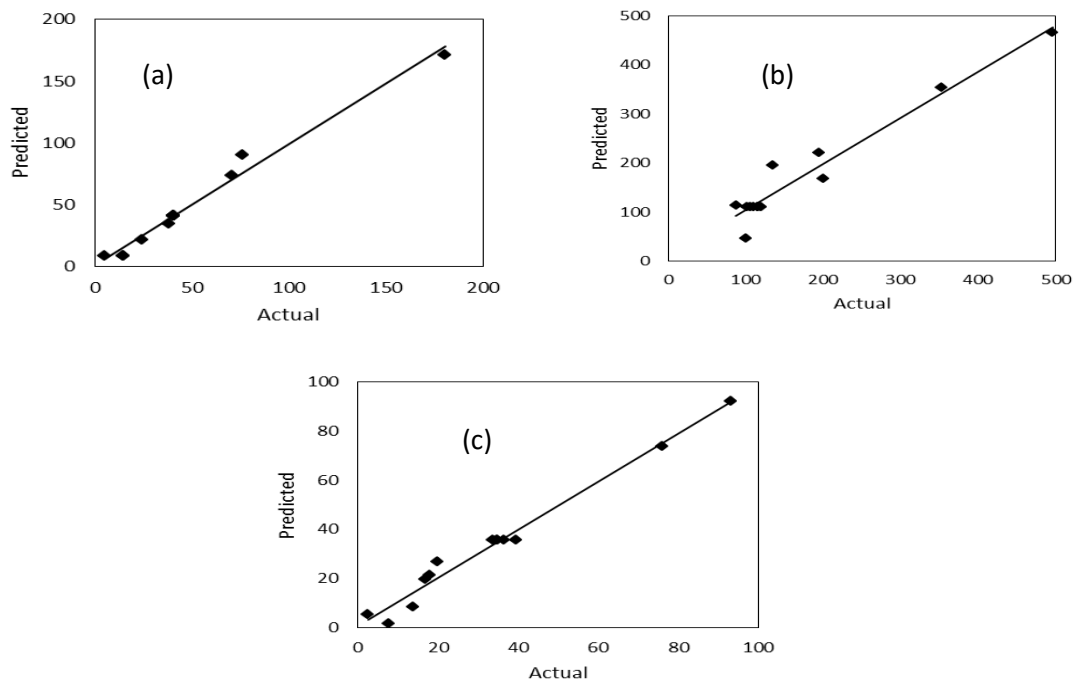


**Figure 61:** A plot of the predicted values from the models against the experimental values: (a) Energy production by the anaerobic process; (b) UV photodegradation energy consumption; (c) Energy ratio

The coefficients of all model factors contributed positively to the model equation. The most influential parameter was OLR<sub>AD</sub> (A) as it had the highest coefficient and F value (Salam et al., 2015). The model was validated by plotting the predicted values against the experimental values (Figure 61a). An R<sup>2</sup> value of 0.9778 was obtained, which imply that the model accurately describes the effect of OLR<sub>AD</sub> and HRT<sub>AD</sub> in the digestion process. A response surface plot depicting the effects of OLR<sub>AD</sub> and HRT<sub>AD</sub> on bioenergy production is shown in Figure 62a. The plots show that at a low HRT<sub>AD</sub> of six days, the bioenergy production did not

increase significantly with an increase in  $OLR_{AD}$ . Likewise, at a low  $OLR$  of  $0.3 \text{ kg COD/m}^3\text{d}$ , the bioenergy production did not significantly increase with an increase in  $HRT_{AD}$ . However, at higher  $HRT_{AD}$  values, there was a massive increase in bioenergy production with an increase in  $OLR_{AD}$ . Similarly, at higher  $OLR_{AD}$ , there was improved bioenergy production with an increase in  $HRT_{AD}$  because when  $OLR_{AD}$  was kept constant at high values (without shock loading) and operated at high  $HRT_{AD}$ , the reactor was able to handle effluent with higher concentration, leading to higher biogas production per unit effluent volume, than if operated at a low  $OLR_{AD}$  or low  $HRT_{AD}$ . Moreover, at a low  $HRT_{AD}$ , the reactor experienced significant microbial washout. A similar trend has been reported for biogas production during anaerobic treatment of various industrial wastewaters (Rastegar et al., 2011). The slight reduction in bioenergy production when  $HRT_{AD}$  was reduced at high and fixed  $OLR_{AD}$  could be attributed to the development of non-methanogens at these conditions (Zinatizadeh et al., 2010). The increased trend in bioenergy production with an increase in  $OLR_{AD}$  at fixed  $HRT_{AD}$  showed that the rate of substrate conversion to biogas increased with an increase in  $OLR_{AD}$ . This could be attributed to an increase in microbial community due to an increase in available feed, which leads to reactor stability even at high  $OLR_{AD}$  in the range studied (Rastegar et al., 2011). Alternatively, the observed increase in organic conversion rate to biogas with an increase in feed concentration could be attributed to the stability of the AFBR owed to immobilisation of microorganisms to small fluidized particles (Borja et al., 2004).

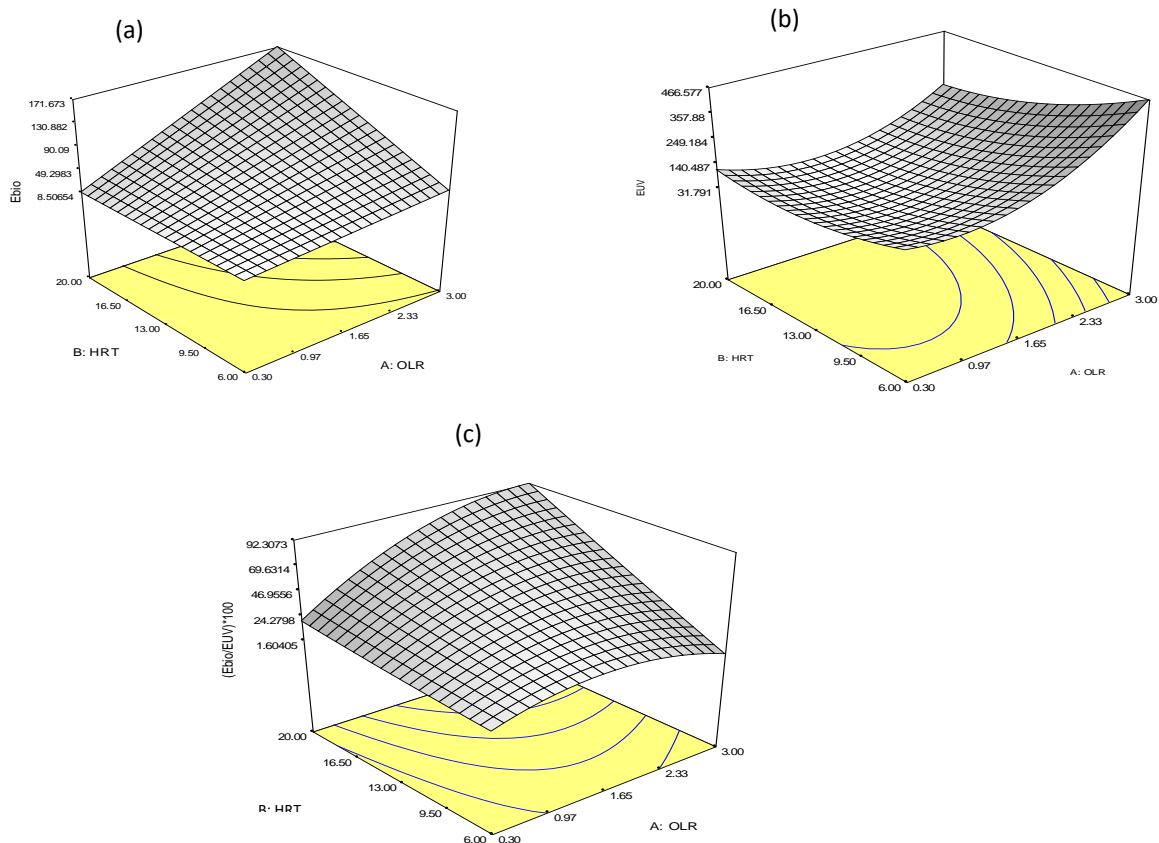


**Figure 62: Response surface plot indicating the effects of  $OLR_{AD}$  and  $HRT_{AD}$  on (a) Bioenergy production; (b) UV lamp energy consumption; and (c) Energy efficiency**

### 6.3.9 UV photodegradation energy consumption

The analysis of the interaction between the applied  $OLR_{AD}$  and  $HRT_{AD}$  in the bioreactor and the energy used by the UV lamp in photodegradation post-treatment was described by a quadratic model (Eq. 57).

$$E_{UV} = 69.02 + 101.54 A - 75.00B + 121.37A^2 + 52.07B^2 - 47.59AB \quad (57)$$

From the model, the quadratic term of the  $OLR_{AD}$  had the strongest effect on the energy consumption of the photodegradation process as indicated by its high coefficient while the linear interaction between the  $OLR_{AD}$  and  $HRT_{AD}$  had the least effect as indicated by its low coefficient. Furthermore, the linear term of  $OLR_{AD}$  and the quadratic terms of both  $OLR_{AD}$  and  $HRT_{AD}$  were additive to the response while the linear term of  $HRT_{AD}$  and the interaction between the two variables had a reducing effect on the response. The model depicts a convex plot attributed to by the quadratic effect of  $OLR_{AD}$  (A) since the quadratic effect of  $HRT_{AD}$  (B) was not significant as shown by the ANOVA (Table 22). The quadratic model was validated by plotting the predicted values against the experimental values (Figure 62b). A straight line with an  $R^2$  value of 0.9418 was obtained, indicating that the model described the dependence of  $E_{UV}$  on  $OLR_{AD}$  and  $HRT_{AD}$  accurately.

Figure 62b shows that generally the energy required by the UV lamp for photodegradation post-treatment increased with an increase in  $OLR_{AD}$  at various  $HRT_{AD}$  values studied as the AD effluent concentration increased with an increase in  $OLR_{AD}$  applied, leading to a high energy requirement for photodegradation post-treatment. At low  $OLR_{AD}$  (0.3 kg COD/m<sup>3</sup>d), an increase in  $HRT_{AD}$  did not significantly affect the energy requirement due to low AD effluent concentration at low  $OLR_{AD}$ .

However, at high  $OLR_{AD}$  (3 kg COD/m<sup>3</sup>d), there was a significant reduction in the energy required with an increase in  $HRT_{AD}$  from six to 20 days due to low AD effluent concentration at high  $HRT_{AD}$  (Zinatizadeh et al., 2010). Generally, a high  $HRT_{AD}$  ensures long contact time between microbes and pollutants, leading to effective removal of biodegradable constituents. Thus, the discharged AD effluent does not contain many biodegradable constituents that could compete with the biorecalcitrant constituents during the photodegradation process, leading to high efficiency. Moreover, operating an AD reactor at high  $HRT$  at fixed  $OLR_{AD}$  leads to more colour reduction due to the increased contact time between the reactants. Therefore, an AD effluent with a low colour intensity can be degraded faster than effluent with a high colour intensity, which causes light attenuation during photodegradation.

### 6.3.10 Energy ratio

A quadratic model in terms of coded factor that describes the relationship between overall energy efficiency of the integrated system and the variables, was expressed as:

$$\varepsilon = 46.64 + 17.31 A + 26.28B - 18.01A^2 + 1.02B^2 + 19.07AB \quad (58)$$

This model suggests that the dependence of the response on the variables is described by a concave-like curvature attributed to by the quadratic term of  $OLR_{AD}$  (A). The quadratic term

of  $HRT_{AD}$  (B) did not considerably contribute to the curvature since it was not significant (as shown in Table 22).

Figure 62c shows a plot of the predicted values against the experimental values where the data points are distributed along a line with a unit slope indicating the validity of the model. Figure 62c shows that at a low  $HRT_{AD}$  (six days), the energy ratio increased with an increase in  $OLR_{AD}$  up to an  $OLR_{AD}$  of 1.65 kg COD/m<sup>3</sup>d, and then it reduced as  $OLR_{AD}$  was further increased to 3 kg COD/m<sup>3</sup>d. This trend was partly because at a lower  $OLR_{AD}$  of 0.3 kg COD/m<sup>3</sup>d, the bioenergy production was low compared with that at a higher  $OLR_{AD}$  of 1.65 kg COD/m<sup>3</sup>d (Rastegar et al., 2011), leading to a low energy ratio. At the same time, at a high  $OLR_{AD}$  of 3 kg COD/m<sup>3</sup>d, the colour intensity of the AD effluent was higher than that at an  $OLR_{AD}$  of 1.65 kg COD/m<sup>3</sup>d; therefore, higher energy was required for photodegradation, which resulted in a decreased energy ratio. Due to these two pulling factors, the best energy efficiency at low  $HRT_{AD}$  was attainable midway between a low and high  $OLR_{AD}$ , which was at a value of 1.65 kg COD/m<sup>3</sup>d.

At a high HRT (20 days), the energy efficiency increased with an increase in  $OLR_{AD}$  – mainly due to an increase in bioenergy production per unit volume with an increase in  $OLR_{AD}$ . In related studies on AD of wastewater, higher methane production per unit feed flow rate was recorded at high  $OLR_{AD}$  and high  $HRT_{AD}$  than at low  $OLR_{AD}$  and low HRT (Zinatizadeh et al., 2010). Moreover, high  $HRT_{AD}$  at high  $OLR_{AD}$  lead to more digestion efficiency, therefore, eliminating most biodegradable constituents that would otherwise compete with the recalcitrant component during photodegradation post-treatment.

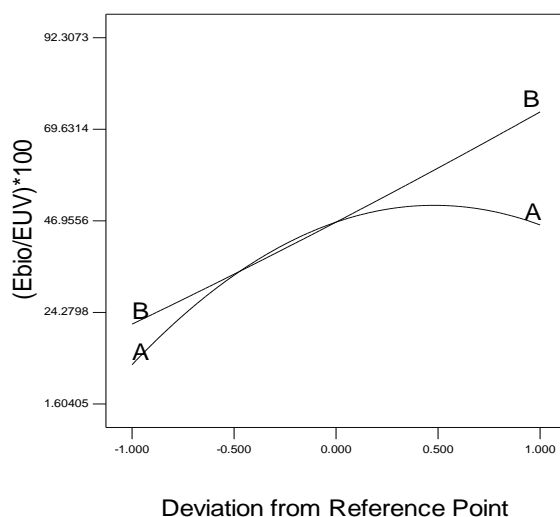


**Figure 63: Perturbation plot for energy efficiency**

An increase in  $HRT_{AD}$  at low  $OLR_{AD}$  did not significantly improve the energy efficiency because at low  $OLR_{AD}$ , bioenergy production per unit feed volume was usually low irrespective of the  $HRT_{AD}$  applied under this study. Operating a bioreactor at low  $OLR_{AD}$  and high  $HRT_{AD}$  is considered uneconomical since a low organic load could be degraded within a short time. It therefore follows that there was no substantial difference in the photodegradation energy requirement for effluent discharged by the bioreactor operating at low  $OLR_{AD}$  at either low or

high  $HRT_{AD}$  as shown in Figure 62b. In fact, operating the bioreactor at high  $HRT_{AD}$  and low  $OLR_{AD}$  can lead to cell death due to starvation.

Perturbation, which indicates the deviation of the energy efficiency from the reference point caused by the variables, is shown in Figure 63. The reference point considered was at  $OLR$  of  $1.7 \text{ kg COD/m}^3\text{d}$  and  $HRT_{AD}$  of 13 days, which is the mid-point. Holding one factor constant at the mid-point while varying the other helps to compare the effect of the variables at a point. In Figure 63, at the reference point, an increase in  $HRT_{AD}$  (B) led to an increase in energy efficiency. Similarly, an increase in  $OLR_{AD}$  led to an increase in efficiency up to a point where further increase in  $OLR_{AD}$  did not increase the efficiency. From the perturbation plot it could also be seen that the effect of  $OLR_{AD}$  was concave-like due to its significant quadratic term, in contrast, the effect of  $HRT_{AD}$  was linear due to its insignificant quadratic term (Table 22).

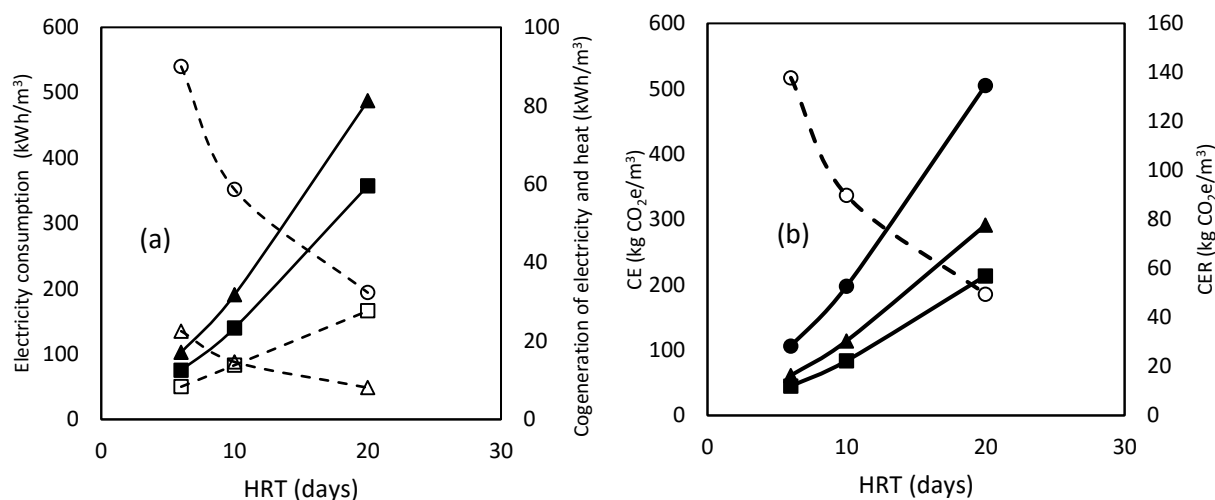
### 6.3.11 Electrical energy and CER analysis

The environmental sustainability of the integrated process was evaluated based on the electrical energy generation from the biomethane produced by the AD process and CER associated with the application of the generated electrical energy in the ensued photodegradation process. The conditions for this study were an  $OLR_{AD}$  of  $3 \text{ kg COD/m}^3\text{d}$  and an  $HRT_{AD}$  of six to 20 days. The fixed  $OLR_{AD}$  of  $3 \text{ kg COD/m}^3\text{d}$  was chosen as it was the highest  $OLR_{AD}$  at which the bioreactor was still stable with a good performance. Assumed biomethane conversion efficiency of 45% to heat and 33% to electricity in a cogeneration process was considered (Moraes et al., 2015). To estimate the CER, a base line emission factor (electricity is used from the national grid) of  $0.957 \text{ kg CO}_2\text{e/kWh}$  of electricity generated was applied (Spalding-Fecher, 2011). The CER achieved by applying the electricity generated from the biomethane was compared with the carbon emission when electricity from the grid was applied to power the UV lamp in the photodegradation post-treatment (Figure 64).

In Figure 64a and Figure 64b, the electricity consumption of the UV lamp and the carbon emission reduced with an increase in  $HRT_{AD}$  while the energy generation and the CER increased with an increase in  $HRT_{AD}$ . This was because at a low  $HRT_{AD}$ , the effluent discharged by the AD process had a higher concentration or colour intensity than the effluent at a high  $HRT_{AD}$ . Therefore, it demanded more electrical energy to drive the UV lamp for the photodegradation post-treatment. Moreover, there was low biogas production per unit feed volume at a low  $HRT_{AD}$  compared with that at a high  $HRT_{AD}$ , leading to low electricity generation. In Figure 64a it was also found that the UV lamp was the most energy-consuming component of the photoreactor as it constituted 80% of electricity requirement while the compressor used for mixing constituted the remaining 20%.

In Figure 64b, the bioenergy application as electricity source for UV lamp led to CER of  $57 \text{ kg CO}_2\text{e/m}^3_{\text{feed}}$ , corresponding to a 31% CER compared with the case when electricity from the grid was applied. The CER could go up to  $134.7 \text{ kg CO}_2\text{e/m}^3_{\text{feed}}$  or 72.5% if the heat produced was used for other activities in the process, such as heating the digester. Yasar et al. (2015) applied a baseline emission factor of  $0.4829 \text{ kg CO}_2\text{/kWh}$  and obtained a CER of about  $55 \text{ kg CO}_2\text{e/m}^3$  when energy generated from anaerobic treatment of distillery effluent in an industrial scale was applied instead of the energy from the conventional grid. Apart from the difference in the applied baseline emission factor, which varies significantly with regions

(Spalding-Fecher, 2011), the CER values obtained by (Yasar et al., 2015) were close to those of this study.



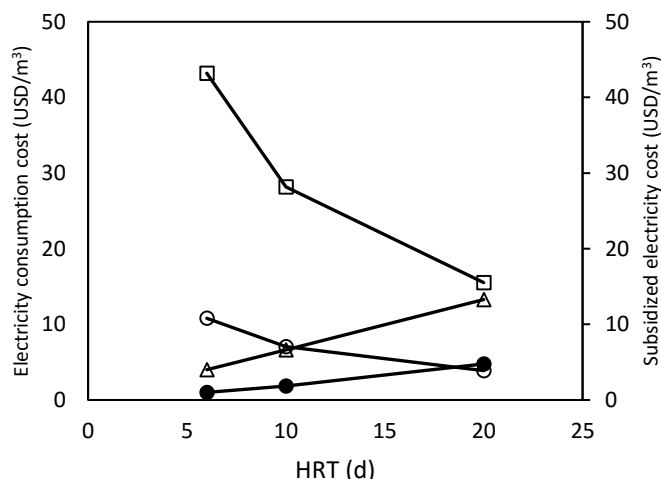
**Figure 64:** (a) Electricity consumption of: (a) UV lamp (○) compressor used for mixing in the photoreactor (△), pump for the AD process (□). Electricity (■) and heat (▲) generated from biogas. (b) Carbon dioxide emission due to electricity consumption by the UV lamp (○) and CER when biomethane was applied as electricity (■) as heat (▲) and a combination of electricity and heat (●)

Figure 64a shows that increasing the HRT<sub>AD</sub> reduced the electricity requirement of the photoreactor, in contrast, it led to an increase in electricity demand of the bioreactor. However, limitations due to the available feed concentration and reactor size could not enable an investigation of HRT<sub>AD</sub> of more than 20 days at OLR<sub>AD</sub> of 3 kg COD/m<sup>3</sup>d. Therefore, economic analysis was used to investigate cost reduction by applying renewable energy in the integrated system at various HRT<sub>AD</sub>.

### 6.3.12 Cost analysis of application of renewable energy in photodegradation

The possible cost reduction due to the application of electricity from biomethane to drive various components of the photoreactor was analysed applying cost of electricity unit of 0.08 USD/kWh (Yasar et al., 2015). Figure 65 shows that the operation cost due to electrical consumption of the photoreactor components reduced with an increase in HRT<sub>AD</sub> due to a reduction in colour intensity of the AD effluent with an increase in HRT<sub>AD</sub>. However, the cost of operating the AD reactor increased with increased HRT<sub>AD</sub> due to the long digestion time.

Considering the electricity requirement of the UV lamp (which is the major electric component of the photoreactor) and that of the AD unit, it could be considered that it was more economical to operate the integrated process at a high HRT<sub>AD</sub> than at a low HRT<sub>AD</sub> in this study. Although increasing the HRT<sub>AD</sub> from six days to 20 days led to an increase in operation cost of the AD process, the increase was only 9 USD/m<sup>3</sup> compared with a reduction of 28 USD/m<sup>3</sup> for the UV lamp operation cost when HRT<sub>AD</sub> was increased from six days to 20 days. Besides, there was a better colour and TOC reduction at high HRT<sub>AD</sub> than at low HRT<sub>AD</sub>.



**Figure 65: Electricity consumption cost of operating the photoreactor, UV lamp (□) compressor (Δ), electricity consumption for bioreactor (▲) and the electricity cost subsidised by applying bioenergy (●)**

The possible cost subsidised by renewable energy applied in photodegradation could be 31% for the UV lamp at a  $HRT_{AD}$  of 20 days while it was as low as 2% for a low  $HRT_{AD}$  of six days. The low value at a low  $HRT_{AD}$  was due to the low bioenergy production coupled with a discharge of high colour intensity from the bioreactor, which hindered photodegradation post-treatment. Generally, the electricity from biomethane could subsidise up to 24% of the total electricity cost for the photodegradation unit, which corresponds to a cost reduction of USD 4.7/ $m^3_{effluent}$ . Fuess and Garcia (2015) reported a cost reduction of 5–15% when energy from distillery effluent was utilised in the distillery industry.

#### 6.4 Conclusion

The pollution removal and energy efficiency of an integrated AD and photodegradation treatment process for distillery effluent were studied. The interaction between the OLR and hydraulic retention of the initial AD step on the efficiency of the combined process was modelled using RSM. It was found that AD as a stand-alone process was effective in TOC reduction but that it was ineffective in colour removal. In contrast, photodegradation as a stand-alone process was efficient in colour removal but performed poorly in TOC reduction. Therefore, it was necessary to combine the two technologies in such a way that AD preceded photodegradation as it led to both colour and TOC reduction of above 95%.

The integrated process was found to be efficient in energy utilisation as the renewable energy from the AD could supply up to 31% of the electricity requirement of the UV lamp in the photodegradation process, leading to an operational cost reduction of USD 4.8/ $m^3_{effluent}$ . As a result, the process led to environmental conservation as the CER when electricity from bioenergy was used to power the UV lamp was 28.8 kg  $CO_{2e}/m^3$ . This reduced the carbon dioxide emission by 30% compared with when electricity from the grid was used to power the UV lamp. Therefore, the integrated process is suitable for treating distillery effluent.

## 6.5 References

- Acharya, B.K., Mohana, S. & Madamwar, D. (2008). Anaerobic treatment of distillery spent wash - a study on upflow anaerobic fixed film bioreactor. *Bioresource Technology*, 99, 4621–6.
- Al-Momani, F., Touraud, E., Degorce-Dumas, J., Roussy, J. & Thomas, O. (2002). Biodegradability enhancement of textile dyes and textile wastewater by VUV photolysis. *Journal of Photochemistry and Photobiology A: Chemistry*, 153, 191–197.
- Bagheri, M. & Mohseni, M. (2015). Impact of hydrodynamics on pollutant degradation and energy efficiency of VUV/UV and H<sub>2</sub>O<sub>2</sub>/UV oxidation processes. *Journal of Environmental Management*, 164, 114–20.
- Borja, R., Gonzalez, E., Raposo, F., Millan, F. & Martin, A. (2002). Kinetic analysis of the psychrophilic anaerobic digestion of wastewater derived from the production of proteins from extracted sunflower flour. *Journal of Agricultural and Food Chemistry*, 50, 4628–4633.
- Borja, R., Rincón, B., Raposo, F., Domínguez, J.R., Millán, F. & Martín, A. (2004). Mesophilic anaerobic digestion in a fluidised-bed reactor of wastewater from the production of protein isolates from chickpea flour. *Process Biochemistry*, 39, 1913–1921.
- Chaudhari, P.K., Mishra, I.M. & Chand, S. (2007). Decolourization and removal of chemical oxygen demand (COD) with energy recovery: Treatment of biodigester effluent of a molasses-based alcohol distillery using inorganic coagulants. *Colloids and Surfaces A: Physicochemical and Engineering Aspects*, 296, 238–247.
- Chen, Z.-B., Cui, M.-H., Ren, N.-Q., Chen, Z.-Q., Wang, H.-C. & Nie, S.-K. (2011). Improving the simultaneous removal efficiency of COD and color in a combined HABMR-CFASR system based MPDW. Part 1: Optimization of operational parameters for HABMR by using response surface methodology. *Bioresource Technology*, 102, 8839–47.
- Duerr, M., Gair, S., Cruden, A. & McDonald, J. (2007). Hydrogen and electrical energy from organic waste treatment. *International Journal of Hydrogen Energy*, 32, 705–709.
- Fernández, N. et al. (2008). Performance evaluation of an anaerobic fluidized bed reactor with natural zeolite as support material when treating high-strength distillery wastewater. *Renewable Energy*, 33, 2458–2466.
- Fuess, L.T. & Garcia, M.L. (2015). Bioenergy from stillage anaerobic digestion to enhance the energy balance ratio of ethanol production. *Journal of Environmental Management*, 162, 102–14.
- Hampannavar, U. & Shivayogimath, C. (2010). Anaerobic treatment of sugar industry wastewater by Upflow anaerobic. *International Journal of Environmental Science and Technology*, 1, 631–639.
- Kalavathi, D., Uma, L. & Subramanian, G. (2001). Degradation and metabolization of the pigment-melanoidin in distillery effluent by the marine cyanobacterium *Oscillatoria boryana* BDU 92181. *Enzyme and Microbial Technology*, 29, 246–251.

- Moraes, B.S. et al. (2014). Anaerobic digestion of vinasse from sugarcane biorefineries in Brazil from energy, environmental, and economic perspectives: Profit or expense? *Applied Energy*, 113, 825–835.
- Moraes, B.S., Zaiat, M. & Bonomi, A. (2015). Anaerobic digestion of vinasse from sugarcane ethanol production in Brazil: Challenges and perspectives. *Renewable and Sustainable Energy Reviews*, 44, 888–903.
- Oller, I., Malato, S., Sánchez-Pérez, J.A. (2011). Combination of Advanced Oxidation Processes and biological treatments for wastewater decontamination: A review. *Science of the Total Environment*, 409, 4141–66.
- Rastegar, S.O., Mousavi, S.M., Shojaosadati, S.A. & Sheibani, S. (2011). Optimization of petroleum refinery effluent treatment in a UASB reactor using response surface methodology. *Journal of Hazardous Materials*, 197, 26–32.
- Rincón, B. et al. (2006). Kinetic models of an anaerobic bioreactor for restoring wastewater generated by industrial chickpea protein production. *International Biodeterioration and Biodegradation*, 57, 114–120.
- Salam, K.K., Agarry, S.E., Arinkoola, A.O. & Shoremekun, I.O. (2015). Optimization of operating conditions affecting microbiologically influenced corrosion of mild steel exposed to crude oil environments using response surface methodology 7, *British Biotechnology Journal*, 68–78.
- Sankaran, K., Premalatha, M., Vijayasekaran, M. & Somasundaram, V.T. (2014). DEPHY project: Distillery wastewater treatment through anaerobic digestion and phyco-remediation: A green industrial approach. *Renewable and Sustainable Energy Reviews*, 37, 634–643.
- Satyawali, Y. & Balakrishnan, M. (2008). Wastewater treatment in molasses-based alcohol distilleries for COD and color removal: a review. *Journal of Environmental Management*, 86, 481–97.
- Shu, Z., Bolton, J.R., Belosevic, M. & El Din, M.G. (2013). Photodegradation of emerging micropollutants using the medium-pressure UV/H<sub>2</sub>O<sub>2</sub> advanced oxidation process. *Water Research*, 47, 2881–9.
- Spalding-Fecher, R. (2011). What is the carbon emission factor for the South African electricity grid? *Journal of Energy in Southern Africa*, 22, 8–12.
- Wang, J.-L. & Wu, L.-B. (2004). Wastewater treatment in a hybrid biological reactor (HBR): nitrification characteristics. *Biomedical and Environmental Sciences*, 17, 373–379.
- Wilson, P.C. (2013). Water Quality Notes: Alkalinity and Hardness 1 Ecological/Management. Univ. Florida, IFAS Ext. 1–6.
- Yasar, A., Ahmad, N., Chaudhry, M.N., Rehman, M.S.U. & Khan, A.A.A. (2007). Ozone for color and COD removal of raw and anaerobically biotreated combined industrial wastewater. *Polish Journal of Environmental Studies*, 16, 289–294.
- Yasar, A., Ahmad, N. & Khan, A.A.A. (2006). Energy requirement of ultraviolet and AOPs for the post-treatment of treated combined industrial effluent. *Coloration Technology*, 122, 201–206.

- Yasar, A., Ali, A., Tabinda, A.B. & Tahir, A. (2015). Waste to energy analysis of Shakarganj sugar mills; biogas production from the spent wash for electricity generation. *Renewable and Sustainable Energy Reviews*, 43, 126–132.
- Zinatizadeh, A.A.L., Pirsahab, M., Bonakdari, H. & Younesi, H. (2010). Response surface analysis of effects of hydraulic retention time and influent feed concentration on performance of an UASFF bioreactor. *Waste Management*, 30, 1798–1807.

## 7 CFD MODELLING

### 7.1 Introduction

South Africa, as a water-stressed nation, is faced with the great challenge of addressing the water crisis (Nastar & Ramasar, 2012). Several South African regions are highly dependent on summer rainfall. With the current dwindling water supplies, South Africa needs robust and efficient technologies to treat the current available water. One of the primary causes of human, animal and aquatic health problems is the increase in contaminated water caused by industries such as petroleum, pharmaceutical, beverages and mining. Petroleum refineries are very large and complex chemical processes that provide us with useful products that include jet fuel, petrol, kerosene, diesel and feedstock for the petrochemical industry. Wastewater from petroleum refineries often contain high concentrations of organic pollutants, which are often released into the environment. These organic pollutants include aliphatic, aromatic and poly-aromatic compounds. Phenol and phenolic derivatives are among the mostly found organic pollutants present in petroleum wastewater. They are extremely harmful to microorganism life, aquatic life, the environment and humans (Zulfakar et al., 2011).

Commonly applied wastewater treatment techniques (such as coagulation, bio-decomposition, chemical precipitation, adsorption and catalytic wet air oxidation to remove toxic organic compounds) are quite often inadequate (Abhang et al., 2011). These processes have the disadvantage of transferring the pollutant from one phase into another, thereby producing secondary wastes (Primo et al., 2007). Applying AOP to degrade organic pollutants is efficient as it converts the pollutants into less harmful products. FBRs, often used in the AOP, consist of three phases (gas, liquid and solid) and quite often the mixing inside the reactor is a challenge. Therefore, analysis of mixing inside the reactor is often conducted by using CFD as it is a low-cost reactor optimisation technique. The aim of this study was to apply RSM and CFD techniques to optimise the operating conditions of the photodegradation of petroleum wastewater.

### 7.2 Methodology

The study involved investigating the treatment of petroleum wastewater by means of the heterogeneous photocatalytic oxidation process. To understand and optimise hydrodynamics and homogeneity inside the fluidized bed photoreactor, CFD simulations were done. Photodegradation experiments were conducted to determine the efficiency of this process, moreover, RSM was applied to optimise the photodegradation operating parameters. The reaction kinetics were investigated to understand the reaction mechanism of the photodegradation. The methods of experimentation, simulation and statistical modelling are described in this section.

#### 7.2.1 *Mathematical modelling*

##### 7.2.1.1 *Governing equations*

Three-dimensional transient CFD models were used to solve the local hydrodynamics inside the photocatalytic bubble column reactor. The Eulerian–Eulerian approach was used to describe the flow characteristics of each phase. In this approach, liquid is the continuous phase, whereas gas is dispersed. This means that both phases (liquid and gas) are treated as interpenetrating continua (Qi et al., 2011). Furthermore, this approach permits the modelling

of multiple separate, yet interacting phases for which equations such as mass and momentum are solved for each phase (ANSYS, 2010; Boyjoo et al., 2014). The governing differential continuity equation, which neglects the interphase mass transfer, for each phase in the photocatalytic bubble column reactor is given as:

$$\frac{\partial}{\partial t}(\epsilon_k \rho_k) + \nabla(\epsilon_k \rho_k \vec{u}_k) = 0 \quad (59)$$

where  $\epsilon_k$ ,  $\rho_k$  and  $\vec{u}_k$  are the volume fraction, density and velocity vector of phase  $k$ , respectively. The subscript  $k$  represents liquid, gas or solid phase. The momentum equation is given as:

$$\frac{\partial}{\partial t}(\epsilon_k \rho_k \vec{u}_k) + \nabla(\epsilon_k \rho_k \vec{u}_k \vec{u}_k) = -\epsilon_k \nabla P - \nabla(\epsilon_k \tau_k) + \epsilon_k \rho_k \vec{g} + \vec{F}_k \quad (60)$$

where  $\vec{g}$  and  $p$  are the gravitational acceleration and pressure gradient, respectively.  $\vec{F}_k$  represents the interfacial forces exerted on phase  $k$  due to the presence of phase  $j$ .  $\tau_k$  is the stress term of gas bubbles and is given by:

$$\tau_k = -\mu_{eff,k} \left[ (\nabla \vec{u}_k) + (\nabla \vec{u}_k)^T - \frac{2}{3} I(\nabla \vec{u}_k) \right] \quad (61)$$

where  $\mu_{eff,k}$  is the effective viscosity of the liquid, which in turn consists of three terms, namely, molecular viscosity, turbulent viscosity and bubble-induced turbulence.

$$\mu_{eff,l} = \mu_l + \mu_{T,l} + \mu_{BIT,l} \quad (62)$$

In addition, the gas phase effective viscosity is given as:

$$\mu_{eff,G} = \mu_{eff,l} \frac{\rho_G}{\rho_L} \quad (63)$$

Bubble-induced turbulence is as a result of the displacement of the liquid phase caused by the gas flowing through the liquid phase (Zhang et al., 2006). Sato et al. (1981) used this model (Eq. 64) to predict the bubble-induced turbulence in bubble column reactors:

$$\mu_{BIT,l} = \rho_L C_{\mu,BIT} \epsilon_G d_B |u_G - u_L| \quad (64)$$

where  $d_B$  is the bubble diameter and  $C_{\mu,BIT}$  is a model constant set to 0.6 in accordance to previous studies (Masood et al., 2014; Pourtousi et al., 2015). The interphase force term is due to phenomena such as cohesion, friction, pressure and other effects; therefore, a suitable expression linked to the interphase force term is needed to close Eq. 60.

$$\sum_{j=1}^n \vec{F}_k = \sum_{j=1}^n K_{gl} (\vec{u}_g - \vec{u}_l) \quad (65)$$

where  $\vec{u}_g$  and  $\vec{u}_l$  are the gas and liquid phases velocities and  $K_{gl}$  is the interphase momentum exchange coefficient.

In fluid-fluid flow scenarios, the secondary phases are bubbles or particles. For example, when modelling a bubble column reactor consisting of a liquid phase and a gas phase (unequal number of phases), the liquid phase is modelled as the primary fluid due as the gas phase will form bubbles or droplets (dispersed). The momentum interphase exchange coefficient in such processes is described by:

$$K_{gl} = \frac{\rho_g f}{6\tau_g} d_g A_i \quad (66)$$

where  $f$  is the friction function and is expressed based on the respective interphase exchange coefficient model,  $A_i$  is the interfacial transfer area and  $\tau_g$  is the particulate relaxation time:

$$\tau_g = \frac{\rho_g d_g^2}{18\mu_g} \quad (67)$$

where  $\mu_g$  and  $d_g$  are the viscosity and diameter of the secondary phase, respectively.

The interfacial area is a cross-sectional area that exists when two different phases come into contact and is expressed per unit volume of mixture. The modelling of this variable is essential due as it assists in predicting the transfer of energy, momentum and mass from one fluid to another. Therefore, when modelling a multiphase reactor using the Eulerian model, the interfacial area was calculated by resolving the algebraic relationship between the interfacial area concentration and the bubble diameter specified (ANSYS, 2010). The interfacial area model originates from the surface area to volume ratio of the particle (Eq. 68).

$$A_i = \frac{\pi d_g^2}{\frac{1}{6} \pi d_g^3} = \frac{6}{d_p} \quad (68)$$

However, there are various algebraic interfacial area models that can be used to model the interfacial area. In the current study, the symmetric model was used (Eq. 69). The diversity of this model is that it includes the volume fraction, which directs the interfacial area concentration to approach 0 as the volume fraction approaches 1 (ANSYS, 2010).

$$A_i = \frac{6\epsilon_g(1-\epsilon_g)}{d_g} \quad (69)$$

### 7.2.1.2 Interfacial forces

In the current study, a combination of all interfacial forces was used as recommended by literature. The source of the drag force is caused by the resistance experienced by the bubbles as they move through the liquid. The pressure distribution that surrounds the bubble creates form drag and the viscous stress creates skin drag (Tabib et al., 2008). The interphase momentum transfer due to the drag force is given as:

$$\vec{F}_{lg}^D = \frac{3}{4} \frac{C_{D,lg}}{d_g} \rho_l \epsilon_g |\vec{u}_g - \vec{u}_l| (\vec{u}_g - \vec{u}_l) \quad (70)$$

where  $C_D$  is the drag coefficient and  $d_g$  is the bubble diameter. The superficial gas velocity in this study was varied between 5.77 mm/s and 23.1 mm/s, signifying a homogeneous flow regime. In this regime, the bubbles are assumed to be spherical, and to have similar sizes, shapes and velocities, and the bubble breakup, collision and coalescence are negligible (Pourtousi et al., 2015). Therefore, the Grace et al. (1978) relation was chosen to compute the drag coefficient and is given by:

$$C_D = \frac{4}{3} \frac{g d_b \Delta \rho}{u_T^2 \rho_l} \quad (71)$$

where  $d_b$  is the mean bubble diameter,  $\Delta \rho$  is the density difference between the liquid and gas phases and  $u_T$  is the terminal rise velocity of the bubble and is given by (ANSYS, 2010):

$$u_T = \frac{\mu_l}{\rho_l d_b} Mo^{-0.149} (J - 0.857) \quad (72)$$

where  $Mo$  is the Morton number related to the fluid property and is defined by:

$$Mo = \frac{\mu_l^4 g \Delta \rho}{\rho_l^2 \sigma^3} \quad (73)$$

where  $\sigma$  is the surface tension and  $J$  is given by the piecewise function:

$$J = \begin{cases} 0.94H^{0.757} & 2 < H \leq 59.3 \\ 3.42H^{0.441} & H > 59.3 \end{cases} \quad (74)$$

$H$  is expressed as:

$$H = \frac{4}{3} Eo Mo^{-0.149} \left( \frac{\mu_l}{\mu_{ref}} \right)^{-0.14} \quad (75)$$

where  $\mu_{ref} = 0.0009$  kg/(m.s) is the reference viscosity of water at a specific temperature and pressure (Qi et al., 2011).  $Eo$  is the Eötvös number defined as:

$$Eo = \frac{g \Delta \rho d_b^2}{\sigma} \quad (76)$$

The lift force acts on the particles of the secondary phase (bubbles) and is mainly due to the velocity gradients in the primary phase. Therefore, the lift force becomes more significant for larger bubble sizes. This force is created by the net effect of pressure and stress exerted on the surface of the secondary phase. The lift force acting on the primary ( $l$ ) and secondary ( $g$ ) phases can be calculated as:

$$\vec{F}_{lg} = -C_L \rho_l \epsilon_g (\vec{u}_g - \vec{u}_l) \times (\nabla \times \vec{u}_l) \quad (77)$$

The sign convention of this force depends on the orientation of the slip velocity with respect to the gravity vector.  $C_L$  is the lift coefficient, which was computed using the Saffman–Mei lift model (ANSYS, 2010):

$$C_L = \frac{3}{2\pi\sqrt{\text{Re}_\omega}} C'_L \quad (78)$$

where  $C'_L = 6.46$  and  $0 \leq \text{Re}_p \leq \text{Re}_\omega \leq 1$ . Here,  $\text{Re}_p$  is the particle Reynolds number and is the voracity Reynolds number. In addition, the model was extended by Mei and Klausner (1994) by empirically representing it as:

$$C'_L = \begin{cases} 6.46 \times f(\text{Re}_p, \text{Re}_\omega) & \text{Re}_p \leq 40 \\ 6.46 \times 0.0524 (\beta \text{Re}_p)^{1/2} & 40 < \text{Re}_p < 100 \end{cases} \quad (79)$$

where

$$\beta = 0.5 \left( \frac{\text{Re}_\omega}{\text{Re}_p} \right) \quad (80)$$

$$f(\text{Re}_p, \text{Re}_\omega) = \left( 1 - 0.3314 \beta^{0.5} \right) e^{-0.1 \text{Re}_p} + 0.3314 \beta^{0.5} \quad (81)$$

The wall lubrication force can be used to model bubbly flows (liquid-gas) using the Eulerian approach. The wall lubrication force drives the secondary phase away from the wall, resulting in the secondary phase concentrating in the area near but not immediately to the wall. The wall lubrication force exerted on the secondary phase is given by (ANSYS, 2010):

$$\vec{F}_{w,l} = C_w \rho_l \epsilon_s \left[ (\vec{u}_l - \vec{u}_g) \right]^2 \vec{n}_w \quad (82)$$

where  $\vec{n}_w$  is the unit normal pointing away from the wall;  $C_w$  is the wall lubrication coefficient and is computed using the Antal et al. (1991) model:

$$C_w = \max \left( 0, \frac{C_{w1}}{d_b} + \frac{C_{w2}}{y_w} \right) \quad (83)$$

where  $C_{w1}$  and  $C_{w2}$  are the non-dimensional coefficients. For the current study, they were specified to be  $-0.0064$  and  $0.016$  (Krepper et al., 2005), respectively.  $y_w$  is the distance nearest to the wall and when:

$$y_w \leq - \left( \frac{C_{w2}}{C_{w1}} \right) d_b \quad (84)$$

where the values of  $C_{w2}$  and  $C_{w1}$  become default when:

$$y_w \leq 5d_b \quad (85)$$

The effects of turbulent fluctuations on the liquid velocity, caused by the turbulent eddies in the continuous phase, interact with the bubbles by transporting them from a region of high concentration to a region of low concentration (ANSYS, 2010). This phenomenon is described by the turbulent dispersion force that encapsulates the interphase turbulent momentum transfer and acts as a turbulent diffuser for the dispersed flow. The turbulent dispersion force, which was modelled using the Burns et al. (2004) model in the current study, can be derived from the Favre averaging of the drag term:

$$\vec{F}_{TD,l} = -\vec{F}_{TD,g} = C_{TD} K_{lg} \frac{D_l}{\sigma_{lg}} \left( \frac{\nabla \epsilon_g}{\epsilon_g} - \frac{\nabla \epsilon_l}{\epsilon_l} \right) \quad (86)$$

where  $C_{TD}$  is the turbulent dispersion coefficient, which was assigned a value of 0.2 for the current study.  $\sigma_{lg}$  is the Schmidt number; a value of 0.9 is typically used (ANSYS, 2010).

### 7.2.1.3 Turbulence modelling

Modelling turbulence in a multiphase fluid flow problem is an extremely complex task due to the increase in the number of terms that require closure in the momentum equations. Closure models are essential in turbulence modelling as they assist in unfolding the effects of turbulent variations of velocities and scalar variables (ANSYS, 2010). The standard  $k$ - $\epsilon$  model was used in the current study to capture the turbulence characteristics in the liquid phase. The choice of using the standard  $k$ - $\epsilon$  model is due to its simplicity, its low computational requirements, being relatively inexpensive and being preferred to predict the liquid velocity and gas hold-up profiles under low superficial gas velocity (Pourtousi et al., 2015). Furthermore, it has been shown that it gives a fair prediction of the flow field. When the standard  $k$ - $\epsilon$  model is applied, the turbulent eddy viscosity model is used to determine the averaged fluctuating turbulent characteristics (length scale and characteristic time). The turbulent eddies can be defined in terms of the characteristic time as:

$$\tau_{t,l} = \frac{3}{2} C_\mu \frac{k}{\epsilon} \quad (87)$$

where  $\tau_{t,l}$  is the characteristic time. In addition, the energetic turbulent eddies can be described by the length scale ( $L_{t,l}$ ) as:

$$L_{t,l} = \sqrt{\frac{3}{2}} C_\mu \frac{k^{3/2}}{\epsilon} \quad (88)$$

The turbulent eddy viscosity ( $\mu_{T,l}$ ) can be shown by the following equation:

$$\mu_{T,l} = \rho_l C_\mu \frac{k^2}{\epsilon} \quad (89)$$

where  $k$  and  $\epsilon$  are the turbulent kinetic energy and turbulent kinetic energy dissipation rate, respectively, and are calculated from their governing equations:

$$\frac{\partial}{\partial t} (\rho_l \epsilon_l k) + \nabla (\rho_l \epsilon_l u_l k) = -\nabla \left( \epsilon_l \frac{\mu_{eff,l}}{\sigma_k} \nabla k \right) + \epsilon_l (G - \rho_l \epsilon) \quad (90)$$

$$\frac{\partial}{\partial t} (\rho_l \epsilon_l \epsilon) + \nabla (\rho_l \epsilon_l u_l \epsilon) = -\nabla \left( \epsilon_l \frac{\mu_{eff,l}}{\sigma_\epsilon} \nabla \epsilon \right) + \epsilon_l \frac{\epsilon}{k} (C_{\epsilon 1} G - C_{\epsilon 2} \rho_l \epsilon) \quad (91)$$

where  $\sigma_k = 1$  and  $\sigma_\varepsilon = 1$  are the Prandtl numbers. The standard values of all the model constants are  $C_\mu = 0.09$ ,  $C_{\varepsilon 1} = 1.44$  and  $C_{\varepsilon 2} = 1.92$ . The term  $G$  in Eq. 90 and Eq. 91 is the production of turbulent kinetic energy and is formulated by:

$$G = \tau_L : \nabla u_L \quad (92)$$

In the current study, the effect of the dispersed phase on the turbulence of the multiphase equations was considered since the Eulerian multiphase approach was used along with the standard  $k$ - $\varepsilon$  turbulence model. The terms ( $\Pi_{lg}$  and  $\Pi_{eq}$ ) are representation of the source terms and are due to the influence of the dispersed phase. The instantaneous equation which is linked to the continuous phase is derived from the source term  $\Pi_{lg}$ .

$$\Pi_l = C_s \sum_{p=1}^M \frac{K_{lg}}{\varepsilon_l \rho_l} X_{lg} [k_{lg} - 2k_l + \vec{U}_{lg} \cdot \vec{U}_{dr}] \quad (93)$$

where  $k_{lg}$  is the covariance of the velocities for both the liquid and gas phase,  $C_s$  is a user-modifiable model constant which was specified as 1 (default value),  $\vec{U}_{lg}$  is the relative velocity and  $\vec{U}_{dr}$  is the drift velocity computed as:

$$\vec{U}_{dr} = -D_{lg} \cdot \left( \frac{\nabla \varepsilon_g}{\varepsilon_g} - \frac{\nabla \varepsilon_l}{\varepsilon_l} \right) \quad (94)$$

where  $D_{lg}$  is the fluid-particulate dispersion tensor.

$$k_{lg} = 2k_l \left( \frac{b + \eta_{lg}}{1 + \eta_{lg}} \right) \quad (95)$$

$$k_g = k_l \left( \frac{b^2 + \eta_{lg}}{1 + \eta_{lg}} \right) \quad (96)$$

$$X_{lg} = \frac{\rho_g}{\rho_g + C_{VM} \rho_l} \quad (97)$$

where  $X_{lg} \sim 1$  for granular flows.

The formulation of the turbulence models for the dispersed phase is shown by the characteristic particle relaxation time ( $\tau_{gl}^F$ ), which is associated with the inertial effects exerted on the dispersed phase.

$$\tau_{gl}^F = \frac{\rho_l d_g^2}{18 \mu_c f(\text{Re}, \varepsilon_l)} \left( 1 + C_{VM} \frac{\rho_l}{\rho_g} \right) \quad (98)$$

The energetic turbulent eddies can be represented by the time scale ( $\tau_l^t$ ), described as:

$$\tau_l^t = \frac{3C_\mu k_l}{2\varepsilon_l} \quad (99)$$

The cross-trajectory is the main characteristic that affects the eddy particle interaction and is described as:

$$\tau_{gl}^t = \frac{\tau_l^t}{\sigma_1 \sqrt{(1 + C_\beta \xi_\tau^2)}} \quad (100)$$

where  $\sigma_1$  is equated to 1 and  $C_\beta$  is described as:

$$C_\beta = 1.8 - 1.35 \cos^2 \theta \quad (101)$$

$\xi_\tau^2$  can be calculated as:

$$\xi_\tau^2 = \frac{|\vec{u}_g - \vec{u}_l|}{\sqrt{\frac{2k_l}{3}}} \quad (102)$$

## 7.2.2 Numerical approach

CFD has a substantial contribution in the modelling of chemical industrial equipment due to its ability to model complex hydrodynamic phenomena efficiently. The shortfalls regarding the application of CFD are the endless parameters that need to be adjusted to achieve accuracy and convergence at minimal expense. Previous simulations have shown that the most influential parameters that affect accuracy and convergence in transient simulations are: grid size, discretization scheme and time step size. Furthermore, 12 simulations were carried out by varying the aforementioned parameters comparing to experimental results from Kulkarni et al. (2007) as a reference case.

In the current study, a set of governing equations, explained in Section 7.2.1, were solved numerically by following these stages:

- (i) Generating the appropriate grid domain.
- (ii) Transforming the governing equations into algebraic equations.
- (iii) Choosing the discretization schemes.
- (iv) Formulating the discretized equation at every grid location.
- (v) Formulating the pressure equation.
- (vi) Developing a suitable iteration scheme to obtain a final solution.

These solution steps were carried out using ANSYS Fluent 16.0 software. The equations of motion and continuity were solved, coupled with  $k$ - $\epsilon$  equations, to obtain a complete flow pattern by scrutinising the gas hold-up, liquid velocity and turbulence modelling profiles.

### 7.2.2.1 Geometry

The geometry studied is similar to that discussed in the *Reactor operation* section. It consists of a cylindrical body comprising four side ports and a conical top section suited for degassing. The cylindrical section has an inside diameter of 40.8 mm with a height of 600 mm. The conical section has an inside diameter of 80 mm with a height of 100 mm. The three-dimensional geometry was sliced into half, thereby reducing the computation domain and time and imposing an assumption of symmetrical flow.

### 7.2.2.2 Grid generation

A grid-independent study was conducted using three types of grid (fine, medium and coarse). The grids were created using an ANSYS mesh as shown in Figure 66, where all grids consisted of hexahedral cells structurally placed throughout the computational domain. When compared with the tetrahedral or triangle mesh, the hexahedral mesh can estimate a complex geometry resulting in fewer cells, lower computational cost and better numerical analysis (Pourtoysi et al., 2015). The finer grid consisted of 500 000 elements with an element size of 1.2 mm. The medium grid consisted of 166 000 elements with an element size of 2.56 mm. The coarser grid consisted of 80 000 elements with an element size of 25 mm.

The inflation feature was activated to capture the boundary layer at the walls and consisted of a maximum of five layers. Inflation is a boundary layer capturing method in CFD that is useful for resolving gradient variations at the wall of a variable of interest (ANSYS, 2011). The orthogonal quality of the fine, medium and coarse grids were 0.253, 0.245 and 0.247 respectively; these values are well within the acceptable range (ANSYS, 2010). Grid-independent studies are still essential for multiphase contacting equipment such as fluidized bed (photo)reactors. Detailed grid-independent studies have revealed the relationship between particle size and cell size. Cloete et al. (2014) reported that small particle sizes require finer grids, whereas larger particle sizes ( $\sim 500 \mu\text{m}$ ) are less strict to grid sizes. Overall, grid-independent studies are useful in reducing the number of simulations and computational time.

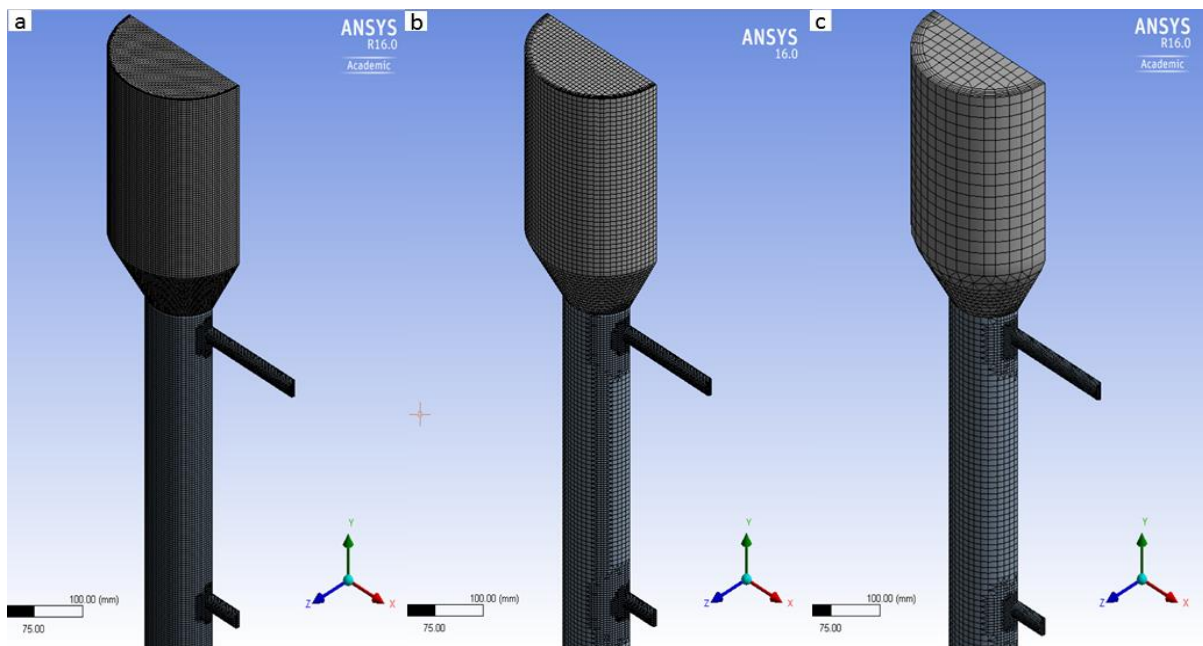


**Figure 66: Simulation grid for an FBR : (a) Fine cells; (b) Medium cells and (c) Coarse cells**

### 7.2.2.3 Initial and boundary conditions

All simulations were carried out using air as the gas phase and deionised water as the liquid phase. The walls were set as stationary walls with a no-slip condition for both phases (Kulkarni et al., 2007). The air inlet was defined as a fully open inlet where the gas velocity was computed based on the superficial gas velocity of 20 mm/s with an air volume fraction of 1. The pressure outlet boundary condition was applied at the liquid outlet and the degassing for the gas outlet

(Li et al., 2009). The initial conditions specified are essential because they influence the direction and accuracy of the solution. Therefore, to initialise the solution, parameters such as turbulence, volume fraction, axial, radial and tangential liquid and gas velocities were assigned the value of 0 at  $t = 0$  s as shown by Table 23.

For all the simulations, the gas distributor (which is a sintered plate) was modelled as a uniform gas inlet with a superficial gas velocity being specified (Li et al., 2009). The bubble diameter at the inlet of the gas distributor was assumed to be 1.96 mm based on experimental data (Kulkarni et al., 2007). The use of a single mean bubble size in bubble columns is a reasonable assumption when operating within the homogeneous flow regime (Liu & Hinrichsen, 2014). The backflow volume fraction was specified as 1 to reduce the entrainment of liquid.

**Table 23: Solution initiation**

Parameter	Value
$u_l, v_l, w_l, v_g, w_g$ (mm/s)	0
$u_g$ (mm/s)	20
$\epsilon_g$	$1 \times 10^{-08}$
$k$ (J/kg)	0
$\epsilon$ (m <sup>2</sup> /s <sup>3</sup> )	0

#### 7.2.2.4 Numerical procedure

All simulations were carried out using ANSYS Fluent 16.0 software, which uses the finite control volume discretization method. There are several discretization methods: finite difference, Lattice Boltzmann and finite control volume; however, the finite control volume method can compute single and multiphase flow accurately inside a computational domain consisting of uniform and non-uniform grid (Pourtousi et al., 2015). The equations of continuity and momentum balance were solved, together with  $k$ - $\epsilon$  equations, using the Euler two-fluid approach to obtain a complete flow pattern. This approach captures water (primary phase) as a continuous phase and air as a secondary dispersed phase thereby solving the continuity and momentum equations for each phase. The CFD simulations were carried out by varying the number of cells, discretization scheme and time step size to determine the combination that would produce the best accurate simulation data with minimal simulation time. The interfacial forces were kept constant in all simulations and are listed in Table 24.

**Table 24: Interfacial forces obtained from literature**

Force	Law	Constant	Source
Drag	Grace		Qi et al. (2011)
Lift	Saffman		Qi et al. (2011)
Wall lubrication	Antal et al.	$cw1 = 0.0064, cw2 = 0.016$	Krepper et al. (2005)
Turbulent dispersion	Burns et al.	0.2	
Turbulent interaction	Sato	0.6	Default

The phase coupled semi-implicit method for pressure-linked equations (SIMPLE) algorithm, which is an extension of the SIMPLE algorithm for multiphase flow, was used for pressure-velocity coupling and correction. The time step size was varied and all simulations were computed for 30 s to obtain pseudo-steady state. The pseudo-steady-state period was obtained by allowing the fluctuations of the surface monitors to stabilise, which occurred after 30 s of simulation time. The under-relaxation parameters were kept constant along with the convergence criteria of  $1.0 \times 10^{-03}$  (Kulkarni et al., 2007). The CFD simulations were validated by comparing them to experimental data obtained from Kulkarni et al. (2007) and the average sum of square errors was used as a response parameter. The average sum of square errors data between simulation and experiment was computed as:

$$E_i = \sum_{i=1}^N (x_i - \hat{x}_i)^2 \quad (103)$$

$$\bar{E} = (E_1 + E_2 + \dots + E_n) / n \quad (104)$$

where  $E_i$ ,  $x_i$  and  $\hat{x}_i$  are the relative error, predicted and experimental values of point  $i$ , respectively.  $\bar{E}$  is the average of all the relative errors (average sum of square errors).

### 7.2.3 Experimental

#### 7.2.3.1 Materials and chemicals

The photocatalyst that was used in the current study was the commercially available titanium dioxide Degussa P25 due to its affordability, availability, insolubility in water, resistance to various chemicals and non-toxicity (Shahrezaei et al. 2012a). Titanium dioxide mainly consists of anatase ( $\pm 98\%$ ) with a particle size of 30 nm (nano-sized) and a surface area of 49.2–50 m<sup>2</sup>/g (Shahrezaei et al., 2012b; Ohno et al., 2001). It was purchased from Sigma Aldrich (South Africa). Hydrochloric acid [32% (v/v)] and sodium hydroxide (solution) were used to adjust the pH level of the stock solution, and were purchased from Labchem and Associated Chemical Enterprises, respectively. Phenol, which was used as a model pollutant to simulate wastewater, was purchased from Labchem. The chemicals used were of analytical reagent-grade quality and were used without any further purification. All photodegradation and hydrodynamics experiments were conducted using deionised water obtained from a Milli-Q<sup>®</sup> Direct Water Purification System that purified the tap water to reach a resistivity of 18.2 M $\Omega$ ·cm (25°C) and a TOC value of 5 ppb.

#### 7.2.3.2 Catalyst and wastewater preparation

For economic reasons, a catalyst should be able to be recycled or regenerated in order to be reused to reduce the cost of the catalyst loading. A limiting factor with the TiO<sub>2</sub> photocatalyst is its nano-size character, which makes it difficult to separate from the petroleum wastewater post-treatment. Due to this limiting factor, the TiO<sub>2</sub> photocatalyst in the current study was agglomerated to form denser particle sizes using colloidal silica, consequently, enhancing separation after treatment. The petroleum wastewater was simulated by synthesising a stock solution consisting of phenol (model contaminant) at a specific concentration (30 ppm). Phenol was used as a model pollutant because it is the most common pollutant present in petroleum and/or industrial wastewater systems.

A catalyst composite, containing 60% TiO<sub>2</sub> in silica solution, was synthesised based on a study by Khune et al. (2014). Specific amounts of TiO<sub>2</sub> and colloidal silica solution were mixed by hand together inside a beaker to form a Bingham plastic mixture (non-Newtonian). The mixture was then laid on a glass bowl and oven-dried at 60°C to remove moisture. The dried sample was crushed and screened to a particle size range of 300–1000 µm. The screened particles were washed with 0.1 M HCl to eliminate left-over alkalinity. The acidified particles were neutralised several times using deionised water and air-dried for 24 hours to obtain the final composite catalyst. During the neutralisation process, the pH level of the wash was monitored until it reached a neutral value (~6.8).

#### 7.2.3.3 Analytical methods

Phenol was used as a model pollutant. The samples were filtered through a 25 mm syringe filter consisting of a 0.45 µm glass fibre prefilter (GHP) membrane before analysis. The concentration of phenol was determined using a PerkinElmer Flexar™ FX-10 ultrahigh performance liquid chromatography (UHPLC) system. The system consisted of a PerkinElmer Series photodiode array plus detector, auto-sampler, Brownlee Validated C8 column (150 mm × 4.6 mm, 5 µm particle size) and two UHPLC pumps. The PDA detector operated at specific excitation and emission wavelengths of 275 nm and 313 nm, respectively. The mobile phase was made up of methanol and pure water at 60% and 40% (v/v), respectively, which was pumped at a flow rate of 1.0 mL/min. The injection volume was 50 µL and the detection response time was 0.1 s.

The TOC was analysed using a Teledyne Tekmar TOC Torch analyser. The Torch analyser uses static pressure concentration to analyse TOC using high temperature combustion. It has an auto-sampler with three vial rack choices, automated calibration and inter-dilution that dilutes overrange samples to within the working calibration, PC driven control and has a carbon detection level range of 50 ppb to 30 000 ppm.

#### 7.2.3.4 Experimental design

There are five operating variables (reaction time, pH level, initial concentration of pollutant, superficial gas velocity and catalyst loading) that mostly influenced the photodegradation of organic pollutants as shown in literature (Shahrezaei et al., 2012a; Cheng et al., 2012). Therefore, the influence of these reaction conditions on the photodegradation of phenolic wastewater was investigated using RSM. The experimental design used in the current study was full factorial with axial points. It was selected due to its ability to examine the results, changing several variables simultaneously thereby revealing the interdependency of the parameters. While this design is complex, its advantages are less costly and less time-consuming. Table 25 shows the factorial design setup consisting of four variables ( $k = 4$ ) and the coded variables, determined by using Eq. 105 were set at five levels:

- -2 (minimum)
- -1 (low)
- 0 (central)
- +1 (high)
- +2 (maximum)

After conducting the experiments according to the experimental matrix (Table 2), RSM was conducted by applying the central composite design using Design Expert<sup>®</sup> Software of Stat-Ease Inc. (version 6.0.6) to model and optimise the reaction conditions.

$$x_i = \left( \frac{z_i - z_i^0}{\Delta z_i} \right) \quad (105)$$

where  $x_i$  is the coded level,  $\Delta z_i$  is the distance between the real value at the central point and the real value in the low or high level of a variable (step change),  $z_i$  is the real value and  $z_i^0$  is the real value in the central point.

**Table 25: Experimental design**

Parameter	Levels				
	$-\alpha$ (-2)	-1	0	+1	$+\alpha$ (+2)
Initial pH level	2	3.5	5	6.5	8
Catalyst loading (g/L)	0	1	2	3	4
Reaction time (min)	60	120	180	240	300
Superficial gas velocity (mm/s)	5.77	8.66	11.55	17.32	23.10

Accordingly, the overall experimental design consisted of 30 experiments, determined by using Eq. 25, which were made up of eight axial points ( $n_A$ ), 16 full factorial points ( $n_F$ ) and six replications at the centre ( $n_C$ ). In central composite design, the major operating parameters, namely, pH level (A), catalyst loading (B), superficial gas velocity (C) and reaction time (D) were considered as independent variables, whereas phenol degradation (%) was observed as a response variable. A sequential model fitting test was conducted to select a suitable model. A second-order polynomial model (Eq. 20) was used to fit the data found from the 30 experiments. ANOVA was used to attain the interaction between the process variables and the response parameter, determine the statistical significance and reliability of each term in the polynomial model, and determine the graphical analysis of the data. The regression coefficients in the polynomial equation were used to produce three-dimensional surface response and contour plots. The process variables were optimised by solving the regression equation and analysing data graphically.

#### 7.2.4 Photodegradation experiments

The photocatalytic degradation of phenol was performed using a solar photocatalytic FBR. All photodegradation experiments were conducted outdoors (rooftop from 09:00 to 15:00) to use sunlight as the UV source. The reactor was operated in batch mode. Figure 67 shows a schematic diagram of the reactor, which is cylindrical ( $H = 600$  mm and  $d_i = 40.8$  mm) with a top conical section ( $H = 100$  mm and  $d_i = 80$  mm) that was used for degassing. The reactor consisted of four strategically placed side ports, where the top (wastewater outlet) and bottom (wastewater inlet) side ports were used for wastewater recirculation by a peristaltic pump. The purpose of wastewater recirculation – although it somewhat complicated the hydrodynamic behaviour as opposed to having a static column of liquid – was assisting in the hydrodynamic mixing within the reactor.

The reactor was made out of borosilicate glass, a material which has been used extensively by researchers for solar photocatalysis (Boyjoo et al., 2013; Shahrezaei et al., 2012b). Shiota et al. (2016) demonstrated that borosilicate (Pyrex type) has good photon emission capabilities. During all experiments, 850 mL of aqueous phenol feed solution with a concentration of 30 ppm was transferred into the reactor. The initial pH of the feed solution was adjusted accordingly using HCl (1.0 M) or NaOH (1.0 M) and the pH level was measured using a pH meter (Inolab model no. 7110). The composite catalyst was loaded into the reactor and a peristaltic pump was used for wastewater recirculation. A compressor was used to feed air into the reactor, through the bottom, where it was evenly distributed by a sintered plate type distributor with a pore size of 10–15  $\mu\text{m}$ . The bed was fluidized by the air.

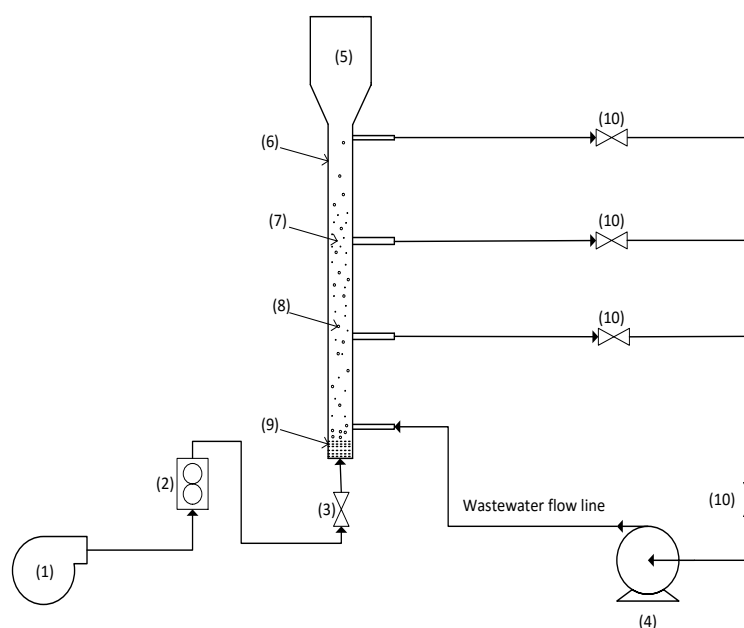


**Figure 67: Experimental setup of a solar photocatalytic FBR: (1) Compressor; (2) Flow meter; (3) Non-return valve; (4) Peristaltic pump; (5) Degassing zone; (6) Fluidized bed photoreactor; (7) Catalyst particles; (8) Air bubbles; (9) Gas distributor; and (10) Ball valves**

### 7.2.5 Reaction kinetics experiments

The Langmuir–Hinshelwood (L–H) model (Eq. 106) is generally used to determine the reaction kinetics of organic water impurities such as aniline, phenol and its derivatives. It was reported that the L–H model follows pseudo-first-order decay kinetics (Shahrezaei et al., 2012a). Many researchers prefer the L–H model due to its ability to account for both adsorption ( $b$ ) and photodegradation ( $k$ ) kinetics. The adsorption and photodegradation reaction kinetics were evaluated by monitoring the TOC as a response variable for the degradation of phenol.

$$-\frac{dC}{dt} = k_r \frac{bC}{1 + bC} \quad (106)$$

The kinetic experiments were set up (Figure 67) and operated similarly to the photodegradation experiments. However, the TOC analyses were conducted in 30-minute intervals for a period of three hours. The optimum operating conditions obtained from the photodegradation experiments were used to conduct the reaction kinetic experiments. The TOC reduction ( $\mathcal{G}_R$ ) was determined by:

$$g_R = \frac{C_{\text{TOC}_0} - C_{\text{TOC}}}{C_{\text{TOC}}} \times 100\% \quad (107)$$

where  $C_{\text{TOC}_0}$  and  $C_{\text{TOC}}$  are the concentrations of TOC initially and after, respectively.

To evaluate the results of Bechambi et al. (2015) and Kim Phuong et al. (2016), where it was reported that when the initial concentration of a pollutant is low and/or adsorption is relatively weak, then Equation 108 can be employed. The adsorption study was conducted first by covering the reactor with a dark black plastic to prevent light energy from penetrating into the reactor. As soon as TOC reached equilibrium, the plastic was removed and photodegradation commenced.

$$\ln\left(\frac{C_o}{C}\right) = k_r b t = K_{app} t \quad (108)$$

where  $C_o$  and  $C$  are the initial and final concentration of organic pollutant and  $K_{app}$  is the apparent rate constant used as a simple kinetic variable for different photocatalysts (Bechambi et al., 2015).

Samples of 50 mL were taken from the agitated wastewater solution at 30-minute intervals, filtered through a 25 mm syringe filter consisting of a 0.45  $\mu\text{m}$  glass fibre prefilter membrane and analysed using the Teledyne Tekmar TOC Torch analyser. The TOC data was used to fit both the linear and second-order models to determine the reaction order. In addition, the coefficient of regression ( $R^2$ ) was used to determine the best fitting empirical model and the chosen empirical model was used to determine the apparent reaction rate constant.

## 7.3 Results and Discussion

### 7.3.1 CFD simulation

The influence of CFD setting methods (time step size, discretization scheme and grid size) that significantly affect simulation accuracy and convergence have been discussed and presented in this section. Optimisation of these setting methods has been examined using four response variables, namely, axial liquid velocity, local gas hold-up and turbulence profiles. The model developed was validated by studying the effect of superficial gas velocity on the global gas hold-up where the CFD simulations were compared with experimental results.

#### 7.3.1.1 Grid independence

A grid-independent study was conducted as shown previously in Figure 66. Three types of grid (coarse, medium and fine) were generated using ANSYS mesh. For all the cases of this study, the setting methods such as discretization scheme, time step size, turbulence model and interfacial forces were kept constant. It is worth noting that the purpose of the grid-independent study was not to confront the comparison between simulation and experimental results but rather to evaluate how grid resolution affects simulation results. This was done by computing the sum of square errors for each grid size as shown in Table 26. The results obtained show that the fine grid size gave the lowest error (0.0308) whereas the coarse grid size gave the highest error (0.0524).

A grid size with finely structured cells produces reasonable accuracy because the grid is aligned with the discretization of the governing equations of each cell (Laborde-Boutet et al., 2009). Furthermore, fine grid structures work well for studies consisting of particle sizes similar to the grid in size (Cloete et al., 2014). There was no significant difference between the medium and coarse grids; therefore, to simplify and reduce the number of simulations to be conducted, only fine and coarse grids were considered in the numerical optimisation study.

**Table 26: Grid independence study**

<b>Grid resolution</b>	<b>Error</b>
Fine (500 000)	0.0308
Medium (166 000)	0.0506
Coarse (80 000)	0.0524

### 7.3.1.2 Response surface analysis

Contour plots are a good approach to obtain insight into the effect of each variable in a factorial experiment (Fakhri et al., 2016). The current experiment consisted of several factors, which therefore makes it a quantitative experiment: contour plots are useful to visualise the effects of several factors on a response parameter. Figure 68 shows a contour plot of the effect of a discretization scheme and number of cells on a response parameter (error), whereby the time step size was kept constant (0.001). Literature has shown that an increase in the number of cells results in a more accurate (less error) solution at a cost of prolonged computational time, whereas a decrease in the number of cells produces a less accurate solution with less computational time (Laborde-Boutet et al., 2009).

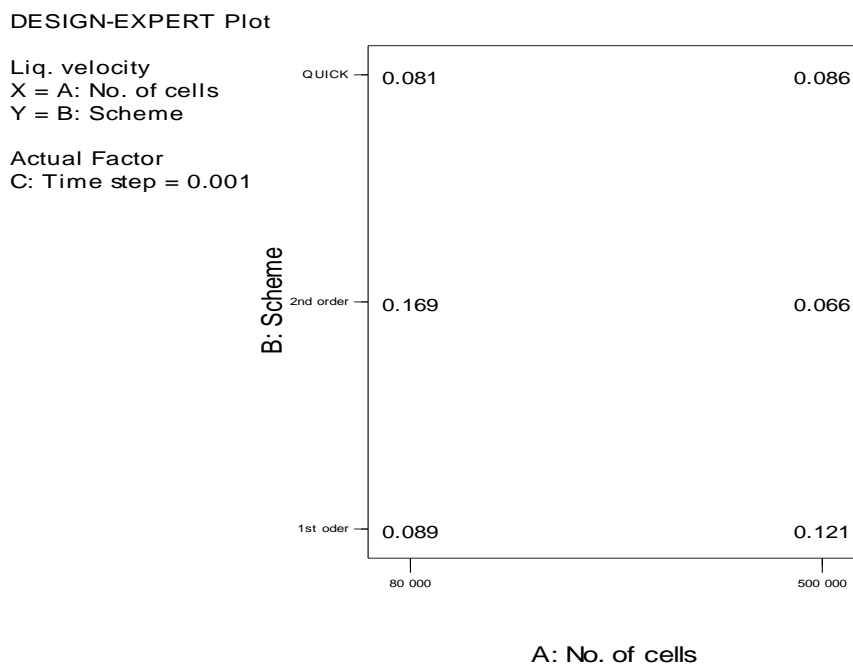


**Figure 68: Effect of discretization scheme and number of cells on a response parameter (error) where the time step size was kept constant (0.001)**

This can be seen in Figure 68 where the second-order scheme obtained an error of 0.169 for 80 000 cells, which decreased to 0.066 for 500 000 cells. However, the first-order and QUICK scheme did not display the same trend because the QUICK scheme is refractory to converge, particularly in a fine mesh, which results in an erroneous solution (Li & Zhong, 2015). The first-order scheme is quite straightforward to converge and requires less computational time, however, it results in a less accurate solution. The misalignment between the grid and the flow, particularly, in the liquid recirculation zones increases the numerical diffusion error in the first-order scheme (Laborde-Boutet et al., 2009). It is evident when observing the difference between the first-order and QUICK scheme for both number of cells. There is a decrease in error, which signifies that the QUICK scheme is more accurate than the first-order scheme.

### 7.3.1.3 Axial liquid velocity profiles

Figure 69 compares CFD and experimental data for axial liquid velocity profiles at different axial locations ( $H/D = 0.2$ ,  $H/D = 2.6$  and  $H/D = 5.0$ ) of the reactor. The plot for axial liquid velocity profile displayed a radial variation for all three graphs; the liquid velocity had an upward movement at the centre and a downward movement near the wall, which was caused by the recirculation of the liquid as the gas flows up the column (Kulkarni et al., 2007). Bubbles tend to move at higher velocities than liquid in the central region, therefore, the dissipation rate is less than the energy input rate. This form of energy transfer maintains the liquid recirculation rate (Kulkarni et al., 2007). The experimental data in Figure 69a shows a vortex trend between 0.2 and 0.5 (normalised radial distance), which is towards the distributor region where gas is introduced into the reactor. This was accurately captured by the second-order scheme.

It has been reported that the second-order scheme uses a multidimensional linear reconstruction method thus resulting in second-order accuracy (ANSYS, 2010) and good convergence. This method uses the vortex value of a cell to compute the gradients of scalar variables at the cell centre. The QUICK scheme uses the weighted average of the central interpolations and the scalar quantity of the second-order upwind, thereby resulting in a more accurate solution but which is tougher to converge and requires more processing power. Laborde-Boutet et al. (2009) studied the influence of numerical discretization schemes. They reported that high-order schemes reduce the numerical diffusion errors significantly. However, higher-grade numerical schemes (QUICK and third-order MUSCL scheme) are recommended for rotating and swirling flows (Laborde-Boutet et al., 2009) and are persistent in converging.

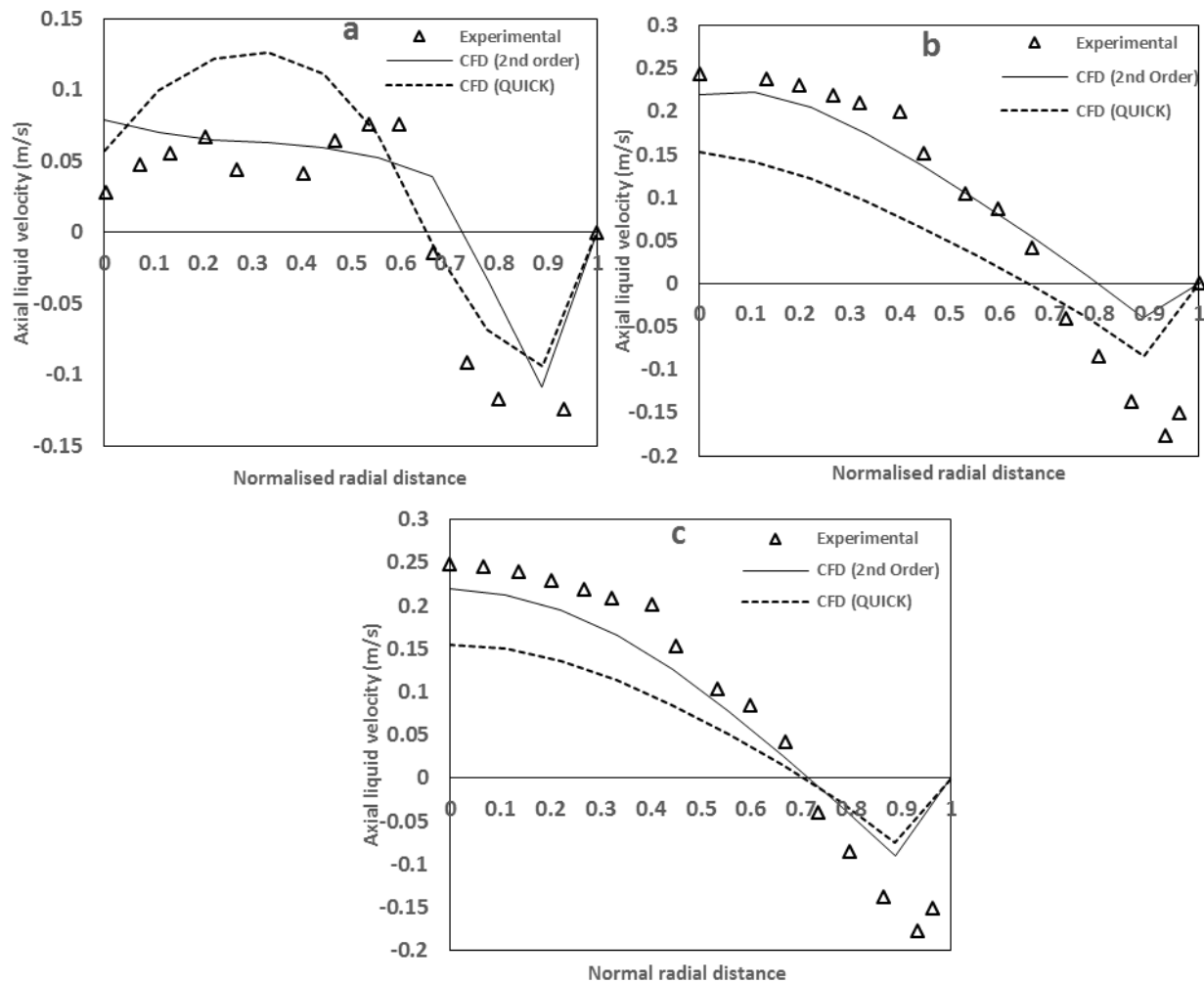


**Figure 69: Comparison between the simulated and experimental axial liquid profiles at different axial positions: (a)  $H/D = 0.2$ ; (b)  $H/D = 2.6$  and (c)  $H/D = 5.0$**

The central upward movement of the liquid varied in the axial direction due to change in the gas hold-up profile from the distributor to the disengagement zone. The second-order scheme accurately captured the axial liquid velocity profiles in all three locations and gave the best prediction. However, the CFD prediction of the axial liquid velocity was poor towards the wall, which was due to the presence of small eddies that limit the ability of the standard  $k-\epsilon$  model to model near the wall turbulence. The axial liquid velocity data showed a volatile unstructured profile towards the bottom of the reactor ( $H/D = 0.2$ ) and the profile developed well at distances away from the distributor region. The volatile unstructured profile obtained in Figure 70a is due to the turbulence introduced by the bubbles as they entered the reactor. A suitable way to visualise eddy turbulence in the liquid phase, shown in Figure 70a, is by using a contour plot. Figure 70 compares an XY plot (Figure 70a) and a contour plot (Figure 70b) where both plots represent the axial liquid velocity at an axial location of  $H/D = 0.2$ . The axial liquid velocity shown in Figure 70a was drawn from the black line shown in Figure 70b and represents data drawn from the centre of the reactor all the way to the wall.

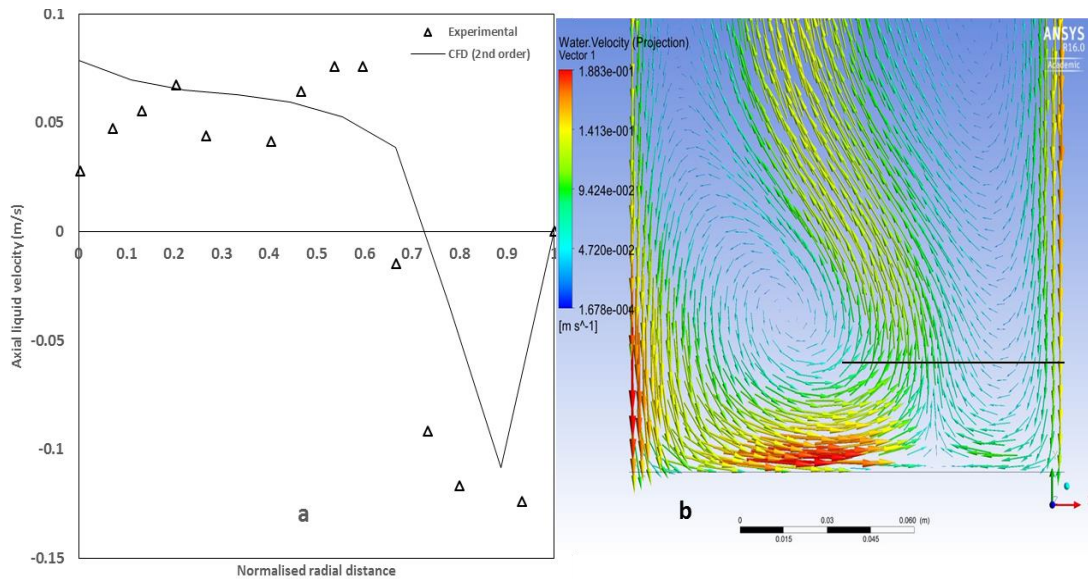


**Figure 70: Comparison between (a) XY plot and (b) vector plot of axial liquid velocity profile**

As stated earlier, Figure 70a exhibits a vortex trend between the normalised radial distances of 0.2 to 0.5. This kind of trend was captured properly by the contour plot. In Figure 70b, specifically on the black line towards the centre of the reactor, there is recirculation of the liquid that is caused by entering bubbles. As you move near the wall of the reactor, there is a downward flow of the liquid velocity as shown by the downward facing vector line arrows. This downward flow shown by the contour plot can also be seen in the XY plot (Figure 70a) where the liquid velocity is negative at normalised radial distances of 0.75 to 0.95. Therefore, the contour plot has supported the trend that was shown by the XY plot.

#### 7.3.1.4 Gas hold-up profiles

An efficient and simple way to understand mixing within the reactor is to study the variation of gas hold-up. Figure 71 shows the plot of gas hold-up at different axial locations with a superficial gas velocity of 20 mm/s. The simulations were carried out in the homogeneous regime, implying that the bubbles move with virtually similar velocities, sizes and with minimal coalescence and breakup. This creates an added advantage of specifying a single bubble diameter (1.96 mm). The simulation results (Figure 71) gave a high gas hold-up towards the centre and a radial decrease when approaching the wall with an average radial gas hold-up of ~0.116.

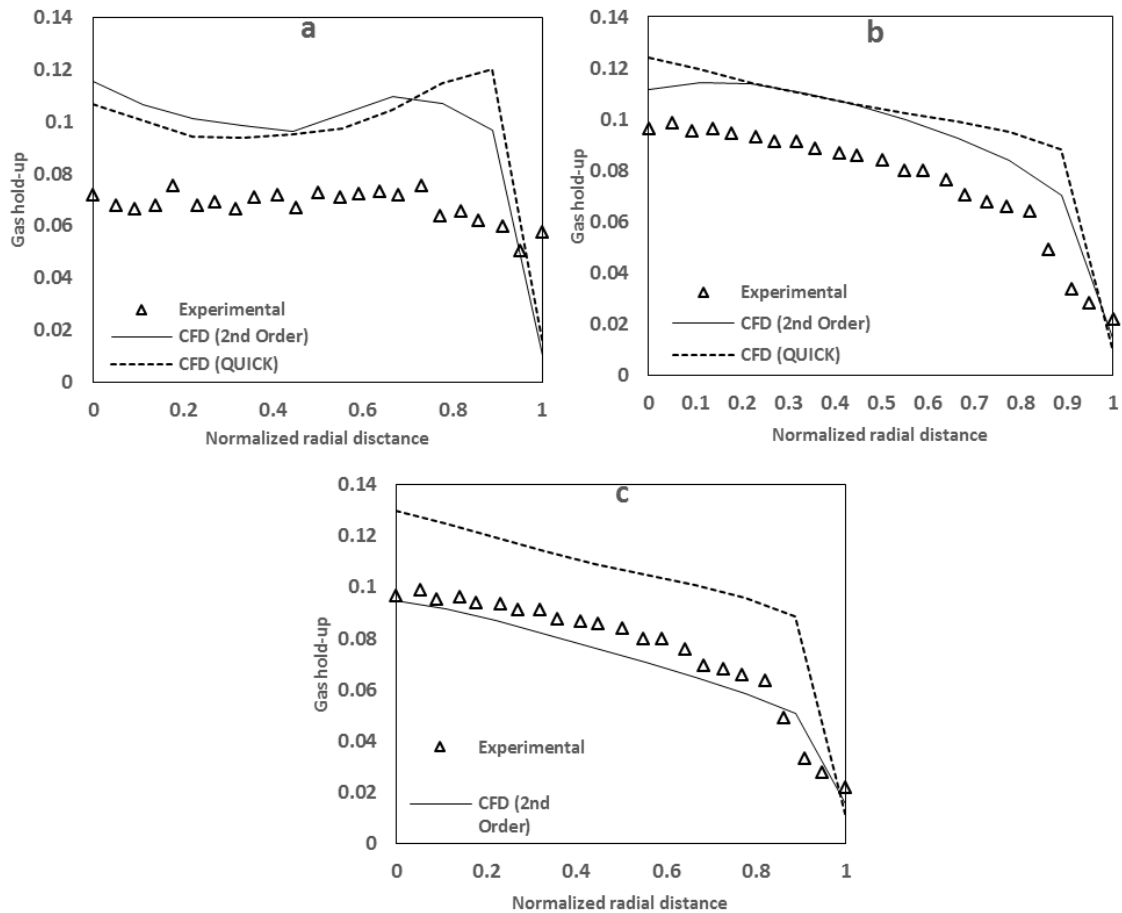


**Figure 71: Comparison between the simulated and experimental gas hold-up profiles at different axial positions : (a)  $H/D = 0.2$ ; (b)  $H/D = 2.6$  and (c)  $H/D = 5.0$**

It is stated in literature (and shown in Figure 69) that the liquid velocity varies at different axial locations of the reactor. Therefore, the lift force induced by the liquid causes the bubbles to rise faster towards the centre of the reactor and lower towards the wall (Kulkarni et al., 2007). This is comparable to the results of Kulkarni et al. (2007) and Tabib et al. (2008) who obtained an average radial gas hold-up of  $\sim 0.085$  and  $\sim 0.10$ , respectively. The prediction of the gas hold-up was poor towards the distributor region (Figure 71a) and developed well at distances away from the distributor (Figure 71b and c), which imply that the free surface modelling was suitable towards the top. The gas hold-up radial profile develops due to the axial changing reduced the pressure gradient, which increases the bubble free area towards the disengagement zone. This results in more gas bubbles towards the centre and less near the wall. The CFD gas hold-up profile for second-order compared well with the experimental data in Figure 71b and Figure 71c. Similar to the axial liquid velocity data, the gas hold-up data was flat towards the distributor region ( $H/D = 0.2$ ) due to the gas being introduced, and developed a radial profile at distances away from the distributor region. The second-order scheme predicted gas hold-up the best, particularly at distances away from the distributor region.

Figure 72 compares an XY plot and a contour plot for radial profile of gas hold-up. The data for Figure 9a was obtained from the black line shown in Figure 72b at an axial distance of  $H/D = 2.6$ . Figure 72b shows an aerial view of the gas hold-up: the gas hold-up is  $\sim 0.115$  at the centre of the reactor and radial decreases to a value less than 0.02 near the wall of the reactor.

As the bubbles rise, they entrain some of the liquid and due to mass conservation, an equal amount of liquid needs to fall back. The falling liquid pushes the bubbles towards the centre, which causes the bubbles to concentrate towards the central region. In addition, it is pleasing to see the contour plot in agreement with the XY plot.

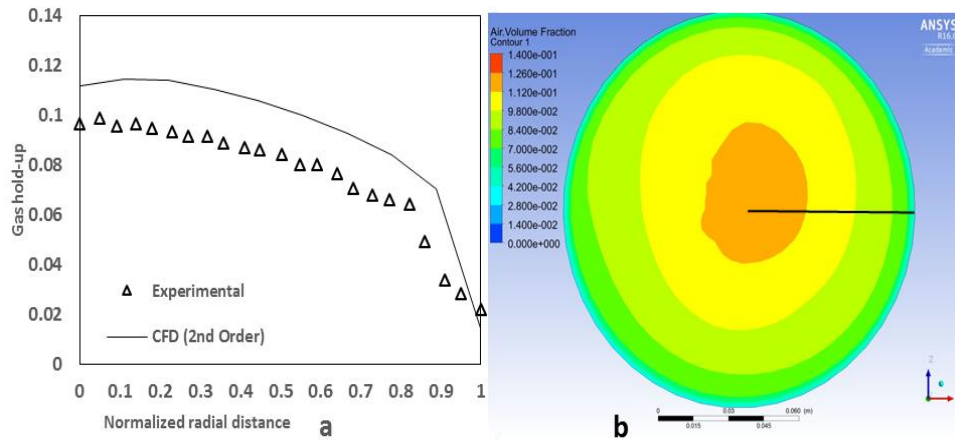


**Figure 72: Comparison between: (a) XY plot and (b) contour plot of radial gas hold-up**

### 7.3.1.5 Turbulent kinetic energy profiles

Modelling turbulence is often a complex task. Turbulent models can be investigated by comparing the turbulent kinetic energy ( $k$ ) and turbulent dissipation rate ( $\epsilon$ ) where the bubble-induced turbulence is modelled. In the current study, the standard  $k$ - $\epsilon$  model coupled with near-wall enhancement treatment were investigated.

The flow patterns predicted by the CFD simulations need to satisfy the energy balance. It has been shown in literature that the energy,  $E$ , supplied by the bubbles to the liquid is described by (Kulkarni et al., 2007; Tabib et al., 2008):

$$E = \frac{\pi}{4} D^2 (\rho_l - \rho_g) g H \epsilon_l [V_l + (C_B - 1) \bar{\epsilon}_g V_S] \quad (109)$$

where  $V_S$  is the slip velocity,  $\epsilon_l$  is the liquid volume fraction and  $C_B$  represents the influence of the bubble-induced turbulence that is transported to the liquid phase.

As the bubble moves through the liquid phase, it transfers its pressure energy to the liquid. This energy is converted into turbulent kinetic energy due to the drag force. At steady-state conditions, the total energy carried by a swarm of bubbles is mostly used to pump the stagnant liquid, from bottom to top, resulting in an intense liquid recirculation (Kulkarni et al., 2007). This is also confirmed by the axial liquid profiles (Figure 69). Thus, the energy related with the liquid is less at the bottom than at the top. This is shown by Figure 73 where the turbulent kinetic energy increases at distances away from the distributor region. However, the induced turbulent liquid motion is locally dissipated (turbulent dissipation rate) through eddies found in the liquid phase.

The turbulent kinetic energy showed an overall trend of constant value towards the centre, which decreased near the wall (Figure 73). At distances away from the distributor region, there was an increase in the turbulent kinetic energy, which corresponds to literature. Since the energy provided by the bubbles to the liquid is due to the drag force and the lift force causes

the bubbles to concentrate towards the central region, the turbulent kinetic energy tends to be higher in the centre of the reactor than near the wall.

The second-order curve accurately predicted the turbulent kinetic energy towards the distributor (Figure 73a) and deviated slightly at distances away from the distributor region (Figure 73b and Figure 73c) but predicted the overall trend of the experimental data better than QUICK. The standard  $k-\varepsilon$  model is grounded on the assumption of isotropic flow. This suggests that it assumes that the normal stress components are equal to each other (Tabib et al., 2008). This causes the turbulent characteristics to be equally distributed resulting in inaccurate turbulence profiles.

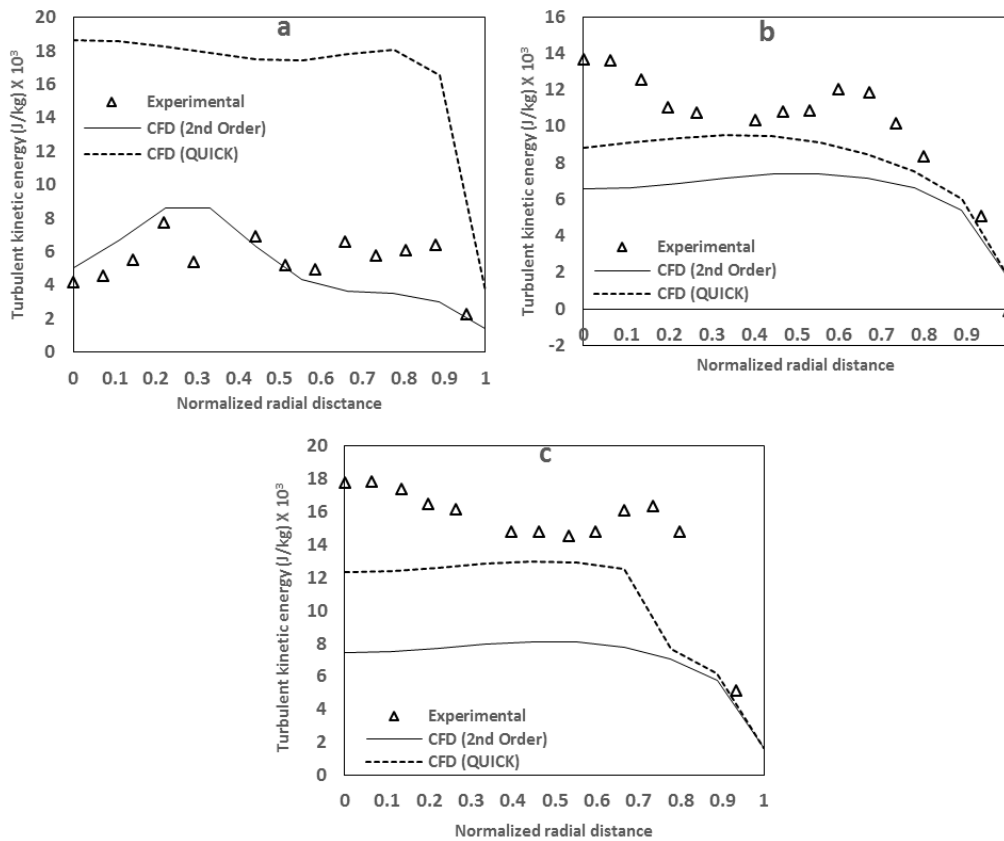


**Figure 73: Comparison between the simulated and experimental turbulent kinetic energy profiles at different axial positions: (a)  $H/D = 0.2$ ; (b)  $H/D = 2.6$  and (c)  $H/D = 5.0$**

### 7.3.1.6 Turbulent dissipation rate

Figure 74 shows the radial variation of the turbulent dissipation rate at different column heights. The radial and axial variation of the turbulent dissipation rate is obtained from the turbulent model used and subsequently computed by suitable volume integration (Tabib et al., 2008). Since the turbulent dissipation rate is the rate at which the turbulent kinetic energy is dissipated by the small eddies, it should equate to the energy introduced by the bubbles (Eq. 109). The dissipation rate profiles showed a constant value towards the centre and an increase from  $r/R = 0.2$  to  $r/R = 0.8$  and a sharp increase near the wall. This identical trend was reported by Liu and Hinrichsen (2014), and Kulkarni et al. (2007). Similar to turbulent kinetic energy, the dissipation rate increased away from the distributor due to an increase in the turbulent kinetic energy away from the distributor. The turbulent dissipation rate data corresponds well with the

turbulent kinetic energy data. The second-order curve gave the best prediction while QUICK deviated significantly from experimental data away from the distributor.

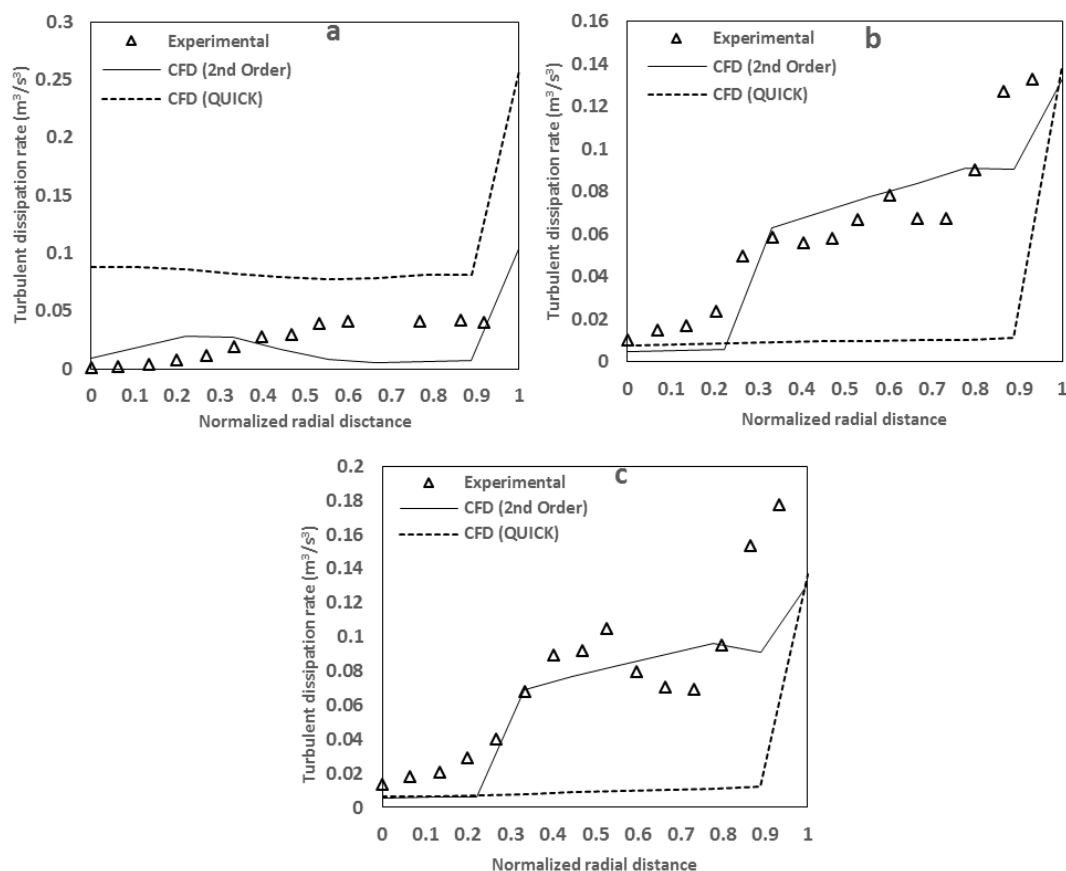


**Figure 74: Comparison between the simulated and experimental turbulent dissipation rate profiles at different axial positions: (a)  $H/D = 0.2$ ; (b)  $H/D = 2.6$  and (c)  $H/D = 5.0$**

### 7.3.1.7 Bubble size distribution

Fluidized bed photoreactors often use air mainly for mixing, along with other factors. It is therefore necessary to model and understand bubble distribution in a fluidized bed photoreactor. The first few bubbles that enter the reactor through the distributor often determine the formulation of the initial bubble size. As the bubbles travel up the reactor, the initial bubble size range changes due to factors such as vorticity caused by shear flow, varying bubble rise velocities, wake entrainment, size deformation and liquid phase turbulence (Li et al., 2009). The bubble size deformation, which is usually referred to as bubble breakup or coalescence, is caused by turbulent eddies that result in non-uniform bubble sizes and shapes.

The population balance model or multiple size group model is often used to model and capture the phenomena of bubble breakup, coalescence and bubble size distribution. In the current study, which uses a quantitative approach, the bubble size distribution was experimentally determined at four different superficial gas velocity size ranges (8.66 mm/s to 23.10 mm/s). It is worth noting that the superficial gas velocity range studied is well within the homogeneous regime and bubble size deformation (bubble breakup and coalescence) is therefore insignificant. Figure 75 shows that the superficial gas velocity significantly affects the bubble

size. An increase in the superficial gas velocity (from 8.66 mm/s to 23.10 mm/s) resulted in an increase in the bubble size (from 3 mm to 11 mm).

Figure 75d shows that the bubbles have a spherical cap-like shape, which is formed at high superficial gas velocities. The superficial gas velocity range used in the current study is well within the homogeneous regime, although a superficial gas velocity of 23.10 mm/s gave a bubble size of 11 mm. Besagni and Inzoli (2016) referred to this characteristic as the pseudo-homogenous regime; they further stated that at this regime, the bubbles entrain the smaller swarm of bubbles through their wake causing the breakup phenomenon. This high bubble size obtained at a low superficial gas velocity is a result of the type of distributor used (sintered plate). According to Li et al. (2009), the bubble size distribution along with the gas hold-up is strongly influenced by the distributor design. Furthermore, these two parameters are used to determine the interfacial area between the gas and liquid phases. They further reported that the sintered plate distributor results in higher average gas hold-up and bubble sizes than other forms of distributors (pipe and orifice).

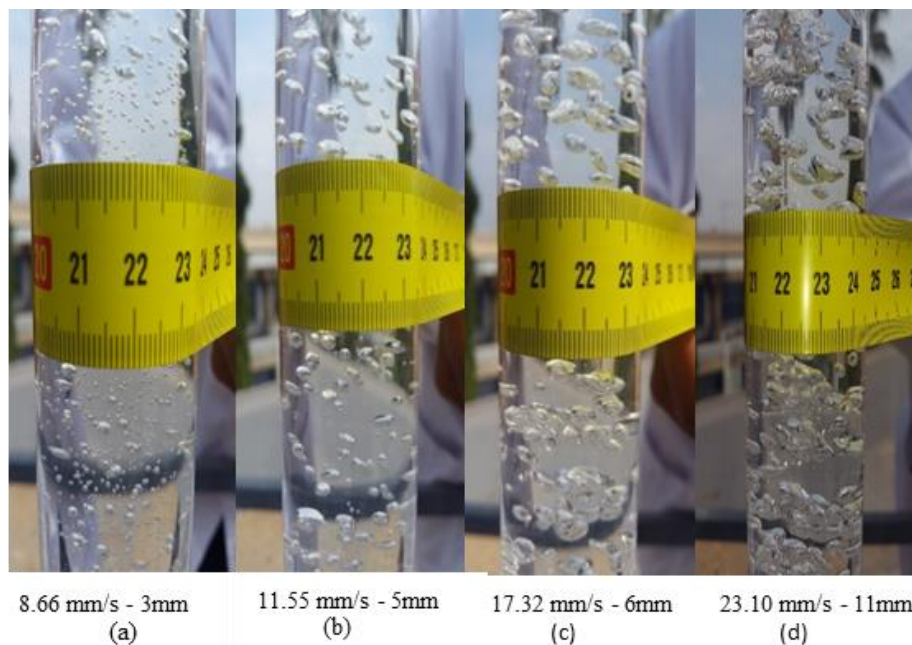


**Figure 75: Effect of superficial gas velocity on the bubble distribution**

### 7.3.1.8 Effect of superficial gas velocity

The mathematical model developed in this study predicted the experimental data of Kulkarni et al. (2007) fairly well using the optimised setting methods. To verify the effectiveness of the model, it was further employed to study the effects of superficial gas velocity on the global gas hold-up. The simulation data was compared with the experimental global gas hold-up results determined by us in reference. The optimal setting methods, as shown by Table 27, were used for all the simulation cases from here onwards.

**Table 27: Optimum setting methods for CFD simulations**

Parameter	Setting
Grid size	500 000 cells, 1.2 mm
Discretization scheme	Momentum: second-order upwind Volume fraction: QUICK Turbulence equations: second-order upwind
Time step size	0.001

The global gas hold-up measurements were carried out to validate the effectiveness of the developed model and to characterise the hydrodynamic behaviour of the reactor. The global gas hold-up ( $\epsilon_G$ ) is defined as the average volumetric gas fraction present in the entire domain of the reactor, which was determined by observing the displaced height of the clear liquid (Ellenberger & Krishna, 2003; Li & Zhong, 2015).

$$\epsilon_G = \frac{H - H_D}{H} \quad (110)$$

where  $H_D$  is the displaced height during gas sparging and  $H$  is the static clear liquid height with no gas sparging.

Figure 76 shows the effect of superficial gas velocity on the global gas hold-up in the reactor. The simulation data was compared with the experimental results. The simulation data showed a good prediction of the experimental results from a superficial gas velocity of 11.55 mm/s to 17.32 mm/s. The reactor was operated in the homogenous regime based on the superficial gas velocities studied. Therefore, literature has shown that as the bubbles travel to the top surface of the reactor, gas properties such as size, shape and velocity are constant and can be specified easily in the simulation (Pourtousi et al., 2015). It was found that an increase in superficial gas velocity results in an increase in the global gas hold-up. The increase in global gas hold-up is due to an increase in the number of bubbles present in the reactor. The increase in superficial gas velocity increases the number of bubbles, resulting in an increase in the interfacial drag force on the bubbles, which in turn reduces the bubble rise velocity (Rollbusch et al., 2015).

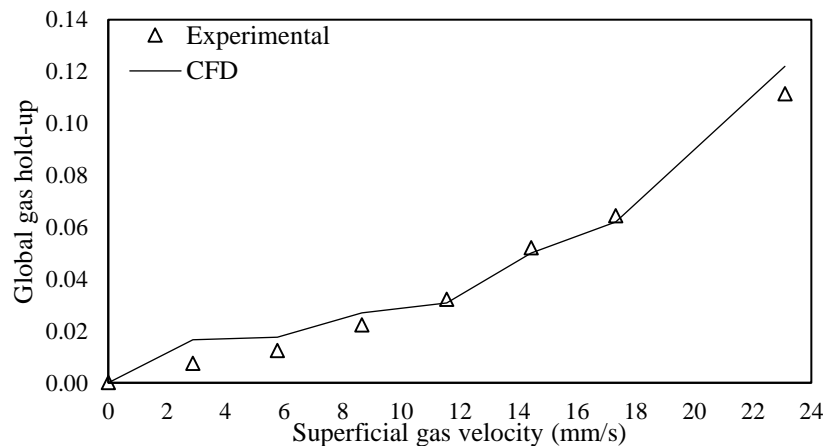


**Figure 76: Effect of superficial gas velocity on the global gas hold-up: Comparison between CFD simulation and experimental results**

A similar trend was also found by Pourtousi et al. (2015) where they determined the effect of superficial gas velocity on the overall gas hold-up. At a superficial gas velocity of 15 mm/s, they obtained an overall gas hold-up of ~0.048, whereas in the current study, a superficial gas velocity of 14.44 mm/s gave a global gas hold-up of 0.052 and 0.050 for experimental and simulation, respectively. This agreement of the simulation data with the experimental results shows that the developed model is effective and may be applied to study other phenomena such as mass transfer.

### 7.3.2 Photodegradation

#### 7.3.2.1 Model fitting and statistical analysis

RSM seeks to find the relationship between the process variables and the response variable. The process variables that predominantly affect the efficiency and performance of the system were selected based on past experiments. The central composite design was used to determine the collective effects of the process variables on the photodegradation of phenol. The response variable (photodegradation percentage) for both experimental and predicted along with the combination of the respective process variables are shown in Table 28. Based on the experimental response, the maximum degradation of phenol achieved was 65.9%, whereas the minimum degradation obtained was 7.83%. The photodegradation efficiency obtained in the current study was relatively low compared with literature, which was due to increasing the particle size.

Shahrezaei et al. (2012b) conducted a process modelling and kinetic study on the photodegradation of petroleum wastewater using TiO<sub>2</sub> catalyst. The maximum degradation they obtained was 80.84% using a nano-sized catalyst. Zulfakar et al. (2011) used a nano-sized TiO<sub>2</sub> catalyst, similar to Shahrezaei et al. (2012b), to photodegrade phenol. The catalyst was immobilised and they achieved a maximum degradation of ~100%. In the current study, the maximum degradation (65.9%) was achieved in three hours with a particle size range of 300–1000 µm and a catalyst loading 1 g/L.

**Table 28: Full factorial central composite design experimental matrix with experimental and expected responses**

Run	A: Initial pH level	B: Catalyst loading (g/L)	C: Reaction time (min)	D: Superficia l velocity (mm/s)	Degradation (%)	
					Experimental	Predicted
1	3.5	1	120	8.66	35.94	34.20
2	6.5	1	120	8.66	40.52	47.28
3	3.5	3	120	8.66	53.55	43.60
4	6.5	3	120	8.66	42.82	57.64
5	3.5	1	240	8.66	38.13	43.99
6	6.5	1	240	8.66	54.27	54.51
7	3.5	3	240	8.66	50.34	31.52
8	6.5	3	240	8.66	36.15	43.00
9	3.5	1	120	17.32	51.90	41.25
10	6.5	1	120	17.32	48.10	44.36

Run	A: Initial pH level	B: Catalyst loading (g/L)	C: Reaction time (min)	D: Superficia l velocity (mm/s)	Degradation (%)	
					Experimental	Predicted
11	3.5	3	120	17.32	55.57	52.78
12	6.5	3	120	17.32	56.50	56.84
13	3.5	1	240	17.32	65.90	68.83
14	6.5	1	240	17.32	52.92	59.07
15	3.5	3	240	17.32	58.74	48.18
16	6.5	3	240	17.32	50.50	46.69
17	2	2	180	11.55	58.80	53.64
18	8	2	180	11.55	56.71	58.23
19	5	0	180	11.55	7.83	9.63
20	5	4	180	11.55	31.80	39.09
21	5	2	60	11.55	28.31	38.61
22	5	2	300	11.55	45.20	41.25
23	5	2	180	5.77	34.97	44.79
24	5	2	180	23.10	42.00	58.54
25	5	2	180	11.55	46.00	46.15
26	5	2	180	11.55	45.00	48.25
27	5	2	180	11.55	46.20	44.32
28	5	2	180	11.55	46.80	46.15
29	5	2	180	11.55	46.00	47.36
30	5	2	180	11.55	46.90	48.15

Accordingly, literature studies using TiO<sub>2</sub> as a photocatalyst achieve high photodegradation efficiency with nano-sizes whereas the current study obtained a relatively low photodegradation efficiency at micrometre sizes. This is an indication that an increase in the particle size of the catalyst results in a decrease in the performance of the system as an increase in the particle size (from nanometre to micrometre) causes a decrease in the surface area and available active sites for adsorption and photodegradation of pollutants. Therefore, it is recommended to find a balance between the catalyst particle size and the photodegradation performance. In addition, a study on the effect of catalyst particle size on the photodegradation performance should be conducted to obtain the optimum particle size.

The two responses, predicted and experimental, were determined through the combination of the process variables as shown in Table 28. The predicted values were computed using the final second-order empirical model (Eq. 111) in terms of coded factors using the Design Expert<sup>®</sup> Software of Stat-Ease Inc. The predicted values presented a sufficient correlation to the experimental values, although there was a slight deviation in some other experimental runs. The experimental data was fitted to several models (cubic, factorial and linear); however, it was found through their subsequent ANOVA that the photodegradation of phenol was best described by the second-order empirical model. From 111, the main effects of initial pH level (A) had a significant negative influence on the photodegradation of phenol. This shows that an increase in the initial pH level will result in a decrease in the photodegradation efficiency.

$$y = 46.15 - 4.77A + 3.60B + 0.16C + 1.85D + 2.95A^2 - 4.04B^2 - 0.43C^2 + 1.88D^2 - 1.14AB - 0.52AC - 1.37AD + 0.66BC + 0.66BD + 0.50CD \quad (111)$$

To evaluate the adequacy of the empirical second-order model, both the ANOVA and significance tests were employed. The significance test was used to determine the regression coefficients of the empirical second-order model. The ANOVA method was used to evaluate the significance of the empirical second-order model (Jiang et al., 2013), and the results are shown in Table 29. The evaluation is done by determining the probability ( $P$ ) value and Fisher's test ( $F$ ) for each regression coefficient in the model. The significance of the interaction between the process variables is determined by the Fisher's test, thereby creating a pattern between the interaction of the process variables (Petrović et al., 2015). This means that the higher the values of the Fisher's test, the lower the  $P$  values. Furthermore, the  $F$  values are computed for each tested model and the model with the most significant terms is selected (Fakhri et al., 2016).

**Table 29: ANOVA of the empirical second-order model**

Source	Sum of Squares	DF	Mean Square	F Value	P > F	
Model	2099.96	14	139.59	98.56	<0.0001	Significant
<i>A</i>	267.13	1	267.13	31.65	0.0453	
<i>B</i>	0.22	1	0.22	7.17	0.2275	
<i>C</i>	14.95	1	14.95	65.36	0.0546	
<i>D</i>	371.49	1	371.49	54.63	0.0411	
$A^2$	249.51	1	249.51	38.14	0.0452	
$B^2$	161.96	1	161.96	6.78	0.2334	
$C^2$	134.81	1	134.81	1.59	0.0979	
$D^2$	35.85	1	35.85	61.44	0.0501	
<i>AB</i>	0.92	1	0.92	3.63	0.3077	
<i>AC</i>	6.57	1	6.57	7.15	0.2278	
<i>AD</i>	106.83	1	106.83	10.14	0.1937	
<i>BC</i>	478.19	1	478.19	24.29	0.0212	
<i>BD</i>	11.74	1	11.74	9.09	0.2039	
<i>CD</i>	25.21	1	25.21	1.68	0.4182	
Residual	381.84	15	72.12	–	–	
<i>Lack of Fit</i>	354.85	10	35.92	9.54	0.1084	Not significant
<i>Pure Error</i>	26.99	5	5.4	–	–	
Cor Total	2481.8	29				

From Table 29, the  $F$  value for the model was found to be 98.56, which resulted in a  $P$  value less than 0.0001. This means that the model is suitable for this study (significant). The  $P$  values were used to specify the interaction strength between the independent variables (Petrović et al., 2015). In addition, model terms that obtain  $P$  values less than 0.05 are statistically significant. As per Table 29, the pH level ( $A$ ), superficial gas velocity ( $D$ ), quadratic of pH level ( $A^2$ ) and interaction of catalyst loading and reaction time ( $BC$ ), and catalyst loading and superficial gas

velocity ( $CD$ ) are considered significant model terms. Other model terms are insignificant and it is recommended to eliminate them as to simplify the empirical second-order model.

The presence of systematic errors in the model are detected by means of residual analysis. Two factors that often contribute to the residual variance are: pure experimental error and lack of fit. The pure error is computed by considering the difference between the experimental values at the same conditions in a random sequence (Petrović et al., 2015). The variations in the model terms are represented by the lack of fit. The  $P$  value for lack of fit was found to be 0.1084, indicating that it was statistically insignificant. The coefficient of determination ( $R^2$ ) in the current study was found to be 0.975. This signifies that 97.5% of the variation found in the response variable can be described by the model, whereas 2.5% is residual variability (Islam et al., 2009). Furthermore, the adjusted coefficient of determination ( $R_{adj}^2$ ) was found to be acceptable (0.954), indicating the significance of the model. It is worth noting that Eq. 81 is highly significant ( $P$  value  $< 0.0001$ ), with an acceptable coefficient of determination ( $R^2 = 0.954$ ) and is therefore adequate to predict the photodegradation of phenol.

### 7.3.2.2 Three-dimensional response surface analysis

The interaction between the process variables can be understood better by plotting three-dimensional response surface plots, which are discussed in detail in this section. These surface plots are graphical demonstrations of the developed empirical second-order model (Eq. 111). They assist in analysing the interaction among the process variables (Fakhri et al., 2016) and determining the optimum level for each process variable to degrade phenol. In addition, there is an infinite number of combinations for any two tested processes variables; therefore, these plots reveal the type of interaction between these variables (Petrović et al., 2015).

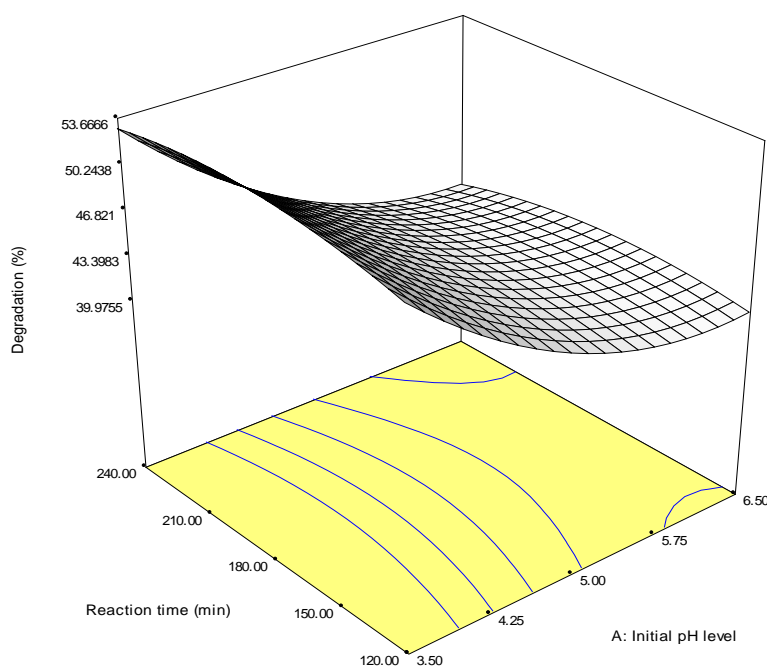
Literature has shown that petroleum wastewater contains various organic compounds (Coelho et al., 2006) and quite often these organic pollutants differ greatly when it comes to solubility in water, speciation behaviour and hydrophobicity (Shahrezaei et al., 2012b). In addition, some of these pollutants can occur in negative, neutral or positive forms in solution. These discrepancies in ionic behaviour can affect the photodegradation efficiency of the process significantly. Consequently, the initial pH level of the solution plays a major role in the photodegradation efficiency of the system.

Figure 77 shows the effect of initial pH level and reaction time on the degradation of phenol. A decrease in the initial pH level resulted in an increase in the photodegradation of phenol. The influence of initial pH on the photodegradation efficiency can be described by the point of zero charge (pzc), whereby this value was reported to be 6.2 for  $TiO_2$  (Shahrezaei et al., 2012b). This suggests that the surface of  $TiO_2$  is negatively charged in alkaline solutions ( $pH > 6.2$ ) and, conversely, that it is positively charged in acidic conditions ( $pH < 6.2$ ). This was also confirmed by the empirical second-order model where the initial pH level had a negative regression coefficient ( $-4.77 A$ ), which suggests that the initial pH level has a negative significant influence on the photodegradation of phenol.

Since phenol and its derivatives are negatively charged in aqueous solutions due to the  $-OH$  groups (Shahrezaei et al., 2012b), it is expected that their electrostatic attraction to the catalyst particles will be more favourable in acidic conditions and repulsive in alkaline conditions.

Therefore, the initial pH results revealed that the photodegradation of phenol is favourable in acidic conditions as opposed to alkaline conditions. From the current study, at these acidic conditions (pH = 3.5), the maximum photodegradation of phenol was found to be 52.2%. Shet and Vidya (2016) studied the photodegradation of phenol using a silver-doped TiO<sub>2</sub> photocatalyst. They obtained a maximum photodegradation of 70% at a pH level of 3 and a reaction time of 360 minutes.

Figure 77 illustrates that an increase in the reaction time from 120 minutes to 210 minutes increased the photodegradation of phenol from 39.9% to 52.8%, whereas the photodegradation of phenol remained constant with a further increase in the reaction time beyond 210 minutes. When the process reaches a reaction time of 210 minutes, it implies that the process has reached equilibrium. Photocatalytic reactions are believed to be significantly directed by two factors: mass transfer and photon efficiency, and the reaction mechanism is dissimilar to traditional heterogeneous catalytic reactions (Zulfakar et al., 2011). Catalyst loading is an important process variable that affects the photodegradation efficiency of organic pollutants in a fluidized bed photoreactor. It has been found that in photocatalytic systems, a high catalyst loading is ineffective due to excess catalyst particles preventing UV light penetration, which reduce photodegradation efficiency. Therefore, an optimum catalyst loading is necessary to avoid the hindering of the UV light penetration. It is also good practice to ensure good economic usage of the catalyst to reduce the cost of catalyst loading (Zulfakar et al., 2011).



**Figure 77: Effect of reaction and initial pH level on the photodegradation of phenol**

Figure 78 shows the effect of catalyst loading and initial pH level on the photodegradation of phenol. Since a composite catalyst was used, the values displayed here (1.0–3.0 g/L) were those of TiO<sub>2</sub> and not those of the composite catalyst as a whole. The catalyst dosage range chosen in this study was based on preliminary experiments that have shown that an increase in the TiO<sub>2</sub> particle size necessitates an increase in catalyst dosage. The results from Figure 78 show

that increasing the catalyst loading from 1.0 g/L to 2.0 g/L results in an increase in the photodegradation of phenol. This is due to an increase in the number of active sites available for adsorption and photodegradation of phenol. However, a further increase beyond 2.0 g/L results in a decrease in the photodegradation efficiency. Literature has shown that there is a limiting value at high catalyst loading (Shahrezaei et al., 2012b). This suggests that increasing the catalyst loading beyond the limiting value causes a blockage of the UV light penetration due to an excessive amount of catalyst particles (Apollo et al., 2014). Therefore, the optimum catalyst loading in the current study was chosen as 2.0 g/L, which gave a photodegradation efficiency of 47.3%.

The central idea of a fluidized bed photoreactor is fluidization; air was used in the current study for fluidization (and agitation). The use of air is important due because it plays two major roles in photodegradation: mixing inside the reactor and the oxygen acts as an electron scavenger that prevents electron-hole recombination. The mixing inside the reactor (hydrodynamics) has been discussed and it was shown that the gas hold-up assists in understanding the mixing in the reactor. It was also shown that the superficial gas velocity has a significant impact on the global gas hold-up.

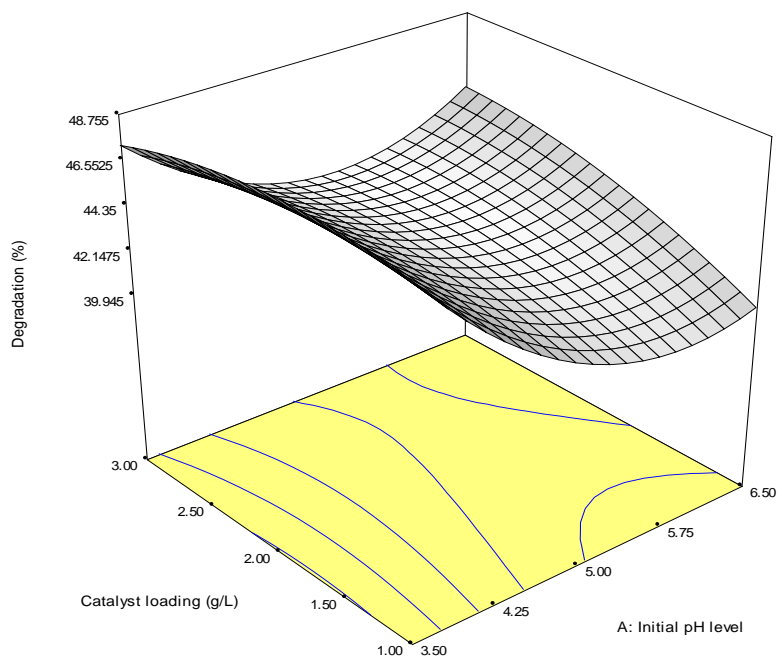


**Figure 78: Effect of catalyst loading and initial pH level on the photodegradation of phenol**

Figure 79 shows the effect of superficial gas velocity and catalyst loading on the photodegradation of phenol. The results show that an increase in the superficial gas velocity results in an increase in the photodegradation efficiency. The optimum superficial gas velocity was found to be 17.32 mm/s, which gave a maximum photodegradation efficiency of 48.6%. The superficial gas velocity was varied within the homogeneous regime (8.66–17.32 mm/s). Per the hydrodynamic study, the bubble size distribution is uniform and the global gas hold-up is below 0.13 (Figure 76). An increase in the superficial gas velocity results in an increase in the number of bubbles present in solution due to an increase in the drag force, thus increasing the global gas hold-up. This increase in the global gas hold-up results in an increase in the

availability of oxygen (to prevent electron-hole recombination) and enhances the mixing inside the reactor.

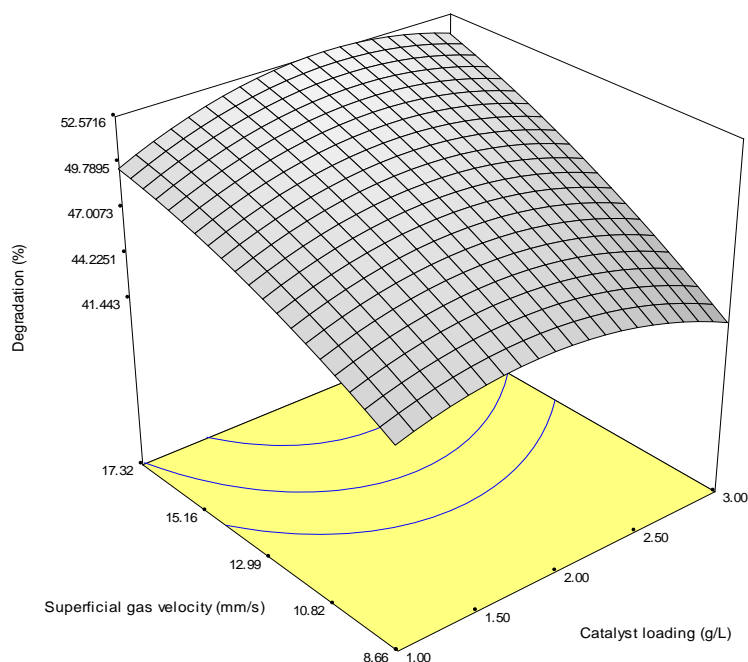


**Figure 79: Effect of superficial gas velocity and catalyst loading on the photodegradation of phenol**

### 7.3.3 Reaction kinetics

In the current study, the adsorption reaction constant ( $b$ ) was found to be insignificant, consequently, the term in the denominator of Eq. 106 (L–H model) was neglected ( $bC \sim 0$ ). Eq. 06 was then transformed into a linearized algebraic equation (Eq. 108) where the apparent reaction rate constant ( $K_{app}$ ) was determined by using the gradient of the slope and  $t$  is the reaction time in minutes. The apparent reaction rate encapsulates both the degradation reaction rate ( $k_r$ ) and the adsorption reaction rate ( $b$ ) constants; it was assumed that  $b$  was negligible compared with  $k_r$ . The assumption was confirmed by conducting adsorption experiments at optimum conditions to evaluate the composite catalysts' adsorption capacity. The initial concentration of phenol for the adsorption study was 30 ppm and only 7.33% of phenol was adsorbed after 75 minutes. Therefore, it is evident that the rate of adsorption was minimal.

The photodegradation kinetics of phenol under solar irradiation and  $\text{TiO}_2$  catalyst were studied. The kinetic experiments were conducted using the optimum photodegradation operating conditions that were found using RSM to be: superficial gas velocity of 17.32 mm/s, catalyst loading of 2.0 g/L, initial pH level of 3.5 and reaction time of 210 minutes. An initial concentration of 30 ppm (for phenol) was used for all reaction kinetic experiments and sampling was done at different time intervals. The reaction rate data was modelled using both first-order (L–H model) and second-order kinetics by measuring the concentration of phenol at different time intervals. From the slope of the graph in Figure 80a, the apparent reaction rate constant was found to be  $0.0046 \text{ min}^{-1}$ , which is within the range of what Shahrezaei et al. (2012b) obtained to be  $0.007\text{--}0.013 \text{ min}^{-1}$ . The regression coefficient ( $R^2$ ) was found to be 0.9931. A high value of  $R^2$  evidently shows that the L–H model was applied with a good degree of precision. In addition, the  $R^2$  obtained in this study was similar to that found by Shahrezaei

et al. (2012b) ( $R^2 > 0.997$ ). This means that it can be used to predict future outcomes. The second-order model was applied to the reaction rate data and gave a low value for  $R^2 = 0.9698$  and  $K_{ap} = 0.0002 \text{ L}/(\text{mg}\cdot\text{min})^{-1}$  (Figure 80b).

Apollo et al. (2014) studied the photodegradation kinetics of phenol and methyl orange using solar irradiation and ZnO catalyst supported on silica. Although they did not use the L–H model, they showed that the degradation kinetics of phenol using ZnO-SiO<sub>2</sub> catalyst followed the pseudo-first-order kinetics. At an initial concentration of 30 ppm (phenol), they obtained a rate constant of 0.0107 and  $R^2$  of 0.9941.

By understanding the photodegradation kinetics of phenol under optimum conditions, further experiments were conducted to monitor the reduction of TOC using the optimum conditions. It has been reported that as the hydroxyl radicals destroy phenol, they are converted into its derivatives (intermediates) and those derivatives are further converted into H<sub>2</sub>O, CO<sub>2</sub> and weak acids (Shahrezaei et al., 2012b). Furthermore, literature shows that the intermediates significantly affect the apparent reaction rate constant (Zulfakar et al., 2011). Therefore, it is necessary to understand the reaction chain by monitoring the TOC reduction during the photocatalytic degradation of phenol. TOC can indirectly reveal the degradation of both phenol and phenolic derivatives (intermediates).

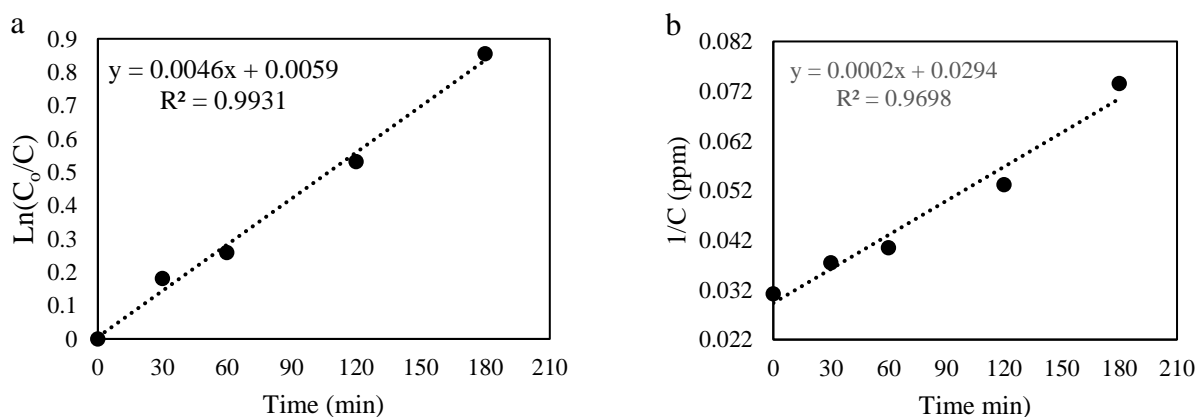


**Figure 80: Linear fit for photodegradation reaction: a) L–H (first-order) model; b) Second-order model**

Figure 81 shows the effect of the optimum conditions on the reduction of TOC at different time intervals. After 210 minutes of irradiation, only 63.7% of TOC reduction was achieved. From the RSM results, it was shown that 52.7% of phenol is degraded in 150 minutes. Therefore, it is evident that beyond 150 minutes, there is still phenol and its intermediates present in solution. Zulfakar et al. (2011) investigated the photodegradation of phenol using an immobilised TiO<sub>2</sub> photocatalyst and UV light. They reported that the main intermediates formed during the degradation of phenol are p-benzoquinone, catechol, hydroquinone and resorcinol. They further mentioned that these intermediates tend to compete with phenol for the available active sites on the catalyst, which results in a decrease in the apparent reaction rate constant. In addition, the formation of intermediates is highly dependent on the initial concentration of phenol.

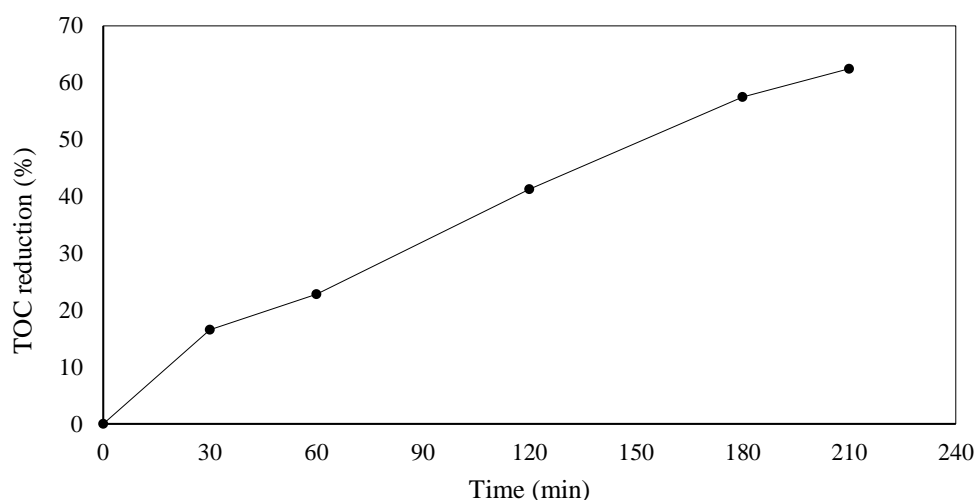


**Figure 81: Reduction of TOC at different time intervals**

#### 7.4 Conclusion

The purpose of this study was to use CFD techniques to investigate the flow dynamics and turbulence inside the fluidized bed photoreactor. Furthermore, RSM was applied to optimise the operating conditions for the photocatalytic degradation of petroleum wastewater. The CFD model was developed by investigating hydrodynamic conditions such as axial liquid velocity, radial gas hold-up profiles, turbulent kinetic energy and turbulent kinetic dissipation rate. The plot for axial liquid velocity profile displayed a radial variation for all three graphs, whereby the liquid velocity had an upward movement at the centre and a downward movement near the wall. The local gas hold-up was high at the centre and had a radial decrease when approaching the wall with an average radial gas hold-up of  $\sim 0.116$ . The CFD data showed a good agreement with the experimental data from Kulkarni et al. (2007). A thorough analysis of the hydrodynamic conditions clarified the flow pattern and turbulence inside the reactor. The numerical optimisation technique (desirability) was applied to determine the optimal CFD model settings. The developed model was validated by studying the effect of superficial gas velocity on the global gas hold-up, and the CFD data was compared with the gas hold-up experimental results obtained by us in reference. It was found that the developed model predicted the experimental results fairly well, thereby displaying its effectiveness and applicability to study other phenomena such as mass transfer or reaction kinetics.

The process variables that predominantly affect the efficiency and performance of petroleum wastewater degradation were optimised using RSM. The photodegradation efficiency in the current study was found to be relatively low as compared with literature, which was attributed to the increase in catalyst particle size (from nanometre to micrometre). The optimum operating conditions were found using RSM to be: superficial gas velocity of 17.32 mm/s, catalyst loading of 2.0 g/L, initial pH level of 3.5 and reaction time of 210 minutes. The developed second-order empirical model presented a sufficient correlation to the photodegradation experimental data values, although there was a slight deviation in some other runs. In addition, the adequacy of the model was evaluated by applying both the ANOVA and significant test. It was found that the empirical model is highly significant ( $P$  value  $< 0.0001$ ) with an acceptable

coefficient of determination ( $R^2 = 0.954$ ). It is therefore adequate to predict the photodegradation of phenol.

The reaction kinetics for the photocatalytic degradation of petroleum wastewater (phenol) were evaluated using the L–H model. It was found that the photocatalytic degradation of petroleum wastewater follows pseudo-first-order reaction kinetics. Fitting the linear curve on the reaction data gave a high regression coefficient ( $R^2 = 0.9931$ ), which is comparable to literature. This shows that the linear model can be potentially applied to predict future outcomes accurately. The TOC photodegradation data (Figure 81) showed a removal efficiency of 63.7%, which was low when compared with literature. This was caused by reducing the composite catalyst surface area and restricting the experiments to reach equilibrium. Binding the catalyst by using silica reduces the photodegradation efficiency but improves the filtration process, which was shown by the sedimentation experiments. It is therefore evident from the sedimentation experiments that increasing the particle size of  $\text{TiO}_2$  significantly reduces the cost of filtration at an expense of low process performance. Therefore, one has to find an optimum balance between the cost of filtration and process efficiency.

## 7.5 References

- Abhang, R.M., Kumar, D. & Taralkar, S. V. (2011). Design of photocatalytic reactor for degradation of phenol in wastewater. *International Journal of Chemical Engineering and Applications*, 2(5), 3144–3148.
- ANSYS, I. (2010). ANSYS FLUENT Theory Guide, 80.
- ANSYS, I. (2011). ANSYS Meshing User's Guide, 1–522.
- Antal, S.P., Lahey, R.T. & Flaherty, J.E. (1991). Analysis of phase distribution in fully developed laminar bubbly two-phase flow. *International Journal of Multiphase Flow*, 17(5), 635–652.
- Apollo, S. (2014). Solar photodegradation of methyl orange and phenol using silica supported ZnO catalyst. *International Journal of Innovation, Management and Technology*, 5(3), 5–8.
- Bechambi, O., Sayadi, S. & Najjar, W. (2015). Photocatalytic degradation of bisphenol A in the presence of C-doped ZnO: Effect of operational parameters and photodegradation mechanism. *Journal of Industrial and Engineering Chemistry*, 32, 201–210.
- Besagni, G. & Inzoli, F. (2016). Bubble size distributions and shapes in annular gap bubble column. *Experimental Thermal and Fluid Science*, 74, 27–48. Available at: <http://dx.doi.org/10.1016/j.expthermflusci.2015.11.020>.
- Boyjoo, Y., Ang, M. & Pareek, V. (2013). Some aspects of photocatalytic reactor modeling using computational fluid dynamics. *Chemical Engineering Science*, 101, 764–784.
- Boyjoo, Y., Ang, M. & Pareek, V. (2014). CFD simulation of a pilot scale slurry photocatalytic reactor and design of multiple-lamp reactors. *Chemical Engineering Science*, 111, 266–277.
- Burns, A.D. et al. (2004). The Favre averaged drag model for turbulent dispersion in Eulerian multi-phase flows. (392), 1–17.

- Cheng, Z. et al. (2012). Photocatalytic degradation of bisphenol A using an integrated system of a new gas-liquid-solid circulating fluidized bed reactor and micrometer Gd-doped TiO<sub>2</sub> particles. *Journal of Environmental Sciences (China)*, 24(7), 1317–1326.
- Cloete, S., Johansen, S.T. & Amini, S. (2014). Grid independence behaviour of fluidized bed reactor simulations using the two fluid model: Effect of particle size. *Powder Technology*, 269, 153–165.
- Coelho, A. et al. (2006). Treatment of petroleum refinery sourwater by advanced oxidation processes. *Journal of Hazardous Materials*, 137(1), 178–184.
- Ellenberger, J. & Krishna, R. (2003). Shaken, not stirred, bubble column reactors: Enhancement of mass transfer by vibration excitement. *Chemical Engineering Science*, 58(3–6), 705–710.
- Fakhri, A. et al. (2016). Photodegradation of Erythromycin antibiotic by  $\gamma$ -Fe<sub>2</sub>O<sub>3</sub>/SiO<sub>2</sub> nanocomposite: Response surface methodology modeling and optimization. *Journal of Molecular Liquids*, 214, 378–383.
- Islam, M.A., Sakkas, V. & Albanis, T.A. (2009). Application of statistical design of experiment with desirability function for the removal of organophosphorus pesticide from aqueous solution by low-cost material. *Journal of Hazardous Materials*, 170(1), 230–238.
- Jiang, W. et al. (2013). Optimization of photocatalytic performance of TiO<sub>2</sub> coated glass microspheres using response surface methodology and the application for degradation of dimethyl phthalate. *Journal of Photochemistry and Photobiology A: Chemistry*, 262, 7–13.
- Khune, M., Akach, J. & Ochieng, A. (2014). Solar photodegradation of phenol using a composite catalyst of silica and TiO<sub>2</sub>. *International Conference on Chemical Engineering & Advanced Computational Technologies*, 24-25, 2–5.
- Kim Phuong, N.T. et al. (2016). Adsorption and photodegradation kinetics of herbicide 2,4,5-trichlorophenoxyacetic acid with MgFeTi layered double hydroxides. *Chemosphere*, 146, 51–59.
- Krepper, E., Lucas, D. & Prasser, H.M. (2005). On the modelling of bubbly flow in vertical pipes. *Nuclear Engineering and Design*, 235(5), 597–611.
- Kulkarni, A.A., Ekambara, K., Joshi, J.B. (2007). On the development of flow pattern in a bubble column reactor: Experiments and CFD. *Chemical Engineering Science*, 62(4), 1049–1072.
- Laborde-Boutet, C. et al. (2009). CFD simulation of bubble column flows: Investigations on turbulence models in RANS approach. *Chemical Engineering Science*, 64(21), 4399–4413.
- Lee, K., Ku, H. & Pak, D. (2016). OH radical generation in a photocatalytic reactor using TiO<sub>2</sub> nanotube plates. *Chemosphere*, 149, 114–120.
- Li, G., Yang, X. & Dai, G. (2009). CFD simulation of effects of the configuration of gas distributors on gas-liquid flow and mixing in a bubble column. *Chemical Engineering Science*, 64(24), 5104–5116.

- Li, W. & Zhong, W. (2015). CFD simulation of hydrodynamics of gas-liquid-solid three-phase bubble column. *Powder Technology*, 286, 766–788. Available at: <http://dx.doi.org/10.1016/j.powtec.2015.09.028>.
- Liu, Y. & Hinrichsen, O. (2014). Study on CFD-PBM turbulence closures based on k- $\epsilon$  and Reynolds stress models for heterogeneous bubble column flows. *Computers and Fluids*, 105, 91–100.
- Masood, R.M.A., Rauh, C. & Delgado, A. (2014). CFD simulation of bubble column flows: An explicit algebraic Reynolds stress model approach. *International Journal of Multiphase Flow*, 66, 11–25.
- Nastar, M. & Ramasar, V. (2012). Transition in South African water governance: Insights from a perspective on power. *Environmental Innovation and Societal Transitions*, 4, 7–24.
- Ohno, T. et al. (2001). Morphology of a TiO<sub>2</sub> photocatalyst (Degussa, P-25) consisting of anatase and rutile crystalline phases. *Journal of Catalysis*, 203(1), 82–86.
- Petrović, S. et al. (2015). Process modelling and analysis of plasma electrolytic oxidation of titanium for TiO<sub>2</sub>/WO<sub>3</sub> thin film photocatalysts by response surface methodology. *Surface and Coatings Technology*, 269, 250–257.
- Pourtousi, M., Ganesan, P. & Sahu, J.N. (2015). Effect of bubble diameter size on prediction of flow pattern in Euler-Euler simulation of homogeneous bubble column regime. Measurement: *Journal of the International Measurement Confederation*, 76, 255–270.
- Pourtousi, M., Sahu, J.N. & Ganesan, P. (2014). Effect of interfacial forces and turbulence models on predicting flow pattern inside the bubble column. *Chemical Engineering and Processing: Process Intensification*, 75, 38–47.
- Primo, O. et al. (2007). Mathematical modelling of phenol photooxidation: Kinetics of the process toxicity. *Chemical Engineering Journal*, 134(1-3), 23–28.
- Qi, N. et al. (2011). CFD modelling of hydrodynamics and degradation kinetics in an annular slurry photocatalytic reactor for wastewater treatment. *Chemical Engineering Journal*, 172(1), 84–95.
- Rollbusch, P. et al. (2015). Experimental investigation of the influence of column scale, gas density and liquid properties on gas holdup in bubble columns. *International Journal of Multiphase Flow*, 75, 88–106.
- Sato, Y., Sadatomi, M. & Sekoguchi, K. (1981). Momentum and heat transfer in two-phase bubble flow-I. Theory. *International Journal of Multiphase Flow*, 7(2), 167–177.
- Shahrezaei, F. et al. (2012a). Photocatalytic degradation of aniline using TiO<sub>2</sub> nanoparticles in a vertical circulating photocatalytic reactor. *International Journal of Photoenergy*, 2012, 1–8.
- Shahrezaei, F. et al. (2012b). Process modeling and kinetic evaluation of petroleum refinery wastewater treatment in a photocatalytic reactor using TiO<sub>2</sub> nanoparticles. *Powder Technology*, 221, 203–212.
- Shet, A. & Vidya, S.K. (2016). Solar light mediated photocatalytic degradation of phenol using Ag core–TiO<sub>2</sub> shell (Ag@TiO<sub>2</sub>) nanoparticles in batch and fluidized bed reactor. *Solar Energy*, 127, 67–78.

- Shiota, T. et al. (2016). Photon emission induced by brittle fracture of borosilicate glasses. *Journal of Luminescence*, 173, 208–212.
- Tabib, M. V., Roy, S.A. & Joshi, J.B. (2008). CFD simulation of bubble column-An analysis of interphase forces and turbulence models. *Chemical Engineering Journal*, 139(3), 589–614.
- Zhang, D., Deen, N.G. & Kuipers, J.A.M. (2006). Numerical simulation of the dynamic flow behavior in a bubble column: A study of closures for turbulence and interface forces. *Chemical Engineering Science*, 61(23), 7593–7608.

## 8 LIGHT DISTRIBUTION IN A FLUIDIZED BED PHOTOCATALYTIC REACTOR

### 8.1 Introduction

Photocatalysis is normally carried out in reactors that bring pollutants, catalyst particles and photons in contact (Braham & Harris, 2009). The most efficient reactors have a UV lamp installed inside the reactor and the catalyst applied in suspended form. The suspended catalysts can be fluidized with wastewater or compressed air. Air fluidization is considered less costly and has the additional advantage of supplying an oxygen source for the photocatalysis reaction. The design, analysis and scale-up of an air FBR should account for all the factors that affect the rate of photocatalysis, namely, catalyst, bubble, pollutant and light distribution. Attempts can be made to improve the homogeneity of catalyst, bubbles and pollutants in the reactor. However, the light distribution in the reactor will always be inhomogeneous. This has serious implications for reactor design and operation. Preceding studies in this report have looked at photocatalyst development and photoreactor hydrodynamics using CFD. However, the light distribution has not been looked at. To improve photoreactor design and the efficiency of the AD-photocatalysis process, the light distribution in the reactor needs to be analysed.

Light distribution is crucial as it is the basis of important photocatalytic reactor design parameters such as the local volumetric rate of energy absorption (LVREA), intrinsic kinetics and photocatalysis efficiency parameters. Experimental determination of light distribution is unfeasible; instead, simulation has been used to establish the light distribution in the reactor. The most rigorous light distribution simulations have been carried out by solving the radiation transport equation (RTE) (Eq. 111). For photocatalysis systems, the scattering terms in the RTE renders an analytical solution to the RTE impossible. Instead, numerical methods have been developed for solving the RTE. The most rigorous of these numerical methods are the deterministic discrete ordinates/finite volume methods (Boyjoo et al., 2013) and the stochastic Monte Carlo method (Moreira et al., 2010; Valades-Pelayo et al., 2014a; Valades-Pelayo et al., 2014b). Methods with several simplifying assumptions such as the six-flux method (Puma et al., 2010) and P1 method (Orozco et al., 2009) have also been used to solve the RTE.

The accuracy of the Monte Carlo method for light distribution simulation has been highlighted by several researchers (Moreira et al., 2010; Valades-Pelayo et al., 2014b). The Monte Carlo method solves the RTE stochastically by tracking a statistically adequate number of photons from the lamp until they are absorbed in the slurry or lost in the reactor wall/sensor. Moreira et al. (2010) and Valades-Pelayo et al. (2014b) developed a Monte Carlo algorithm for solving the light distribution in a slurry photocatalytic reactor. They validated the Monte Carlo model by measuring transmitted radiation at the reactor wall. Valades-Pelayo et al. (2014a) used a spectroradiometric probe to provide a better validation for their Monte Carlo model. All these previous studies were carried out in a liquid FBR in which the catalyst loading was the only variable that had any influence on light distribution.

Air bubbles have been reported to influence the light distribution in photocatalytic reactors (Trujillo et al., 2007). As a result, several authors (Trujillo et al., 2007; Trujillo et al., 2010; Boyjoo et al., 2013; Boyjoo et al., 2014) have incorporated the influence of bubbles in their radiation models. A recent study by Motegh et al. (2013) concluded that the influence of

bubbles on the photocatalysis reaction rate was not substantial. More clarity on the influence of bubbles on light distribution is needed. Previous bubble studies were based on the model proposed by Trujillo et al. (2007), which accounted for bubbles by modifying the slurry scattering and absorption coefficients. In this work, the more rigorous Monte Carlo model is proposed in which the influence of bubbles is modelled explicitly by directly computing the interaction between photons and bubbles. Such a rigorous model is expected to provide a more accurate picture of the influence of bubbles on the light distribution. The aim of this work was to develop and validate a Monte Carlo model for simulating the light distribution in an annular fluidized bed photocatalytic reactor at different catalyst loadings and air flow rates.

## 8.2 Methodology

### 8.2.1 Reactor setup

The annular FBR photocatalytic reactor (Figure 82) consisted of a 2.2 mm thick reactor wall and a 1.4 mm thick glass sleeve made of clear borosilicate glass. The reactor wall had an outer diameter of 65 mm while the glass sleeve's outer diameter was 34 mm. Air was supplied to the reactor from an oil-free compressor (Jun-Air) through a borosilicate glass porous distributor with a pore size of 10–16  $\mu\text{m}$ . The total height of the reactor was 900 mL with a working height of 600 mm and a liquid capacity of 1.25 L. The reactor was irradiated internally by an 18 W low-pressure black light blue lamp (Philips T26 BLB) with a characteristic emission wavelength of 368 nm and a photon emission rate of  $2.22 \times 10^{-5}$  Einsteins/s positioned inside the glass sleeve. A radiation sensor (CR2 cosine receptor) was fitted outside the reactor and held in place by a plastic support. The cosine receptor was connected to the spectroradiometer (Stellarnet, Black Comet SR) using a fibre optic cable. The radiation sensor was installed on the reactor wall midway between the lamp ends (Figure 82). At this location, the radiation sensor captured a fraction of the emitted photons that escaped the reactor at the wall. The sum of these escaping photons was referred to as the total transmitted radiation (TTR).

### 8.2.2 Monte Carlo model

For an absorbing and scattering medium, the RTE with no emission terms has been developed as (Cassano & Alfano, 2000):

$$\frac{dI_{\lambda}(s,\Omega)}{ds} = -\kappa_{\lambda}I_{\lambda}(s,\Omega) - \sigma_{\lambda}I_{\lambda}(s,\Omega) + \frac{1}{4\pi}\sigma_{\lambda}\int_0^{4\pi} p(\Omega' \rightarrow \Omega)I_{\lambda}(s,\Omega')d\Omega' \quad (112)$$

where  $I_{\lambda}$  was the spectral light intensity,  $s$  was the light path length,  $\Omega$  was the direction of light travel,  $\kappa_{\lambda}$  was the absorption coefficient,  $\sigma_{\lambda}$  was the scattering coefficient and  $p(\Omega' \rightarrow \Omega)$  was the probability of a light scatter from direction  $\Omega'$  to  $\Omega$ . The RTE was solved stochastically using the Monte Carlo method. This was carried out by tracking the movement of photons from the lamp until they were lost in the slurry, wall or radiation sensor. Random numbers, uniformly distributed between 0 and 1, were used in the Monte Carlo simulation. The details of the Monte Carlo algorithm incorporating air bubbles are given in Appendix A.

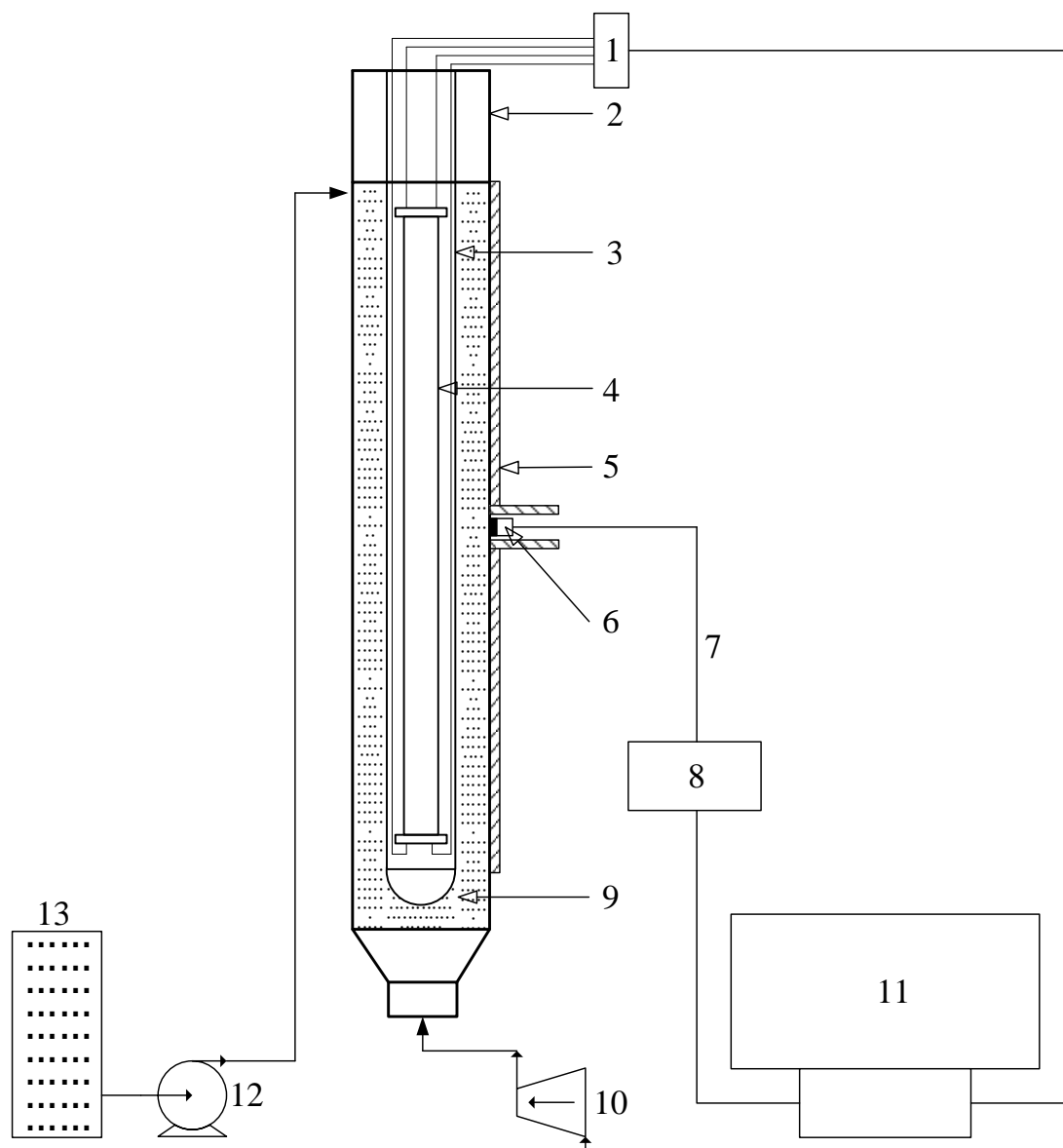


**Figure 82: Radiation field measurement setup: (1) Tridonic PCA, (2) Reactor wall, (3) Lamp sleeve, (4) Black light lamp, (5) Radiation sensor support, (6) Radiometric sensor, (7) Fibre optic cable, (8) Spectroradiometer, (9) Catalyst slurry, (10) Air compressor, (11) Computer, (12) Peristaltic pump, (13) Feed mixing tank**

### 8.2.3 TTR experiments

TTR refers to the fraction of emitted photons that reach the sensor positioned on the outside of the reactor wall. TTR measurements were carried out on the reactor wall using the spectroradiometer sensor at different catalyst loadings and gas flow rates. A catalyst slurry was prepared by mixing Aeroxide P25 TiO<sub>2</sub> purchased from Acros Organics in deionised water (Millipore Milli-Q). The slurry with a catalyst loading of 0.025 g/L was added into the reactor and compressed air was introduced into the reactor at a flow rate of 80 L/h. Thereafter, the UV lamp was switched on and left to warm for 30 minutes. Afterwards, TTR measurements were taken at the wall of the reactor using the spectroradiometer. The air flow rate was reduced gradually to take TTR measurements at other air flow rates. At an air flow rate of 0, the air flow was cut off and TTR measurements were taken immediately to minimise catalyst settling.

After taking TTR measurements at all air flow rates, the catalyst loading in the reactor was increased by introducing a measured quantity of ultrasonicated catalyst slurry into the reactor.

### 8.3 Results and Discussion

#### 8.3.1 Experimental TTR measurements

TTR measurements are a convenient method of validating the Monte Carlo method by measuring the photons escaping from the reactor at the reactor wall. TTR measurements were carried out at different catalyst loadings (0.025–0.6 g/L). The experimental results (Figure 83) show an exponential decrease in the TTR from 3617  $\mu\text{W}/\text{cm}^2$  to 46  $\mu\text{W}/\text{cm}^2$  with an increase in the catalyst loading from 0.025 g/L to 0.6 g/L. The decrease in the TTR with an increase in catalyst loading can be attributed to the increase in the obstruction of light due to scattering and absorption. The TTR values obtained in this work are higher than those reported by Valades-Pelayo et al. (2014a). For example, at a catalyst loading of 0.1 g/L, Valades-Pelayo et al. (2014a) reported a TTR of around 1200  $\mu\text{W}/\text{cm}^2$  at a radial location of 30.6 mm, which is lower than the value of 1815  $\mu\text{W}/\text{cm}^2$  obtained in this work. This can be attributed to the differences in reactors and lamps employed in two experiments. The TTR experiments also showed that an increase in the air flow rate resulted in a slight increase in the TTR at all catalyst loadings. For example, at a catalyst loading of 0.1 g/L, an increase in the air flow rate from 0 L/h to 80 L/h resulted in an increase in the TTR from 1815  $\mu\text{W}/\text{cm}^2$  to 1868  $\mu\text{W}/\text{cm}^2$ . This trend will be explained in detail later on in Section 8.3.3.

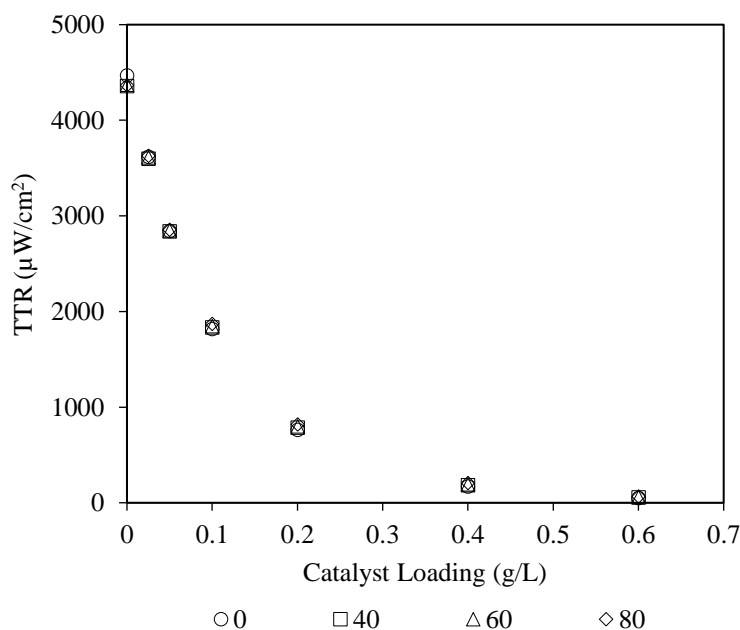
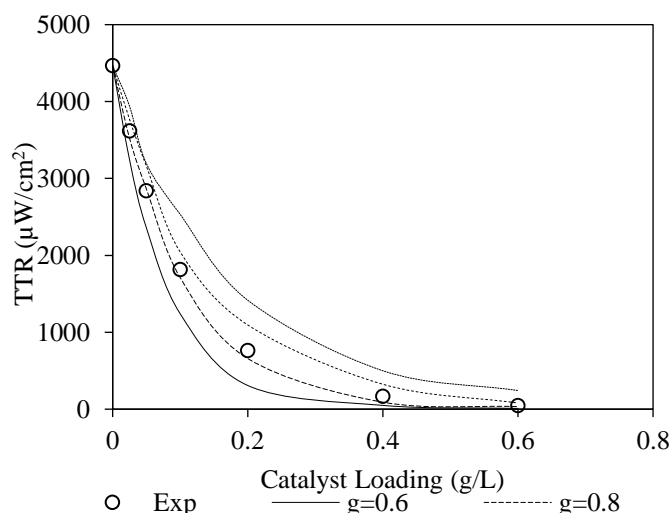


Figure 83: Experimental TTR measurements at different catalyst loadings and air flow rates

#### 8.3.2 Effect of scattering parameter

The light distribution and TTR from the reactor were simulated using a Monte Carlo simulation. To characterise the nature of catalyst scattering, simulations were carried out at different catalyst loadings and scattering parameters at an air volume fraction of 0 L/h. The results (Figure 84) show an exponential decrease in the TTR with an increase in the catalyst loading. Furthermore, the results show an increase in the TTR with an increase in the scattering

parameter from 0.6 to 0.95 at all catalyst loadings. The Henyey–Greenstein scattering parameter governs the direction in which light is scattered by particles. The scattering parameter can range between  $-1$  and  $1$ . A scattering parameter of  $-1$  refers to complete backward scatter,  $1$  refers to complete forward scatter and  $0$  refers to isotropic scatter in all directions. The increase in the TTR with increasing forward scattering parameter was due to an increase in the forward scattering and photon flight towards the reactor wall resulting in an increase in the TTR.



**Figure 84: Effect of the Henyey–Greenstein phase function scattering parameter and catalyst loading on the TTR**

Using a root mean square error (RMSE) criterion, the scattering parameter with the best fit was obtained and confirmed to be 0.81 (Table 30). This shows that the P25  $\text{TiO}_2$  catalyst used in this work was found to scatter UV light in the forward direction as reported by several authors (Satuf et al., 2005; Valades-Pelayo et al., 2014b).

However, the value of the scattering parameter obtained in this work was slightly higher than the value of 0.68 reported by Valades-Pelayo et al. (2014b). This can be attributed to the fact that Valades-Pelayo et al. (2014b) used the  $\text{TiO}_2$  optical properties reported by Romero et al. (1997) while this work used the data set published by Romero et al. (2003). The inter-relationship between scattering phase functions and catalyst optical properties has been discussed by Satuf et al. (2005). They show that the choice of a scattering phase function has a marked effect on the  $\text{TiO}_2$  optical properties and vice versa. For the same model, the use of different optical properties would require different scattering parameters in order to achieve accurate simulation.

**Table 30: RMSE of different scattering parameter values**

Scattering parameter	RMSE
0.6	363.8353
0.8	72.5502
0.81	104.0287
0.9	211.7794
0.95	434.5447

### 8.3.3 Effect of bubbles

The effect of bubbles on the TTR was simulated by the Monte Carlo method with bubble diameter and gas hold-up as Monte Carlo inputs. The bubble diameter was measured from photographs of the reactor under operation and found to be 6 mm on average. Global gas hold-up was measured using the quick-stop method (Ochieng et al., 2002) and found to be 0.0232, 0.0482 and 0.0705 at air flow rates of 40 L/h, 60 L/h and 80 L/h, respectively. All Monte Carlo simulations were carried out using a scattering parameter of 0.81. The Monte Carlo simulation results (Figure 85a–d) showed good agreement between experimental and simulated TTR values at various catalyst loadings and air flow rates. At the different air flow rates, the Monte Carlo simulation captured the exponential decrease accurately in the TTR with increasing catalyst loadings. The errors in the Monte Carlo simulation could be attributed to the assumption of spherical bubble shape and uniform bubble size. In a realistic FBR, bubbles have a range of sizes due to bubble coalescence and breakup. Also, bubbles are seldom perfectly spherical due to breakup, coalescence and hydrostatic pressure. It is noteworthy that accurate simulations were obtained for all the air flow rates while maintaining the same scattering parameter. This suggests that air flow did not significantly alter the agglomeration state of the catalysts. Otherwise a change in the scattering parameter would have been necessary to achieve accurate simulation (Valades-Pelayo et al., 2015).

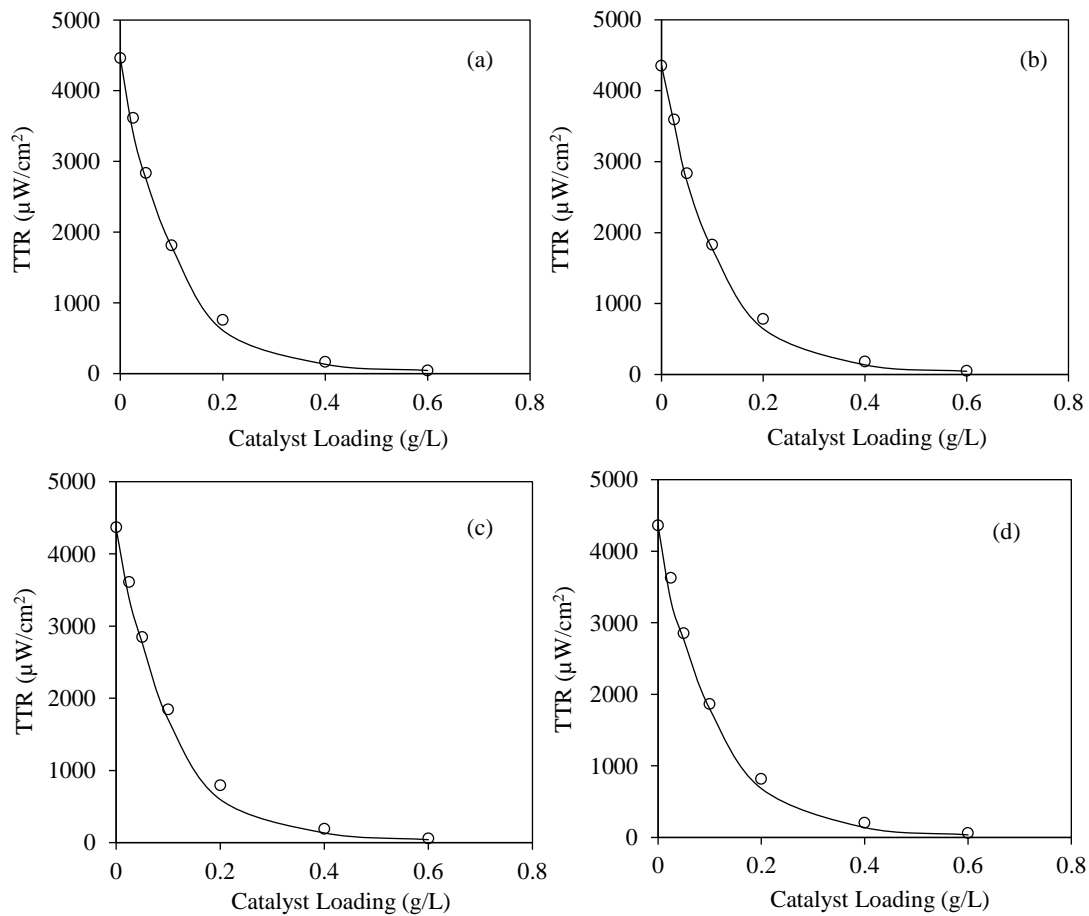


**Figure 85: Comparison of experimental and simulation TTR values at different catalyst loadings and air flow rates: (a) 0 L/h, (b) 40 L/h, (c) 60 L/h, (d) 80 L/h**

The TTR, which gives an indication of the photons escaping through the reactor walls, could be used to validate the Monte Carlo model. However, the TTR data does not give an indication of the light distribution in the reactor. The light distribution in the reactor can be determined using the Monte Carlo model, which has been validated by TTR measurements. For photocatalysis, the light distribution in the reactor is normally characterised by the volumetric rate of energy absorption (VREA), which refers to the quantity of light absorbed by the catalyst in the whole reactor (Valades-Pelayo et al., 2014b). To better clarify the influence of bubbles on the light distribution, the effect of air flow rate on the VREA was investigated. The VREA results (Figure 8.5) showed an expected exponential increase in the VREA with catalyst loading at the different air flow rates. For example, at an air flow rate of 40 L/h, an increase in the catalyst loading from 0.25 g/L to 0.6 g/L resulted in an increase in the VREA from 775  $\mu\text{W}/\text{cm}^3$  to 4756  $\mu\text{W}/\text{cm}^3$ . The VREA results also showed an insignificant increase in the VREA with an increase in the air flow rate. For example, at a catalyst loading of 0.1 g/L, an increase in the gas flow rate from 0 L/h to 80 L/h resulted in an increase in VREA from 2698  $\mu\text{W}/\text{cm}^3$  to 2745  $\mu\text{W}/\text{cm}^3$ .

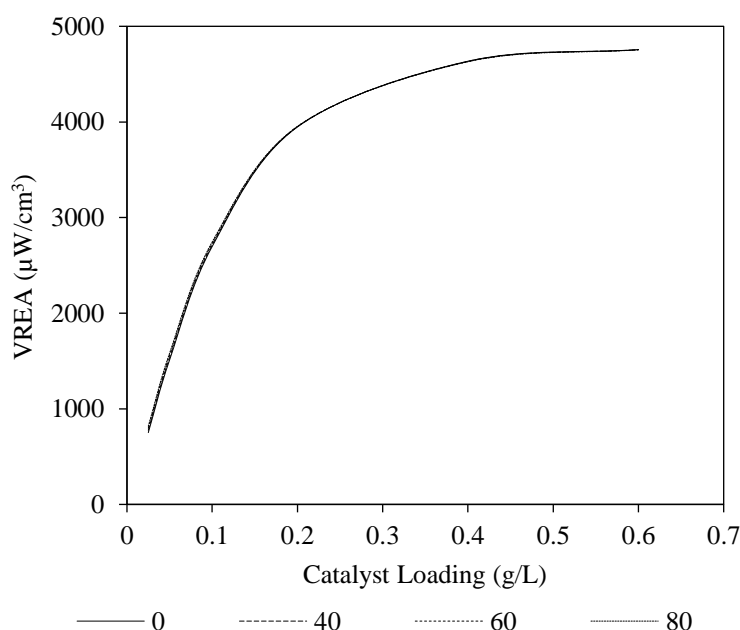


**Figure 86: VREA at different catalyst loadings and air flow rates**

The VREA is a critical parameter often used in computing photocatalytic intrinsic kinetics (Puma et al., 2010). In photocatalytic reactor design, the VREA can be used as an analogue of the reaction rate constant. As a result, several authors (Moreira et al., 2010; Valades-Pelayo et al., 2014b) have used the VREA to determine the optimum catalyst loading from light distribution experiments without the need for carrying out photocatalysis experiments. From an analysis of the effect of catalyst loading on the VREA (Figure 86), the optimum catalyst loading can be determined as the amount of catalyst beyond which no increase in the VREA is observed. At the optimum catalyst loading, the maximum amount of light is utilised at the lowest catalyst loading. The optimum catalyst has been determined from VREA as the catalyst loading at the onset of the asymptote (Valades-Pelayo et al., 2014b). For the reactor and light source used in this study, the optimum catalyst loading was determined to be 0.4 g/L at all air flow rates.

Both TTR and VREA values show that the air flow rate had a negligible effect on the light distribution in the reactor. This observation is consistent with the findings of Motegh et al. (2013). The negligible influence of air flow rate can be explained by an analysis of the photon-catalyst and photon-bubble scattering events that are responsible for light distribution. During the Monte Carlo simulation, the number of photon-catalyst and photon-bubble events were tracked. Figure 87 shows the sum of the photon-catalyst and photon-bubble events at different catalyst loadings and air flow rates. The number of photon-catalyst-bubble events was observed to increase with an increase in the catalyst loading. However, an increase in the gas flow rate resulted in only a marginal change in the number of photon-catalyst-bubble scattering events. This was because the number of photon-catalyst events was very high compared with the number of photon-bubble events. As a result, light distribution in the reactor was mainly driven by catalyst particles.

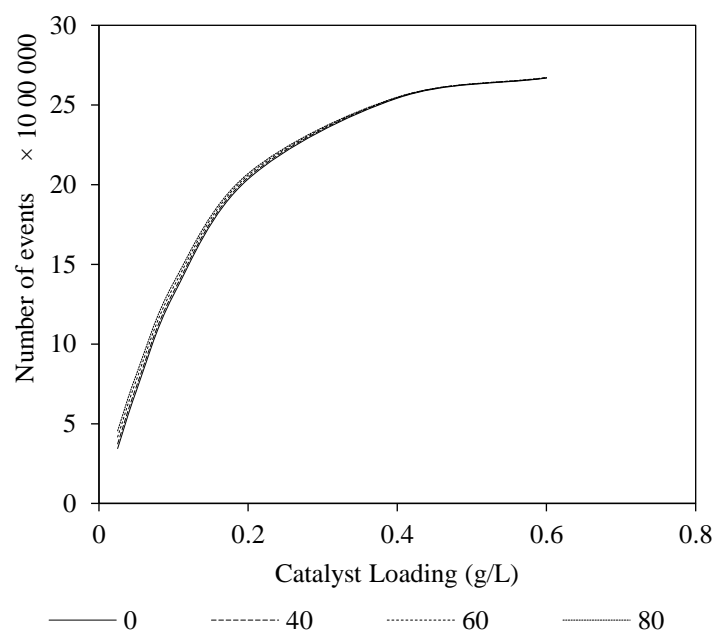


**Figure 87: Sum of photon-bubble and photon-catalyst scattering events at different catalyst loadings and air flow rates**

Bubbles had a very limited role in the light distribution even at high gas flow rates. Figure 88a–Figure 88d compare the experimental TTR measurements with the Monte Carlo simulation carried out without including photon-bubble interactions. The simulation shows good agreement with experimental data at the different air flow rates. This suggests that photon-bubble interactions can be neglected without considerable loss in accuracy during the Monte Carlo simulation. Neglecting the photon-bubble interactions has the advantage of increasing the speed of the Monte Carlo simulation.

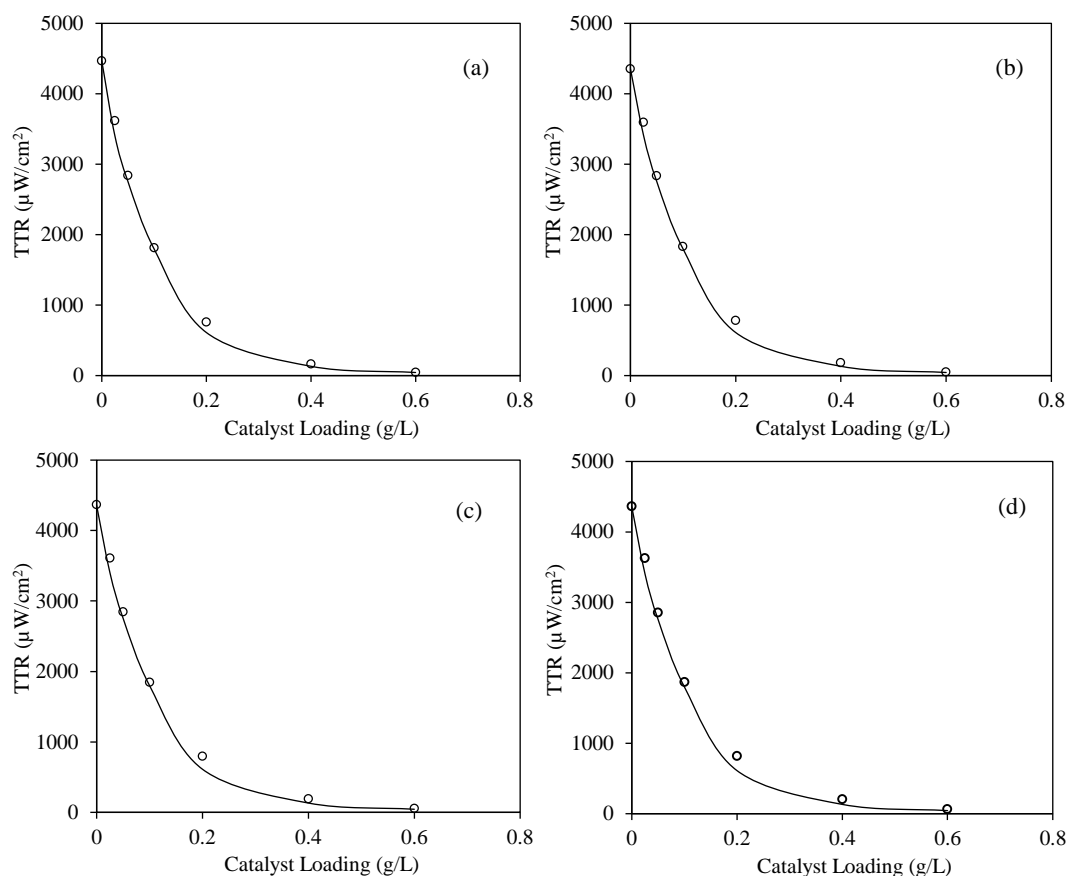


**Figure 88: Comparison of experimental TTR with simulation values carried out by neglecting bubble-photon interactions in the Monte Carlo simulation: (a) 0 L/h, (b) 40 L/h, (c) 60 L/h, (d) 80 L/h**

## 8.4 Conclusion

In this work, a Monte Carlo light distribution model incorporating bubbles was developed to simulate the light distribution in an annular fluidized bed photocatalytic reactor. The model was validated by experimental TTR measurements at different catalyst loadings and air flow rates. The catalyst was found to display forward scatter with a scattering parameter of 0.81. Both experiments and simulation showed that air flow rate had a negligible effect on the light distribution. This was attributed to the insignificance of bubble scattering as compared with the catalyst scattering and the fact that air flow had a negligible effect on the catalyst agglomeration. The light distribution in the FBR could be simulated accurately without accounting for bubbles. For the reactor setup and light source used, the optimum catalyst was predicted to be 0.4 g/L using light distribution analysis.

## 8.5 References

- Boyjoo, Y., Ang, M. & Pareek, V. (2013). Light intensity distribution in multi-lamp photocatalytic reactors. *Chemical Engineering Science*, 93, 11-21.
- Braham, R.J. & Harris, A.T. (2009). Review of major design and scale-up considerations for solar photocatalytic reactors. *Industrial & Engineering Chemistry Research*, 48(19), 8890-8905.
- Cassano, A.E. & Alfano, O.M. (2000). Reaction engineering of suspended solid heterogeneous photocatalytic reactors. *Catalysis Today*, 58(2), 167-197.

- Changrani, R. & Raupp, G.B. (1999). Monte Carlo simulation of the radiation field in a reticulated foam photocatalytic reactor. *AIChE Journal*, 45(5), 1085-1094.
- Imoberdorf, G.E., Taghipour, F., Keshmiri, M. & Mohseni, M. (2008). Predictive radiation field modeling for fluidized bed photocatalytic reactors. *Chemical Engineering Science*, 63(16), 4228-4238.
- Malato, S., Fernández-Ibáñez, P., Maldonado, M.I., Blanco, J. & Gernjak, W. (2009). Decontamination and disinfection of water by solar photocatalysis: Recent overview and trends. *Catalysis Today*, 147(1),1-59.
- MATLAB. (2015). Natick, MA: Mathworks.
- Moreira, J., Serrano, B., Ortiz, A. & De Lasa, H. (2010). Evaluation of photon absorption in an aqueous TiO<sub>2</sub> slurry reactor using Monte Carlo simulations and macroscopic balance. *Industrial & Engineering Chemistry Research*, 49(21), 10524-10534.
- Motegh, M., Van Ommen, J.R., Appel, P.W., Mudde, R.F. & Kreutzer, M.T. (2013). Bubbles scatter light, yet that does not hurt the performance of bubbly slurry photocatalytic reactors. *Chemical Engineering Science*, 100, 506-514.
- Ochieng, A., Ogada, T., Sisenda, W. & Wambua, P. (2002). Brewery wastewater treatment in a fluidised bed bioreactor. *Journal of Hazardous Materials*, 90(3), 311-321.
- Orozco, S.L., Arancibia-Bulnes, C.A. & Suárez-Parra, R. (2009). Radiation absorption and degradation of an azo dye in a hybrid photocatalytic reactor. *Chemical Engineering Science*, 64(9), 2173-2185.
- Pareek, V., Chong, S., Tadó, M. & Adesina, A.A. (2008). Light intensity distribution in heterogenous photocatalytic reactors. *Asia-Pacific Journal of Chemical Engineering*, 3(2), 171-201.
- Puma, G.L., Puddu, V., Tsang, H.K., Gora, A. & Toepfer, B. (2010). Photocatalytic oxidation of multicomponent mixtures of estrogens (estrone (E1), 17 $\beta$ -estradiol (E2), 17 $\alpha$ -ethynylestradiol (EE2) and estriol (E3) under UVA and UVC radiation: Photon absorption, quantum yields and rate constants independent of photon absorption. *Applied Catalysis B: Environmental*, 99(3), 388-397.
- Valades-Pelayo, P.J., Del Rio, J.M., Solano-Flores, P., Serrano, B. & De Lasa, H. (2014a). Establishing photon absorption fields in a Photo-CREC Water II Reactor using a CREC-spectroradiometric probe. *Chemical Engineering Science*, 116, 406-417.
- Valades-Pelayo, P.J., Moreira, J., Serrano, B. & De Lasa, H. (2014b). Boundary conditions and phase functions in a Photo-CREC Water-II reactor radiation field. *Chemical Engineering Science*, 107, 123-136.
- Valades-Pelayo, P.J., Sosa, F.G., Serrano, B. & De Lasa, H. (2015). Eight-lamp externally irradiated bench-scale photocatalytic reactor: Scale-up and performance prediction. *Chemical Engineering Journal*, 282, 142-151.

## **9 OVERALL CONCLUSION**

This study is a further development of the previous study that showed the feasible integration of AD with AOP to improve biogas production and methane yield. In this study, the focus was on developing photocatalysts further and optimising the operating parameters for both AD and AOP in order to generate bioenergy that can help reduce the cost of running AOP. Both studies have now shown that the performance of the integrated system depends not only on the sequence but also on the hydraulic retention in the AD. The study further showed that different simulation and modelling techniques such as CFD, Monte Carlo and RSM can be used for designing and optimising the operating conditions. Future work is needed to improve performance indicators such as mixing, irradiation penetration or distribution, mass transfer and catalyst efficiency.

*Page left blank intentionally*

## APPENDIX

### APPENDIX A: MONTE CARLO ALGORITHM

#### Bubble location

An algorithm adapted from Imoberdorf et al. (2008) was used to specify the random location of bubble centroids under the following restrictions and assumptions:

- i. All bubbles were assumed to be spherical with a uniform diameter of 6 mm.
- ii. To keep a bubble from intersecting with a reactor boundary, bubble centroids were offset from all reactor boundaries by the radius of bubble.
- iii. The minimum distance between two bubble centroids was specified to be equal to the bubble diameter to prevent bubble overlap.

The number of bubbles ( $n_b$ ) was calculated from the gas hold-up as:

$$n_b = \frac{3\varepsilon_g}{4\pi r_B^3} \quad (A1)$$

where  $\varepsilon_g$  was the gas hold-up and  $r_B$  was the bubble radius.

A random bubble centroid location in cartesian coordinates ( $x_B, y_B, z_B$ ) was specified using equations A2–A5 in order to satisfy constraint (ii). If a specified bubble was found to overlap another bubble (constraint (iii)), it was discarded and another random bubble generated. This process was continued until the required number of bubble centroids had been specified.

$$b_R = (r_{GS} + r_B) + (r_W - r_{GS} - 2r_B)R_1 \quad (A2)$$

$$x_B = b_R \cos(2\pi R_2) \quad (A3)$$

$$y_B = b_R \sin(2\pi R_2) \quad (A4)$$

$$z_B = (2R_3 - 1)(r_{SL} - r_B) \quad (A5)$$

where  $b_R$  was the bubble radial location,  $r_{GS}$  was the outer glass sleeve radius,  $r_W$  was the reactor radius,  $r_{SL}$  was the reactor semi-length and  $R_1, R_2, R_3$  were random numbers. Figure A1a–c shows random bubble centroid distributions for different air flow rates obtained using Eqs. A1–A5. As required, the simulated bubble centroids were randomly distributed within the reactor annulus (Figure 82) and increased with an increase in the number of bubbles.

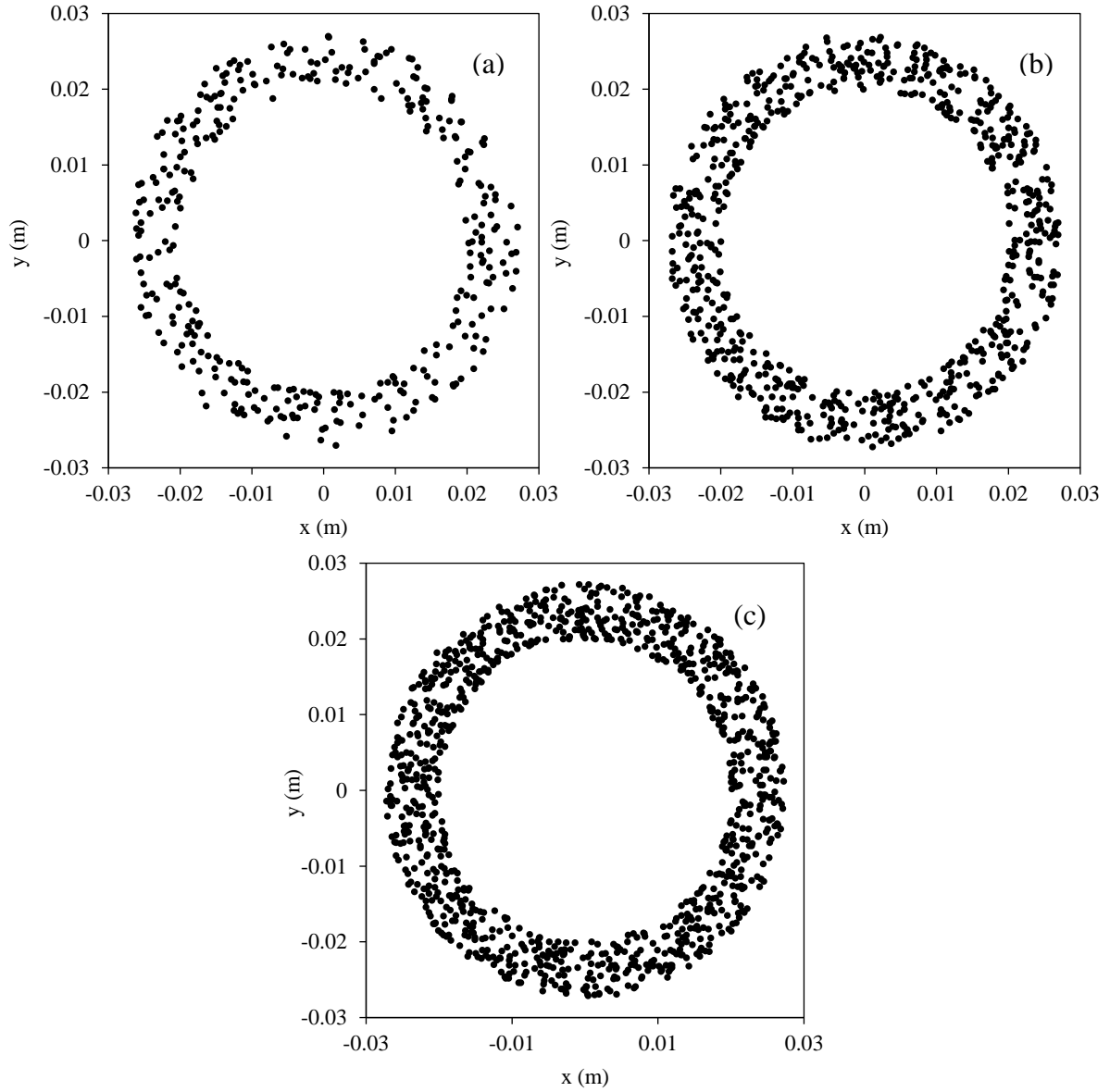


**Figure A1: Random bubble centroid distributions at various air flow rates. (a) 40 L/h, (b) 60 L/h, (c) 80 L/h**

### Lamp emission

The lamp emission was modelled using a stochastic volumetric emission model (Imoberdorf et al., 2008), which treated photons as originating from random locations within the lamp volume. The random angular emission location ( $\phi_L$ ) within the lamp volume was determined as:

$$\phi_L = 2\pi R_4 \quad (A6)$$

from which the radial lamp emission location in cartesian coordinates ( $x_L, y_L$ ) was given as:

$$x_L = r_L R_5 \cos(\phi_L) \quad (A7)$$

$$y_L = r_L R_5 \sin(\phi_L) \quad (A8)$$

where  $r_L$  was the lamp radius and  $R_4$  and  $R_5$  were random numbers.

The lamp emission intensity along the axial coordinate has been found to be highest at the middle of the lamp and lowest at the lamp extremities. Tsekov et al. (1997) represented this trend using the probability density function:

$$P_z = 0.5 \frac{z - a}{\sqrt{r_L^2 + (z + a)^2}} - \frac{z - a - L}{\sqrt{r_L^2 + (z - a - L)^2}} \quad (A9)$$

where  $P_z$  is the probability of a photon being emitted from an axial location  $z$  on the lamp surface,  $a$  is the axial distance between the lamp and the reactor wall, and  $L$  is the height of the reactor. The axial emission location was randomly selected using a cumulative probability density function derived from the model by Tsekov et al. (1997). Black light lamps have an emission spectrum such that photons emitted from the lamp can have a range of wavelengths. Figure A2 shows the emission spectrum of the lamp measured using the spectroradiometer with the radiometer sensor positioned on the surface of the lamp. The lamp spectrum shows that the lamp emits photons between 350 nm and 387 nm with the majority of emitted photons having a wavelength of 368 nm. The wavelength of the emitted photon was randomly chosen using a cumulative probability density function derived from the lamp spectrum.

After specifying the photon emission location and wavelength, the direction of photon flight was specified using random azimuth and zenith angles. The random azimuth angle ( $\phi$ ) was specified as:

$$\phi = 2\pi R_6 \quad (A10)$$

The random zenith angle of photon flight was specified as:

$$\theta = \text{acos}(2R_7 - 1) \quad (A11)$$

where  $R_6$  and  $R_7$  were random numbers.

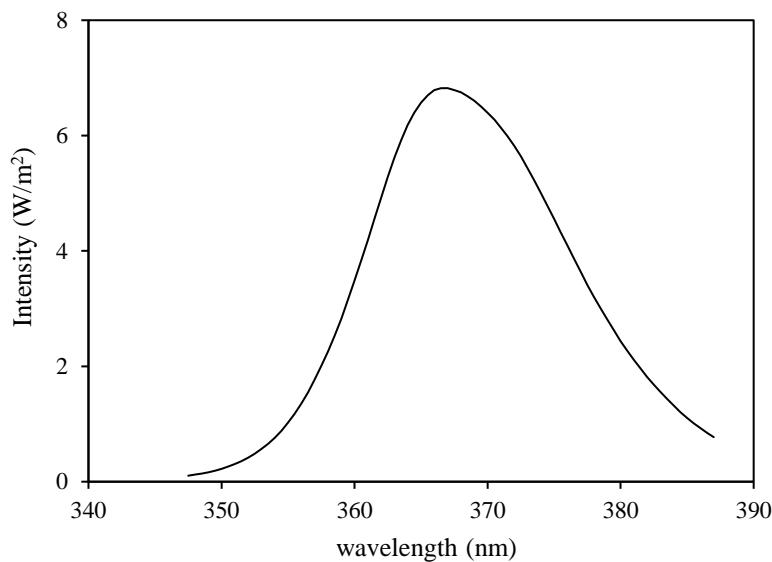


**Figure A2: Black light lamp spectra**

## Photon path

Once the photon direction was specified, the photon was moved across the air gap until it hit the inner glass sleeve. At this point, there was a 5.17% probability of the photon being absorbed by the glass sleeve. This absorption event was calculated using another random number  $R_8$ . If  $R_8 < 0.0517$ , the photon was absorbed; otherwise, the photon was transmitted through the glass sleeve with refraction. The change in direction due to refraction was computed using Fresnel laws for unpolarised light. After the photon crossed the glass sleeve, the photon started moving within the slurry. The free photon path length in the slurry during which time no photon absorption or scattering occurred was determined as (Pareek et al., 2008):

$$l = -\frac{\ln(R_9)}{\beta_\lambda} \quad (A12)$$

where  $R_9$  was a random number and  $\beta_\lambda$  was the spectral extinction coefficient that is the sum of the water absorption coefficient, catalyst absorption coefficient and catalyst scattering coefficient at a wavelength of  $\lambda$ .

Once the photon had moved a distance  $l$  within the slurry, its new location in Cartesian coordinates was determined as:

$$x_N = x_O + (\sin \theta \cos \phi) l \quad (A13)$$

$$y_N = y_O + (\sin \theta \sin \phi) l \quad (A14)$$

$$z_N = z_O + (\cos \theta) l \quad (A15)$$

where  $x_N$ ,  $y_N$ ,  $z_N$  were the new updated cartesian coordinates while  $x_O$ ,  $y_O$ ,  $z_O$  were the previous coordinates.

## Absorption and scattering events

At this point, the photon was either absorbed or scattered. The absorption event was determined as (Changrani & Raupp, 1999):

$$R_{10} < \frac{\kappa_\lambda}{\kappa_\lambda + \sigma_\lambda} \quad (A16)$$

where  $R_{10}$  was a random number while  $\kappa_\lambda$  and  $\sigma_\lambda$  were the absorption and scattering coefficients, respectively. The spectral scattering and absorption coefficients used in this work were obtained from Romero et al. (2003). If the photon was absorbed, its energy was stored in a location matrix composed of 10 radial regions and 60 axial regions. The LVREA was computed as:

$$LVREA(s) = \kappa_\lambda G_\lambda(s) \quad (A17)$$

where  $G_\lambda(s)$  was the photon energy at a certain discretized location in the reactor. The VREA was obtained by summing the LVREA values at all the discretized locations.

If the photon was not absorbed, it was scattered. The scattering azimuth direction ( $\phi_s$ ) was calculated as:

$$\phi_s = 2\pi R_{11} \quad (A18)$$

The scattering zenith direction was determined using the Henyey–Greenstein function and a random number as (Moreira et al., 2010):

$$\cos(\theta_s) = \begin{cases} \frac{1}{2g} \left[ 1 + g^2 - \left( \frac{1 - g^2}{1 - g + 2gR_{12}} \right)^2 \right], & \text{if } g \neq 0 \\ 2R_{12} - 1, & \text{if } g = 0 \end{cases} \quad (A19)$$

where  $R_{10}$ ,  $R_{11}$  and  $R_{12}$  were random numbers and  $g$  was the Henyey–Greenstein phase function scattering parameter whose value lies between  $-1$  and  $1$ . A  $g$  value of  $-1$ ,  $0$  and  $1$  refers to completely backward, isotropic and completely forward scattering, respectively. The zenith scattering angle ( $\theta_s$ ) was then calculated as:

$$\theta_s = \text{acos}(\cos(\theta_s)) \quad (A20)$$

In case the photon flight path in the slurry intersected a bubble, the photon was reflected on the bubble or transmitted by refraction through the bubble. The reflection or transmission event was determined based on the photon incident angle on the bubble. The change of directions due to refraction were computed using Fresnel equations of unpolarised light. The reflected or transmitted photon then continued its flight through the slurry.

The series of absorption and scattering events in the slurry and bubbles were continued until the photon either hit the outer glass sleeve, reactor wall or the sensor. On hitting the outer glass sleeve, the photon could be absorbed or transmitted to the air gap with refraction from where it was reflected off the lamp. A photon that hit the reactor wall could be absorbed (with a probability of 8%) or transmitted by refraction to the air outside the reactor. The transmitted photon could hit the radiometer sensor or be lost outside the reactor. If the photon hit the sensor, its energy was added to the TTR variable and then it was considered lost. Once a photon was lost, a new photon was emitted from the lamp, which involved going back to step 1.

A large number of photons packets ( $10^7$ ) was emitted and tracked through the reactor. In this way, the light distribution in the reactor was determined by analysing the photon energy absorbed at different locations in the slurry. Figure A3 shows a section of the photocatalytic reactor illustrating photon flight from the lamp to the radiometer sensor. The Monte Carlo algorithm was written and solved in MATLAB (MATLAB, 2015).

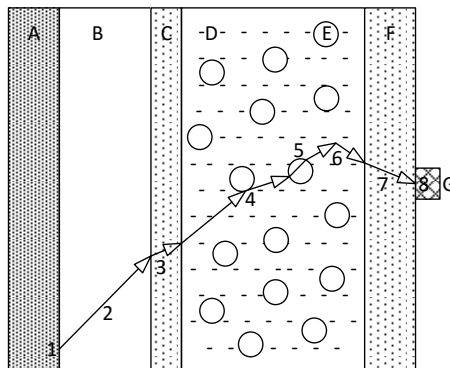


**Figure A3: Photon flight in the reactor: (1) Emission location, (2) Air gap photon flight, (3) Glass sleeve refraction, (4) Bubble scattering, (5) Bubble transmission, (6) Slurry scattering, (7) Reactor wall refraction, (8) Sensor absorption. (A) Lamp, (B) Air gap, (C) Glass sleeve, (D) Catalyst slurry, (E) Bubble, (F) Reactor wall, (G) Radiometer sensor**

## APPENDIX B: ANAEROBIC BIODEGRADATION OF SYNTHETIC ABATTOIR WASTEWATER

### B.1 Effect of hydrodynamics on liquid hold-up profiles

Figure B1 shows a rapid COD decrease with an increase in the recirculation flow rate up to about 3.33 cm/s. A further increase in recirculation rate did not result in any observable increase in the COD reduction; this corresponds to a 51% reduction in five hours. The results indicate that the reaction could be mass transfer limiting at low recirculation flow rates. However, this reduction of 51% is still very low; hence, in further studies the effect of other parameters such as the initial concentration and the substrate molecular structure has to be investigated. This low COD reduction could be due to exhaustion of nutrients and metabolic activity during the degradation process. Similar results have been reported by Ince et al. (2000).

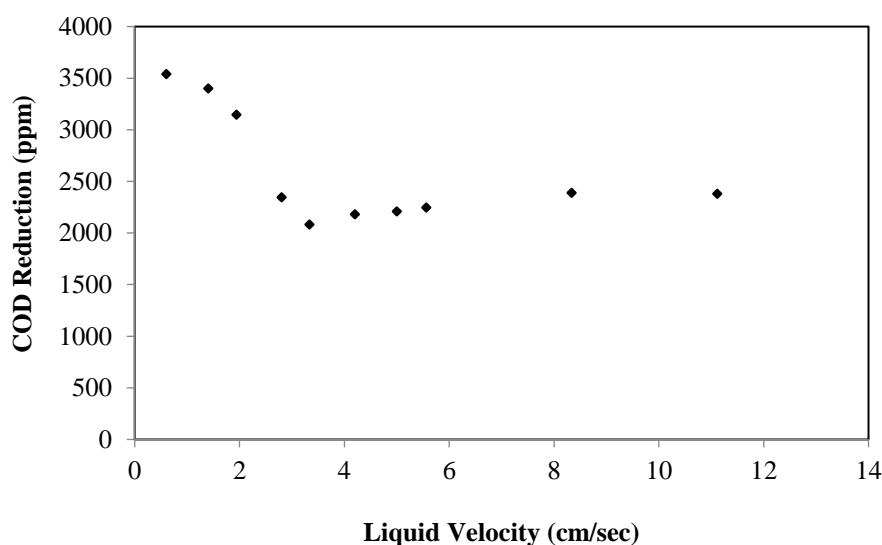
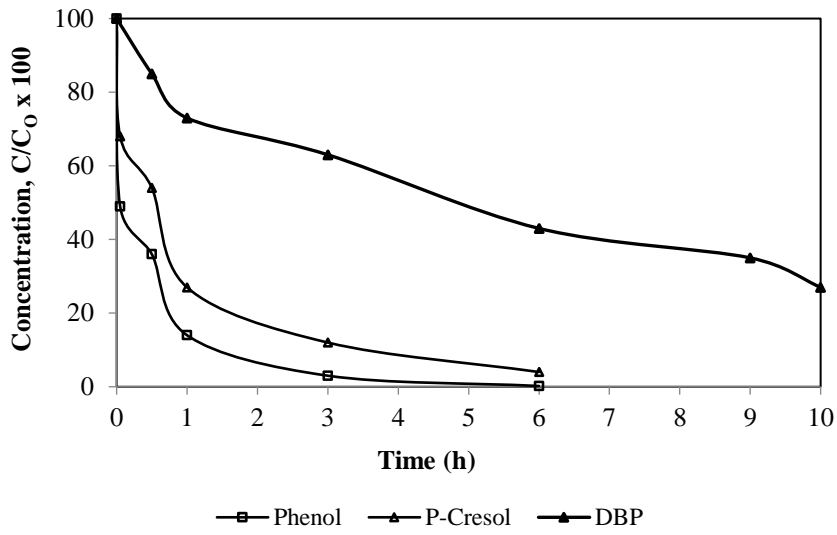


Figure B1: Variation of COD reduction with liquid velocity

#### B.1.2 Anaerobic digestion of different substrates

Further investigation was done on the obtained optimum recirculation velocity of 3.33 cm/s with different substrates at low initial concentration. The substrates used were phenol, p-cresol and dibutyl-phthalate with initial concentrations of 100 ppm, 110 ppm and 200 ppm. Figure B2 shows that phenol was degraded by 98% and p-cresol by 95%, respectively, over contact time of about six hours at 37°C. However, dibutyl-phthalate was degraded by 75%, which could be due to its structural complexity. High phenol and p-cresol degradation could result from the formation of an active biomass in the reactor after addition of the nutrients. During AD, the bacterial activity and growth tend to decrease by one half for each 10% drop below 35°C, which leads to the AD period being prolonged under low temperature, and energy consumption of the process increased. However, Gallert et al. (1998) reported that higher temperature (37–55°C) can lead to an increase in toxicity and instability of certain compounds formed during anaerobic treatment.



**Figure B2: Degradation of aromatics in abattoir wastewater using FBB at flow rate of 3.33 cm/sec for 120 mm bed height support**